Carbon Nanotubes

Recent Advances, New Perspectives and Potential Applications

Edited by Mohammed Muzibur Rahman,
Abdullah Mohammed Asiri
and Mohammad Asaduzzaman Chowdhury

Carbon Nanotubes - Recent Advances, New Perspectives and Potential Applications

Edited by Mohammed Muzibur Rahman, Abdullah Mohammed Asiri and Mohammad Asaduzzaman Chowdhury

Contributors

Sudipta Sen, Nabin Baran Manik, Hassan A.H. Alzahrani, Esther Torres-Santillan, Selene Capula-Colindres, Gerardo Teran, Carmen M. Reza-San German, Miriam Estrada-Flores, Oscar Guadalupe Rojas Valencia, Jay Shankar Kumar, Ashok Kumar, Sanjay Kumar, Shalu Rani, Ritesh Bhardwaj, Youssef Nadir, Hassan Belahrach, Abdelilah Ghammaz, Aze-Eddine Naamane, Mohammed Radouani, Challa Gangu Naidu, Challa V. Ramana, Yarraguntla Srinivasa Rao, Dadi Vasudha, Kollabathula Vara Prasada Rao, Koppisetty B. Rajeshbabu, Gandi Anusha, Abdullah Abdulhameed, Mohammed Muzibur Rahman, Abu Taleb, Mohammed Naif Al-sharif, Mohammed Ali Al-mutair, Saleh Almasoudi, Osama Madkhali

Notice

Statements and opinions expressed in the chapters are these of the individual contributors and not necessarily those of the editors or publisher. No responsibility is accepted for the accuracy of information contained in the published chapters. The publisher assumes no responsibility for any damage or injury to persons or property arising out of the use of any materials, instructions, methods or ideas contained in the book.

We are IntechOpen,
the world's leading publisher of
Open Access books
Built by scientists, for scientists

6,300+
Open access books available

171,000+
International authors and editors

190M+
Downloads

156
Countries delivered to

Our authors are among the
Top 1%
most cited scientists

12.2%
Contributors from top 500 universities

Interested in publishing with us?
Contact book.department@intechopen.com

Numbers displayed above are based on latest data collected.
For more information visit www.intechopen.com

Meet the editors

Mohammed Muzibur Rahman has been a professor at the Center of Excellence for Advanced Materials Research (CEAMR) and Chemistry Department at King Abdulaziz University, Saudi Arabia since 2019. He obtained his BSc and MSc from Shahjalal University of Science and Technology, Sylhet, Bangladesh, in 1999 and 2001 respectively, and his Ph.D. from Chonbuk National University, South Korea, in 2007. Between 2007 and 2011 he held postdoctoral fellowships in pioneering research centers and universities in South Korea, Japan, and Saudi Arabia., He has published more than 430 research articles, 41 book chapters, and 10 US patents, and has edited 26 books. His principal research interests are carbon nanotubes, sensors, nanotechnology, nanocomposites, nanomaterials, carbon nanofibers, photocatalysis, semiconductors nanoparticles, electro-catalysis; ionic liquids, surface chemistry and electrochemistry.

Abdullah Mohamed Asiri is a professor of organic photochemistry. He has been head of the Chemistry Department at King Abdul Aziz University since 2009 and is the founder and director of the Center of Excellence for Advanced Materials Research (CEAMR). He received his Ph.D. from the University College of Wales, Cardiff, UK in 1995. His research interests are color chemistry, synthesis of novel photochromics, thermochromic systems, synthesis of novel coloring matters and dyeing of textiles, materials chemistry, nano-chemistry, nanotechnology, polymers, and plastics. He is the editor-in-chief of *King Abdulaziz University Journal of Science*. He is also a member of the editorial boards of *Pigments and Resin Technology* (UK), *Organic Chemistry in Sight* (New Zealand), and *Recent Patents on Materials Science* (USA). He is the Vice-President of the Saudi Chemical Society (Western Province Branch).

Mohammad Asaduzzaman Chowdhury is a professor of mechanical engineering at Dhaka University of Engineering and Technology (DUET), Gazipur, Bangladesh with about 21 years of teaching and research experience. His research interests are engineering tribology, surface engineering, automation and robotics, coating technology, polymer and composite materials, and characterization of materials. He is an editorial board member of many reputed international journals. He has published many research and review papers in refereed international journals and conference proceedings. He works as a consultant, advisor and expert member of many government and autonomous organizations, and is an editorial board member of many reputed international journals. He is involved in a variety of cultural and social activities, and writes articles, stories, lyrics and poems for newspapers and other media.

Contents

Preface

Advances in the instrumentation used to evaluate nanostructure models now enable us to understand almost all the events that take place in carbon materials at the nano level. *Carbon Nanotubes - Recent Advances, New Perspectives and Potential Applications* reviews the state of the art of carbon materials, their synthesis, characterization, and potential applications. Nanotechnological aspects of the synthesis, growth and development of CNTs are covered, as well as new paths and emerging frontiers. The discussion includes fundamentals and conventional applied experimental routes, the interaction of carbon materials and, finally, the interface of nanoscience and nanotechnology.

This book seeks to bridge the gap between undergraduate, graduate, and research studies in applied carbon material sciences, with a view to introducing scientists to the opportunities offered by applied carbon science and the associated technology. I hope that this contribution will bring new entrants into the fields of applied science and nanotechnology, and will help scientists to develop their own specializations.

Mohammed Muzibur Rahman and Abdullah Mohammed Asiri
Department of Chemistry,
King Abdulaziz University,
Jeddah, Saudi Arabia

Mohammad Asaduzzaman Chowdhury
Dhaka University of Engineering and Technology,
Gazipur, Bangladesh

Section 1

State-of-the-Art Synthesis

Chapter 1

CuO and MWCNTs Nanoparticles Filled PVA-PVP Nanocomposites: Morphological, Optical, Dielectric, and Electrical Characteristics

Hassan A.H. Alzahrani

Abstract

Copper dioxide (CuO) nanoparticles and multiwall carbon nanotubes (MWCNTs)-filled poly(vinyl alcohol) (PVA) and poly(vinyl pyrrolidone) (PVP) blend matrix (50/50 wt%)-based polymer nanocomposites (PNCs) have been prepared employing the solution-cast method. The X-ray diffraction explores the semicrystalline morphologies of these PNCs. The FTIR, SEM, and AFM measurements of PNCs expose the development of the miscible mix, polymer-polymer and polymer-nanoparticle interactions, and the influence of CuO and MWCNTs nanofillers on the morphology aspects on the main chain of PVA/PVP blend. The nanofiller loading for x = 14 wt% in the PVA–PVP blend matrix significantly enhances the crystalline phase, diminishing the optical energy gap to 2.31 eV. The DC conductivity is found to be maximum for x = 14 wt% loading concentration. The dielectric and electrical characteristics of these PNCs are investigated for an applied frequency range from 1 kHz to 1 MHz. The dielectric permittivity values increase substantially, owing to the decrease in the nano-confinement phenomenon at low frequency. The rise in applied frequency reduces dielectric permittivity and impedance values and enhances AC electrical conductivity. These PNCs having good dielectric and electrical characteristics can be used as frequency tunable nano-dielectric material in electronic devices.

Keywords: PVA, PVP, nanoparticles, nanocomposites, electrical properties, fillers

1. Introduction

Architectural polymers have become a subset of polymers with strong structural, optical, and electrical capabilities, outstanding geometrical durability, high weather resistance, and excellent fatigue strength [1–4]. This initiated the mixing of polymers, also known as polymer blending, a kind of engineering polymer that is similar to metallic ingots, and is created by combining at least two polymers to create a

separate material with varying basic properties [5–8]. The method of polymer blends includes melting, solvent blending, latex melding, partial blocking or grafting copolymerization, and the development of interpenetrating polymeric networks [9, 10]. Out of all previously stated, solvent blending is a very cost-effective and straightforward method of producing polymer mixtures. The solvent blending encompasses combining two or more polymers that are frequently immiscible and have compatible components. The interoperability should improve the frequency of the microstructures as well as the capabilities of the substance in terms of structural and bonding properties. In this regard, the poly(vinyl alcohol) (PVA) and poly(vinyl pyrrolidone) (PVP) mixture has developed remarkable qualities, including high elasticity, flexibility, nontoxicity, good mechanical strength, and thermal stability [11–13]. These configurations also have water-soluble, miscible, excellent electro-optic properties, and composite materializing attributes [2, 14]. Many investigators are involved in their research activities using PVA-PVP mixtures filled with nanoparticles to create a new polymer nanocomposite (PNCs) for any suitable technological applications [2, 15–17]. Because of their diverse advancement in different new tech, nanoparticles to be fully integrated into the polymer matrix, copper oxide (CuO), and multiwall carbon nanotubes (MWCNTs) have emerged as excellent nanofillers [18, 19]. The CuO nanoparticles belong to a class of transition metal oxide, with monoclinic structures and p-type semiconducting properties. These highly stable CuO nanofillers also have intriguing properties including outstanding thermophysical properties, good dispersion, photovoltaic capabilities, and antibacterial activity [19, 20]. Other nanofiller multiwall carbon nanotubes (MWCNTs), on the other hand, encompass many popped graphene sheets with structural complexity and variation. MWNTs, on the other hand, benefit from huge manufacturing facilities, low unit costs of production, improved thermodynamic features, and chemically resilient components. These MWCNTs can be used in sensitive gas detection materials, dielectric materials, and technologically challenging applications such as field emission and optoelectronic screens [14, 21–23]. This current chapter explores the fabrication of PVA-PVP: (15-x)CuO(x) MWCNTs nanocomposite by the means of solvent casting method for filler levels x = 0, 1, 5, 7.5, 10, 14, and 15wt percent. The preparation of composites by solvent casting method will have benefits such as uniform thickness, enhanced gloss, flexibility, low cost, and also no defects (die lines, extrusion, etc.). The fabricated PNCs are then investigated to explore the structural, optical, dielectric, and electronic properties of any potential device fabrication.

2. Experiments and results

In this current chapter, I have used CuO as one of the nanofillers. In the order to the synthesis of CuO nanofillers, I used crucial laboratory solution grades throughout the investigation. The required reagents (Cu $(C_2H_3O_2)_2$) and NaOH for the preparation were procured from Sigma-Aldrich, Germany. 0.02 mol of liquid copper acetate is treated with 1 ml glacial acetic acid. The combination is boiled at 110°C for 1 hour agitating with 500 rpm. 1 M NaOH acid is added to the sample outlined earlier, resulting in the formation of a dark cloud. Using a centrifuge, the precipitation caused by the mixture is retrieved to produce copper oxide nanofillers. This CuO aggregate is washed thoroughly with deionized water several times until all NaOH contaminants are removed until neutral pH values are achieved. The achieved CuO was then dried

for 8 hours in an oven at 500°C to remove the humidity component, yielding an approximate 94 percent.

On the other hand, nanofiller carbon nanotubes are considered due to unique properties such as enhanced configurability dispersal, compatibility, or reduced toxicity. 75 mg of multiwalled carbon nanotubes (MWCNTs with 3.5 nm diameter, 1–10m length, purity >90%, and specific surface area > 500 m2/g) was procured from Sigma-Aldrich and soaked in hydrochloric acid (HCl) for 24 hours. These soaked MWCNTs in HCl solution are mixed with 500 ml of distilled water and swirled for 20 minutes at a vigorous stirring rate of 500 rpm. The agitated blend was then screened through a Whatman Nylon filter membrane with a pore size of 0.1 m. The acquired remnant mixture is thoroughly treated until the pH level of the filtrated mixture is neutral. Following that, the MWCNTs were dried in a vacuum oven at 6000°C for 20 hours to remove the water component. Alternate MWCNTs were finely dispersed in a 3:1 volume proportion of sulfuric acid (H_2SO_4) and nitric acid (HNO_3) and homogenized for 2 hours using a probe ultrasonicator (PCI Analytics, India). After rinsing the dispersed mixture with distilled water until the filtrated solution is neutral, it is screened through a 0.1-m Whatman Nylon filter membrane. The precursor is cooked in a vacuum oven, and 73.2 mg of carboxylated MWCNTs (MWCNT-COOH) is produced.

PNCs are made by mixing 8 g of Mowiol 4–88 (PVA from Sigma-Aldrich, Germany, with a mean molecular weight of 31,000) with 80-ml deionized water and agitating for 60 minutes at 90°C to generate a transparent liquid. Similarly, 8 g of polyvinyl pyrrolidone (PVP, average molecular weight 40,000, Sigma Aldrich Germany) was combined with 80-ml deionized water. To make an acceptable liquid, this mixture is swirled for 2 hours at 70°C and 500 rpm. A motorized mixer was used to remix the clear, viscous liquid for 1 hour at room temperature (at 300 rpm). The resulting thick mixture is divided into eight equal parts. The following equation produces PVA-PVP:(15-x)CuO(x) MWCNTs nanocomposites with varied "x" nanofiller loadings:

$$x\% = \frac{W_d}{(W_d + W_p)} X100 \qquad (1)$$

where W_d and W_p signify the weight of the embedded nanofillers and host polymer blend, respectively.

The synthesized ZnO and MWCNTs nanofillers with weights of x = 0, 1, 5, 7.5, 10, 14, and 15 have been embedded in the matrix. Moreover, ultrasonicator is utilized to fill the nanofillers in every region of the PVA-PVP mix for 10minutes or until all nanofillers are evenly disseminated. Each component of the PVA-PVP:(15-x)CuO(x) MWCNTs solution is put on a glassware petri-dish and dried overnight in an oven at 500°C. Each nanocomposite is scraped and wrapped in a silver sheet before being kept in a vacuum environment for further examination.

The prepared PNCs have a thickness of 165–180 nm predicted using a DektaK stylus profilometer (Bruker). The structural parameters of PNCs are established *via* Cu-K reflections (=15406A) by the Empyrean third-generation Malvern Panalytical X-ray Diffractometer. **Figure 1** depicts the XRD spectra of PVA-PVP:(15-x)CuO(x) MWCNTs at various loading levels of the "x" filled compound x = 0 to 1, 5, 7.5, 10, 14, and 15% wt. Filled MWCNTs exhibit a small uptick in the diffraction angle of MWCNTs at 26.52 degrees (JCPDS file no: 48–1449). Peaks at 2 = 21.6°, 29.7°, 36.5°, 42.4°, and 61.4°, which are comparable to (014), (111), (200), and (113), indicate the
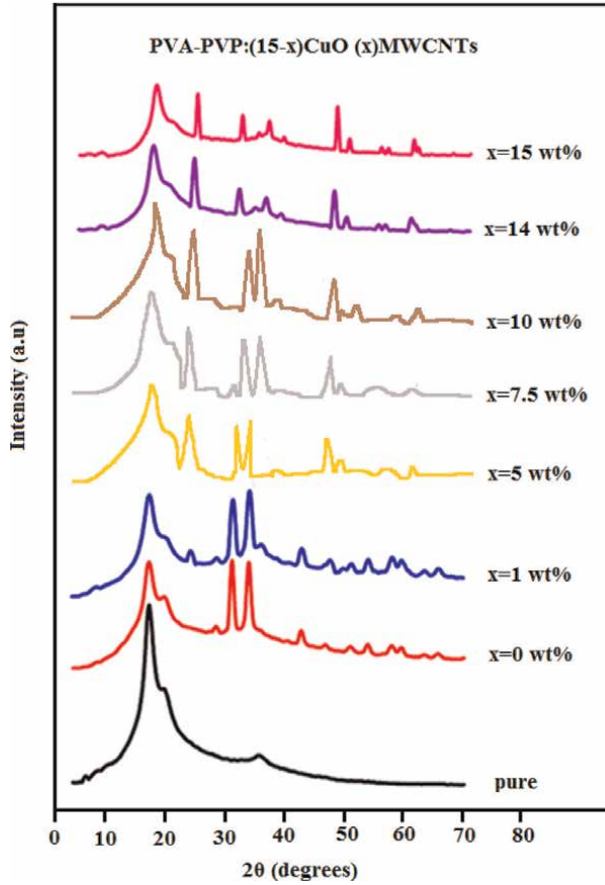
Figure 1.
XRD spectra of PVA-PVP:(15-x)CuO(x)MWCNTs PNCs.

presence of CuO nanoparticles. A broad, considerable rise is seen at scattering angles 19^0 to 20^0, which suggests the confirmation of the presence of a PVA semicrystalline peak (more precisely, of polyvinyl acetate). The PVP polymer long chain is indicated by the peak at 21.21^0, which corresponds to a d-value of 4.1544. Because of the incorporation of nanofillers, the breadth of semicrystalline peaks in PVA-PVP nanocomposite varies, revealing an increase in crystalline parameters. The strength of the crystallized spikes of PVA-PVP increases with filler level, and the results were mostly declared for filler level x = 14 percent. The OH group of the PVA-PVP back-bone sequence and CuO/MWCNT nanofillers work together to improve complex conformation, resulting in crystalline phase gain. As the filler level rises, the PVA-PVP peaks shift to a lower angle.

Table 1 also shows each microstructural strain (also referred to as strain), disloca-tion density (also referred to as density), and crystallinity (also known as phase) of PVA-PVP: (15-x)CuO(x)MWCNTs with varying filler dosage. The crystallite size in polymer nanocomposite evaluates molecular instability by integrating nanoparticles in the spine of the PVA-PVP polymer. We created an algorithm to describe the crystallinity behavior of composite materials using PowderX software (http://powdex. eng.umich.edu). The presence of intrinsic filler ions across the crystalline-state

Dopants concentrations (wt%)	% Crystallinity	D (nm)	Microstrain (ε) x 10^{-3}	δ (10^{16} lines/m^2)
Pure PVA-PVP	54.81	3.79	12.94	6.9618
0	53.96	9.89	4.313	1.022
1	55.01	10.06	4.224	0.988
5	56.03	10.91	3.780	0.840
7.5	57.12	11.78	2.133	0.720
10	57.67	12.52	1.997	0.637
14	58.92	13.88	1.487	0.519
15	56.71	12.59	1.812	0.630

Table 1.
Crystalline parameter values of PVA-PVP/(15-x)CuO(x)MWCNTs.

interstitial regions of the PVA-PVP backbone might be interpreted as a PVA main chain with nanofillers [24]. The "**x**" denotes filler weight concentration and for x = 14 percent, and the maximum crystallinity is observed. Recrystallization might play a significant role in the unexpected variation in defect characteristics of nanocomposites. Because of certain properties, the structural regularities of the PVA-PVP host molecule change when MWCNTs and CuO nanofillers are added. As a consequence, these factors improve the crystalline properties of PVA-PVP nanocomposites.

The occurrence of surface roughness as well as morphological changes in the filled composites was measured by the means of the solver-PRO (NT-MDT) AFM instrument. The tapping-mode AFM investigation evaluates the surface and roughness of the manufactured composites. **Figure 2(a)** and **(b)** shows two-dimensional (2D) AFM images of nanocomposite for unadulterated and optimal filler level x = 10wt percent. The root-medium-square (RMS) surface roughness of the composites is determined using the AFM topography in the scan region (**Table 2**). The RMS surface roughness
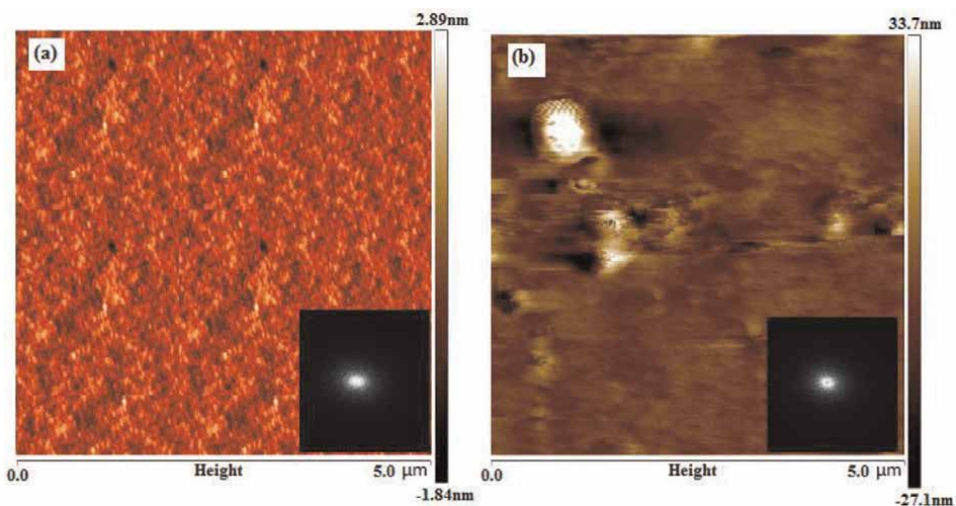
Figure 2.
AFM images (2D) with FFT transform spatial information of (a) pure PVA-PVP and (b) PVA-PVP with nanofillers for x = 14 wt% filler concentration.

Parameter	Mean	Minimum	Maximum	Sigma
Total count	8.000	8.000	8.000	0.000
Density	0.320 (/μm^2)	0.320 (/μm^2)	0.320 (/μm^2)	0.000 (/μm^2)
Height	14.508 (nm)	5.172 (nm)	42.576 (nm)	14.187 (nm)
Area	58031.082 (nm^2)	9536.743 (nm^2)	321960.438 (nm^2)	100274.750 (nm^2)
Diameter	216.134 (nm)	110.193 (nm)	640.260 (nm)	164.844 (nm)

Table 2.
AFM parameters of PVA-PVP:(15-x)CuO (x)MWCNTs of optimum filler loading x = 14 wt%.

measurements are 1.3 nm for x = 14 wt percent. The incorporation of nanofiller MWCNTs and CuO into the PVA-PVP mix improves the roughness of the RMS up to x = 14 wt percent loading. An improvement in the roughness indicates an improvement in the crystalline properties of nanocomposites. AFM images also display the linked images' quick two-dimensional fast Fourier transform (FFT). This 2-D FFT converts spatial info to frequency, which is highly valuable for analyzing the morphology of the nanocomposite surface. In the FFT images, the white dots represent the periodicity of surface morphology. The white point density is higher in the x = 14 wt percent filler level than in the pure PVA-PVP mix film. As a result, we may conclude that MWCNTs and CuO nanofillers are randomly oriented inside the PVA-PVP matrix, resulting in a large patch of scattered intensity at the center. **Figure 3** shows PVA-PVP 3-D photographs: (15-x)CuO (x)MWCNTs with x = 14 wt% nanofiller concentration. Within the PVA matrix, AFM suggests the particle heights of the order 33.7 nm having an average specific diameter of nearly 118.43 nm.

The cryo-scanning model SEM EVO 18 ALTO 1000 estimates the morphological structure, particle size estimation, and content of PNCs. **Figure 4** depicts SEM surface morphology, signposting both the nanofillers are equally dispersed in PVA-PVP for x = 14 wt%. It is also clear that the PVA-PVP combination shows the complex
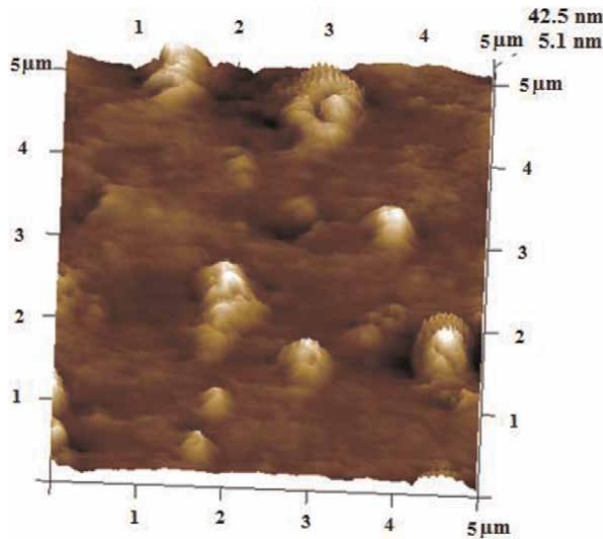
Figure 3.
AFM 3-dimensional photograph of PVA-PVP (15-x)CuO(x)MWCNTs for x = 14 wt%.
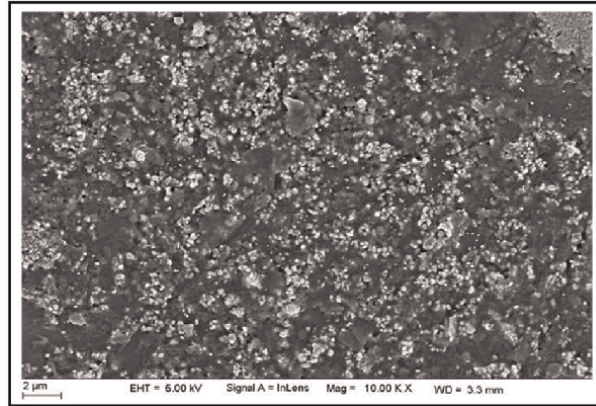
Figure 4.
SEM photographs of PVA-PVP:(15-x)CuO(x)MWCNTs for x = 14 wt%.
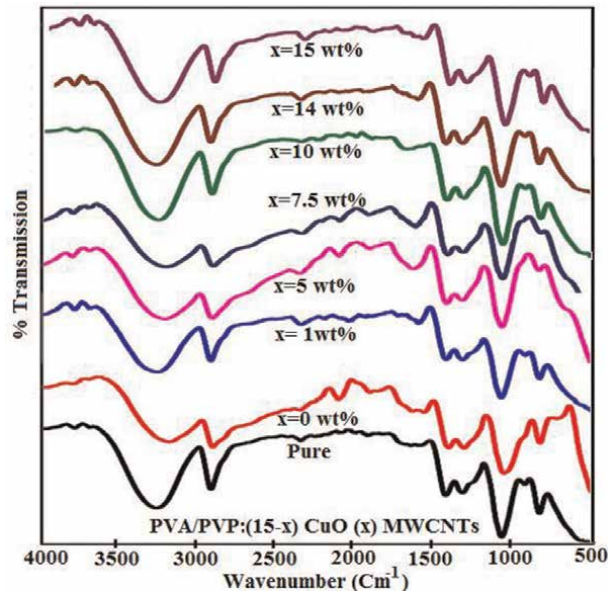
Figure 5.
FTIR spectra of PVP/PVA(15-x)CuO(x) MWCNTs PNCs.

entanglement with both added nanofillers CuO and MWCNTs, resulting in a homogeneous nanocomposite film. For optimal concentration x = 14wt percent, the entangling or binding between MWCNTs and CuO nanofillers is high. The high concentration of solely MWCNTs or CuO nanofillers restricts (x = 15wt percent or x = 0 wt percent) enhancement of the nanocomposites' structural behavior.

The FTIR spectra of PNCs are procured with 50 scans and 2 cm^{-1} precision using a KBr Pellets Varian Excalibur FTIR Spectrometer in the 500 to 4000 cm^{-1} range. In **Figure 5**, continuum demonstrated typical bending and stretching vibration of a structural class of constructed PVA-PVP:(15-x)CuO(x) MWCNTs PNCs. The presence of the O-H hydroxyl group in a pure PVP/PVA mix is indicated by the broad and extreme range peaks detected regularly at 2857–3631 cm^{-1}. The shifting of the O-H

band in the altered PVA-PVP mix corresponds to the amount of added nanofiller levels. The addition of filler up to x = 14wt percent changes the OH stretching frequencies to lower wavenumbers than pure PVA-PVP blends. The association of CuO and MWCNT nanofillers with the PVA/PVP-OH group is a key factor in enhancing the structural, optical, and electrical features. The narrowing of the hydroxyl band due to the nanofillers enhancement induces the semicrystalline in nanocomposite material. The rise in nanofillers leads to the OH vibrational bands of alcohol and phenols, at 3577 cm^{-1}, to shift toward the higher wavenumbers. In comparison with the pure PVA-PVP mix, the inclusion of nanofiller up to x = 14wt percent resulted in a shortening of the hydroxyl band. The peaks signifying at 2570 cm^{-1} represent a typical band of C-C oscillations of the PNCs. The primary chain PVA-PVP spectra are represented by three bands at 2492 and 2320, showing 141 cm^{-1} which shows the interaction of C-H symmetric distortion, CH$_2$ deformation, and C=O stretching with the loaded nanofillers [25]. The FTIR spectra show that the nanofillers CuO and MWCNTs move the several bands toward the lower frequency range. These modifications symbolize that the additional nanofillers entangle with C-H compounds in the PVA-PVP to generate complicated conformations [26]. An active absorption with band associated with symmetric and asymmetric stretching C=O of the PVA-PVP mix backbone structure originates at 1714–1011 cm^{-1}. The absorption peaks seen at 918 cm^{-1} indicate the PVA-PVP blend's syndiotactic structure. The addition of nanofillers improves the syndiotactic of the PVA-PVP mix, resulting in dense molecular packing and stronger intermolecular hydrogen bonding. These causes lead the molecular mobility to vanish, resulting in an increase in crystallinity inside the polymer matrix. Thus, the crystalline characteristics of PVP-PVA(15-x)CuO(x) MWCNTs PNCs were determined by the local surface chemistry, internal structural ordering of nanofillers, and strain engendered by nanofillers with the PVA-PVP host matrix.

Shimadzu UV-visible spectrometer is used to evaluate optical characteristics such as the energy gap of PVA-PVP (15-x)CuO(x) MWCNTs. **Figure 6** presents the UV-visible spectra of PNCs for varied dose amounts. The optical absorption coefficient increases as the loading dose increases. The intensity of the absorption bands increases with nanofiller content and exhibits redshifts, indicating an improvement in charge delocalization within the PVA-PVP network [27]. The formation of a complex
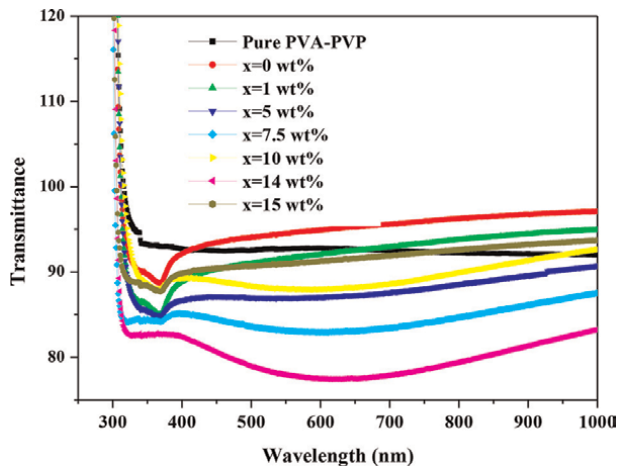
Figure 6.
UV-visible spectra of PVA-PVP:(15-x)CuO(x)MWCNTs PNCs.

between the host matrix and nanofillers enhances the shift in the absorption band. These intricate hydrophobic interactions increase nanofiller entanglement (complex conformation) with the host matrix, resulting in crystalline characteristics. The creation of complex conformation was found to be greatest until the filling level reached x = 10wt percent, modifying the wavelength of the absorption peaks and resulting in maximum absorption intensity. **Figure 7** exposes the indirect permitted transition of PNCs supplied by linear behavior at room temperature. The result of an extending of the linear component of the depicted curve from a measure of optical energy bandgap E_g of the PVA-PVP: (15-x)CuO (x) MWCNTs to $(hv)^{0.5} = 0$ is the optical energy bandgap E_g of PNCs. The graph depicts the respective bandgaps of PNCs for different loading levels. The reduction in the optical energy gap as filler loading increases for x = 10wt percent is due to nanofillers occupying interstitial locations between PVA-PVP chains and encouraging complex conformations [28]. This causes a charge exchange mechanism between the nanofillers and the PVA-PVP chain network, resulting in a smaller energy gap and increased conductivity in the PVA-PVP/(15-x) CuO(x) MWCNTs nanocomposites.

The DC electrical conductivity of MWCNT and CuO nanofillers (x = 0, 1, 5, 7.5, 10, 14, and 15wt percent) inside the PVA-PVP matrix is explored in **Table 3**. The DC
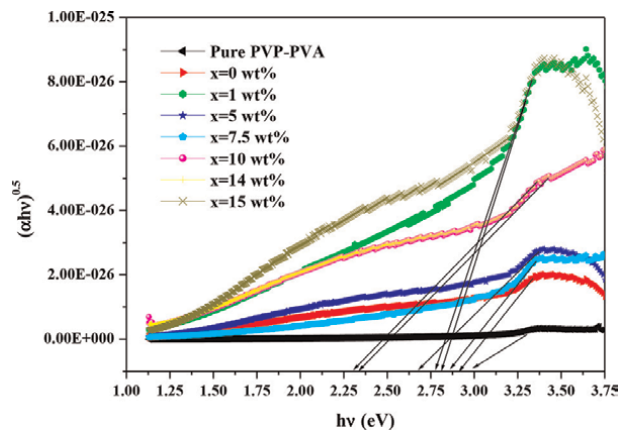
Figure 7.
Deviation of energy gap (E_g) for various loading levels.

Sl No	Filler concentration (wt%)	Resistance(Ω)	Conductivity (σ in S/cm)
1	Pure PVA-PVP	$10.534x\ 10^6$	$1.423\ x10^{-11}$
2	0	$9.337x\ 10^6$	$1.605\ x10^{-11}$
3	1	$8.134x10^5$	$1.841x10^{-10}$
4	5	$7.970x10^5$	$1.882x10^{-10}$
5	7.5	$6.334x10^4$	$2.368x10^{-9}$
6	10	$2.943\ x10^4$	$5.096x10^{-9}$
7	14	$1.123x10^4$	$13.35x10^{-9}$
8	15	$2.278x10^4$	$6.584x10^{-9}$

Table 3.
DC conductivity parameters of PVA-PVP:(15-x)CuO(x)MWCNTs PNCs.

conductivity of PNCs increases by 13.35 x 10^{-9} S/cm at nanoparticles volume fraction x = 14wt percent. The PVA-PVP chain network embedded with nanofillers promotes the charge transfer complexes within the nanocomposites (CTCs). The semicrystalline PVA-PVP nanocomposites that generate CTCs have an increased conductivity in amorphous regions of the polymer matrix as a consequence of reduced barrier heights. With a (bi) polaron wave function overlay on the PVA-PVP chain, rapid intrachain wavelike movement is made possible by the PVA-PVP network's PVA-PVP for electron conveyance. This fallout in leaping motion from site to site is initiated by the contacts of (bi)polaron with neighboring chains [29]. Fluctuations in carrier activity caused by nanofiller loading may lead to reduced activation energies. Interstitial PVA-PVP chains may include MWCNTs and CuO nanofillers, which may be considered to be dispersed throughout the amorphous phase. Hydrogen bonds between the nanofillers and the PVA-PVP chain conduct charge between the nanofillers and the PVA-PVP network. The interfacial barrier is increased and the likelihood of insulator chain transitions is decreased by lowering the crystalline-amorphous contact. This is explained by the percolation theory, which states that the nanoparticles create a conducting path between two charging sites.

Contrary to neutral conjugated polymers, counterions must be considered when transporters are included. There are (bi)polaron traps created by the coulomb interaction of counterions due to the low loading level. As the loading level is raised from x = 0 to 14%, coulomb traps are reduced, allowing the carriers to move inside and across chains. These traps overlap by decreasing the barrier and encouraging movement at x = 14wt percent ideal filled. Carrier transportation interchain is considerably affected by nanocomposites' shape and microstructure conditions that reduce conductivity above x > 14wt percent [30].

The thermal degradation at heating intervals of 10 °C/min is archived utilizing Shimadzu Thermogravimetric-45H in a temperature range of 35 to 650°C. **Figure 8** shows the thermal behavior of crucial PVP-PVA mix and filled PNCs with stages of loading x = 0,1,5,7.5,10,14, and 15wt. A considerable weight loss between 120°C and 255°C resulted in the fragmentation of macromolecular chains [31]. The thermal breakdown of the PVA-PVP main chains is responsible for the significant substantial weight loss over 260°C. In the majority of the experiments, a peak between 550 and
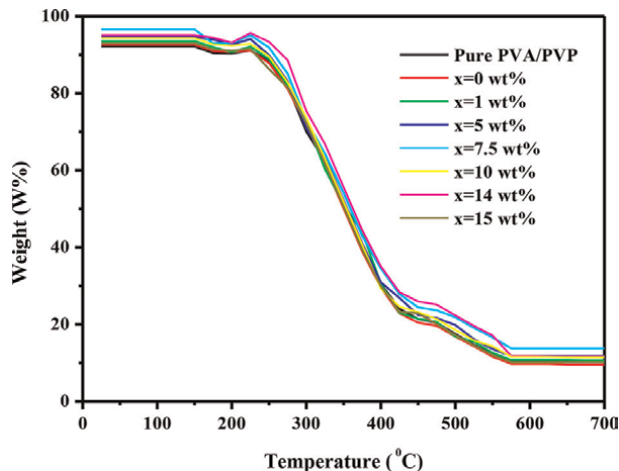
Figure 8.
TGA thermograms of PNCs for different filler levels.

650°C was discovered, which was attributed to carbonization and degradation of the polymer mixture [32]. Thermal stability is also improved by shifting the curves to higher temperatures and increasing the nanofiller loading levels. The improved thermal stability could be attributed to the superior thermal properties of the additional nanofillers, which promote heat dissipation in PVA-PVP matrices [33]. The interfacial contact and morphological variations inside the PNC for an optimal filler level x = 14 wt percent may promote heat dissipation and successfully postpone the disintegration of nanocomposites. The enhancement of the interfacial contact between embedded nanofillers and PVA-PVP PNCs dispersion up to x = 14wt percent loading promotes improvement in thermal stability when compared with pure PVA-PVP blend.

The TGA curves give the thermodynamics parameters obtained by employing the following two processes mainly Coats–Redfern method and the Broido method [34]. Determining the undecomposed initial "Y" number of molecules for different temperatures (T), a graph of ln [ln (1/Y)] versus 1/T shows a quite close straight path. Calculated slope using successive lines yields the activation energy [35]. **Table 4** shows how activation energy (E) measurements in Coats, Redfern, and Broido technique, reducing with the rise in nanofillers loading to the optimal loading value. This demonstrates the significant impact of the inclusion of nanoparticles in the polymer backbone of the PVA-PVP mix.

Fluorescence spectrophotometer-Cary eclipse (Varian) PL spectra are employed for determining the photoluminescent spectrum using emission and arousal slit size 5 nm, scanning rate 120 nm/min, data interval 1 nm (average time 0.5 s), PMT voltage 600 V, and exc = 325 nm wavelength by excitation. **Figure 9** signposts the photoluminescence of PVP/PVA(15-x)CuO(x) MWCNTs PNCs with a percentage loading levels for x = 0, 1, 5, 7.5, 10, 14, and 15wt. PL is an approach for measuring electrical properties that is influenced by the complex particles aspect created by crystallinity. At room temperature, PL studies for generated PNCs were performed at a surge wavelength of 375 nm. By ignoring a specified harmonic reflection order, the PNCs produce thrilling pinnacles at 380 nm and accurate, strong emission bands throughout the visual range of 650 nm [36]. The planar PVA-PVP polymer molecules are represented by the first strong PL in the near UV-vis regions. The electronic displacement of the OH side chain in the three distinct aqueous, isotactic, syndiotactic, and atactic polymer configurations corresponds to the broad emission

Nanofiller loading concentration "x" (wt%)	Coats–Redfern method (KJ/mol)	Broido method (KJ/mol)	Percentage crystallinity
Pure PVA-PVP	260.2	257.5	50.77
0	258.3	254.9	52.84
1	254.7	250.1	53.17
5	250.7	246.7	54.11
7.5	243.8	238.4	54.78
10	236.3	231.8	55.11
14	227.6	222.7	56.34
15	237.1	234.2	55.01

Table 4.
Activation energy and percentage crystallinity of unfilled and filled PNCs employing Coats–Redfern and Broido techniques.
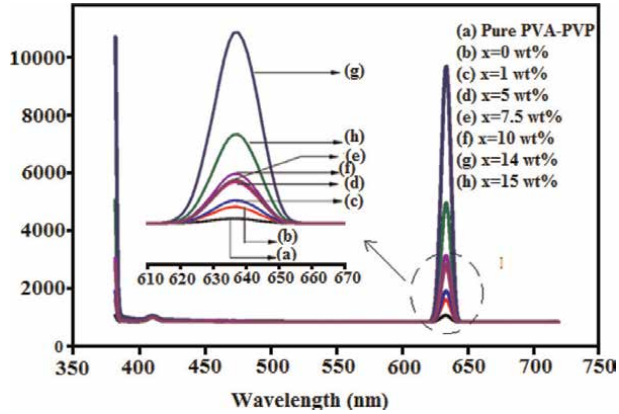
Figure 9.
PL spectra of synthesized PNCs.

spectrum discovered for PVA-PVP nanocomposite [37]. The electron-hole interaction of MWCNTs with CuO nanofillers is reminiscent of a pronounced emission band at 638 nm. Some scientists ascribe the wideband PL emission of PVP-PVA(15-x)CuO(x) MWCNTs nanocomposites to CuO structural deficiencies (green regions), such as oxygen vacancies, and MWCNTs, as well as specific contaminants (yellow and orange areas) [38].

PNCs real and complex dielectric nanocomposites are assessed utilizing the 4200-SCS Keithley parameter analyzer at rooms from 1 kHz to 1 MHz across frequency bands. The spectroscopy of complex dielectric permittivity (real part ε' and imaginary part ε'') and the dielectric loss tangent (tan δ) of PVA-PVP/(15–x)CuO (x) MWCNTs composites at variable doses at room temperature are shown in **Figures 10–12**. **Figure 10** shows how the PNCs ε' values decrease when the frequency is increased [39]. **Figure 10** shows that the ε' values of the unclassified PVA-PVP blend mix declined nonlinearly from 14.62 to 6.32 as the applied frequency increased from 1 kHz to 1 MHz, but the ε' values of PNCs dropped virtually consistently in the range
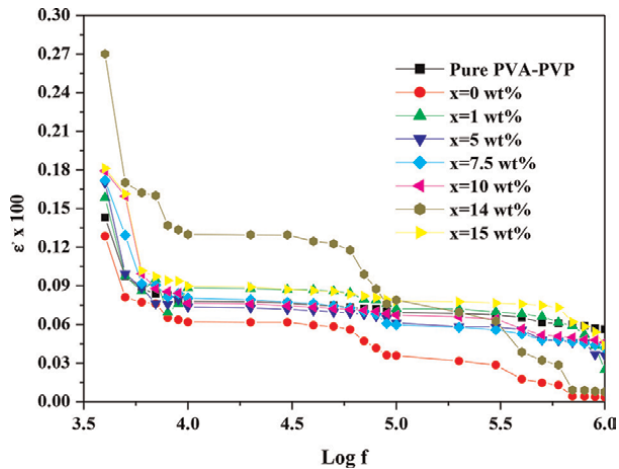
Figure 10.
Deviation of the real dielectric constant of PVA-PVP:(15-x)CuO(x)MWCNTs PNCs for different filler concentrations.
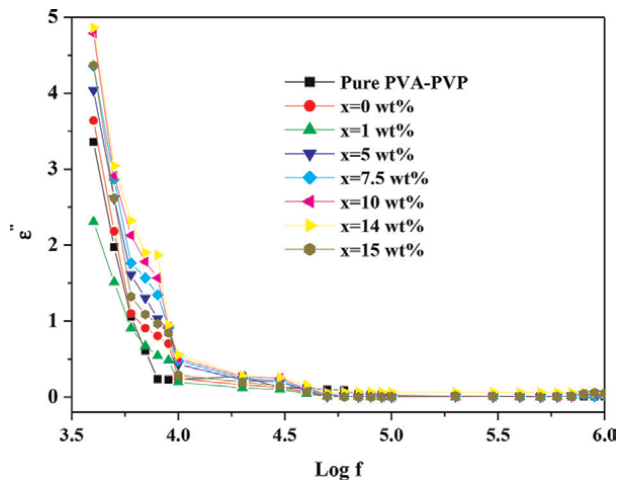
Figure 11.
Variation of imaginary dielectric constant for different filler loadings.
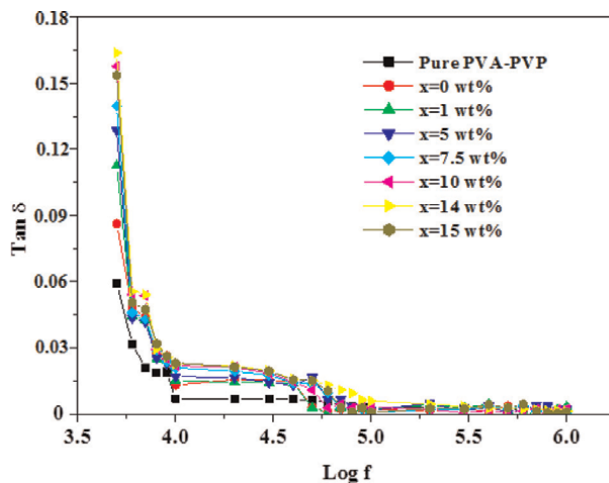
Figure 12.
Variation of tan δ versus frequency of PNCs.

26.97–2.81, indicating adjustable frequency response. The large drop in ε' values over the lower frequency range of x = 14 wt percent loading is proof of the nanoconfinement effect's major influence on the PVA-PVP network. The nanoconfinement effect is widely understood to be principally due to higher dipolar unit obstruction in the PVA-PVP network caused by nanofillers with a time-different electric field, which reduces the dipolar polarization of the PVP-PVA(15-x)CuO(x) MWCNTs PNCs [40]. The fact that the measurements of ε'' for PVP/PVA(15-x)CuO (x) MWCNTs PNCs for x = 14wt percent are similar to those of the other filler content nanocomposites demonstrates that the nanocontainment impact plays no effect in the higher-frequency dielectric polarization. In comparison with unfilled PVA-PVP mix film, the ε'' and Tan values in **Figures 11** and **12** declined significantly at low frequencies and displayed a rather stable behavior. The findings reveal that adding x = 14 wt% nanofiller to the PVA-PVP mix reduces low-frequency dielectric losses considerably.

Additionally, the ε'' values of PNC films have decreased significantly, with a further increase in loading level up to x = 14wt percent. For higher applied frequencies (i.e., f > 10 kHz), the ε'' and Tan δ values first declined considerably with the rise in frequency and then rose significantly. Throughout 1 kHz and 10 kHz, the ε'' and Tan δ spectra of PVP/PVA(15-x)CuO(x) MWCNTs nanocomposites show diminishing trends for x = 14wt percent loading level. Simultaneously, the dielectric relaxation frequency range between 10 kHz and 1 MHz decreases, leading to conductivity [41]. Thus, up to x = 14wt percent, these PNCs exhibit a steady gain in parameter values with an increase in frequency, and at higher applied frequencies, these composites demonstrate a dipolar relaxation process.

3. Conclusion

This chapter conveys the impacts of structural, optical, thermal, dielectric, and electrical properties of CuO nanoparticles and multiwall carbon nanotubes (MWCNTs)-filled PVA and PVP blend matrix (50/50wt percent) for x = 0,1,5,7.5, 10,14, and 15wt percent. For x = 14wt percent loading, X-ray diffraction research reveals an improvement in crystallinity of PNCs. The FTIR, SEM, and AFM measurements of PVA-PVP:(15-x)CuO (x)MWCNTs for x = 0,1,5,7.5, 10,14, and 15wt percent provide information on the miscible mix, PVA-PVP interaction and polymer-nanoparticle interfaces, and the influence of CuO and MWCNTs nanofillers on the morphology aspects of the PVA-PVP blend network. For optical investigations signposting for x = 14wt percent, the nanofiller dispersion in the PNCs matrix appreciably improves the crystalline phase, reducing the optical energy gap to 2.31 eV. The rise in optimal loading up to x = 14wt percent enhances the DC conductivity by 13.35x10–9 S/cm. Ignoring a certain harmonic order of reflection, photoluminescence investigations of PNCs show thrilling pinnacles at 380 nm and precise, strong emission bands throughout the visual range of 650 nm. TGA experiments exhibit that increasing the interface contact between MWCNTs with CuO nanofillers and PVA-PVP PNCs dispersion up to x = 14 wt% loading level may augment the thermal stability in comparison with pure PVA-PVP blend. The dielectric and electrical properties of these PNCs are examined over frequency ranges ranging from 1 kHz to 1 MHz. The establishment of a percolating network *via* the PNCs is caused by an increase in the nanofiller level up to x = 14wt percent in the PNCs matrix. Because of the reduction in the nanoconfinement phenomena, these variables significantly increase the dielectric permittivity values. As the applied frequency increases, the real sections of dielectric permittivity decrease and electrical conductivity increases. This PVA-PVP:(15-x)CuO (x)MWCNTs with excellent dielectric and electrical properties may be employed in electronic circuits as frequency adjustable dielectric PNCs.

Acknowledgements

Conflict of interest

The author declares no conflict of interest.

Author details

Hassan A.H. Alzahrani
Department of Chemistry, University of Jeddah, College of Science and Arts at Khulis, Jeddah, Saudi Arabia

*Address all correspondence to: hahalzahrani@uj.edu.sa

IntechOpen

References

[1] Demir MM, Memesa M, Castignolles P, Wegner G. PMMA/zinc oxide nanocomposites prepared by in-situ bulk polymerization. Macromolecular Rapid Communications. 2006;**27**(10):763-770

[2] Abdelrazek EM, Elashmawi IS, El-Khodary A, Yassin A. Structural, optical, thermal and electrical studies on PVA/PVP blends filled with lithium bromide. Current Applied Physics. 2010;**10**: 607-613

[3] Todd Alam M, Otaigbe JU, Rhoades D, Holland GP, Cherry BR, Kotula PG. Nanostructured polymer blends: Synthesis and structure. Polymer. 2005;**46**(26):12468-12479

[4] Baskaran R, Selvasekarapandian S, Kuwata N, Kawamura J, Hattori T. Conductivity and thermal studies of blend polymer electrolytes based on PVAc–PMMA. Solid State Ionics. 2006; **177**:2679-2682

[5] Kumar KK, Ravi M, Pavani Y, Bhavani S, Sharma AK, Narasimha Rao VVR. Investigations on PEO/PVP/NaBrcomplexed polymer blend electrolytes for electrochemical cell applications. Journal of Membrane Science. 2014;**454**:200-211

[6] Rithin Kumar NB, Acharya S, Alhadhrami A, Prasanna BM, Gurumurthy SC, Bhat S. Role of TiO$_2$/ZnO nanofillers in modifying the properties PMMA nanocomposites for optical device applications. Iranian Journal of Science and Technology, Transactions A: Science. 2021;**45**:2169-2179. DOI: 10.1007/s40995-021-01183-4

[7] Phiwdang K, Suphankij S, Mekprasart W, Pecharapa W. Synthesis of CuO nanoparticles by precipitation method using different precursors. Energy Procedia. 2013;**34**:740-745

[8] Rajeswari N, Selvasekarapandian S, Sanjeeviraja C, Kawamura J, Asath Bahadur S. A study on polymer blend electrolyte based on PVA/PVP with proton salt. Polymer Bulletin. 2014;**71**: 1061-1080

[9] Subba Reddy CV, Sharma AK, Narasimha Rao VVR. Electrical and optical properties of a polyblend electrolyte. Polymer. 2006;**47**:1318-1323

[10] Dai ZD, Ansaloni L, Gin DL, Noble RD, Deng LY. Journal of Membrane Science. 2017;**523**:551-560

[11] Yalagala B, Khandelwal S, Deepika J, Badhulika S. Wirelessly destructible MgO-PVP-graphene composite based flexible transient memristor for security applications. Materials Science in Semiconductor Processing. 2019;**104**: 104673

[12] Ali FM, Kershi RM, Sayed MA, Abou Deif YM. Evaluation of structural and optical properties of Ce3 + ions doped (PVA/PVP) composite films for new organic semiconductors. Physica B Condensed Matter. 2018;**538**: 160-166

[13] Mahendia S, Kandhol G, Deshpande UP, Kumar S. Determination of glass transition temperature of reduced graphene oxide-poly(vinyl alcohol) composites using temperature-dependent Fourier transform infrared spectroscopy. Journal of Molecular Structure. 2016;**1111**:46-54

[14] Bhajantri RF, Ravindrachary V, Poojary B, Harisha A, Crasta V. Studies on fluorescent PVA + PVP + MPDMAPP

composite films. Polymer Engineering and Science. 2009;**49**(5):903-909

[15] Azam A, Ahmed AS, Oves M, Khan MS, Memic A. Size-dependent antimicrobial properties of CuO nanoparticles against gram-positive and -negative bacterial strains. International Journal of Nanomedicine. 2012;**7**:3527-3535

[16] Peng X, Wong SS. Functional covalent chemistry of carbon nanotube surfaces. Advanced Materials. 2009;**21**(6):625-642. DOI: 10.1002/adma.200801464

[17] Jeyaraman R, Kadarkaraithangam J, Arumugam M, Govindasamy R, Abdul A. Synthesis and antimicrobial activity of copper nanoparticles. Materials Letters. 2011;**71**:114-116

[18] Liu Z, Jiao L, Yao Y, Xian X, Zhang J. Aligned, Ultralong single-walled carbon nanotubes: From synthesis, sorting, to electronic devices. Advanced Materials. 2010;**22**(21):2285-2310. DOI: 10.1002/adma.200904167

[19] Park SH, Lee WJ. Hierarchically mesoporous CuO/carbon nanofiber coaxial shell-core nanowires for lithium ion batteries. Scientific Reports. 2015;**5**:9754

[20] Sahooli M, Sabbaghi S, Saboori R. Synthesis and characterization of mono sized CuOnanoparticles. Materials Letters. 2012;**81**:169-172

[21] Zidan HM. Journal of Applied Polymer Science. 2003;**88**:1115-1120

[22] Rithin Kumar NB, Crasta V, Praveen BM. Enhancement of optical, mechanical and micro structural properties in nanocomposite films of PVA doped with WO3 nanoparticles. International Journal of Structural Integrity. 2015;**6**(3):338-354

[23] Hemanth Kumar GN, Lakshmana Rao J, Gopal NO, Narasimhulu KVC, Chakradhar RPS, Varada Rajulu A. Spectroscopic investigation Mn+2 ions doped polyvinyl alcohol films. Polymer. 2004;**45**:5407-5415

[24] Abdelrazek EM, Abdelghany AM, Oraby AH, Asnag GM. Investigation of mixed filler effect on optical and structural properties of PEMA films. International Journal of Engineering and Technology. 2012;**12**:98-102

[25] Saini I, Rozra J, Chandak N, Aggarwal S, Sharma PK, Sharma A. Tailoring of electrical, optical and structural properties of PVA by adding Ag nanoparticles. Materials Chemistry and Physics. 2013;**139**:802-810

[26] Davis EA, Mott NF. Conduction in non-crystalline systems. V. Conductivity, optical absorption and photoconductivity in amorphous semiconductors. Philosophical Magazine. 1970;**22**:0903-0922

[27] Mott NF. Conduction in non-crystalline systems: IV. Anderson localization in a disordered lattice. Philosophical Magazine. 1970;**22**:7-29

[28] Collins BA, Cochran JE, Yan H, Gann E, Hub C, Fink R, et al. Polarized X-ray scattering reveals non-crystalline orientational ordering in organic films. Nature Materials. 2012;**11**:536-543

[29] Noriega R, Rivnay J, Vandewal K, Koch FP, Stingelin N, Smith P, et al. A general relationship between disorder, aggregation and charge transport in conjugated polymers. Nature Materials. 2013;**12**:1038-1044

[30] Kang SD, Snyder GJ. Charge-transport model for conducting polymers. Nature Materials. 2017;**16**:252-257

[31] Patel SN, Glaudell AM, Peterson KA, Thomas EM, O'Hara KA, Lim E, et al. Morphology controls the thermoelectric power factor of a doped semiconducting polymer. Science Advances. 2017;**3**: e1700434

[32] Kim H-S, Yang H-S, Kim H-J, Park H-J. Journal of Thermal Analysis and Calorimetry. 2004;**76**:395-404

[33] Zuo G, Liu X, Fahlman M, Kemerink M. High Seebeck coefficient in mixtures of conjugated polymers. Advanced Functional Materials. 2018;**28**: 1703280

[34] Coats AW, Redfern JP. Nature. 1964; **201**:68-69

[35] Broido A. Journal of Polymer Science: Part A. 1969;**2**(7):1761-1773

[36] Gananatha Shetty B, Crasta V, Rithin Kumar NB, Rajesh K, Bairy R. Parutagouda Shankaragouda Patil, promising PVA/TiO2, CuO filled nanocomposites for electrical and third order nonlinear optical applications. Optical Materials. 2019;**95**:109218. DOI: 10.1016/j.optmat.2019.109218

[37] Mora ES, Barojas EG, Rojas ER, Gonzalez RS. Solar Energy Materials & Solar Cells. 2007;**91**:1412-1415

[38] Mazzera M, Zha M, Calestani D, Zappettini A, Lazzarini L, Salviati G, et al. Nanotechnology. 2007;**18**:355707

[39] Rithin Kumar NB, Crasta V, Praveen BM. Dielectric and electric conductivity studies of PVA (Mowiol 10-98) doped with MWCNTs and WO_3 nanocomposites films. Materials Research Express. 2016;**3**(5):055012

[40] Mardare D, Rusu GI. Comparison of the dielectric properties for doped and undoped TiO_2 thin films. Journal of Optoelectronics and Advanced Materials. 2004;**6**:333-336

[41] Rao V, Ashokan PV, Shridhar MH. Studies of dielectric relaxation and a.c. conductivity in cellulose acetate hydrogen phthalate-poly (methyl methacrylate) blends. Materials Science and Engineering A. 2000;**281**:213-220

Chapter 2

A Concise Review on Carbon Fiber-Reinforced Polymer (CFRP) and Their Mechanical Significance Including Industrial Applications

Challa Gangu Naidu, Challa V.V. Ramana,

Yarraguntla Srinivasa Rao, Kollabathula Vara Prasada Rao,

Dadi Vasudha, Gandi Anusha and Koppisetty B. Rajeshbabu

Abstract

Excellent characteristics of carbon fiber-reinforced polymer (CFRP) include light weight, high strength, high modulus, and high temperature resistance. CFRP has a wide range of potential applications in the domains of public safety, aviation, and high-end non-military people products. Different methods have been used to modify the CFRP in order to increase surface action, harshness, and wettability, improving the interfacial binding between the fiber and network for better mechanical properties. Finally, a few CFRP-related difficulties are looked at, and future directions in interfacial support research are predicted. In this day and age, innovation-focused applications are becoming more significant, and the use of mechanical cycles is progressing swiftly and steadily. Due to their exceptional performance, such as low weight, high specific strength, and high specific stiffness, carbon fiber-reinforced polymer (CFRP) composites have a wide application viewpoint in the aerospace, military, and wind power sector high-quality civilian products. Currently, there is still a significant discrepancy between the theoretical calculation of the CFRP and the actual force. Improving the interface rationally is the key to solving this fundamental issue. The development, properties, and contemporary applications of CFRP composite materials, as well as their processing and boring activities, are discussed in this overview along with recent innovations and potential future applications.

Keywords: CFRP, macro systems, machinability, reinforcement, high specific strength

1. Introduction

Recently, carbon fiber has emerged as one of the most important supporting materials due to its incredible strength, modulus, and high temperature resistance (**Figure 1**). Many logical efforts have been made to enhance and analyze their exhibition, particularly composite frameworks [1–5]. Despite these advantages and efforts,
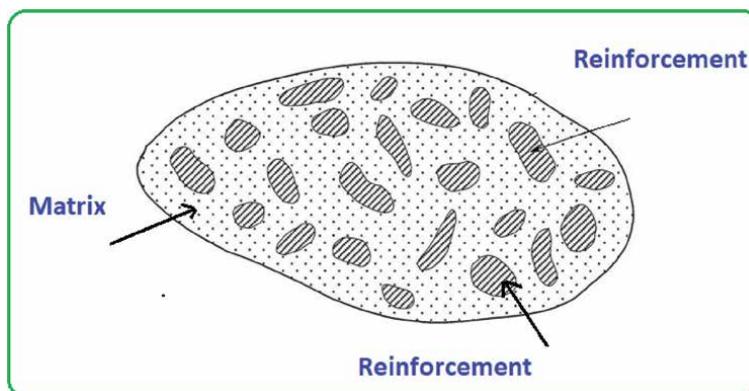
Figure 1.
Schematic representation of composite material structure.

it should be noted that a composite framework's interfacial bond between the carbon strands and the framework is too weak to ensure excellent mechanical performance [6, 7]. Because van der Waals attraction and the hydrogen force are present at the point of interaction in a composite framework, the degree of bonding at the connection point between the fiber and lattice plays a substantial role in the development of the future mechanical behavior. In addition, numerous functional group interactions through carbon fiber connectivity as well as machinability gradually increased [8, 9], and the level of binding at points of interaction is essential. They can also respond with a variety of different polymer materials.

Metals, plastics, ceramics, and composite materials are the four main groups into which the materials are separated based on their properties (like hardness, strength, thickness, and liquefying temperature). While the qualities, designs, and application areas of each of these materials vary, composite materials have recently emerged as common and valuable designing materials for a wide range of applications. Composite materials should perform better because they are minutely heterogeneous, have significant variations in the mechanical characteristics of their component materials, and have a volumetric ratio of component materials more than 10%.

However, the characteristics of these composites are controlled by the characteristics of the individual components as well as by the junction between the strands and the framework saps (status, access, power, and stuff). All that is needed to sustain composite materials effectively is for enough pressure to pass between the network pitches and strands. The two have a tangible, bodily link that attests to this. Epoxy resins and gums cannot form a strong bind with untreated carbon strands. To combat this, pretreatments of fiber surfaces have been promoted. These are typically oxidative in nature and considerably improve the fiber/network connection in various classes, as shown in **Figure 2**.

Due to their exceptional display, such as their excellent binding nature, and sensible connection improvement, carbon fiber-supported polymer (CFRP) composites have a wide range of application possibilities in the aircraft, military, wind power device, and high-grade common items [10]. The connection point is a unique component of composites that directly affects the effective transfer and distribution of load between the network and support, hence, determining the strength and robustness of composites [11]. However, Carbon fiber exhibits poorly at the interfacial interface with gum due to its jumbled graphite structure, smooth, synthetically
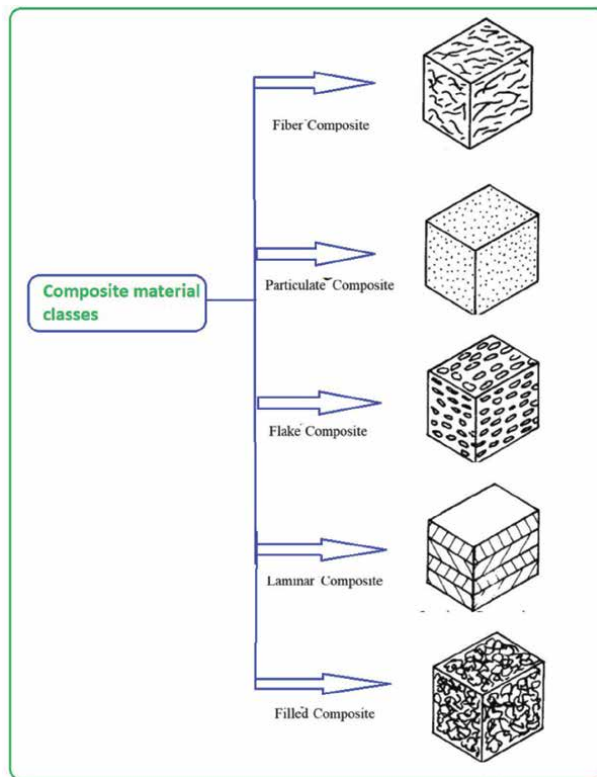
Figure 2.
Representative classes of the composite materials.

inactive surface, and low surface energy [12, 13]. The application of CFRP is therefore severely constrained. In order to address the aforementioned problems, different CFRP enhancement studies have recently been carried out. Displaying a sufficient amount of polar groups on the Carbon fiber surface, primarily carboxyl, hydroxyl [14], epoxy [15], and amino [16] would not only frame synthetic reactions with the gum but also increase the wettability of the Carbon fiber surface. In addition, improving non-covalent bond communication within the network of filaments, such as van der Waals force, hydrogen security link, and electrostatic cooperation [17], could improve the attachment to focus on interfacial qualities without compromising single-fiber elasticity (TS). There have been a variety of methods used to modify carbon fiber up to this point, including oxidation, plasm treatment, estimating/covering [18], fume testimony [19], in-situ self-gathering [20], synthetic uniting [21], and multi-scale underlying surface designs [22], which helped increase the wettability, substance holding, mechanical interlocking between fiber and lattice, and shaping a progress layer to work with the pressure move consistently and lower. Unfortunately, the rising bond may weaken the connection point stage change, causing the break tip to spread out quickly along the connection point course once a break is formed and deboning occurs close to the point of interaction. This would result in decreased influence properties, which is another problem that needs to be addressed urgently. With CFRP's rapid advancement as a cutting-edge designing material, it has become a staple of the assembly sector. Therefore, in order to advance the examination process for high-proficiency change methods, it is crucial to summarize the various points of

interaction treatment techniques for CFRP. In this, we summarized a few significant developments in the CFRP interface change, the most of which occurred in the past 10 years. In addition, our opinions on interface upgrades and support components are listed in the following paragraphs in relation to the aforementioned points.

2. Manufacturing processes

In order to create composite primary components, a variety of assembly techniques are used. These techniques include resting, shaping, winding, pultrusion, and others. We focus on four main assembling techniques among them: (1) the rest-up procedure involves the creation by hand or machine of mats of strands that are permanently preserved by a gum framework. Using this method, it is possible to advance several layers with different fiber directions toward the appropriate sheet thickness and product shape. (2) Trim is a piece of fabric having various cross sections that is used to hide surface changes or for ornamentation. One of the most popular methods for molding plastic pitches is forming. (3) Pitch-soaked fiber strands can be folded over a mandrel using a mechanical fiber-winding cycle to produce oblong or polygonal shapes. (4) In the pultrusion interaction, the fiber rovings and mats are persistently pulled through a tar shower and then dropped into a heated bite of dust. The composite network is fixed into a constant primary shape in terms of cross section thanks to the increased temperature inside bite the dust.

2.1 CFRP surface adsorption

Although it is understood that topical medications help people to hold their fiber-gum better, it is still unclear exactly how this is accomplished. There are three important components that could be added to fibrous materials, according to all the signs.

However, the existing composite approach does not account for the consequences of fiber extraction, fiber bridging, or fiber fracture. This fracture process can be caused by the fact that when bending stress is applied to specimens with various loads, shear stress (t) or transverse tensile stress (t) can be generated at the fiber matrix interfaces. **Figure 3** depicts the fiber matrix interface structures under shear stress when the span length is short. The detailed manufacturer and precursor properties as given in **Table 1**.

2.2 Polymeric composites (CFRP)

Carbon is arguably one of the most important elements found in life. Because it forms the basis for almost everything on the current synthetic platform, including novel materials with physical, chemical, and machinability properties of its equivalents, carbon is a necessary component for life [2, 23, 24]. Low thickness, high strength, and high hardness are the characteristics of carbon fiber. These strands typically have a carbon content of between 80 and 95 percent, can have a staple or fiber structure, have excellent mechanical properties, are lightweight, and have a thickness of 2268 g/cm^3 [2, 25–30]. Numerous advantages of this composite type include its extremely high rigidity/weight ratios, elastic modulus/weight ratios, low coefficient of warm development, high weakness properties, and warm
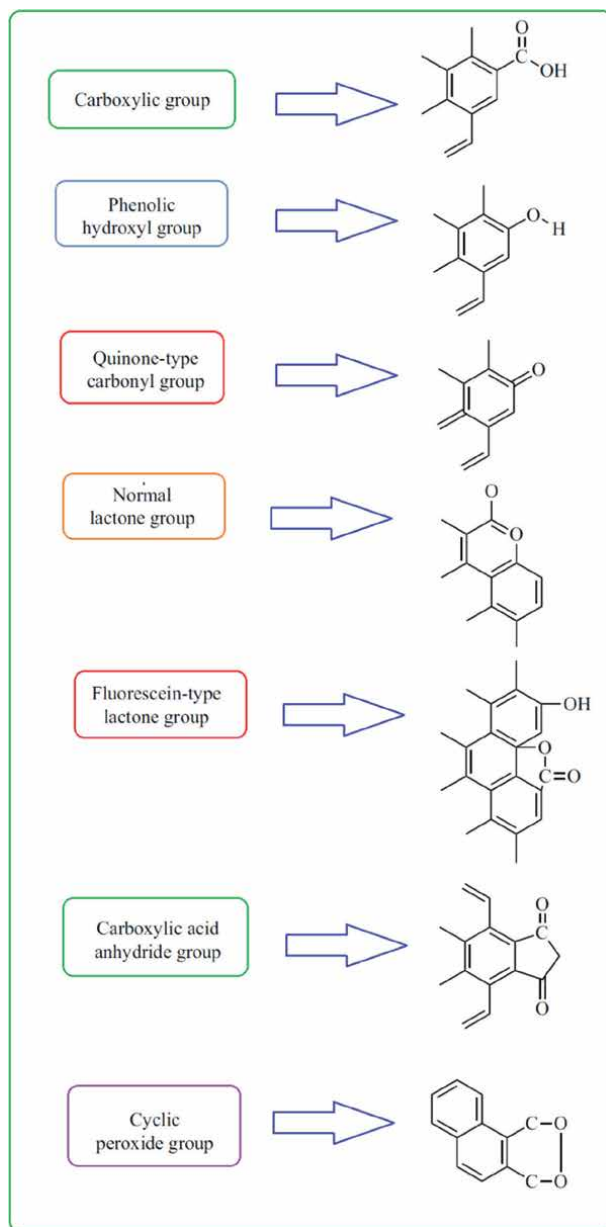
Figure 3.
The oxidative carbon surface and their functional reacting groups/sites.

conductivity. High clear strength of up to 4500 MPa, firmness with damping high-light, and theoretically negligible warm extension coefficient are all characteristics of CFRPs [31–35]. These anticipated characteristics make CFRPs ideal for a wide range of applications, including parts for aviation, automobiles, electronics, clinical, and sporting equipment [36–39]. Its electrical conductivity is quite low, its extensive strength is insufficient, and its molding capacity and alloying nature of synthesized materials are a few of its drawbacks [40–45].

Name of the product	Manufacturer	Precursor type	Properties
P100	Amoco	Pitch	High modulus
T300	Amoco	PAN	High strength
HMS	Hercules Inc.	PAN	High modulus
HMU	Hercules Inc.	PAN	High modulus
Type I	Not reported	PAN	High modulus
Type II	Not reported	PAN	High Strength
AG	Le Carbone Lerraine	PAN	High modulus
AC	Le Carbone Lerraine	PAN	High Strength
HMG-50	Hicto	Rayon	High Strength
Thornel-25	Union carbide	Rayon	High Strength

Schematic portrayal of the conceivable take-up system, aggregation, and circulation of nanofertilizers in crops.

Table 1.
The detailed manufacturer and precursor properties.

2.3 Synthesis of CFRP high-degree purity of reinforced composite materials

Carbon strands can be used in staple fiber, yarn, woven, or weaving constructions as one of the principal support elements for composites [2]. The cross section of the fiber is typically rounded, although other shapes are also possible (rectangular, hexagonal, etc.) [46]. Three classifications of commercially available carbon filaments are distinguished: universally usable (GP), elite execution (HP), and enacted (ACF). As shown in **Figure 4**, business carbon filaments are formed of pitch or poly acrylonitrile (Skillet), natural materials, and global data. Carbon fiber of the skillet type has a high modulus of versatility and a high strength (**Figure 5**). Pitch type, on the other hand, has excellent strength and is inexpensive [2, 34, 47–50]. Typically, 3, 6, and 12 K carbon fibers are made in tow form (K = 1000 filaments). Typically, they are cleaned and sized [2].

It is possible to construct composites with firmness and strength by using solid-fiber support materials that are lightweight [51]. The majority of the weight of composites is supported by the fiber part [46]. Therefore, it is important to decide on the fiber direction that will be used in the composite. The orientation of the fibers also has an impact on surface quality [52, 53]. **Figure 5** depicts the sequential steps in the manufacturing of innovative materials; including polymerization, wet spinning, stabilization, carbonization, and graphitization, melt spinning, infusibilization, and PITCH preparation.

2.4 Mechanical properties of CFRP

Recently, experts and researchers have tended to choose polymer-based composite materials over those made of metal. Thus, an important creative movement where this kind of material will be used is the machining of composite materials [26]. This interaction is necessary to reshape the materials into usable parts by
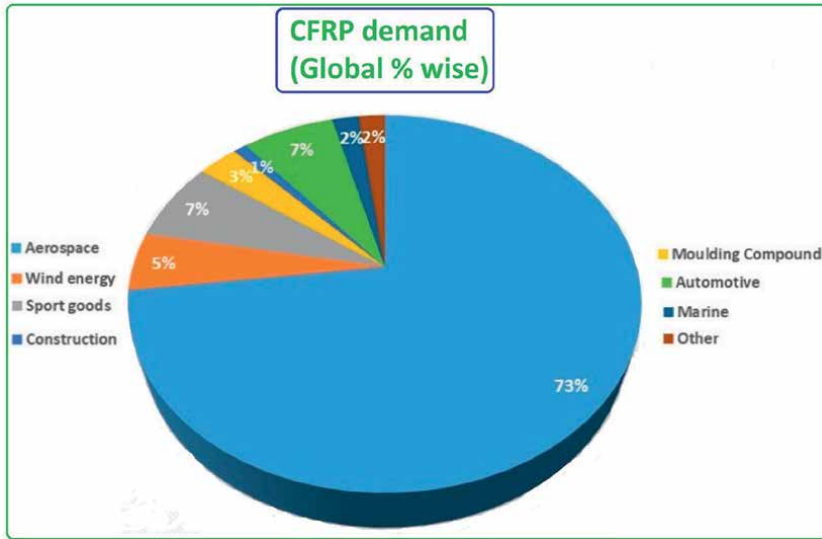
Figure 4.
Global demand of CFRP materials through percentage (%) wise in different sectors.
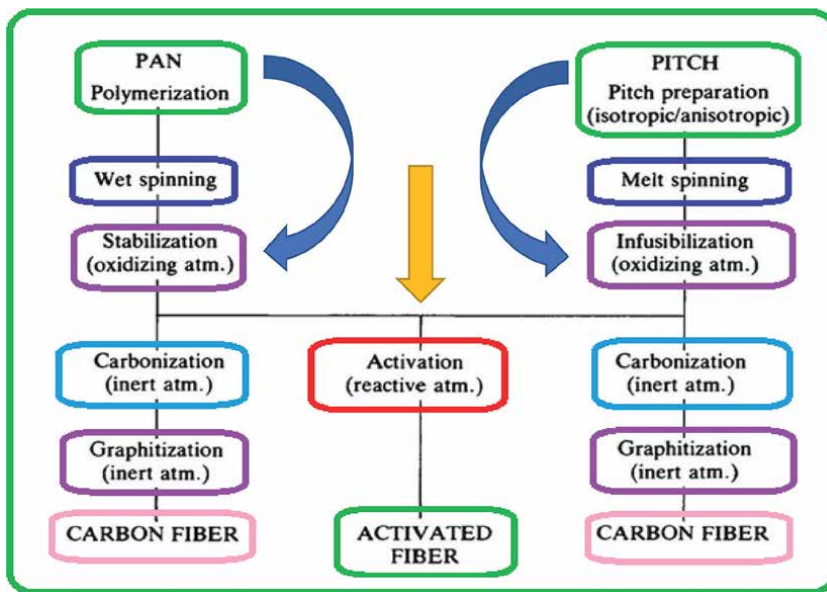
Figure 5.
Production of CFRP through PAN and PITCH-based protocols.

removing inaccessible areas [34]. The majority of the time, composites are produced in close-to-net shape, but they still require post-machining operations like managing, turning, processing, or piercing to alter their resilience, surface finish, and other properties [5, 36, 41, 47, 51].

The machining of CFRPs differs greatly from the machining of metals [53]. Due to the anisotropic, inhomogeneous, grating design, and low thermal conductivity
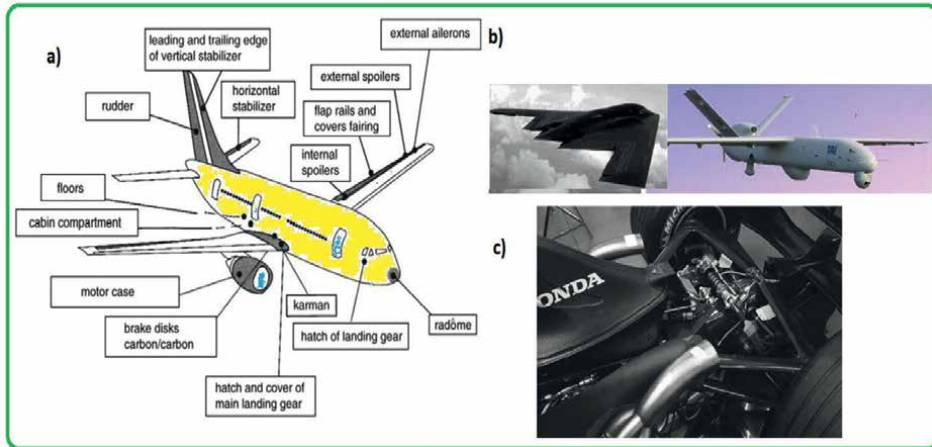
Figure 6.
Schematic representation of (a) Various composites parts used in A320 Airbus air craft (b) CFRP Composite used in a stealth Airbus (Turkish unnamed aircraft ANKA c) CFRP composite used in suspension and gearbox in the Formula 1 racing car.

of CFRP composites, it is problematic. The grating design and poor thermal conductivity of the carbon filaments used in these materials (**Figure 6**) provide the best explanations for why machinability of CFRP composites is not precisely the same as that of other materials.

2.5 CFRP composite materials applications

Following World War II, US manufacturers began developing composite boat hulls and radomes made of fiberglass and polyester (radar cover). In the middle of the 1950s, the automotive industry introduced composites to vehicle bodies (**Figure 7**). The buyers also started offering composite baths, coverings, railings, stepping stools, and electrical components due to the incredibly useful lightweight, and erosion obstruction. A vault building built in Benghazi in 1968 was the first respectable application in a long time, and other designs subsequently followed.

- Automotives

- Commercial spares (Aircrafts, Charted flights, Defense sector spares)

- Energy generation (Water, air, tidal, wind)

- Underground energy (Deep water, oil production, gas pipelines)

- Green energy generation (Hydrogen fuel, Electricity transmission

- Construction field (Civil aviation)
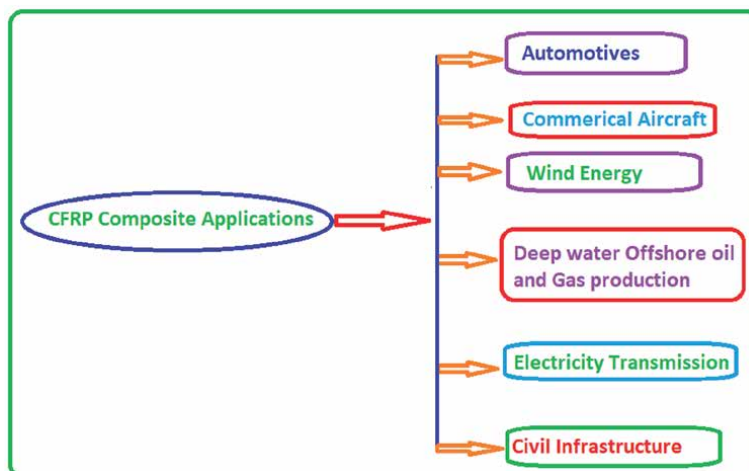
Figure 7.
Different Applications of CFRP composites.

3. Conclusions

Carbon fibers serve as the fiber phase of carbon fiber-reinforced polymer composites, a type of fiber composite material. A series of materials known as carbon fibers are primarily composed of the elemental carbon. The pyrolysis of organic fibers produces this. The aircraft industry's requirement for a material with a mix of high robustness, high rigidity, and low weight served as the primary driving force behind the development of carbon fibers. The market has started to recognize the potential of carbon fibers to offer solutions to a variety of issues related to the deterioration and strengthening of the infrastructure. By effectively utilizing CFRP, structures' useful lives could be greatly extended while requiring less care. In order to meet ever-increasing demands, researchers are still thought to be working to synthesis a high degree of polymers using high performance Carbon fiber as a resin-reinforced composites. Therefore, the synthesis of recent research in this review would serve as a theoretical guide for future design of the interface composition and structure of CFRP and aid in the advancement of the field of enhanced carbon fiber-reinforced polymeric composition.

Acknowledgements

Conflict of interest

All the authors are declared that there is no conflict of interest for this book chapter.

Author details

Challa Gangu Naidu[1*], Challa V.V. Ramana[1], Yarraguntla Srinivasa Rao[2], Kollabathula Vara Prasada Rao[2], Dadi Vasudha[2], Gandi Anusha[2] and Koppisetty B. Rajeshbabu[2]

1 Department of Basic Sciences and Humanities (BS&H), Vignan's Institute of Information Technology (VIIT), Visakhapatnam, India

2 Department of Pharmaceutical Analysis, Vignan Institute of Pharmaceutical Technology, Visakhapatnam, India

*Address all correspondence to: naiduiict@gmail.com; naidu064@gmail.com

IntechOpen

References

[1] Donnet JB, Bansal RC. Carbon Fibers. 2nd ed. New York: Marcel Dekker; 1990. p. 470

[2] Morgan PE. Carbon Fibers and their Composites. Boca Raton, FL, USA: CRC Press; 2005

[3] Park SJ. Carbon Materials. Seoul: Daeyoungsa; 2006

[4] Seong MC, Jung H-T. Highly enhanced mechanical properties of polypropylene-long carbon fiber composites by a combined method of coupling agent and surface modification of long carbon fiber. Macromolecular Research. 2014;**22**:1066-1073

[5] Schwartz M. Composite Materials Handbook. 2nd ed. New York: McGraw-Hill; 1992

[6] Wu S. Polymer Interface and Adhesion. New York: Marcel Dekker; 1982

[7] Park SJ, Seo MK, Ma TJ, Lee DR. Effect of chemical treatment of kevlar fibers on mechanical interfacial properties of composites. Journal of Colloid and Interface Science. 2002:252-249

[8] Ho KK, Lamoriniere S, Kalinka G, Schulz E, Bismarck A. Interfacial behavior between atmospheric-plasma-fluorinated carbon fibers and poly(vinylidene fluoride). Journal of Colloid and Interface Science. 2007;**313**:476

[9] Yosomiya R, Morimoto K, Nakajima A, Ikada Y, Suzuki T. Adhesion and Bonding in Composites. New York: Marcel Dekker; 1990

[10] Liu L, Jia C, He J, Zhao F, Fan D, Xing L, et al. Interfacial characterization, control and modification of carbon fiber reinforced polymer composites. Composites Science and Technology. 2015;**121**:56-72

[11] Hochard C, Aubourg PA, Charles JP. Modelling of the mechanical behavior of woven-fabric CFRP laminates up to failure. Composites Science and Technology. 2001;**61**(2):221-230

[12] He M, Xu P, Zhang Y, Liu K, Yang X. Phthalocyanine nanowires@ GO/carbon fiber composites with enhanced interfacial properties and electromagnetic interference shielding performance. Chemical Engineering Journal. 2020;**388**:124255

[13] Wu Y, Wang Z, Xu L, Wang H, Peng S, Zheng L, et al. Preparation of silver-plated carbon nanotubes/carbon fiber hybrid fibers by combining freeze-drying deposition with a sizing process to enhance the mechanical properties of carbon fiber composites. Composites Part A: Applied Science and Manufacturing. 2021;**146**:106421

[14] Gao B, Zhang J, Hao Z, Huo L, Zhang R, Shao L. In-situ modification of carbon fibers with hyperbranched polyglycerol via anionic ring-opening polymerization for use in high-performance composites. Carbon. 2017;**123**:548-557

[15] Zhao F, Huang Y. Grafting of polyhedral oligomeric silsesquioxanes on a carbon fiber surface: Novel coupling agents for fiber/polymer matrix composites. Journal of Materials Chemistry. 2011;**21**(11):3695

[16] Ma L, Meng L, Wang Y, Wu G, Fan D, Yu J, et al. Interfacial properties and impact toughness of dendritic

hexamethylenetetramine functionalized carbon fiber with varying chain lengths. RSC Advances. 2014;**4**(74):39156-39166

[17] Wu Q, Yang X, Wan Q, Zhao R, He J, Zhu J. Layer-by-layer assembled nacre-like polyether amine/GO hierarchical structure on carbon fiber surface toward composites with excellent interfacial strength and toughness. Composites Science and Technology. 2020;**198**:108296

[18] Yuan H, Zhang S, Lu C, He S, An F. Improved interfacial adhesion in carbon fiber/polyether sulfone composites through an organic solvent-free polyamic acid sizing. Applied Surface Science. 2013;**279**:279-284

[19] Zheng L, Wang Y, Qin J, Wang X, Lu R, Qu C, et al. Scalable manufacturing of carbon nanotubes on continuous carbon fibers surface from chemical vapor deposition. Vacuum. 2018;**152**:84-90

[20] Wang C, Xia L, Zhong B, Yang H, Huang L, Xiong L, et al. Fabrication and mechanical properties of carbon fibers/ lithium aluminosilicate ceramic matrix composites reinforced by in-situ growth SiC nanowires. Journal of the European Ceramic Society. 2019;**39**(15):4625-4633

[21] Zhao M, Meng L, Ma L, Ma L, Yang X, Huang Y, et al. Layer-by-layer grafting CNTs onto carbon fibers surface for enhancing the interfacial properties of epoxy resin composites. Composites Science and Technology. 2018;**154**:28-36

[22] Feng P, Song G, Li X, Xu H, Xu L, Lv D, et al. Effects of different "rigid-flexible" structures of carbon fibers surface on the interfacial microstructure and mechanical properties of carbon fiber/epoxy resin composites. Journal of Colloid and Interface Science. 2021;**583**:13-23

[23] Ferreira JR, Coppini NL, Neto FL. Characteristics of carbon-carbon composite turning. Journal of Materials Processing Technology. 2001;**109**(1-2):65-71

[24] Buckley JD, Edie DD. Carbon-Carbon Materials and Composites. New Jersey: Noyes Publications; 1993

[25] Philippe S, Figueiredo JL. Carbon Materials for Catalysis. Hoboken, NJ: Wiley; 2009

[26] Chawla KK. Composite Materials: Science and Engineering. New York: Springer Science & Business Media; 2012

[27] Asthana R, Kumar A, Dahotre NB. Materials Processing and Manufacturing Science. Elsevier, Boston, MA: Science & Technology Books; 2005

[28] Fitzer E. Carbon fibers-present state and future expectations. In: Carbon Fibers Filaments and Composites. Dordrecht: Springer. DOI: 10.1007/978-94-015-6847-0_1

[29] Eyckens DJ, Arnold CL, Simon Ž, Gengenbach TR, Henderson LC. Composites Part A: Applied Science and Manufacturing. 2021;**140**:106147

[30] Szabó L, Milotskyi R, Fujie T, Tsukegi T, Wada N, Ninomiya K, et al. Frontiers in Chemistry. 2019;**7**:757

[31] Pecat O, Rentsch R, Brinksmeier E. Influence of milling process parameters on the surface integrity of CFRP. In: Fifth CIRP Conference on High Performance Cutting. 2012. Vol. 1. pp. 466-470

[32] Tagliaferri V, Diilio A, Visconti IC. Laser cutting of fiber-reinforced polyesters. Composites. 1985;**16**(4):317-325

[33] Haynes WM. CRC Handbook of Chemistry and Physics. 95th ed. Boca Raton: CRC Press, LCC; 2012

[34] Mallick PK. Fiber-Reinforced Composites: Materials, Manufacturing, and Design. 3rd ed. Boca Raton: Taylor & Francis. CRC Press; 2008

[35] William D, Callister J, Rethwisch DG. Materials Science and Engineering: An Introduction. 8th ed. New York: Wiley; 2009

[36] Shyha IS et al. Drill geometry and operating effects when cutting small diameter holes in CFRP. International Journal of Machine Tools and Manufacture. 2009;**49**(12-13):1008-1014

[37] Wang YG et al. Cutting performance of carbon fiber reinforced plastics using PCD tool. Advances in Materials Research. 2011;**215**:14-18

[38] Chao PY, Hwang YD. An improved Taguchi's method in design of experiments for milling CFRP composite. International Journal of Production Research. 1997;**35**(1):51-66

[39] Hult J, Rammerstorfer FG. Engineering mechanics of fiber reinforced polymers and composite structures. In: CISM International Centre for Mechanical Sciences (CISM). Vol. 348. 1994

[40] Zemann R, Kain L, Bleicher F. Vibration assisted machining of carbon fiber reinforced polymers. In: 24th DAAAM International Symposium on Intelligent Manufacturing and Automation; Vol. 69. 2014. pp. 536-543

[41] Teti R. Machining of composite materials. CIRP Annals - Manufacturing Technology. 2002;**51**(2):611-634

[42] Soutis C. Carbon fiber reinforced plastics in aircraft construction. Materials Science and Engineering A: Structural Materials: Properties, Microstructures and Processing. 2005;**412**(1-2):171-176

[43] Hull D, Clyne TW. An Introduction to Composite Materials. 2nd ed. Cambridge University Press; 1996

[44] Karnik SR et al. Delamination analysis in high speed drilling of carbon fiber reinforced plastics (CFRP) using artificial neural network model. Materials and Design. 2008;**29**(9):1768-1776

[45] Zółkiewski S. Selection and impact of parameters in composite materials designing. In: 13th World Congress in Mechanism and Machine Science, Guanajuato, México. 2011

[46] Groover MP. Fundamentals of Modern Manufacturing: Materials Processes, and Systems. New York: Wiley; 2007

[47] Chung DDL. Carbon Fiber Composites. Washington: Butterworth-Heinemann; 1994

[48] Burchell TD. Carbon Materials for Advanced Technologies. Pergamon: Elsevier; 1999

[49] Takahashi K et al. Heat conduction analysis of laser CFRP processing with IR and UV laser light. Composites Part A: Applied Science and Manufacturing. 2016;**84**:114-122

[50] Suresha B et al. Friction and dry sliding wear behavior of carbon and glass fabric reinforced vinyl ester composites. Tribology International. 2010;**43**(3):602-609

[51] Liu DF, Tang YJ, Cong WL. A review of mechanical drilling for composite laminates. Composite Structures. **94**(4):1265-1279

[52] Wang XM, Zhang LC. An experimental investigation into the orthogonal cutting of unidirectional

fiber reinforced plastics. International
Journal of Machine Tools and
Manufacture. 2003;**43**(10):1015-1022

[53] Islam F, Ramkumar J, Milani AS. A
simplified damage prediction framework
for milling of unidirectional carbon
fiber-reinforced plastics. Advanced
Manufacturing: Polymer & Composites
Science. 2015;**1**(4):175-184

Section 2

State-of-the-Art Characterization

Chapter 3

Theoretical Approach of the Propagation of Electromagnetic Waves through Carbon Nanotubes and Behaviour of Carbon Nanotubes as Capacitor Using Electric Hertz Potential

Jay Shankar Kumar and Ashok Kumar

Abstract

The electromagnetic waves and its propagation through material medium described by maxwell's equations. We have identified that electromagnetic waves propagate through carbon nanotubes according to electric hertz potential with solution of Helmholtz equation and satisfied by using the concept of Gaussian beam or wave. When monochromatic electromagnetic wave propagates through a hollow single wall carbon nanotube, its energy absorbed by walls of nanotubes just like a capacitor because of carbon nanotubes have metallic as well as semiconductor characteristic which is shown by density of state and lattice vector. It is verified by Helmholtz equation and Schrödinger's wave equation. Thus, the electromagnetic waves can propagate through carbon nanotubes and carbon nanotubes absorb the energy as a capacitor.

Keywords: carbon nanotube, electromagnetic wave, electric hertz potential, Helmholtz equation, Schrödinger equation, Gaussian beam or wave, capacitor

1. Introduction

A new allotropes of carbon element is carbon nanotube which is in cylindrical form and made by folding of graphene sheet of graphite. By passing time, the various types of carbon nanotubes (carbon nano scrolls, carbon nano cones, carbon nano coils, carbon nanoribbon, carbon nanofibers, etc.) by variousare formed by various processes (Arc Discharge, Laser Ablation or Evaporation, Chemical Vapor Deposition (CVD), Plasma Enhanced Chemical Vapor Deposition (PECVD), etc.). The carbon nanotubes were discovered by S. Iijima in 1991 by fullerene synthesis [1, 2]. There are two forms of carbon nanotube. One is single walled carbon nanotubes that made up of rolling of graphene sheet and its dimeter vary from 0.7 to 3 nm and minimum dimeter

up to ∼0.4 nm. The other nanotubes are multiwalled carbon nanotubes that are made up of multiple concentric cylinders and its dimeter range is of 10–20 nm and space is available between two layers (3.4 Å).

In atomic structure of carbon, six electrons are arranged according to electronic configuration $1s^2\, 2s^2\, 2p^2$ and designated as $1s^2$, 2 s, $2p_x$, $2p_y$, $2p_z$, if atoms bounded in molecules. In graphite sheet, carbon atoms bound together by sp^2 hybrid bonds and similarly, fullerenes, carbon nanotubes, and graphene are also formed by sp^2 hybrid bonds [3]. Graphene is a single layer carbon atoms of graphite and has 120^0 bond angle in hexagons with electronic structure characterized by π-bonds linear dispersion near Fermi surface (**Figures 1–3**). In a hexagonal lattice, the unit vectors $\vec{a}_1\ and\ \vec{a}_2$ in the real space can be written as:

$$\vec{a}_1 = \frac{1}{2}a\left(\sqrt{3}, 1\right)\ ,\ \ \vec{a}_2 = \frac{1}{2}a\left(\sqrt{3}, -1\right) \tag{1}$$
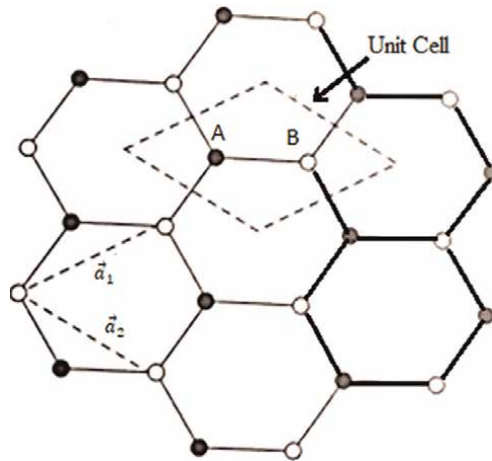
Figure 1.
Crystal structure of graphene with unit cell.
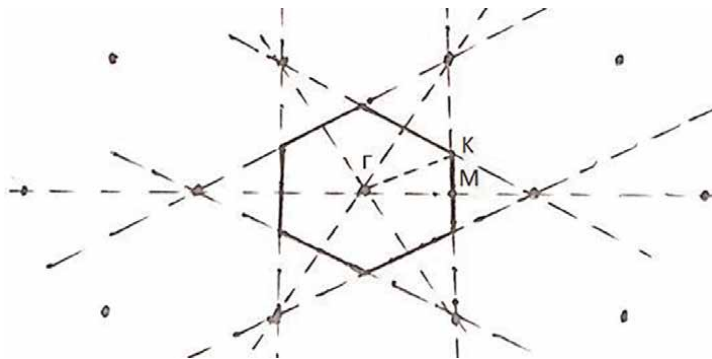
Figure 2.
Wigner-Seitz cell is a primitive cell which represents the Brillouin zone of the reciprocal lattice. To construct this cell, at first join the lattice point passing through central point and then join the other two lattice points each sides just like parallel the lines to both sides. The Brillouin zone of the graphene with location of the symmetrical points K, M and Γ.
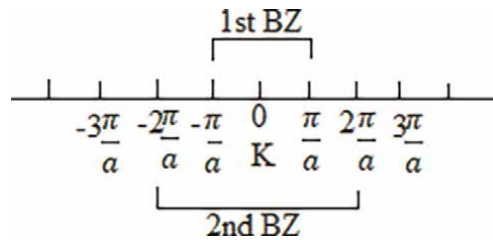
Figure 3.
The first two Brillouin zones of graphene for one dimensional.

Where, *a* represents the lattice constant and equal to $\sqrt{3}a_{c-c}$, here, a_{c-c} shows the bond length (0.144 mm) of carbon-carbon atom.

To describe quantum mechanical properties of the crystals in lattice the Brillouin zone were introduced and we can also describe the behavior of electrons in a perfect crystal on the concept of Brillouin zone. In reciprocal lattice space, a region where closest lattice point of primitive cell is the origin is known as the Brillouin zone (BZ). It is constructed by Wigner and Seitz and called Wigner-Seitz primitive cell i.e., Brillouin zone. In the Brillouin zone, the three symmetrical points is at the centre, corners, and centre edge. We have

$$K = \frac{n\pi}{a}, where, n = \pm1, \pm2, \pm3, \dots .etc. \tag{2}$$

The first and second Brillouin zone is defined between $K = -\frac{\pi}{a}$ to $K = +\frac{\pi}{a}$ in which electron has allowed energy value and $K = -\frac{2\pi}{a}$ to $K = +\frac{2\pi}{a}$ which is forbidden zone.

Carbon nanotube is formed by chiral and translation vector using chiral angle with indices (n, m) and (5, 5). Using Fourier series and transform and Schrödinger's equation, the Bloch theorem is determined with Brillouin zone. Bloch function helps to determine the determinant equation for Schrödinger's equation. The solution of this determinant equation gives energy dispersion over tight binding which shows the band structure of carbon nanotubes and taking wave vector components, metallic character found near Fermi point of graphene with Fermi energy of electrons. The density of state of carbon nanotubes is expressed by expanding the dispersion relation [4] around the Fermi surface. We have the condition for semiconducting and metallic carbon nanotubes near the K points that is proportional to the Fermi velocity $(v_f = 8 \times 10^5 \text{ m/s})$ of the electrons in the graphene.

The Helmholtz equation [5] is obtained by curl of Maxwell's equations and its solution gives the plane monochromatic transverse wave [6, 7]. Helmholtz equation in cylindrical coordinate gives the Gaussian wave or beam and its spot size ensures that it can propagate through the cylindrical carbon nanotube. A monochromatic electromagnetic wave as radiation is called Gaussian beam that provided by a laser source [8]. The Gaussian wave represented by the amplitude function with very small spot size propagates through a carbon nanotube [9]. The parameters of Gaussian wave are the width, the divergence, the radius of curvature. The better beam quality and intensity is represented by the smaller angle of divergence. The propagation distance leads to intensity, spot size, radius of curvature and divergence [10].

When the wave travel through the carbon nanotube [11] then the inner surface of the carbon nanotube absorbs the energy of the wave as a capacitor and shown by the Schrödinger's and Helmholtz relation using the work-energy theorem.

2. Chiral and translation vector

Rolling up of graphene along the chiral vector as

$$\overrightarrow{C_h} = n\overrightarrow{a_1} + m\overrightarrow{a_2} \tag{3}$$

Where, n and m are integers and $\overrightarrow{a_1}$ *and* $\overrightarrow{a_2}$ are lattice vectors. The two corners K and K$'$ are the location of Dirac cones in the Brillouin zone. In reciprocal space, K and K$'$ are as

$$K = \frac{2\pi}{3a}\left(1, \frac{1}{\sqrt{3}}\right) \;,\;\; K' = \frac{2\pi}{3a}\left(1, -\frac{1}{\sqrt{3}}\right) \tag{4}$$

Where, $a(\approx 1.42 A°)$ is the distance of C-C.

In figure θ be the chiral angle between the chiral $\vec{C_h}$ *and* $\vec{a}_1$. The circumference of tube equal to $\vec{C_h}$ given by

$$\vec{C_h} = \frac{\sqrt{3}}{2}a(n+m)\hat{x} + \frac{1}{2}a(n+m)\hat{y} \tag{5}$$

In magnitude,

$$\left|\overrightarrow{C_h}\right| = a\sqrt{n^2 + m^2 + nm} \tag{6}$$

The dimeter d_T of the carbon nanotube obtained if $\left|\vec{a}_1\right| = \left|\vec{a}_2\right| = \sqrt{3}a_{c-c}$ (as)

$$d_T = \frac{\sqrt{3}a_{c-c}}{\pi}\sqrt{n^2 + m^2 + nm} \tag{7}$$

The chiral angle given as

$$cos\theta = \frac{m + 2n}{2\sqrt{n^2 + m^2 + nm}} \tag{8}$$

And also $tan\theta = \frac{\sqrt{3}m}{m + 2n}, 0° \leq \theta \leq 30° \tag{9}$

If the chiral angle is 30° then $n = m$ and the structure is armchair. $\vec{C_h}$ is obtained by the vector addition as $\vec{C_h} = 5\vec{a}_1 + 5\vec{a}_2$ (in **Figure 4**) and now the translation vector $\vec{T}$ is drawn perpendicular to the chiral vector $\overrightarrow{C_h}$ and expressed as (**Figures 5–9**)

$$\vec{T} = t_1\vec{a}_1 + t_2\vec{a}_2 \tag{10}$$

Where, t_1 and t_2 are components of vector $\vec{T}$ and they are written as

$$t_1 = \frac{2m + n}{d_T} \;,\;\; t_2 = -\frac{m + 2n}{d_T} \tag{11}$$

The Eq. (10) written as

$$\vec{T} = \frac{(m-n)}{d_T}\left(\frac{\sqrt{3}}{2}a\hat{x} + \frac{1}{2}a\hat{y}\right) \tag{12}$$
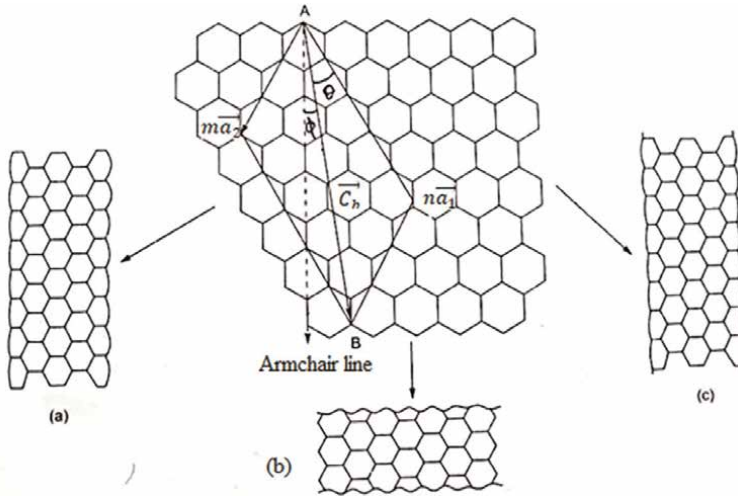
Figure 4.
Rolling graphene sheet along the chiral vectors (a), (b) and (c) show the armchair (m,m) zig-zag (n,0) and the chirl (n,m) nanotubes respectively.
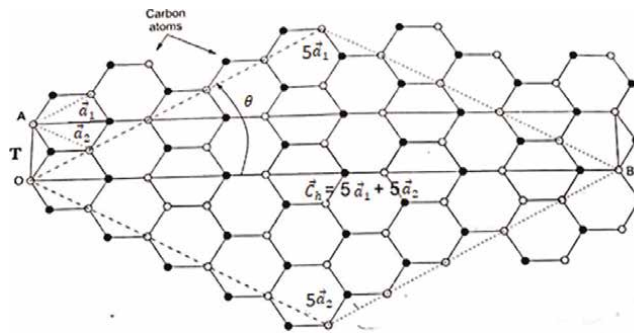
Figure 5.
The crystal structure of the carbon nanotube with the armchair (5,5) and rectangle shows the unit cell of the carbon nanotube and the angle between $\vec{C}_h$ and $\vec{a}_1$ is $0 < \theta < 30°$ called the chiral angle.

In magnitude,

$$\text{In magnitude } \left|\vec{T}\right| = \frac{\left|\vec{C}_h\right|\sqrt{3}}{d_T} \tag{13}$$

In carbon nanotube the hexagons in unit cell of $a(n,m)$ is given by

$$N = \frac{2\left(n^2 + m^2 + nm\right)}{d_T} \tag{14}$$

3. Fourier series in carbon nanotubes

We have general Fourier series of sines and cosines for a periodic function $f(x)$ written as

$$f(x) = A_\circ + \sum_{f>0} A_f \cos\left(\frac{2\pi f x}{a}\right) + \sum_{f>0} B_f \sin\left(\frac{2\pi f x}{a}\right) \tag{15}$$

Where, the f is the positive integer and A_f and B_f are the real constants called Fourier coefficients. Consider the electron number density $n\left(\vec{r}\right)$ is a periodic function as $f(x)$ in the direction of crystal axes which invariant under translation $\vec{T}$. Thus

$$n\left(\vec{r}\right) = n\left(\vec{r} + \vec{T}\right) \tag{16}$$

The factor $\frac{2\pi}{a}$ ensures that $n(x)$ has a period $'a'$ (**Figure 6**);
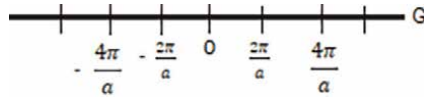
Figure 6.
The periodic function n(x) *of period* a *for the Fourier transform.*

$$n(x + a) = A_\circ + \sum A_f \cos\left(\frac{2\pi f x}{a}\right) + \sum B_f \sin\left(\frac{2\pi f x}{a}\right) = n(x) \tag{17}$$

For this condition, $\frac{2f}{a}$ is in Fourier space of the crystal and we can write the Fourier transform as

$$n(x) = \sum_f n_f e^{\frac{i2\pi f x}{a}} \tag{18}$$

Where, the sum is over all integers: positive, negative and zero. Similarly, the Fourier transform to periodic function $n\left(\vec{r}\right)$ in three dimensions with finding a vector set $\vec{G}$, such as

$$n\left(\vec{r}\right) = \sum_G n_G e^{i\vec{G}\cdot\vec{r}} \tag{19}$$

Where, $\vec{G}$ is a reciprocal lattice vector and expressed as

$$\vec{G} = v_1 \vec{b}_1 + v_2 \vec{b}_2 + v_3 \vec{b}_3 \tag{20}$$

Where, v_1, v_2, *and* v_3 are integers and $\vec{b}_1$, $\vec{b}_2$, and $\vec{b}_3$ are the primitive vectors and also axis vectors of the reciprocal lattice and have the property $\vec{b}_i \cdot \vec{a}_j = 2\pi\delta_{ij}$, where, $\delta_{ij} = 1$ if $i = j$ and $\delta_{ij} = 0$ if $i \neq j$.

The Fourier series for the electron density has the invariance under the crystal translation as $\vec{T} = t_1 \vec{a}_1 + t_2 \vec{a}_2 + t_3 \vec{a}_3$. From (19),

$$n\left(\vec{r} + \vec{T}\right) = \sum_G n_G e^{i\vec{G}\cdot\vec{r}} e^{i\vec{G}\cdot\vec{T}} \tag{21}$$

4. The Schrödinger's equation and the bloch theorem

We have Schrödinger's wave equation in three dimensions as

$$-\frac{\hbar^2}{2m}\nabla^2\psi_k\left(\vec{r}\right) = \epsilon_k\psi_k\left(\vec{r}\right) \tag{22}$$

Where $\epsilon_k = E - U$, E is the kinetic energy and U is the potential energy. The potential function $U(r)$ has the period l of the lattice given as $U(r) = U(r+l)$. The wave function to be periodic in three dimensions with period l as

$$\psi(\rho, \theta, \varphi) = \psi(r+l, \theta, \varphi) \tag{23}$$

This is corresponding to $\psi(x, y, z) = \psi(r+l, y, z)$ because of angles are made with Cartesian axis. So, the form of a traveling plane wave given as

$$\psi_k\left(\vec{r}\right) = e^{i\vec{k}\cdot\vec{r}} \tag{24}$$

Where $\vec{k}$ is the wave vector and $= 0; \pm\frac{2\pi}{l}; \pm\frac{4\pi}{l}$. The solution of Schrödinger's wave equation for periodic potential given by Bloch as

$$\psi_k\left(\vec{r}\right) = u_k\left(\vec{r}\right)e^{i\vec{k}\cdot\vec{r}} \tag{25}$$

Where $u_k\left(\vec{r}\right)$ have the periods of the lattice with $u_k\left(\vec{r}\right) = u_k\left(\vec{r}+\vec{T}\right) = u_k\left(\vec{r}+l\right)$ and u_k is called the Bloch function. This expression (25) is the Bloch theorem (**Figure 7**).
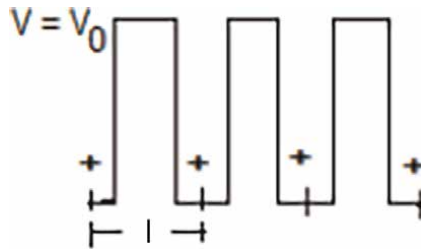
Figure 7.
The periodic potential distribution for the crystal.

When lattice translation carries $\vec{r}$ to $\vec{r}+\vec{T}$ then we have the form of Bloch theorem as

$$\psi_k\left(\vec{r}+\vec{T}\right) = e^{i\vec{k}\cdot\vec{T}}\psi_k\left(\vec{r}\right) \tag{26}$$

The Schrödinger's wave Eq. (22) also written as $\psi = \epsilon\psi$, where H, ψ, and ϵ are the Hamiltonian, the total wave function and the total energy of electron in π-orbital of graphene. The Bloch function u_k from $2p_z$ orbitals of atoms P and Q as

$$u_{P(Q)} = \frac{1}{\sqrt{N}} \sum_{P(Q)} e^{i\vec{k} \cdot \vec{r}_{P(Q)}} X\left(\vec{r} - \vec{r}_{P(Q)}\right) \tag{27}$$

Where $X\left(\vec{r}\right)$ is the orbital $2p_z$ wave function for the isolated carbon atom.

5. Energy dispersion for carbon nanotubes

We have determinant equation for Schrödinger's wave equation as

$$\begin{vmatrix} H_{PP} - \epsilon & H_{PQ} \\ H_{QP} & H_{QQ} - \epsilon \end{vmatrix} = 0 \tag{28}$$

Here $H_{PP} = \int X^*\left(\vec{r} - \vec{r}_P\right) H X\left(\vec{r} - \vec{r}_P\right) d\tau = \epsilon_0$ (29)

and $H_{PQ} = \left(e^{i\vec{k} \cdot \rho_1} + e^{i\vec{k} \cdot \rho_2} + e^{i\vec{k} \cdot \rho_3}\right) \int X^*\left(\vec{r}\right) H X(r - \rho_1) d\tau$

$$= \gamma_0 \left(e^{-\frac{ik_x a}{\sqrt{3}}} + e^{\frac{ik_x a}{2\sqrt{3}}} \cos\left(\frac{k_y a}{2}\right) \right) \tag{30}$$

By the symmetry of graphene lattice, $H_{PP} = H_{QQ}$ and $H_{PQ} = H_{QP}$, now, we have the solution of the Eq. (28) given as

$$\epsilon = H_{PP} \mp \left| H_{PQ} \right| \tag{31}$$

From the Eqs. (29)–(31), the obtained energy dispersion relation as follows

$$\epsilon = \epsilon_0 \mp \gamma_0 \sqrt{1 + 4 \cos\left(\frac{\sqrt{3}k_x a}{2}\right) \cos\left(\frac{k_y a}{2}\right) + 4 \cos^2\left(\frac{k_y a}{2}\right)} \tag{32}$$

Where γ_0 is the tight-binding or transfer integral. The negative sign represents the valence band of the graphene which is formed by π-orbitals bonding but the positive sign indicates the conduction band that is formed by π^*-orbitals antibonding. The energy dispersion of graphene is shown in **Figure 8**.

By expressing K_x and K_y in terms of components for band structure of carbon nanotubes of wave vector perpendicular and parallel to the tube axis and substituting in (32). We have

$$\epsilon(K) = \pm \sqrt{1 + 4 \cos\left(\frac{3C_x Ka}{2C} - \frac{3\pi fa C_y}{C^2}\right) \cos\left(\frac{\sqrt{3}C_y fa}{2C} + \frac{\sqrt{3}fa C_x}{C^2}\right) + 4 \cos^2\left(\frac{\sqrt{3}C_y Ka}{2C} + \frac{\sqrt{3}fa C_x}{C^2}\right)} \tag{33}$$
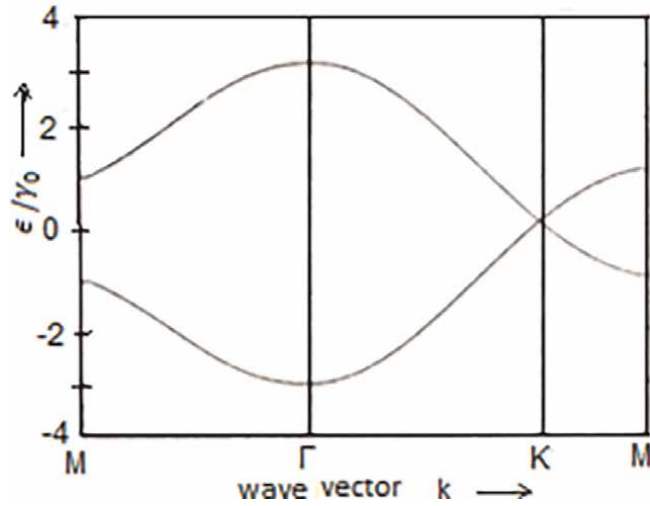
Figure 8.
Energy dispersion of the graphene in the reciprocal space along the symmetrical points.

Where K represents the wave vector along the axial direction and $C_x = \sqrt{3}a\left(n + \frac{m}{2}\right)$ *and* $C_y = \frac{3}{2}am$. For carbon nanotubes, the condition to be metallic of the allowed lines $\left(\frac{2\pi f}{C_y} - \frac{C_x}{C_y}K_x\right)$ cross one of the Fermi points of the graphene.

The band gap of the semiconducting carbon nanotubes depends on the diameter as shown in **Figure 9** and they are inversely proportional to each other. The relationship between the band gap and the radius or as diameter can be obtained in **Figure 10** by closing the two lines to the Fermi point of the graphene and given as (**Figures 11–20**)

$$\epsilon_g \simeq \frac{\sqrt{a}}{R_{CNT}} \tag{34}$$
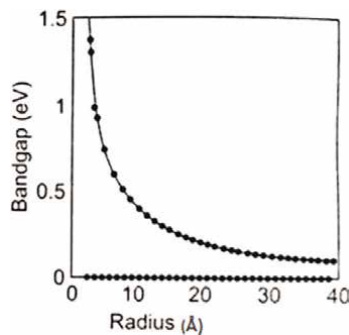
Figure 9.
The bandgap and radius for the zig-zag carbonnanotubes. The bandgap decreases with increasing the diameter for semiconducting carbon nanotubes.
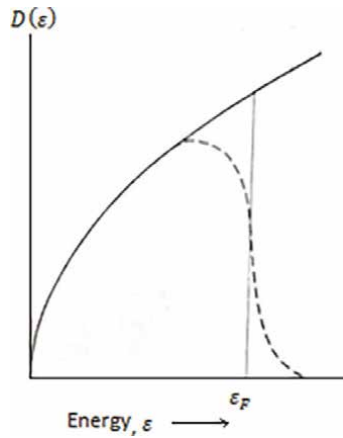
Figure 10.
Density of state as function of energy. The dashed curve shows the density at the finite temperature comparing with the Fermi energy ε_F at the absolute temperature.
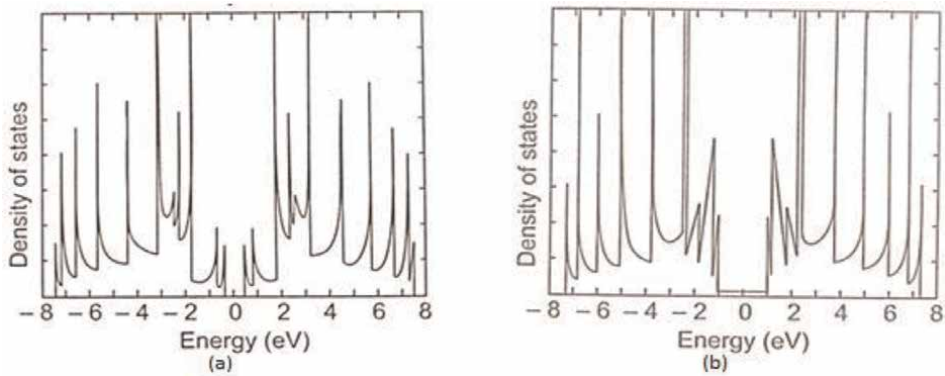
Figure 11.
Density of state for carbon nanotubes calculated from Eqs. (36) and (37) for the armchairs (11, 0) and (12, 0) of the carbon nanotubes and computed from the tight binding.
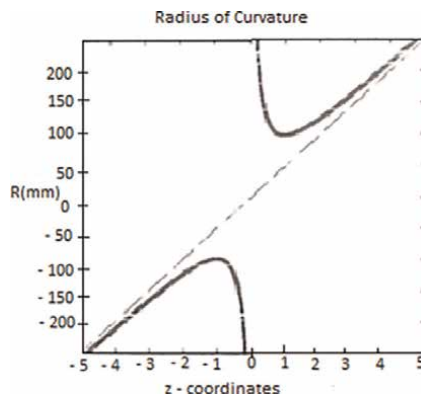
Figure 12.
Radius of curvature around beam waist position of Gaussian wave at a distance of $+z_R$ and $-z_R$ from beam waist. The point source is at beam waist along propagation, the radius of curvature is larger [9].
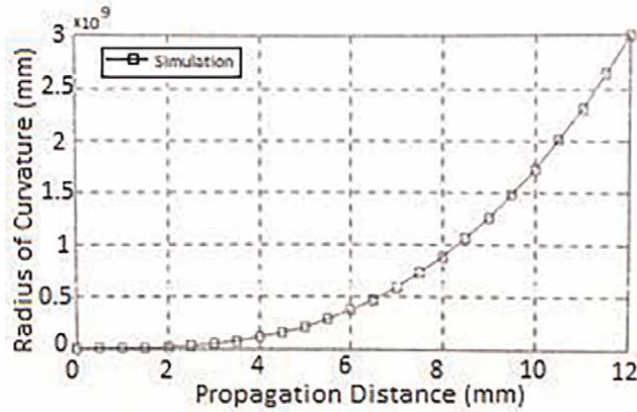
Figure 13.
Radius of curvature of Gaussian beam as a function of the propagation distance. The radius of curvature of the Gaussian beam is increased from 0mm to 2.99×10^9 mm for the propagation distance 0 mm to 12 mm. Therefore, the radius of curvature represents the linear variation with distance [10].
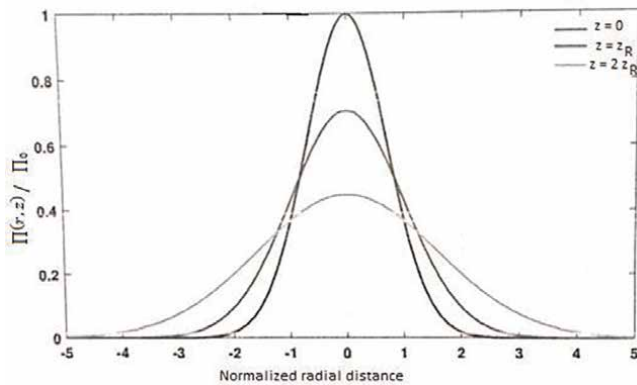
Figure 14.
The Gaussian wave along the radial direction for various "z".
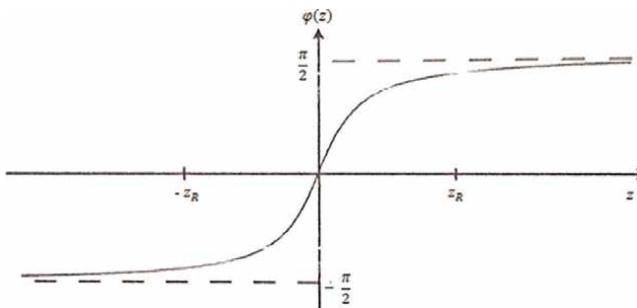
Figure 15.
Guoy phase shift around the Rayleigh length on both sides of the waist if the beam is at origin. There is the π phase shift in the Gaussian wave propagating from $z = -\infty$ to $z = +\infty$ relative to the plane wave called the Guoy effect.
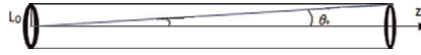
Figure 16.
Angle of divergence with z – axis.
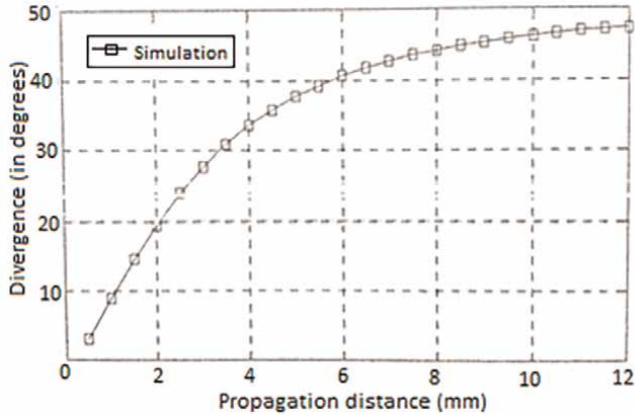
Figure 17.
Divergence of Gaussian beam as the function of the propagation distance. The Eqs. (58) and (59) repersents divergence angle range $(27.67° \leq \theta \leq 35.85°)$ at the distance 3 mm to 4.5 mm. The divergence and the propagation distance are proportional to each other [10].
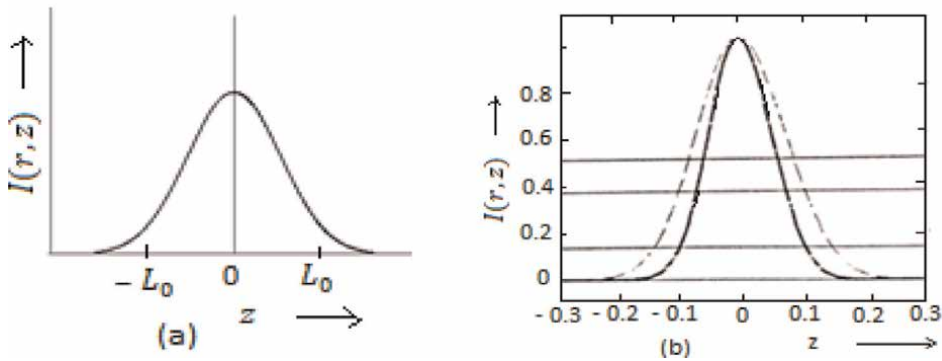
Figure 18.
Figure (a) represents the intensity distribution as function of z with the spot size. Figure (b) represents the amplitude and the intensity of Gaussian wave at beam waist with the dashed line and solid line respectively. They have been normalized to the maximum value. Here, the value of the spot size $L_0 = 0.1$ mm. the horizontal line shows the maximum amplitude by factor 1/e and the maximum intensity by factor $1/e^2$ [7, 9].

6. Fermi energy and density of state

In graphene, the energy of carbon nanotubes in the ground state of N electrons described as the Fermi energy given as
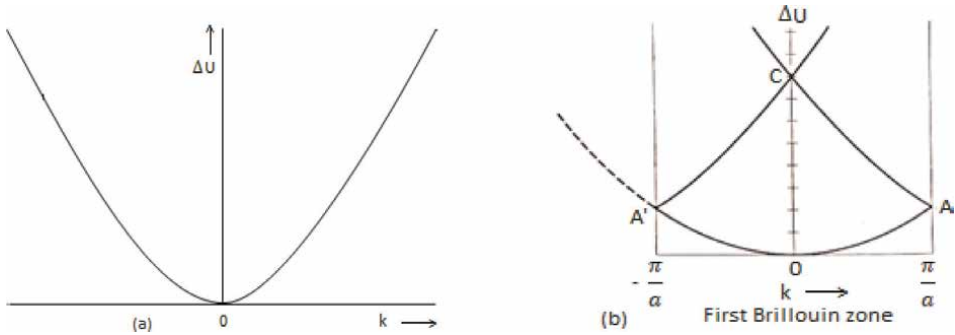
Figure 19.
Plot energy ΔU verses wave vector k *i.e., ΔU α* k². *The construction in figure (b) represents the band structure of crystal of carbon nanotube. The crystal potential as well as Hertzian potential* $\prod_e$ *gives the band gap at A and A' and at C.*
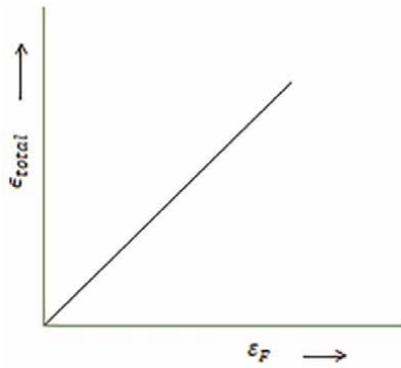
Figure 20.
Plot total stored energy ϵ_{total} *and Fermi energy* ϵ_F.

$$\varepsilon_F = \frac{\hbar^2}{2m}\left(\frac{N\pi}{2l}\right)^2 \tag{35}$$

The Fermi function described by the probability $f(\varepsilon)$ for the particular energy level ε by electron expressed as

$$f(\varepsilon) = \frac{1}{e^{\frac{\varepsilon-\mu}{K_B T}} + 1} \tag{36}$$

Where μ is a function of temperature called the chemical potential. At absolute zero, we have $\mu = \varepsilon_f$ if $\varepsilon = \mu$ then $f(\varepsilon) = \frac{1}{2}$ at all temperatures.

The density of states of carbon nanotubes expressed as

$$D(\varepsilon) = \frac{\sqrt{3}a^2}{2\pi R}\sum_K \int dK(K - K_i)\left|\frac{\partial \varepsilon}{\partial K}\right|^{-1} \tag{37}$$

On expending the dispersion relation (33) around the Fermi surface, we have

$$D(\varepsilon) = \frac{a\sqrt{3}}{\pi^2 R\gamma} \sum_{m=1}^{N} \frac{|\varepsilon|}{\sqrt{\varepsilon^2 - \varepsilon_m^2}} \tag{38}$$

Where $\varepsilon_m = |3m + 1|\left(\frac{a\gamma}{2R}\right)$ for semiconducting carbon nanotubes and $\varepsilon_m = |3m|\left(\frac{a\gamma}{2R}\right)$ for metallic carbon nanotubes. The dispersion near K points is proportional to the Fermi velocity of electrons in graphene, $v_f = 8 \times 10^5 \ m/s$ as –

$$\frac{d\varepsilon}{dK}|_K = \frac{\sqrt{3}}{2} a\gamma_0 = \hbar v_f \tag{39}$$

7. Maxwell's equation and Helmholtz equation

The carbon nanotube is like hollow cylinder and the spaces are available as free space in the carbon nanotube. So, the Maxwell's free space equations are as

$$\vec{\nabla} \bullet \vec{D} = 0 \tag{40}$$

$$\vec{\nabla} \bullet \vec{B} = 0 \tag{41}$$

$$\vec{\nabla} \bullet \vec{E} = -\frac{\partial \vec{B}}{\partial t} \tag{42}$$

$$\vec{\nabla} \bullet \vec{H} = \frac{\partial \vec{D}}{\partial t} \tag{43}$$

Where $\vec{D} = \varepsilon_0 \vec{E} \ and \ \vec{B} = \mu_0 \vec{H}$. Taking the curl of Eqs. (42) and (43) and using (40) and (41), we have

$$\nabla^2 \vec{E} = \mu_0 \varepsilon_0 \frac{\partial^2 \vec{E}}{\partial t^2} \tag{44}$$

$$\text{And } \nabla^2 \vec{H} = \mu_0 \varepsilon_0 \frac{\partial^2 \vec{H}}{\partial t^2} \tag{45}$$

These wave equations with components satisfy the eigen function wave Eq. (12);

$$\nabla^2 \prod = \mu_0 \varepsilon_0 \frac{\partial^2 \prod}{\partial t^2} \tag{46}$$

The plane wave along z-direction, thus, $\prod$ will be the function of z and t i.e.,

$$\prod = \prod(z, t) = \prod_0 \cos \omega\left(t - \frac{z}{C}\right) \tag{47}$$

On deriving (47) and (49), we obtain

$$\left(\nabla^2 + k^2\right) \prod = 0 \tag{48}$$

Where $k = \omega\sqrt{\varepsilon_0\mu_0}$ and $\prod = \prod(r)$ is the electric Hertz vector. The Eq. (49) is known as Helmholtz equation and the solution is given by

$$\prod(r) = \hat{e}_z e^{i\vec{k}\cdot\vec{r}} \tag{49}$$

Where $\hat{e}_z$ is a unit vector along z-direction. Eq. (49) represents the plane wave in transverse nature traveling through carbon nanotubes.

8. Gaussian wave

The Helmholtz Eq. (48) can also be written as

$$\frac{\partial^2\prod}{\partial x^2} + \frac{\partial^2\prod}{\partial z^2} - 2ik\frac{\partial\pi}{\partial z} = 0 \tag{50}$$

Or

$$\left(\nabla_T^2 - 2ik\frac{\partial}{\partial z}\right)\prod(x,y,z) = 0 \tag{51}$$

Where ∇_T^2 is the transverse gradient operator. The above Eq. (51) is termed as the paraxial wave equation and expressed in cylindrical coordinate system as

$$\frac{1}{r}\frac{\partial}{\partial r}\left(r\frac{\partial\prod}{\partial r}\right) - 2ik\frac{\partial\prod}{\partial z} = 0 \tag{52}$$

Where $\prod = \prod(r,z)$ and $r = \sqrt{x^2 + y^2}$ is the transverse radial distance. The solution of Eq. (52) gives

$$\prod = e^{\frac{-ikr^2}{2q(z)}}e^{-iP(z)} \tag{53}$$

Where $q(z)\ \{= q_0 + z\}$ is a complex variable within the reciprocal of Gaussian width; q_0 is the value of q at z = 0 and the imaginary number equal to iz_R, where z_R is a constant and a real part. So, $q(z)$ is known as the complex radius of curvature and it expressed as $q(z) = iz_R + z$ and $\frac{1}{q(z)} = \frac{z}{z^2+z_R^2} - i\frac{z_R}{z^2+z_R^2}$ These are in order for the electromagnetic wave intensity, $I \sim |\prod|^2$ to show r-dependence in the transversal direction, if $|\prod(r,z=0)|^2 = e^{\frac{-kr^2}{z_R}}$, where, the imaginary value of z_R has no radial dependence. z_R is also called Rayleigh distance of Rayleigh range and related to minimum spot size or minimum wave or beam waist, L_0, of Gaussian wave. P(z) gives the information to the phases of the waves. If q_0 is real then we have (**Figures 12–18**) [10];

$$\prod = e^{\frac{-ikr^2}{2q(r)}}e^{-iP(z)} \tag{54}$$

Since $e^{\frac{-ikr^2}{2q(r)}} = 1$ and P(z) is not a function of r; the phase is changed fast with r and the amplitude remains constant. We have $e^{-iP(z)} = \sqrt{1 + \left(\frac{z}{z_R}\right)^2}\,e^{i\tan^{-1}\left(\frac{z}{z_R}\right)}$ that represents amplitude and phase. A Gaussian wave propagating along z-direction in single walled carbon nanotube whose distribution of amplitude on the plane z = 0 is given by

$$\left|\prod(r, z = 0)\right| = e^{-\frac{r^2}{L_0^2}} \tag{55}$$

Where $L_0^2 = \frac{2z_R}{k} = \frac{\lambda_0 z_R}{n\pi} \Rightarrow L_0 = \left(\frac{\lambda_0 z_R}{n\pi}\right)^{\frac{1}{2}}$ and $z_R = \frac{n\pi L_0^2}{\lambda_0}$. The complete expression for the Gaussian wave is

$$\prod(r, z) = \prod_0 \frac{1}{\sqrt{1 + \left(\frac{z}{z_R}\right)^2}} \; e^{-\frac{kz_R r^2}{2\left(z^2 + z_R^2\right)}} \; e^{-i\frac{kz_R r^2}{2\left(z^2 + z_R^2\right)}} \; e^{-i\left(kz - \tan^{-1}\left(\frac{z}{z_R}\right)\right)} \tag{56}$$

This can be also written as

$$\prod(r, z) = \prod_0 \frac{L_0}{L(z)} \; e^{-\frac{r^2}{L^2(z)}} e^{-i\frac{r^2}{2R(z)}} \; e^{-i(kz - \varphi(z))} \tag{57}$$

Where $L(z) \left\{ = L_0 \sqrt{1 + \left(\frac{z}{z_R}\right)^2} \right\}$ is called the spot size and L_0 is the minimum spot size at the origin [7] and R(z) is the radius of curvature and equal to $z\left(1 + \left(\frac{z}{z_R}\right)^2\right)$ and $\varphi(z) \left\{ = \tan^{-1}\left(\frac{z}{z_R}\right) \right\}$ is the Guoy phase shift [12]. If $= z_R$, then we have the spot size $L(z) = 1.414\, L_0$. For the propagation of the Gaussian wave through the carbon nano tube, the minimum spot size, L_0, should be less than or equal to the radius of the single walled carbon nanotube.

The minimum diameter in the terms of 1/e field points is shown by $D_0 = 2L_0$. If $z \gg z_R$, the beam waist becomes $\simeq L_0 z / z_R$. In this case, the divergence angle or beam spreading angle is found.

The divergence angle is defind (when the relation of L and z becomes linear) as;

$$\theta_0 \simeq \tan\theta_0 = \frac{L}{z} = \frac{L_0}{z_R} = \frac{\lambda_0}{n\pi L_0} \tag{58}$$

$$\theta = 2\theta_0 = \frac{4}{\pi} \frac{\lambda_0}{n\, D_0} \tag{59}$$

Where θ_0 is the half of the divergence angle, θ, of the beam or wave.
The intensity distribution of Gaussian wave is given by

$$I(r, z) = \frac{I_0}{1 + \left(\frac{z}{z_R}\right)^2} \; e^{-\frac{2r^2}{L^2(Z)}} \tag{60}$$

$$\text{Or } I(r, z) = I_0 \left(\frac{L_0}{L(z)}\right)^2 e^{-\frac{2r^2}{L^2(Z)}} \tag{61}$$

This represents the transverse intensity distribution. It is measured from the beam centre perpendicular to the direction of propagation. The minimum spot size of the wave in the carbon nanotube at which the amplitude falls by a factor $\frac{1}{e}$ i.e., the intensity reduces by a factor $\frac{1}{e^2}$.

9. Energy storage capacity of the carbon nanotubes

According to laws of conservation of energy, the kinetic energy of charge particle is equal to the potential energy of charge particle. So, $E - U = U_2 - U_1 = \Delta U$. The Schrödinger wave Eq. (23) is also written as $\left(\nabla^2 + \frac{2m}{\hbar^2}(U_2 - U_1)\right)\prod = 0$ and compare with the Eq. (49). We have

$$k^2 = \frac{2m}{\hbar^2}\Delta U \tag{62}$$

$$\Delta U = \frac{\hbar^2}{2m}k^2 \tag{63}$$

By work-energy theorem, we have $W = \Delta U$. The distribution of charge on inner wall of nanotube with Gaussian wave is q and Gaussian wave travels in the nanotube with magnetic and electric field explained by Maxwell's equation. So, we have electric potential in terms of the electric Hertz potential $\prod_e$ [11]. The work done by moving charge of wave on the inner wall is given by

$$W = \prod_e q = \frac{1}{2}C\prod_e^2 \tag{64}$$

The total energy stored in single walled carbon nanotube is obtained as

$$\frac{1}{2}C\prod_e^2 = 4\left(\frac{\pi}{\lambda}\right)^2\left(\frac{2l}{N\pi}\right)^2\varepsilon_F \tag{65}$$

This total energy also expressed as

$$\epsilon_{total} = 16\left(\frac{l}{N\lambda}\right)^2\varepsilon_F \tag{66}$$

The capacitance of the carbon nanotube is expressed as

$$C = 32\left(\frac{l}{N\lambda}\right)^2\varepsilon_F / \prod_e^2 \tag{67}$$

10. Conclusions

The crystal structure of graphene with lattice and chiral vector gives the metallic and semiconducting character that is represented by various graphs and equation with energy dispersion relation and density of state which are found by Bloch theorem, Fourier series and Schrödinger wave equation. The solution of Helmholtz equation gives the plane monochromatic transverse wave and also Gaussian profile. We have found the minimum spot size of Gaussian wave that ensures the propagation of wave through the single walled carbon nanotube along the z-direction and verified by various graphs. The Gaussian beam within the low divergence has better wave quality.

We have also found the relation between the energy and wave vector by using Helmholtz and Schrödinger equation that gives us energy storage capacity of the carbon nanotubes with the electric Hertz potential.

Summarizing, the plane monochromatic transvers Gaussian wave with minimum spot size propagates through the hollow cylindrical carbon nanotube and the energy is stored on the inner wall (or in Fermi surface of nanotube) as a capacitor. The charges are accumulated on the surface with Hertzian potential. The stored energy is inversely proportional to the square of the wavelength and directly proportional to the Fermi energy. At minimum wavelength we have the higher energy.

A. Derivation of Helmholtz Wave Equation

We have $\nabla^2 \prod = \mu_0 \varepsilon_0 \frac{\partial^2 \prod}{\partial t^2}$ The plane wave along z-direction, thus, $\prod$ will be the function of z and t i.e.,

$$\prod = \prod(z,t) = \prod_0 \cos \omega \left(t - \frac{z}{C} \right)$$

Where $\omega = \frac{2\pi c}{\lambda}$ then

$$\frac{\partial \prod}{\partial t} = -\omega \prod_0 \sin \omega \left(t - \frac{z}{c} \right)$$

or

$$\frac{\partial^2 \prod}{\partial t^2} = -\omega^2 \prod_0 \cos \omega \left(t - \frac{z}{C} \right) = -\omega^2 \prod$$

$$= -\left(\frac{2\pi c}{\lambda} \right) \prod = -c^2 k^2 \prod$$

We have $\nabla^2 \prod = \mu_0 \varepsilon_0 \left(-c^2 k^2 \prod \right) \nabla^2 \prod = -k^2 \prod \ since, \mu_0 \varepsilon_0 = \frac{1}{c^2}$

or $\left(\nabla^2 + k^2 \right) \prod = 0$ This required wave equation is called the Helmholtz wave equation.

B. Solution of Helmholtz wave equation

Let the origin of the cylindrical coordinate system (r_m, θ_m, z) be located at the point $z = 0$ on the axis of the mth carbon nanotube in a bundle. So, the Helmholtz wave equation in cylindrical coordinate system written as

$$\left(\frac{\partial^2}{\partial r^2} + \frac{1}{r^2} \frac{\partial^2}{\partial \theta^2} + \frac{1}{r} \frac{\partial}{\partial r} + \frac{\partial^2}{\partial z^2} + k^2 \right) \prod_m (r) = 0$$

Since $\prod_m$ is a function of only r then $\frac{1}{r^2} \frac{\partial^2}{\partial \theta^2}$ and $\frac{\partial^2}{\partial z^2}$ are neglected and let us consider the solution of the above equation written as

$$\prod_m (r) = R(r) = R$$

Now, the Helmholtz wave equation is also written as

$$\frac{\partial^2}{\partial r^2}(R) + \frac{1}{r}\frac{\partial}{\partial r}(R) + k^2(R) = 0$$

Let $R = e^{\alpha r}$ and differentiate it with respect to r then we have

$$\frac{\partial R}{\partial r} = \frac{\partial}{\partial r}(e^{\alpha r}) = \alpha e^{\alpha r}$$

and

$$\frac{\partial^2 R}{\partial r^2} = \alpha^2 e^{\alpha r}$$

Putting these in the above equation and we can write

$$\alpha^2 e^{\alpha r} + \frac{1}{r}\alpha e^{\alpha r} + k^2 e^{\alpha r} = 0$$
$$\text{or } e^{\alpha r}\left\{\alpha^2 + \frac{\alpha}{r} + k^2\right\} = 0$$

We have a bundle of carbon nanotubes, so, $r \to \infty$ and consider $\frac{\alpha}{r}$ has negligible value. Above equation, therefore, written as

$$e^{\alpha r}\left\{\alpha^2 + k^2\right\} = 0$$
$$\alpha^2 = -k^2 \implies \alpha = \pm ik$$

Now, we have

$$R = e^{\pm ikr}$$
$$\prod_m (r) = e^{\pm ikr}$$

In vector form

$$\prod_m (r) = \hat{e}_z e^{i\vec{k}\cdot\vec{r}}$$

This is solution of the Helmholtz wave equation and indicates the plane wave. It is true for all type of the carbon nanotube. $\hat{e}_z$ is the unit vector along the carbon nanotube axis and at the right angles to the direction of propagation and shows the transverse character of wave.

Author details

Jay Shankar Kumar* and Ashok Kumar
University Department of Physics, Bhupendra Narayan Mandal University,
Madhepura, India

*Address all correspondence to: jayphysics108@gmail.com

IntechOpen

References

[1] Iijima S. Helical microtubules of graphitic carbon. Nature. 1991;**354**: 56-58. DOI: 10.1038/354056a0

[2] Iijima S. Single-shell carbon nanotubes of 1-nm diameter. Nature. 1993;**363**: 603-605. DOI: 10.1038/363603a0

[3] Delgado JL et al. The nano-forms of carbon. Journal of Materials Chemistry. 2008;**18**:1417-1426. DOI: 10.1039/b717218d

[4] Kumar JS, Kumar A. Propagation of surface plasmon waves along multi wall carbon nanotube with gold core. Bulletin of Pure and Applied Science. 2021;**40D**(2):88-93. DOI: 10.5958/2320-3218

[5] Shingyu L, Hongkai Z. Gaussian beam summation for diffraction in inhomogeneous media based on the grid-based particle method. Communication in Computer Physics. 2010;**8**(4):758-796. DOI: 10.4208/cicp.190809.090210a

[6] Lopez-Mago et al. Propagation characteristics of cartesian parabolic Gaussian beam. Laser Beam Shaping X1. 2010;**7789**:7789oQ, SPIE.CCC code: 0277-786. DOI: 10.1117/12.859283

[7] Kumar JS, Kumar A. Propagation of the Plane Electromagnetic Wave Through CNTs. Kanpur Philosophers. 2022;**IX(V(II))**:127-131

[8] Pflaum C. A beam propagation method for distorted Gaussian beam. Proceedings in Applied Mathematics and Mechanics. 2019;**19**:1-2. DOI: 10.1002/Pamm.201900034

[9] Alda J. Laser and Gaussian beam propagation and transformation. Encyclopedia of Optical Engineering. 2003;**999**:1013-1013. DOI: 10.1081/E-EoE120009751

[10] Busari et al. Gaussian beam divergence using paraxial approximation. Bayero Journal of Pure and Applied Sciences. 2018;**11**(1):45-49. DOI: 10.4314/bajopas.V11i1.7s

[11] Kumar JS, Kumar A. Surface wave propagation on carbon nanotube bundle and characteristics by high attenuation. Bulletin of Pure and Applied Science. 2021;**40D**(1):49-55. DOI: 10.5958/2320-3218

[12] Lodhia D et al. Phase effects in Gaussian beams on diffraction gratings. Journal of Physics: Conference Series. 2012;**363**:012014. DOI: 1088/1742-6596/363/1/012014

Chapter 4

Carbon Nanotube Alignment Methods

Abdullah Abdulhameed

Abstract

The outstanding properties of carbon nanotubes (CNTs) exist in their nanoscale form. The CNTs must be maintained aligned in the device to preserve these properties in the macroscale and bulk form. Recently, many studies addressed the alignment of CNTs at different scales for different applications. For example, CNTs are aligned vertically simultaneously as they grow on a substrate. Pre-synthesized CNTs can be aligned horizontally on a large scale under the influence of external forces such as electric and magnetic forces. This chapter reviews the latest techniques and methods regarding the horizontal alignment of CNTs. The alignment methods are classified based on the force used to achieve the alignment. The chapter concludes by discussing each method's advantages, disadvantages, and potential applications.

Keywords: carbon nanotubes, alignment, assembly, forces, applications

1. Introduction

Discovering carbon nanotubes (CNTs) by Iijima was an innovation in the field of science and engineering [1]. The remarkable electronic, mechanical, optical, and chemical properties of CNTs made them a promising material in future industries and applications [2–8].

CNT applications have not seen widespread adoption because of the CNT anisotropic nature and the difficulty in placing them into the desired location. Another reason is that CNTs are synthesized in a high-temperature environment, which is incompatible with the current fabrication methods [9]. In addition, there are difficulties in controlling the CNT structure during production [10].

Enforcing the CNT usage with the mentioned limitation may produce materials with considerable variations in their properties and devices that possess anisotropic behavior. Researchers have made efforts to overcome these limitations by improving the synthesis methods to produce high-quality pure CNT that can be grown directly into the device or by further processing the CNT using alignment techniques to purify, transfer, and assemble the CNT to the desired location [11].

In devices, CNTs can be aligned perpendicular or parallel to the substrate. In the first case, the CNTs are aligned vertically simultaneously as they grow on the substrate, as shown in **Figure 1a**. The vertical alignment challenges are the catalyst removal process, compatibility with the device fabrication methods, and the difficulties in transferring the aligned CNTs from the substrate to the target application [12–14].

IntechOpen
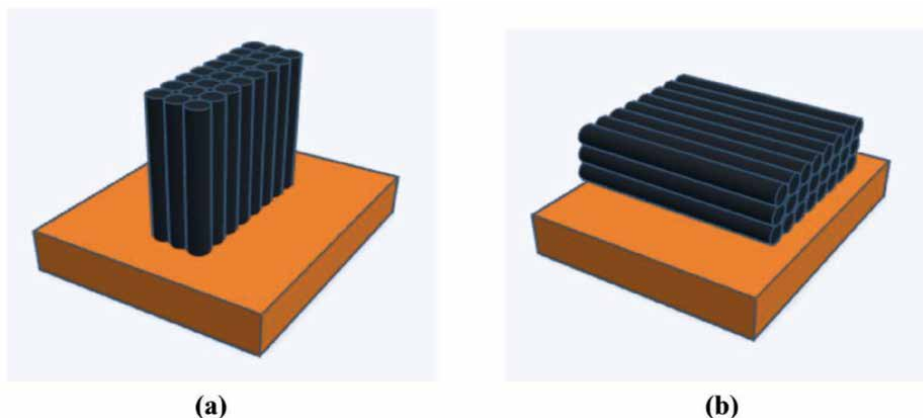
Figure 1.
(a) Vertically aligned CNTs. (b) Horizontally aligned CNTs.

However, pre-synthesized CNTs can be aligned vertically on a substrate under the influence of external forces such as electric fields and magnetic fields [15, 16]. In the case of horizontal alignment, the CNTs are assembled in parallel with the substrate surface, as shown in **Figure 1b**. Several methods are used to assemble and align CNTs vertically [17].

This chapter briefly reviews the methods that are used to align CNTs. The methods are classified based on the force used to achieve the alignment.

2. Alignment by magnetic forces

The principle of CNTs alignment by magnetic force is when strong magnetic fields are applied on CNTs at a macroscopic scale (Magnetophoresis). The CNT segments are aligned in parallel with the magnetic field lines to form long wires up to centimeters in length. The source of the magnetic field can be a permanent magnet, a superconducting magnet, or a resistive-coil magnet [18–20]. The response of CNTs to magnetic fields can also be employed in CNT separation [21].

The magnetic properties of CNTs are known to be very weak; hence, it is hard to assemble CNTs using low magnetic fields. The strength of the required magnetic field depends on the type of CNT. In the case of unmodified CNTs, the required field to align CNTs is in the range of 5 T–25 T, whereas MWCNTs require a less intense magnetic field than SWCNTs under the same conditions [22]. For example, Kimura et al. aligned MWCNTs in a polyester matrix using a superconducting magnet of 10 T. MWCNTs were dispersed in an unsaturated polyester-styrene monomer and then placed in a mold inside a magnet (see **Figure 2a**). MWCNTs are aligned as the polyester matrix polymerization is carried out [19]. The magnetic field intensity to align SWCNT in the same condition was 25 T, as demonstrated by Camponeschi e al. [23].

CNTs are coated with magnetite nanoparticles to effectively enhance their response to low magnetic fields. The required magnetic field to align CNTs is reduced by 1 to 3 orders of magnitude when CNTs are coated or decorated with magnetic nanoparticles such as Ni and Fe_2O_3 [24, 25]. For example, Wu et al. used a weak magnetic field (~50 mT) to align magnetite-carbon nanofiber hybrids (Fe_3O_4/CNT) and form a
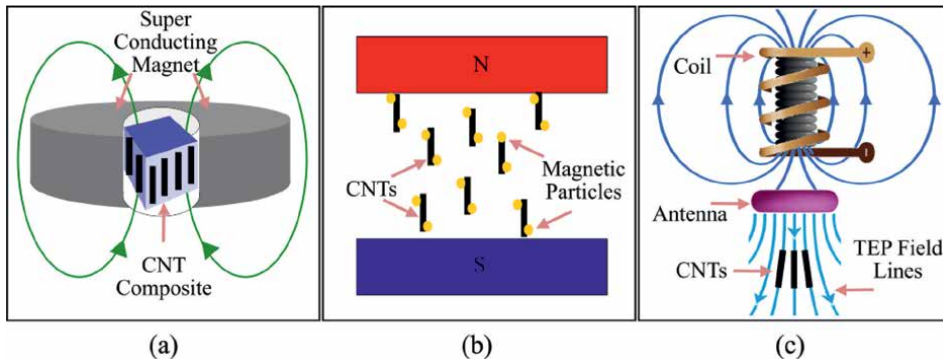
Figure 2.
Alignment by magnetic field using: (a) superconducting magnet [19]. (b) permanent magnet [26]. (c) resistive-coil magnet [20].

chain-like structure in an epoxy resin. **Figure 2b** shows the principle of aligning CNTs decorated with magnetite nanoparticles using a permanent magnet [26].

Teslaphoresis (TEP) is a non-conventional magnetophoretic force proposed by Bornhoeft et al. to overcome the small-scale structure limitation of the alignment methods. They used a Tesla coil's antenna supplied with a high-voltage force to transmit a near-field radio frequency of 2 MHz. The antenna projected a gradient field into the free space. **Figure 2c** shows that CNT wires are self-assembled along the TEP field lines, which are generated by a Tesla coil's antenna [20].

3. Alignment by acoustic forces

Acoustophoresis is a method used to pattern, release, and assemble CNTs using acoustic waves [27]. The acoustic radiation force is usually generated from a piezo-electric surface and then propagates through a CNT suspension, facilitating the tube movement [28]. The acoustic waves are classified into surface acoustic waves (SAWs) and bulk acoustic waves (BAWs).

Seemann KM et al. demonstrated SWCNTs and MWCNTs alignment between pre-structured interdigitated electrodes (IDE) using SAWs. The IDE is printed on a Lithium Niobite ($LiNbO_3$) surface to generate an acoustic field within a gap filled with an aqueous CNT suspension, as shown in **Figure 3a**. The SAWs' propagation within the CNT medium will cause a CNT motion, and the CNTs will be deposited in a specific pattern depending on the wavelength [29].

As demonstrated by Haslam et al., standing BAWs are used to align MWCNTs inside polymer composite resin. The composite is placed between two piezoelectric plates attached to electrical electrodes, as shown in **Figure 3b**. The electrodes supply the piezoelectric plates with an electrical signal to convert them to BAWs. The BAWs propagated through the composite matrix and aligned the MWCNTs in the wave's direction [30].

Zhichao Ma et al. used numerical simulation and experimentation to investigate the mechanism of the SAW-based patterning technique. They found that two different fields affect the patterning process, the acoustic pressure field, and the electric field. The acoustic radiation causes a micro-fluidic flow, while the electric field along the piezoelectric substrate causes a dipole moment. Both the micro-fluidic flow and
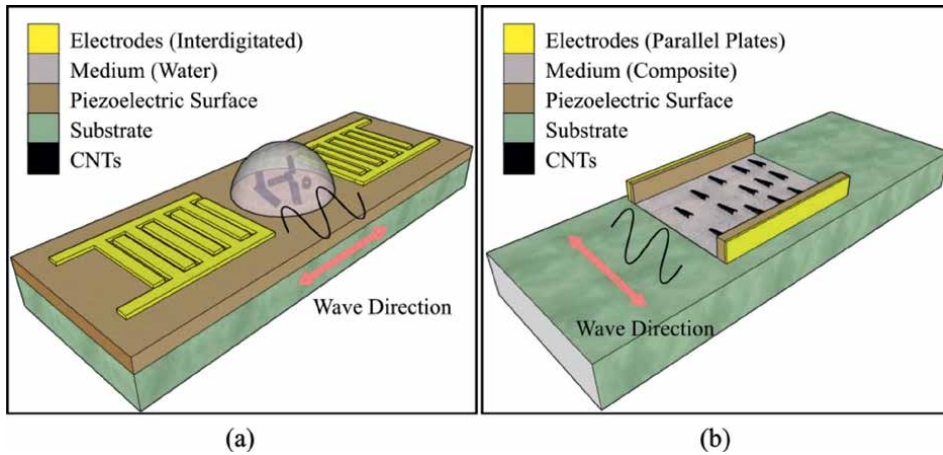
Figure 3.
Alignment by acoustic waves. (a) SAW structure [29]. (b) BAW structure [30].

dipole moment contribute to the patterning and alignment process [31]. Besides the assembly, acoustic waves were used in the synthesis of M-SWCNTs to produce monochromatic ultralong tubes [32].

4. Alignment by chemical forces

Alignment by chemical forces does not require any external field or force because CNTs are self-assembled based on charged molecules or chemical interaction between CNTs and a stimulatory material. For example, a solution-based chemical method such as evaporation-driven dip-casting is used to assemble CNTs on a large-scale area. A hydrophilic and hydrophobic interphase structure is formed on a silicon substrate to deposit SWCNTs, as shown in **Figure 4a**. The CNTs are directly deposited on the SiO_2 hydrophilic substrate without being contaminated by the hydrophobic strip regions [33].

Alignment relay technique (ART) is a new chemical alignment method first reported by Selmani and Schipper. The method is based on preparing a molecularly functionalized surface to sort and align CNTs simultaneously. The alignment process is
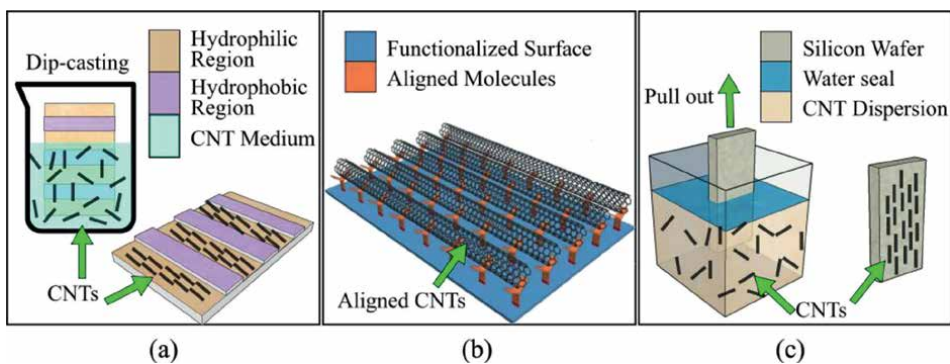
Figure 4.
Alignment by chemical methods. (a) Evaporation-driven Dip-casting [33]. (b) Alignment relay technique [34].
(c) Electrostatic repulsion Dip-coating [36].

passed from liquid crystals (LCs) to small molecules that can interact with CNTs selectively. The CNTs are deposited on the aligned molecules and self-aligned following the molecules' pattern, as shown in **Figure 4b** [34]. Mark J. MacLachlan reported CNTs alignment by ART on an ITO surface functionalized with Iptycene molecules [35].

A combination of electrostatic repulsion and dip-coating method is used to assemble S-SWCNT on an untreated silicon wafer. The wafer dipped into a bi-phasic dispersion of deionized water and chloroform. The dispersion contains S-SWCNTs with positively charged molecules. After the substrate was fully immersed, it was pulled out at a precise speed of 200-1000μm/s to form a thin film of S-SWCNTs deposited on the silicon wafer, as shown in **Figure 4c** [36].

5. Alignment by mechanical forces

Alignment by mechanical forces is most prevalent in polymer matrixes and CNT fibers and can be classified into three different categories, pure shear-induced techniques, extrusion-induced techniques, and flow-induced techniques [37].

The shear-induced techniques use direct shear force, which can be applied in various forms, such as cutting, rubbing, or pushing. In the cutting methods, a knife or blade is used to slice through a CNT composite material. CNTs can be seen on the cut surface aligned with the cutting direction, as shown in **Figure 5a** [38]. The alignment by pushing (or rubbing) is usually used with raw CNT powder synthesized by chemical vapor deposition (CVD). The vertically synthesized CNTs are rubbed against a smooth plastic surface to form a high-density thin film where the alignment is in the rubbing direction, as shown in **Figure 5b** [39]. Along with cutting and rubbing, dispersed CNTs in a polymer matrix can be aligned by pulling [40], friction [41], stretching [42], fracture [43], peeling [44], and uniaxial pressure [45]. The selection of the method depends on the polymer hardness, elasticity, size, and sample stability temperature.

Extrusion techniques such as melt fiber spinning, direct spinning, and electrospinning are used to fabricate long and continuous CNT yarns, wires, and fibers [46–48]. In these techniques, the CNTs are dispersed in a medium and then self-assembled in the drawing direction. However, the differences between the methods are the number of stages and the CNT source where the fiber spun from. For example, the melt fiber
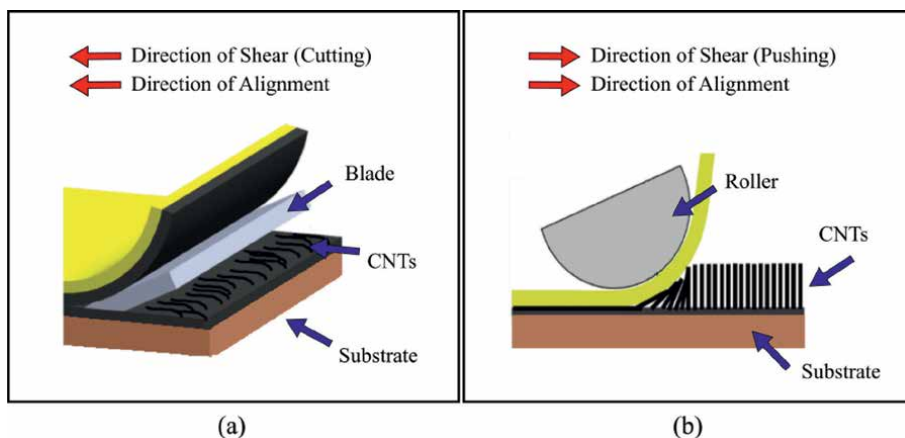
Figure 5.
Alignment by mechanical forces [37]. (a) Cutting [38]. (b) Pushing [39].
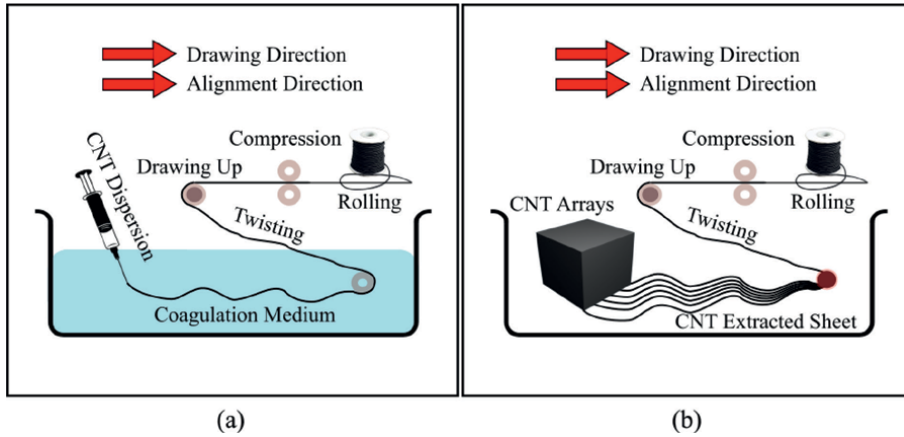
Figure 6.
Alignment by direct spinning in fibers. (a) Wet spinning [50]. (b) Dry spinning [51].

spinning method is used to align CNTs in thermoplastic polymers. Both SWCNTs and MWCNTs are dispersed into molten thermoplastic polycarbonate (PC) using a twin-screw extruder. The dispersion process is followed by melt spinning alignment to produce a fiber with aligned CNTs [49].

Alignment by direct spinning is classified into wet-spinning and dry-spinning methods. In the wet-spinning method, the fibers are prepared via coagulation spinning, where homogeneously CNT dispersion is injected into a co-flowing stream of a polymer solution, as shown in **Figure 6a** [50]. In the second method, the fibers are assembled from vertically aligned CNT arrays or CNT aerogels, as shown in **Figure 6b** [51]. A twisting phase is introduced in both methods during the spinning to align the CNTs in the drawing direction.

Flow-induced techniques, such as gas flow, are used to align CNTs vertically and horizontally on various substrate surfaces. The gas flow method is simple, easy to scale up, and can be used during the growth of CNTs to align them vertically. The method was also used as a post-growth alignment method to align CNTs horizontally on substrates.
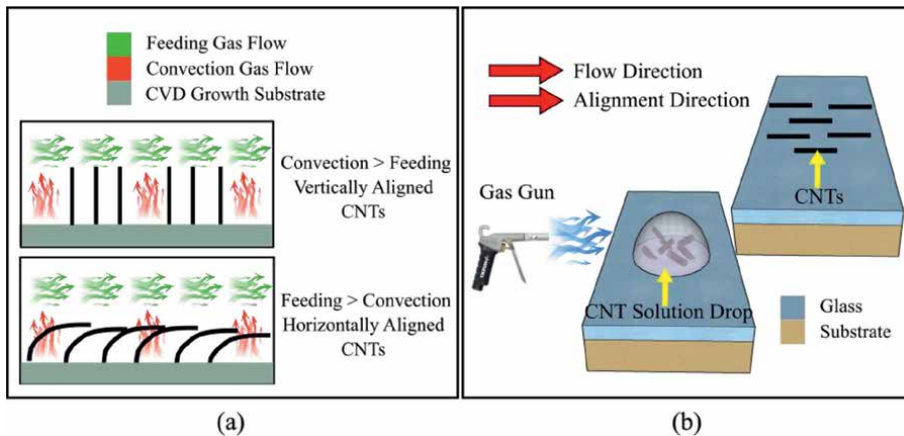
Figure 7.
Alignment by flow-induced techniques. (a) During growth alignment [54]. (b) Post-growth alignment [55].

The alignment during the growth means that CNTs are aligned as they grow by the CVD process. The CVD process uses two stable laminar gas flows to direct the growth of CNTs during their synthesis. These laminar flows are the feeding gas flow and the convection gas flow [52]. The CNTs are vertically aligned due to the temperature difference between the substrate and the surrounding environment. The temperature difference causes a convection gas flow to keep the CNTs growing outward from the substrate surface [53]. At a high feeding gas flow rate, the feeding gas flow dominates the convection gas flow, and therefore, the CNTs are horizontally aligned in the direction of the feeding gas flow, as shown in **Figure 7a** [54].

Flow-induced techniques are also used to align post-grown CNTs horizontally onto prefabricated electrode structures. A drop of a CNT solution is pipetted on a smooth surface and subjected to a gas flow force. The shear force resulting from the gas flow produced a torque on the tubes and led to their alignment, as shown in **Figure 7b**. In addition to the alignment, gas flow simultaneously spreads the solution drops and helps in the drying process [55].

6. Alignment by electric forces

Electrophoretic (EP) and DEP are electric forces that are used to align CNTs between two or more electrodes. The alignment by EP occurs when a surface-charged CNT is subjected to a uniform electric field. The alignment using DEP is based on the CNT dielectric polarization factor, where a non-uniform electric field is used to induce a dipole moment within the CNT itself. EP is mostly used to align CNTs in nanocomposite using parallel plate electrodes, while DEP is used to align CNTs across planner electrodes to form two-terminal devices such as sensors and CNT transistors [56, 57].

Direct current electrophoresis (DC-EP) and alternating current electrophoresis (AC-EP) were first reported by Yamamoto K et al. in 1996 and 1998, respectively, to orientate CNTs using an electric field. In the DC-EP alignment, a CNT sample was obtained from the carbon arc-discharge method, then ultrasonically dispersed in isopropyl alcohol (IPA). The solution was centrifuged to remove large particles and then dropped onto coplanar electrodes made of aluminum with a gap width of 0.4mm. The electric field that was applied to the electrodes was 25×10^3 V in the case of DC-EP and 2.2×10^3 V_{rms} with frequencies ranging from 10 Hz to 10 MHz in the case of AC-EP. Isopropyl ionization helps the CNTs move and align in response to the electric field amplitude and frequency variation [58, 59].

The first time DEP was used in CNT integration was in 2003 by Krupke et al. to separate metallic bundles of SWCNT from a solution and assemble them into a device. The SWCNTs were grown by laser ablation, purified with nitric acid, and suspended in dimethylformamide (DMF). Electrodes were prepared with standard e-beam lithography and connected to an AC power supplier. After dropping the CNT suspension on the chip, the generator was switched on to align the CNTs. After alignment, the drop is blown off gently with nitrogen gas [60]. Later in 2007, A. Vijayaraghavan et al. successfully produced high-density SWCNT devices fabricated on a single chip using alternating current DEP. Several million devices were packaged in a square centimeter [61]. Recent studies concluded that the quality of aligned CNTs using DEP depends on many factors, such as the electrode design [62, 63], suspension quality [64], and CNTs enrichment [65, 66].

The differences between EP and DEP and the resulting CNT motion from each force (translational and rotational) are summarized in **Table 1**. The translational

Force	Electric field	CNT behavior	Electrode configuration
DC-EP	Uniform	CNTs Move Toward One Electrode Based on their Surface Charge.	Parallel Plate Electrodes
AC-EP	Uniform	CNTs Rotate Following the Electric Field Lines	Parallel Plate Electrodes
DEP	Non-Uniform	CNT Rotates Following the Electric Field Lines and Moves Toward the Region with the High Electric Field	Planner Electrodes, IDE

Table 1.
The behavior of a CNT subjected to an electric field.
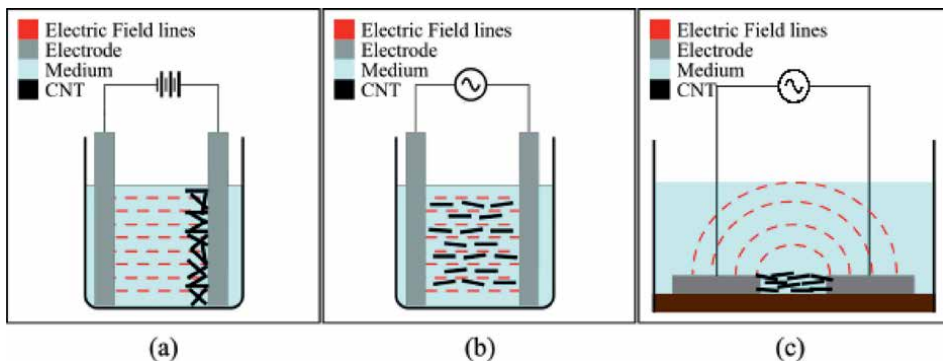
Figure 8.
Alignment by electric forces. (a) DC-EP. (b) AC-EP. (c) DEP.

motion of CNTs is governed by the electrophoretic mobility of charged CNT's surface and tips, while the rotational motion is governed by the relaxation mechanism and the dipole moment created by the locally non-uniform electric field [67]. **Figure 8a** shows a translation motion of CNTs toward the electrode with opposite charges because the electrodes were connected to a DC source, and DC-EP occurred. If the DC source is replaced with an AC source, the CNTs will experience a rotation motion and align with the electric field line due to the AC-EP (see **Figure 8b**). The CNTs would experience both translational and rotational motion if the electrode configuration changed from parallel plates to planner electrodes due to the DEP force, as shown in **Figure 8c**. In the DEP method, electric fields are usually generated by sinusoidal voltage sources [68]. Alternating pulsed currents are also used to assist the alignment [69].

7. Alignment by other methods

The CNT alignment methods vary based on the CNT sample size, from an individual tube to bulk CNT powder. The focused ion beam (FIB) method is an example of controlling an individual tube's orientation. The FIB method uses a focused beam of ions to control an individual tube's alignment angle after coating the tube with metal nanoparticles. The orientation is achieved by attaching the CNT to a pyramidal tip end of a nanoprobe then the CNT is exposed to an external ion beam source. The beam intensity and beam scanning cycles determine the degree of alignment of the metal-coated CNT [70]. On the other side, some methods provide a large-scale CNT
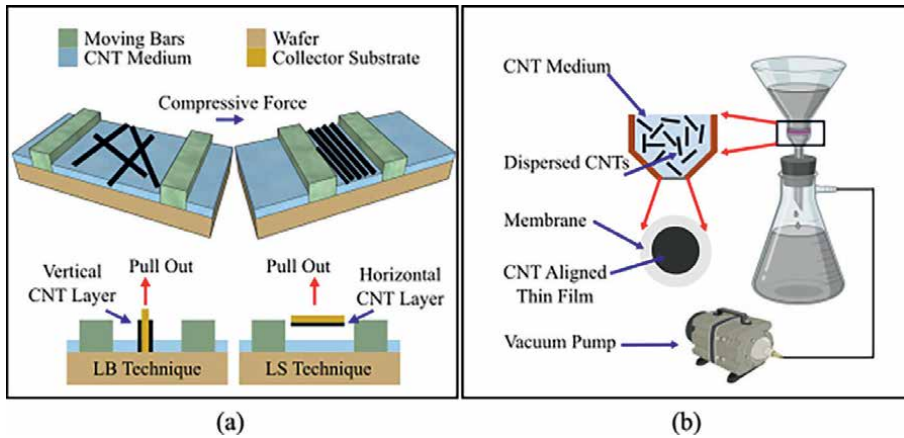
Figure 9.
Other alignment methods. (a) Langmuir-Blodgett and Langmuir–Schaefer methods. (b) Filtration method.

alignment, such as Langmuir–Blodgett method (LB) [71], Langmuir–Schaefer (LS) method [72], and vacuum filtration method [73].

The LB method is used to fabricate monolayers of aligned SWCNTs on oxide substrates. The degree of alignment and packing is improved by pressure cycling and thermal annealing during layers fabrication [71]. The LS method is versatile for the fabrication of high-density arrays of more than 500 tubes/μm. The method is used to assemble high-purity S-SWCNT from 1,2-dichloroethane (DCE) for high-performance transistors [72]. **Figure 9a** illustrates the alignment using LB and LS methods where a uniaxial compressive force is applied using moving bars to assemble CNTs into well-ordered arrays. The mean difference between LB and LS is the collection mechanism where the assembled monolayer arrays are vertically transferred in the case of LB and horizontally transferred in the case of LS using a collector substrate.

Filtration methods are used to prepare high-packing density well-aligned CNT thin films. The degree of alignment is controlled by the filtration rate and the CNT concentration in the solution [73]. The filtration method consists of a conventional filtration setup and vacuum pump to control the medium flow rate through the membrane, as shown in **Figure 9b**.

Ceramic filters [74], blown bubbles [75], viscous shear stress [76], confined shear alignment [77], and nematic liquid alignment [78] are additional film-assembly methods that provide a large-scale alignment regarding the type of CNTs. The confined shear alignment method is used to deposit a uniform film of aligned carbon nanotubes across an $8 \times 8 \text{ cm}^2$ region [77]. The nematic liquid alignment occurs because CNTs exhibit a liquid crystal phase when they are dispersed into a nematic liquid crystal solvent [78].

8. Chapter summary

The superior properties of CNTs are observed when the CNTs are aligned or deposited in a specific order. Random distributed CNTs showed unpredicted behavior and poor electrical performance compared with the aligned CNTs. For those reasons, CNTs alignment is an essential step in the fabrication of CNT-based devices and materials. **Table 2** summarizes the alignment methods and their working scale,

Method	Scale (m)	Application	Advantages	Challenges	Ref.
DEP	10^{-7}–10^{-5}	CNTFET, Sensors	Low Power, Room Temperature, Easy Setup	CNTs dispersity, Limited by the Electrode Geometry, Electrothermal Heating	[79, 80]
EP, Electric Field	10^{-4}–10^{-2}	Composites	Simple and Flexible Setup	Requires High Voltage For Large Sample, Electrodes in Contact with the CNT Sample	[81, 82]
Vacuum Filtration	10^{-2}	Thin Films	Simple Setup, Scalable	Membrane Removal, Flow Rate Control of the CNT Medium	[83]
Teslaphoresis Magnetophoresis	10^{-1}	Connectors	Electrodeless, Real-time Method	Requires a High Magnetic Field, Controllability of the Magnetic Field, Magnetic Particles Removal	[20, 84]
Twisting	10^{0}–10^{1}	Fibers, Wires	Scalable, Relatively Cheap	Complicated Setup, Difficulties in Controlling the Tube-Tube Contacts	[85]
Acoustic	10^{-6}–10^{-4}	CNT Patterns	The sample has no contact with the Electrodes	Limited to Piezo Material Surfaces	[86]

Table 2.
CNTs post alignment methods, applications, and challenges.

applications, advantages, and challenges. It is clear that each method works fine on a specific scale. Outside that scale, challenges start to appear and limit the methods from being universal methods. Thus, the alignment method's selection depends on the application geometry and the compatibility with its fabrication process.

Conflict of interest

The authors declare no conflict of interest.

Author details

Abdullah Abdulhameed
Faculty of Engineering, Department of Electronic Engineering, Hadhramaut
University, Mukalla, Yemen

*Address all correspondence to: dr.a.abdulhameed@gmail.com

IntechOpen

References

[1] Iijima S. Helical microtubules of graphitic carbon. Nature. 1991;**354**:56-58. DOI: 10.1038/354056a0

[2] Zhu S, Ni J, Li Y. Carbon nanotube-based electrodes for flexible supercapacitors. Nano Research. 2020;**13**:1825-1841. DOI: 10.1007/s12274-020-2729-5

[3] Choi SJ, Bennett P, Lee D, Bokor J. Highly uniform carbon nanotube nanomesh network transistors. Nano Research. 2015;**8**:1320-1326. DOI: 10.1007/s12274-014-0623-8

[4] Zhao X, Wu Y, Wang Y, Wu H, Yang Y, Wang Z, et al. High-performance Li-ion batteries based on graphene quantum dot wrapped carbon nanotube hybrid anodes. Nano Research. 2020;**13**:1044-1052. DOI: 10.1007/s12274-020-2741-9

[5] Xie Y, Zhang Z, Zhong D, Peng L. Speeding up carbon nanotube integrated circuits through three-dimensional architecture. Nano Research. 2019;**12**:1810-1816. DOI: 10.1007/s12274-019-2436-2

[6] Abdulhameed A, Halin IA, Mohtar MN, Hamidon MN. pH-sensing characteristics of multi-walled carbon nanotube assembled across transparent electrodes with dielectrophoresis. IEEE Sensors Journal. 2021;**21**:26594-26601. DOI: 10.1109/JSEN.2021.3124324

[7] Abdulhameed A, Mohtar MN, Hamidon MN, Halin IA. ITO Islands as floating electrodes to deposit aligned carbon nanotubes for photovoltaic applications. In: Proceedings of the 2019 IEEE 9th International Nanoelectronics Conferences. New Jersey, United States; 2019. pp. 1-6

[8] Abdulhameed A, Halin IA, Mohtar MN, Hamidon MN. Airflow-assisted dielectrophoresis to reduce the resistance mismatch in carbon nanotube-based temperature sensors. RSC Advances. 2021;**11**:39311-39318. DOI: 10.1039/d1ra08250g

[9] Abdulhameed A, Wahab NZA, Mohtar MN, Hamidon MN, Shafie S, Halin IA. Methods and applications of electrical conductivity enhancement of materials using carbon nanotubes. Journal of Electronic Materials. 2021;**50**:3207-3221. DOI: 10.1007/s11664-021-08928-2

[10] Yang F, Wang X, Zhang D, Yang J, Luo D, Xu Z, et al. Chirality-specific growth of single-walled carbon nanotubes on solid alloy catalysts. Nature. 2014;**510**:522-524. DOI: 10.1038/nature13434

[11] Corletto A, Shapter JG. Nanoscale patterning of carbon nanotubes: Techniques, applications, and future. Advancement of Science. 2021;**8**:2001778. DOI: 10.1002/advs.202001778

[12] Pimparkar N, Kocabas C, Kang SJ, Rogers J, Alam MA. Limits of performance gain of aligned CNT over randomized network: Theoretical predictions and experimental validation. IEEE Electron Device Letters. 2007;**28**:593-595. DOI: 10.1109/LED.2007.898256

[13] Li P, Zhang J. Preparation of horizontal single-walled carbon nanotubes arrays. Topics in Current Chemistry. 2016;**374**:85. DOI: 10.1007/s41061-016-0085-4

[14] Chhowalla M, Teo KBK, Ducati C, Rupesinghe NL, Amaratunga GAJ, Ferrari AC, et al. Growth process

conditions of vertically aligned carbon nanotubes using plasma enhanced chemical vapor deposition. Journal of Applied Physics. 2001;**90**:5308-5317. DOI: 10.1063/1.1410322

[15] Castellano RJ, Akin C, Giraldo G, Kim S, Fornasiero F, Shan JW. Electrokinetics of scalable, electric-field-assisted fabrication of vertically aligned carbon-nanotube/polymer composites. Journal of Applied Physics. 2015;**117**:214306. DOI: 10.1063/1.4921948

[16] Bondino F, Magnano E, Ciancio R, Castellarin Cudia C, Barla A, Carlino E, et al. Stable Fe nanomagnets encapsulated inside vertically-aligned carbon nanotubes. Physical Chemistry Chemical Physics. 2017;**19**:32079-32085. DOI: 10.1039/c7cp05181f

[17] Zhang J, Cui J, Wang X, Wang W, Mei X, Yi P, et al. Recent progress in the preparation of horizontally ordered carbon nanotube assemblies from solution. Physical Status Solidi Applied Material Science. 2018;**215**:1700719. DOI: 10.1002/pssa.201700719

[18] Walters DA, Casavant MJ, Qin XC, Huffman CB, Boul PJ, Ericson LM, et al. In-plane-aligned membranes of carbon nanotubes. Chemical Physics Letters. 2001;**338**:14-20. DOI: 10.1016/S0009-2614(01)00072-0

[19] Kimura T, Ago H, Tobita M, Ohshima S, Kyotani M, Yumura M. Polymer composites of carbon nanotubes aligned by a magnetic field. Advanced Materials. 2002;**14**:1380-1383. DOI: 10.1002/1521-4095(20021002)14:19<1380::AID-ADMA1380>3.0.CO;2-V

[20] Bornhoeft LR, Castillo AC, Smalley PR, Kittrell C, James DK, Brinson BE, et al. Teslaphoresis of carbon nanotubes. ACS Nano. 2016;**10**:4873-4881. DOI: 10.1021/acsnano.6b02313

[21] Gui X, Wei J, Wang K, Wang W, Lv R, Chang J, et al. Improved filling rate and enhanced magnetic properties of Fe-filled carbon nanotubes by annealing and magnetic separation. Materials Research Bulletin. 2008;**43**:3441-3446. DOI: 10.1016/j.materresbull.2008.01.028

[22] Garmestani H, Al-Haik MS, Dahmen K, Tannenbaum R, Li D, Sablin SS, et al. Polymer-mediated alignment of carbon nanotubes under high magnetic fields. Advanced Materials. 2003;**15**:1918-1921. DOI: 10.1002/adma.200304932

[23] Camponeschi E, Florkowski B, Vance R, Garrett G, Garmestani H, Tannenbaum R. Uniform directional alignment of single-walled carbon nanotubes in viscous polymer flow. Langmuir. 2006;**22**:1858-1862

[24] Ma C, Liu HY, Du X, Mach L, Xu F, Mai YW. Fracture resistance, thermal and electrical properties of epoxy composites containing aligned carbon nanotubes by low magnetic field. Composites Science and Technology. 2015;**114**:126-135. DOI: 10.1016/j.compscitech.2015.04.007

[25] Korneva G, Ye H, Gogotsi Y, Halverson D, Friedman G, Bradley JC, et al. Carbon nanotubes loaded with magnetic particles. Nano Letters. 2005;**5**:879-884. DOI: 10.1021/nl0502928

[26] Wu S, Ladani RB, Zhang J, Kinloch AJ, Zhao Z, Ma J, et al. Epoxy nanocomposites containing magnetite-carbon nanofibers aligned using a weak magnetic field. Polymer. 2015;**68**:25-34

[27] Zeng Q, Li L, Ma HL, Xu J, Fan Y, Wang H. A non-contact strategy for controlled enrichment, manipulation, and separation of carbon nanotubes by surface acoustic waves. Applied

Physics Letters. 2013;**102**:213106. DOI: 10.1063/1.4807677

[28] Lim WP, Yao K, Chen Y. Alignment of carbon nanotubes by acoustic manipulation in a fluidic medium. Journal of Physical Chemistry C. 2007;**111**:16802-16807. DOI: 10.1021/jp073456c

[29] Seemann KM, Ebbecke J, Wixforth A. Alignment of carbon nanotubes on pre-structured silicon by surface acoustic waves. Nanotechnology. 2006;**17**:4529-4532. DOI: 10.1088/0957-4484/17/17/040

[30] Haslam MD, Raeymaekers B. Aligning carbon nanotubes using bulk acoustic waves to reinforce polymer composites. Composites. Part B, Engineering. 2014;**60**:91-97. DOI: 10.1016/j.compositesb.2013.12.027

[31] Ma Z, Guo J, Liu YJ, Ai Y. The patterning mechanism of carbon nanotubes using surface acoustic waves: The acoustic radiation effect or the dielectrophoretic effect. Nanoscale. 2015;**7**:14047-14054. DOI: 10.1039/c5nr04272k

[32] Zhu Z, Wei N, Xie H, Zhang R, Bai Y, Wang Q, et al. Acoustic-assisted assembly of an individual monochromatic ultralong carbon nanotube for high on-current transistors. Science Advances. 2016;**2**:e1601572. DOI: 10.1126/sciadv.1601572

[33] Zhang J, Cui J, Wang X, Wang W, Mei X, Long W, et al. Large-scale assembly of single-walled carbon nanotubes based on aqueous solution. Integrated Ferroelectrics. 2018;**190**:39-47. DOI: 10.1080/10584587.2018.1456134

[34] Selmani S, Schipper DJ. Orientation control of molecularly functionalized surfaces applied to the simultaneous alignment and sorting of carbon nanotubes. Angewandte Chemie. 2018;**130**:2423-2427. DOI: 10.1002/ange.201712779

[35] MacLachlan MJ. Bringing nanotubes into line. Angewandte Chemie, International Edition. 2018;**57**:4838-4839. DOI: 10.1002/anie.201801871

[36] Gao B, Zhang X, Qiu S, Jin H, Song Q, Li Q. Assembly of aligned semiconducting carbon nanotubes in organic solvents via introducing inter-tube electrostatic repulsion. Carbon N. Y. 2019;**146**:172-180. DOI: 10.1016/j.carbon.2019.01.095

[37] Goh GL, Agarwala S, Yeong WY. Directed and on-demand alignment of carbon nanotube: A review toward 3D printing of electronics. Advanced Materials Interfaces. 2019;**6**:1801318. DOI: 10.1002/admi.201801318

[38] Ajayan PM, Stephan O, Colliex C, Trauth D. Aligned carbon nanotube arrays formed by cutting a polymer resin-nanotube composite. Science. 1994;**265**:1212-1214

[39] Wang D, Song P, Liu C, Wu W, Fan S. Highly oriented carbon nanotube papers made of aligned carbon nanotubes. Nanotechnology. 2008;**19**:75609. DOI: 10.1088/0957-4484/19/7/075609

[40] Kim Y, Minami N, Zhu W, Kazaoui S, Azumi R, Matsumoto M. Homogeneous and structurally controlled thin films of single-wall carbon nanotubes by the Langmuir-Blodgett technique. Synthetic Metals. 2003;**135**:747-748. DOI: 10.1016/S0379-6779(02)00830-5

[41] Lanticse LJ, Tanabe Y, Matsui K, Kaburagi Y, Suda K, Hoteida M, et al. Shear-induced preferential alignment of carbon nanotubes resulted in anisotropic electrical conductivity of polymer composites. Carbon N. Y.

2006;**44**:3078-3086. DOI: 10.1016/j.
carbon.2006.05.008

[42] Ruan SL, Gao P, Yang XG, Yu TX.
Toughening high performance ultrahigh
molecular weight polyethylene using
multiwalled carbon nanotubes. Polymer.
2003;**44**:5643-5654

[43] Chen W, Tao X. Production
and characterization of polymer
nanocomposite with aligned single
wall carbon nanotubes. Applied
Surface Science. 2006;**252**:3547-3552.
DOI: 10.1016/j.apsusc.2005.05.028

[44] Zhao H, Zhou Z, Dong H, Zhang L,
Chen H, Hou L. A facile method to
align carbon nanotubes on polymeric
membrane substrate. Scientific Reports.
2013;**3**:1-5. DOI: 10.1038/srep03480

[45] Lance MJ, Hsueh CH, Ivanov IN,
Geohegan DB. Reorientation of carbon
nanotubes in polymer matrix composites
using compressive loading. Journal of
Materials Research. 2005;**20**:1026-1032.
DOI: 10.1557/JMR.2005.0139

[46] Haggenmueller R, Gommans HH,
Rinzler AG, Fischer JE, Winey KI.
Aligned single-wall carbon nanotubes
in composites by melt processing
methods. Chemical Physics Letters.
2000;**330**:219-225. DOI: 10.1016/
S0009-2614(00)01013-7

[47] Li YL, Kinloch IA, Windle AH.
Direct spinning of carbon nanotube
fibers from chemical vapor deposition
synthesis. Science. 2004;**304**:276-278

[48] Inagaki M, Yang Y, Kang F. Carbon
nanofibers prepared via electrospinning.
Advanced Materials. 2012;**24**:2547-2566.
DOI: 10.1002/adma.201104940

[49] Sennett M, Welsh E, Wright JB, Li WZ,
Wen JG, Ren ZF. Dispersion and alignment
of carbon nanotubes in polycarbonate.

Applied Physics A: Materials Science &
Processing. 2003;**76**:111-113. DOI: 10.1007/
s00339-002-1449-x

[50] Zheng T, Xu N, Kan Q, Li H, Lu C,
Zhang P, et al. Wet-spinning assembly
of continuous, highly stable hyaluronic/
multiwalled carbon nanotube hybrid
microfibers. Polymers. 2019;**11**:867

[51] Tran C-D. Dry spinning carbon
nanotubes into continuous yarn.
In: Nanotube Superfiber Materials.
Amsterdam, Netherlands: Elsevier; 2014.
pp. 211-242

[52] Huang S, Cai X, Du C, Liu J. Oriented
long single walled carbon nanotubes
on substrates from floating catalysts.
The Journal of Physical Chemistry. B.
2003;**107**:13251-13254. DOI: 10.1021/
jp0364708

[53] Huang S, Woodson M, Smalley R,
Liu J. Growth mechanism of oriented long
single walled carbon nanotubes using
"fast-Heating" chemical vapor deposition
process. Nano Letters. 2004;**4**:1025-1028.
DOI: 10.1021/nl049691d

[54] Reina A, Hofmann M, Zhu D,
Kong J. Growth mechanism of long and
horizontally aligned carbon nanotubes
by chemical vapor deposition. Journal
of Physical Chemistry C. 2007;**111**:7292-
7297. DOI: 10.1021/jp0711500

[55] Hedberg J, Dong L, Jiao J. Air flow
technique for large scale dispersion
and alignment of carbon nanotubes
on various substrates. Applied Physics
Letters. 2005;**86**:1-3. DOI: 10.1063/
1.1897435

[56] Wu S, Peng S, Wang CH.
Multifunctional polymer nanocomposites
reinforced by aligned carbon
nanomaterials. Polymers. 2018;**10**:542

[57] Seichepine F, Rothe J,
Dudina A, Hierlemann A, Frey U.

Dielectrophoresis-assisted integration of 1024 carbon nanotube sensors into a CMOS microsystem. Advanced Materials. 2017;**29**:1606852. DOI: 10.1002/adma.201606852

[58] Yamamoto K, Akita S, Nakayama Y. Orientation of carbon nanotubes using electrophoresis. Japanese Journal of Applied Physics. 1996;**35**:L971

[59] Yamamoto K, Akita S, Nakayama Y. Orientation and purification of carbon nanotubes using ac electrophoresis. Journal of Physics D: Applied Physics. 1998;**31**:L34. DOI: 10.1088/0022-3727/31/8/002

[60] Krupke R, Hennrich F, Weber HB, Kappes MM, Löhneysen HV. Simultaneous deposition of metallic bundles of single-walled carbon nanotubes using Ac-dielectrophoresis. Nano Letters. 2003;**3**:1019-1023. DOI: 10.1021/nl0342343

[61] Vijayaraghavan A, Blatt S, Weissenberger D, Oron-Carl M, Hennrich F, Gerthsen D, et al. Ultra-large-scale directed assembly of single-walled carbon nanotube devices. Nano Letters. 2007;**7**:1556-1560. DOI: 10.1021/nl0703727

[62] Abdulhameed A, Halin IA, Mohtar MN, Hamidon MN. The role of the electrode geometry on the dielectrophoretic assembly of multi-walled carbon nanotube bundles from aqueous solution. Journal of Electrostatics. 2022;**116**:103694. DOI: 10.1016/j.elstat.2022.103694

[63] Abdulhameed A, Yunus NAM, Halin IA, Hamidon MN. Simulation of dielectrophoretic alignment for carbon nanotube on indium tin oxide. Materials Today Proceedings. 2019;**7**:593-600. DOI: 10.1016/j.matpr.2018.12.012

[64] Abdulhameed A, Abdul Halin I, Mohtar MN, Hamidon MN. The role of medium on the assembly of carbon nanotube by dielectrophoresis. Journal of Dispersion Science and Technology. 2020;**41**:1576-1587. DOI: 10.1080/01932691.2019.1631841

[65] Abdulhameed A, Nazim Mohtar M, Hamidon MN, Mansor I, Halin IA. Characterization and selective deposition of carbon nanotubes from carbon nanoparticles mixture using mild acid treatment and electrokinetic manipulation. Materials Research Express. 2021;**8**:55603. DOI: 10.1088/2053-1591/ac017e

[66] Abdulhameed A, Mohtar MN, Hamidon MN, Halin IA. Mild nitric acid treatments to improve multi-walled carbon nanotubes dispersity and solubility in dielectrophoresis mediums. Fullerenes, Nanotubes, and Carbon Nanostructures. 2021;**29**:832-839. DOI: 10.1080/1536383X.2021.1908999

[67] Amani AM, Hashemi SA, Mousavi SM, Pouya H, Arash V. Electric field induced alignment of carbon nanotubes: Methodology and outcomes. In: Carbon Nanotubes – Recent Progress. London, United Kingdom; 2018

[68] Abdulhameed A, Mohtar MN, Hamidon MN, Mansor I, Halin IA. The role of the ac signal on the dielectrophoretic assembly of carbon nanotubes across indium tin oxide electrodes. Microelectronic Engineering. 2021;**247**:111597. DOI: 10.1016/j.mee.2021.111597

[69] Gupta P, Rajput M, Singla N, Kumar V, Lahiri D. Electric field and current assisted alignment of CNT inside polymer matrix and its effects on electrical and mechanical properties. Polymer. 2016;**89**:119

[70] Deng Z, Yenilmez E, Reilein A, Leu J, Dai H, Moler KA. Nanotube manipulation with focused ion beam. Applied Physics Letters. 2006;**88**:1-3. DOI: 10.1063/1.2161395

[71] Li X, Zhang L, Wang X, Shimoyama I, Sun X, Seo WK, et al. Langmuir-Blodgett assembly of densely aligned single-walled carbon nanotubes from bulk materials. Journal of the American Chemical Society. 2007;**129**:4890-4891. DOI: 10.1021/ja071114e

[72] Cao Q, Han SJ, Tulevski GS, Zhu Y, Lu DD, Haensch W. Arrays of single-walled carbon nanotubes with full surface coverage for high-performance electronics. Nature Nanotechnology. 2013;**8**:180-186. DOI: 10.1038/nnano.2012.257

[73] Oh JY, Yang SJ, Park JY, Kim T, Lee K, Kim YS, et al. Easy preparation of self-assembled high-density buckypaper with enhanced mechanical properties. Nano Letters. 2015;**15**:190-197. DOI: 10.1021/nl5033588

[74] De Heer WA, Bacsa WS, Châtelain A, Gerfin T, Humphrey-Baker R, Forro L, et al. Aligned carbon nanotube films: Production and optical and electronic properties. Science. 1995;**268**:845-847

[75] Yu G, Cao A, Lieber CM. Large-area blown bubble films of aligned nanowires and carbon nanotubes. Nature Nanotechnology. 2007;**2**:372-377. DOI: 10.1038/nnano.2007.150

[76] Wang Y, Gao Y, Li W, Zhang M, Zhang J, Wang Q, et al. Applying viscous shear stress to align single-walled carbon nanotubes. In: Proceedings of the 4th Electron Devices Technology and Manufacturing Conference. New Jersey, United States; pp. 1-4

[77] Jinkins KR, Chan J, Jacobberger RM, Berson A, Arnold MS. Substrate-wide confined shear alignment of carbon nanotubes for thin film transistors. Advanced Electronic Materials. 2019;**5**:1800593. DOI: 10.1002/aelm.201800593

[78] Song W, Kinloch IA, Windle AH. Nematic liquid crystallinity of multiwall carbon nanotubes. Science. 2003;**302**:1363

[79] Abdulhameed A, Halin IA, Mohtar MN, Hamidon MN. Optimization of surfactant concentration in carbon nanotube solutions for dielectrophoretic ceiling assembly and alignment: Implications for transparent electronics. ACS Omega. 2022;**7**:3680-3688. DOI: 10.1021/acsomega.1c06323

[80] Abdulhameed A, Mohtar MN, Hamidon MN, Halin IA. Assembly of long carbon nanotube bridges across transparent electrodes using novel thickness-controlled dielectrophoresis. Electrophoresis. 2022;**43**:487-494. DOI: 10.1002/elps.202100268

[81] Ladani RB, Wu S, Kinloch AJ, Ghorbani K, Zhang J, Mouritz AP, et al. Improving the toughness and electrical conductivity of epoxy nanocomposites by using aligned carbon nanofibres. Composites Science and Technology. 2015;**117**:146-158. DOI: 10.1016/j.compscitech.2015.06.006

[82] He X, Gao W, Xie L, Li B, Zhang Q, Lei S, et al. Wafer-scale monodomain films of spontaneously aligned single-walled carbon nanotubes. Nature Nanotechnology. 2016;**11**:633-638. DOI: 10.1038/nnano.2016.44

[83] Walker JS, Fagan JA, Biacchi AJ, Kuehl VA, Searles TA, Hight Walker AR, et al. Global alignment of solution-based

single-wall carbon nanotube films via machine-vision controlled filtration. Nano Letters. 2019;**19**:7256-7264. DOI: 10.1021/acs.nanolett.9b02853

[84] Du C, Li M, Cao M, Feng S, Guo H, Li B. Enhanced thermal and mechanical properties of polyvinlydene fluoride composites with magnetic oriented carbon nanotube. Carbon N. Y. 2018;**126**:197-207. DOI: 10.1016/j. carbon.2017.10.027

[85] Zhang S, Hao A, Nguyen N, Oluwalowo A, Liu Z, Dessureault Y, et al. Carbon nanotube/carbon composite fiber with improved strength and electrical conductivity via interface engineering. Carbon N. Y. 2019;**144**:628-638. DOI: 10.1016/j.carbon.2018.12.091

[86] Strobl CJ, Schäflein C, Beierlein U, Ebbecke J, Wixforth A. Carbon nanotube alignment by surface acoustic waves. Applied Physics Letters. 2004;**85**: 1427-1429. DOI: 10.1063/1.1787159

Chapter 5

Electrical Transport Modeling of Graphene-Based Interconnects

Youssef Nadir, Hassan Belahrach, Abdelilah Ghammaz,
Aze-Eddine Naamane and Mohammed Radouani

Abstract

Due to the downscaling in the design of modern ICs, copper interconnects reach their limitations such as delay, power dissipation, and electromigration. However, a new era of discovered materials, including carbon nanotube, graphene nanoribbon (GNR), and their composite, has been proposed as promising alternatives for interconnect applications. The purpose of this review is to give an overview of the various approaches that are used to model graphene-based interconnects. In this work we focus on why opting for graphene-based interconnect properties as an alternative for copper interconnect replacement; what are the deep theories, which are explaining the electrical transport on those interconnects; and what are the electrical models that are used to model the various kind of graphene-based interconnects.

Keywords: graphene-based interconnects, carbon nanotube (CNT), graphene nanoribbon (GNR), carbon composite, circuit modeling, interconnects

1. Introduction

Following Moore's law defined in 1965, which stipulates that the density of an IC doubles every 18 months while the cost comes down [1], the chip manufacturers have opted for the miniaturization of the microelectronics components [2], as an answer to the high demand for high-performance devices in the microelectronics industry. Nowadays, as shown in **Figure 1** and as stipulated in the recent IRDS metrics [3], there is a need to increase the number of electronic components in several technologies such as mobile systems, cloud systems, internet-of-things edge (IoTe) devices that consist of sensing, computation, security, storage, wireless communication, and cyber-physical systems (CPS) that provide real-time control for physical plants, vehicles, and industrial system (**Figure 1**).

Indeed, to realize the previous IRDS requirements with respect to Moore's law, we need to talk about a new era of specialization that treats nanoelectronics, nanodevices, and nanoscale interconnects.

The current nanoscale regime differentiates between three kinds of interconnects, namely, local, intermediate, and global, as indicated in **Figure 2**.

Indeed, to reach that scale, the first interconnect technology was based on aluminum and SiO_2 as an insulator, but with rapid scaling, this technology suffered from
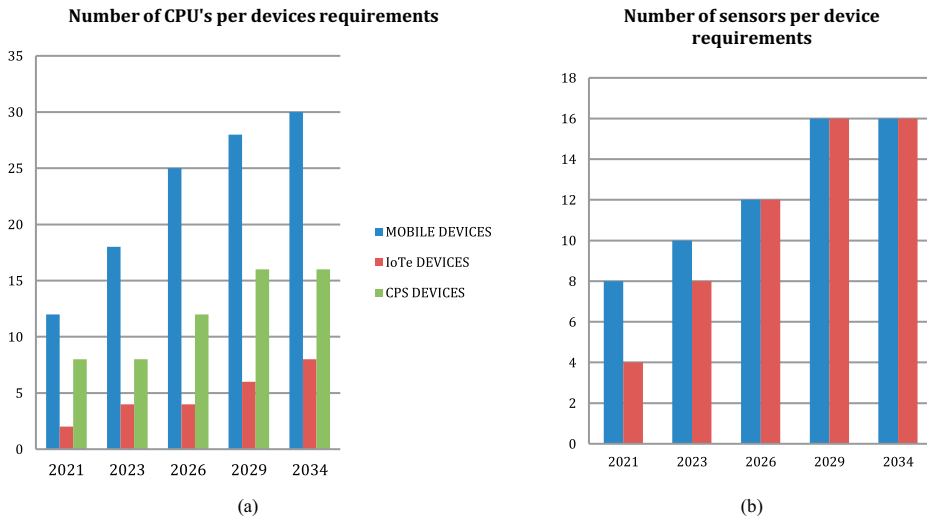
Figure 1.
Electronic components requirements (a) CPU's (b) sensors [3].

high resistivity, which impacted the reliability of VLSI circuits. Later, the industry elected gold, silver, and copper as potential substitutes, since they have an electrical resistivity lower than aluminum, as shown in **Figure 3**.

Gold has a higher resistance to electromigration and shows a little improvement in resistivity in addition to its higher required cost, while silver has a low resistivity but has low resistance to electromigration. On the other hand, copper triumphed over aluminum due to its resistivity, which approximates half of the one of aluminum. Nowadays, Cu is still the standard metal used on on-chip interconnect materials for advanced integrated circuits [6], but with the continuous downsizing of the IC scale, copper will be limited beyond the 14 nm technology node [7], due to its weakness related to the higher resistivity [8], power dissipation, propagation delay, and lower resistance to electromigration phenomenon [5]. In addition, some studies demonstrate that the maximum limit of current density (6.10^6 A/cm^2) that can be carried by copper conductors has been exceeded due to the electromigration phenomenon [9]. To get over the copper deficiencies, researchers have proposed graphene-based inter-connects such as carbon nanotubes (CNTs) or a composite formed either by CNTs and copper (Cu-CNTs) or graphene nanoribbons (GNR), and copper as a replacement option for copper since they present potential of higher performance, as described in **Table 1**.

While there have been several review articles published over the recent years related to nanocarbon circuit modeling, in addition to the leak of updates on the previous survey, there is no one showing the analytical model explaining the electrical transport inside graphene-based interconnects, hence the importance of this work. In this book chapter, we overview the reason for the evolution of the graphene-based interconnects as a potential alternative for copper defects. The remaining parts of the chapter are organized as follows. Properties of carbon nanotube, graphene, and copper composites are described in Section 2. Section 3 presents the two theory modeling analytically the electrical transport inside nanowires. Section 4 discusses several compact models of CNTs proposed by the previous research. Finally, Section 5 concludes the review with some perspectives.
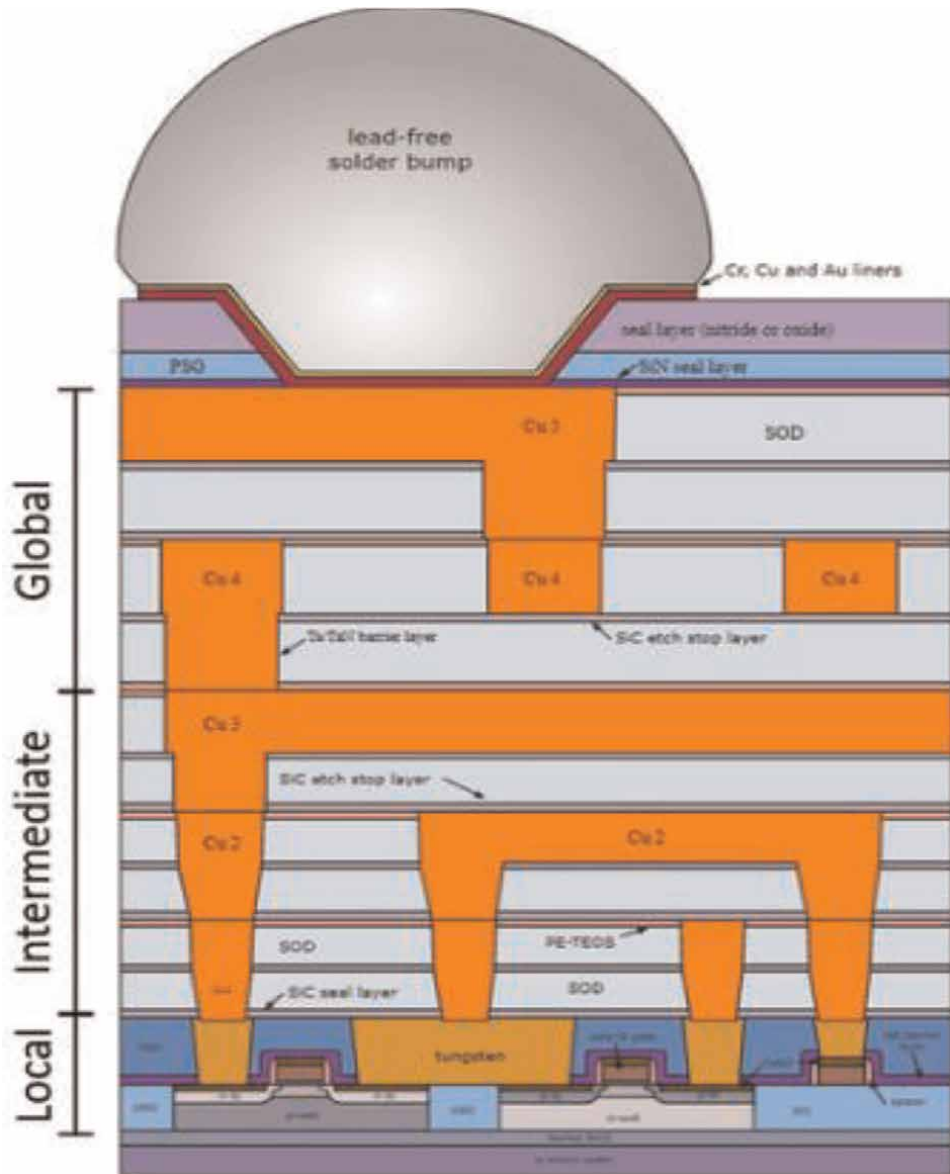
Figure 2.
Cross-section of interconnects in modern VLSI device [4].
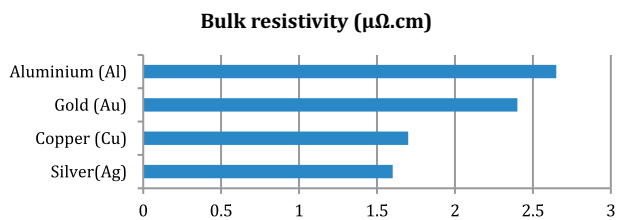
Figure 3.
Bulk resistivity of certain metals [5].

	Cu	CNT	GNR	Cu–CNT
Maximum current density (A/cm^2)	$<1.10^7$	$>1.10^9$	$>10^8$	6.10^8
Thermal conductivity (W/mK)	385	$(3–10).10^3$	$(3 –5).10^3$	$\sim$800
Conductivity (S/cm)	$5.8.10^5$	$(2.7–7).10^5$	$2.6.10^4$	$(2.3–4.7).10^5$

Table 1.
Summary of some electrical properties of Cu, CNT, GNR, and Cu-CNT [10–27].

2. Properties of graphene-based interconnects and their composite

There are different electrically conductive allotropes of carbon in nature, for instance, "fullerenes," "graphene," "graphite," and "diamond." The roll-up of a single layer of carbon atoms locked in a hexagonal grid "graphene sheet" creates carbon nanotubes (CNTs), which can be either metallic or semiconductor depending on their chirality. In fact, since the discovery of single-shell carbon nanotubes by Ijima and Ichihashi in 1993, research has distinguished three kinds of CNTs—single-walled CNTs (SWCNTs), multi-walled CNTs (MWCNTs), which consists of concentrical nested CNTs, and double-walled CNTs, which is a particular case of the second type. The CNTs have presented interesting properties such as a thermal conductivity higher than 3500 W/mK, lightweight ($\sim$2 g/cm^3) [28], higher corrosion resistance [29], a current density in excess of 4.10^9 A/cm^2 [7], and an electrical conductivity approximating 10^7 S/m, as shown in **Table 2**. The CNTs are not fabricated by a natural process and therefore they can be synthesized following various experimental methods either physical one, such as the arc discharge (AD) [30, 31] and laser ablation (LA) [32, 33], or chemical one, such as various techniques for chemical vapor deposition (CVD)[34–37].

Graphene, on the other hand, is another alternative option to potentially replace Cu for interconnects [13]. It is a 2D monolayer of carbon disposed into a honeycomb lattice, and as shown in **Figure 4a**, a quasi-1D graphene nanoribbon can be used as interconnects [14]. It was first isolated in 2004 by Geim and Novoselov by mechanical exfoliation of graphite crystals using an adhesive tape method [16], and their work was honored with the 2010 Nobel Prize in Physics. Further studies showed that it can be fabricated by unzipping the CNTs. The comparison of the CNTs with GNRs shows that the second material can be easily controlled horizontally and is more compatible with conventional lithography [15].

Additionally, composite-based CNTs are supposed to substitute copper interconnect in the near future. Indeed, copper-CNT composite is manufactured by electrodepositing Cu into prefabricated CNTs. Studies show that Cu-CNT with a lighter weight has a conductivity, which is higher 100 times than copper at a specific temperature. In plus, high electromigration resistance was also noticed by Cheng et al. [38].

	Dominant CNT type	CNT length [μm]	Tensile strength [GPa]	Electrical conductivity [S/m]
Lintec: dry spun from a CNT forest [11]	MWNT	<500	<1	10^5
DexMat: wet spun from a CNT acid solution [12]	DWNT	<20	0.4–2.8	$(3–10).10^6$

Table 2.
Properties of some available commercial CNTs.
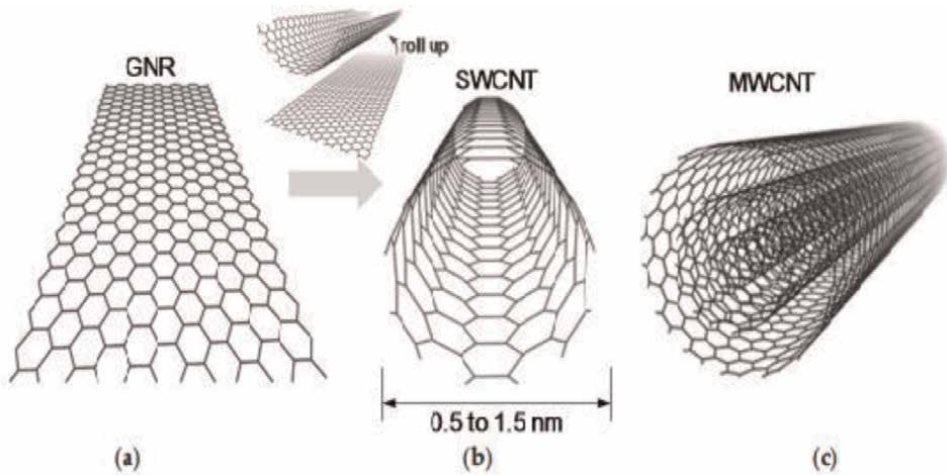
Figure 4.
Schematics of (a) GNR, (b) SWCNT, and (c) MWCNT [17].

Moreover, according to Cheng et al. [38], another copper composite encapsulating by a few layers of graphene forms a sort of barrier and is predicted as a substitute for copper. Studies have shown that the preceding composite shows a low-resistance parallel conducting path for signal conduction. In fact, graphene in itself has physical and electrical properties similar to CNTs [26], but with the advantage to be easy for fabrication. Studies affirm their fabrication either using chemical vapor deposition (CVD) and by intercalation doping by $FeCl_3$ [39] or by unzipping CNTs. Further, by conducting various experiments, the current density of doped multi-layer GNRs was found to be 2.10^8 A/cm^2.

3. Analytical model for nanowires

In the literature, two kinds of analytical transport theory have been demonstrated. One is called the semiclassical transport theory based on the Boltzmann transport equation (BTE) and is widely used since it gives an explanation of modeling nanowires as R, L, and C transmission lines. The other one is more complex; it is known as the quantum transport theory and uses a modified Schrödinger equation to explain the quantum transport in nanowires.

3.1 Semiclassical transport model

3.1.1 Boltzmann Transport Equation

Since the nanoscale is comparable to the phonon mean free path, it is mandatory to use the Boltzmann transport equation (BTE). There are many numerical methods that have been applied to solve it, such as the lattice Boltzmann method, Monte Carlo method, and discrete ordinates method (DOM) [40]. The BTE is written as [41]:

$$\frac{\partial f}{\partial t} + \vec{v}.\vec{\nabla}f - \frac{e}{\hbar}\vec{\xi}.\overrightarrow{\nabla_k}f = S_{op}f \tag{1}$$

where $\vec{v}, e, h, \vec{\xi}, f$, and $S_{op}f$ are the electron velocity, the electron charge, the plank constant, the electrostatic field, the carrier distribution function, and the complex scattering processes that continually redistribute electrons among the available velocity states, respectively.

The carrier distribution function $f = f\left(\vec{x}, \vec{k}, t\right)$ depends explicitly on the position $\vec{x}$, the wave vector $\vec{k}$, and time t. By projecting on the x-axis, we obtain:

$$\frac{\partial f}{\partial t} + v.\frac{\partial f}{\partial x} - \frac{e}{\hbar}\xi.\frac{\partial f}{\partial k} = S_{op}f \tag{2}$$

In addition, the total energy variable E is written as:

$$E = e_m(k) + U(x,t) - \mu(x,t) \tag{3}$$

where $e_m(k)$, $U(x,t)$, and $\mu(x,t)$ are the wave energy, the electrostatic potential, and the electrochemical potential, respectively. We can now rewrite the second and the third term of (2) by introducing f_0 is the equilibrium Fermi Function:

$$v.\frac{\partial f}{\partial x} = v.\frac{\partial f_0}{\partial x} = v.\frac{\partial f_0}{\partial E}.\frac{\partial E}{\partial x} = v.\frac{\partial f_0}{\partial E}.\frac{\partial(U-\mu)}{\partial x} \tag{4}$$

and:

$$\frac{e}{\hbar}\xi.\frac{\partial f}{\partial k} = e.\xi.\frac{\partial f_0}{\partial(\hbar k)} = \frac{\partial U}{\partial x}.\frac{\partial f_0}{\partial(\hbar k)} = \frac{\partial U}{\partial x}.\frac{\partial f_0}{\partial E}.\frac{\partial E}{\partial(\hbar k)} \tag{5}$$

where the partial difference of the electrostatic potential can be written as:

$$e.\xi = \frac{\partial U}{\partial x} \tag{6}$$

In relativistic kinetics, the energy is written as:

$$E = p.v = \hbar.k.v \tag{7}$$

where p is the wave pseudo-momentum.
If we replace (7) in (5), we get:

$$\frac{e}{\hbar}\xi.\frac{\partial f}{\partial k} = v.\frac{\partial U}{\partial x}.\frac{\partial f_0}{\partial E} \tag{8}$$

Knowing (4) and (8), (2) can be written as:

$$\frac{\partial f}{\partial t} + v.\frac{\partial f_0}{\partial E}.\frac{\partial(U-\mu)}{\partial x} - v.\frac{\partial U}{\partial x}.\frac{\partial f_0}{\partial E} = S_{op}f \tag{9}$$

Thus:

$$\frac{\partial f}{\partial t} + v.\left(\frac{-\partial f_0}{\partial E}\right).\frac{\partial\mu}{\partial x} = S_{op}f \tag{10}$$

We may take into consideration the magnetic potential A; in this case, (1) will be written as [41]:

$$\frac{\partial f}{\partial t} + v.\left(\frac{-\partial f_0}{\partial E}\right).\left(\frac{\partial \mu}{\partial x} + \frac{\partial A}{\partial t}\right) = S_{op}f \tag{11}$$

If we multiply each side of the previous equation by the following sum over k-space $\sum_{k}\left(\frac{-e.v}{L}\right)$ and write:

$$A = L_M.I \tag{12}$$

where $L, L_M,$ and I are the wire's length, the magnetic inductance, and the current intensity, respectively.

We define the kinetic inductance as:

$$\sum_{k}\left(\frac{-e.v}{L}\right).v.\left(\frac{-\partial f_0}{\partial E}\right) = \frac{1}{L_K} \tag{13}$$

and τ is the relaxation time that describes how fast the system reaches thermodynamic equilibrium, we write:

$$\sum_{k}\left(\frac{-e.v}{L}\right).S_{op}f = \frac{I}{\tau} \tag{14}$$

We notice the writing of the current intensity I:

$$\sum_{k}\left(\frac{-e.v}{L}\right).\frac{\partial f}{\partial t} = \frac{\partial I}{\partial t} \tag{15}$$

In sum, we get the following equation:

$$\left(1 + \frac{L_M}{L_K}\right)\frac{\partial I}{\partial t} + \frac{I}{\tau} = \frac{1}{L_K}.\frac{\partial\left(\frac{\mu}{e}\right)}{\partial x} \tag{16}$$

By defining $(R = \frac{L_K}{\tau})$ and $(\phi_n = -\frac{\mu}{e})$, (16) is written under the following form:

$$(L_M + L_K)\frac{\partial I}{\partial t} + RI = \frac{\partial(-\phi_n)}{\partial x} \tag{17}$$

The first conclusion is that the previous equation shows that a nanowire may be modeled as equivalent to a series R, L circuit.

3.1.2 Maxwell equations

The Maxwell-Ampere equation is written as:

$$\overrightarrow{rot}\,\overrightarrow{B} = \mu_0\overrightarrow{j} + \mu_0\varepsilon_0\frac{\partial\overrightarrow{E}}{\partial t} \tag{18}$$

We apply the divergence to the previous equation, by noticing $(div(\overrightarrow{rot\ B}) = 0)$, then we write:

$$\mu_0 div\left(\overrightarrow{j}\right) + \mu_0 \varepsilon_0 \frac{\partial div(\overrightarrow{E})}{\partial t} = 0 \tag{19}$$

In addition, the Maxwell-Gauss is written as:

$$div(\overrightarrow{E}) = \frac{\rho}{\varepsilon_0} \tag{20}$$

By placing (20) in (19), we write:

$$\frac{\partial j}{\partial x} = \frac{-\partial \rho}{\partial t} \tag{21}$$

By defining the charge density per unit length δl:

$$\delta \rho = -e \frac{\delta n}{\delta l} \tag{22}$$

and:

$$e \delta n = C_E \delta\left(\frac{U}{e}\right) \tag{23}$$

where n is the electron density and C_E is the electrostatic capacity, and (21) will be written as:

$$\frac{\partial I}{\partial x} = C_E \frac{\partial\left(\frac{U}{e}\right)}{\partial t} \tag{24}$$

We pose:

$$C_Q = -e^2\left(\frac{\partial n}{\partial E}\right) \tag{25}$$

Thus:

$$e \delta n = -C_Q\left(\frac{\delta E}{e}\right) = -C_Q\left(\frac{\delta(U - \mu)}{e}\right) \tag{26}$$

Putting in Eqs. (23) and (26), we write:

$$\delta U = \frac{C_Q}{C_E + C_Q} \delta \mu \tag{27}$$

Replacing (27) in (24) and defining $(\frac{\mu}{e} = -\phi_n)$, we get the following:

$$\frac{\partial I}{\partial x} = -\frac{C_Q C_E}{C_E + C_Q} \frac{\partial\left(\frac{-\mu}{e}\right)}{\partial t} \tag{28}$$

Finally:

$$\frac{\partial I}{\partial x} = \frac{-C_Q C_E}{C_E + C_Q} \frac{\partial \phi_n}{\partial t} \tag{29}$$

The previous equations demonstrate that any model of a nanowire CNTs or graphene-based interconnects might be studied by considering it as a transmission line composed by a resistance, electrostatic inductance, magnetic inductance, electrostatic capacitance, and a quantum one. Secondly, the resolution of the telegrapher's equations may be used to overcome the electrical or magnetic nanowire-based phenomenon. To do so we may use a statistical method, such as the Monte Carlo method, a temporal analysis method, such as the finite difference time domain, or a direct one, for instance, the Bessel line or Arnold method.

3.2 Quantum transport model

Quantum transport has been modeled by the non-equilibrium Green's function (NEGF) method, which was introduced in the 1960s by the classic work of Martin, Schwinger [42], Kadanoff, Baym [43], Keldysh [44], and others and has been discussed in many review articles, such as Danielewicz [45] and Mahan [46]. After the advent of mesoscopic physics in the 1980s, this method was combined with the Landauer approach [47–49], and this "NEGF-Landauer method" has been widely used in the field of nanoelectronics for device modeling and technology development [50]. Indeed, this approach consists of studying the transport by starting from the usual time-independent Schrödinger equation:

$$E\psi = H\psi \tag{30}$$

And by transforming the previous equation to the matrix and adding two terms representing the outflow and inflow from the contact, and noting [I] and [H], respectively, the identity and Hamiltonian matrix, we get:

$$E[I]\{\psi\} = [H]\{\psi\} + \underbrace{[\Sigma]\{\psi\}}_{OUT\ FLOW} + \underbrace{\{s\}}_{IN\ FLOW} \tag{31}$$

Using this modified Schrödinger equation, the wave function can be written as:

$$\{\psi\} = [EI - H - \Sigma]^{-1}\{s\} \tag{32}$$

By defining:

$$G^R = [EI - H - \Sigma]^{-1} \tag{33}$$

We will have:

$$\{\psi\} = G^R\{s\} \tag{34}$$

We define as well:

$$G^A = \left[G^R\right]^+ \tag{35}$$

$$[G^n] \sim \{\psi\}\{\psi\}^+ \tag{36}$$

$$\left[\Sigma^{in}\right] \sim \{s\}\{s\}^{+} \tag{37}$$

where the sign $^{+}$ represents the conjugate transpose of the matrix, by multiplying (34) by its conjugate transpose we get:

$$\underbrace{\{\psi\}\{\psi\}^{+}}_{G^{n}/2\pi} = \left[G^{R}\right]\underbrace{\{s\}\{s\}^{+}}_{\Sigma^{in}/2\pi}\left[G^{A}\right] \tag{38}$$

Thus, we have obtained the non-equilibrium Green function:

$$G^{n} = G^{R}\Sigma^{in}G^{A} \tag{39}$$

In this equation, the wave function is the one-electron wave function whose square gives the probability of finding an electron. When averaged over all electrons in an ensemble, it gives the electron density.

To obtain the current equation, we start from the time-dependent version of the modified Schrödinger equation:

$$i\hbar\frac{d}{dt}\psi = \left[H + \sum\right]\psi + s \tag{40}$$

And the conjugate transpose form of the previous equation may be written as:

$$-i\hbar\frac{d}{dt}\psi^{+} = \psi^{+}\left[H + \sum{}^{+}\right] + s^{+} \tag{41}$$

Thus, we obtain:

$$i\hbar\frac{d}{dt}\psi\psi^{+} = \left(i\hbar\frac{d}{dt}\psi\right)\psi^{+} + \psi\left(i\hbar\frac{d}{dt}\psi^{+}\right) \tag{42}$$

and:

$$\frac{d}{dt}\psi\psi^{+} = \frac{\left[(H + \sum)\psi\psi^{+} - \psi\psi^{+}(H + \sum{}^{+})\right] + \left[ss^{+}G^{A} - G^{R}ss^{+}\right]}{i\hbar} \tag{43}$$

We define: $\psi\psi^{+} = \frac{G^{n}}{2\pi}$ and: $ss^{+} = \frac{\Sigma^{in}}{2\pi}$.
The Eq. (43) will be written as:

$$\frac{d}{dt}\psi\psi^{+} = \frac{\left[(H + \sum)G^{n} - G^{n}(H + \sum{}^{+})\right] + \left[\Sigma^{in}G^{A} - G^{R}\Sigma^{in}\right]}{i2\pi\hbar} \tag{44}$$

To find the change of any quantity, we can multiply by the corresponding operator Q_{op} and take the trace to obtain:

$$\frac{dQ_{op}}{dt} = -\frac{i}{h}Trace\left(\left[(HG^{n} - G^{n}H) + \left(\sum G^{n} - G^{n}\sum{}^{+}\right)\right]Q_{op} + \left[\Sigma^{in}G^{A} - G^{R}\Sigma^{in}\right]Q_{op}\right) \tag{45}$$
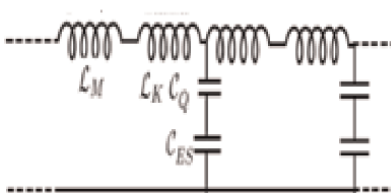
For instance, we could define the terminal current operator I_{op} as:

$$I_{op} = -\frac{i}{h}\left(\left[\sum G^n - G^n \sum{}^+\right] + \left[\Sigma^{in}G^A - G^R\Sigma^{in}\right]\right) \qquad (46)$$

4. Compact model

4.1 Single-walled carbon nanotube models
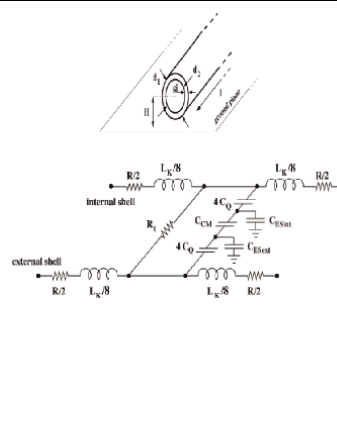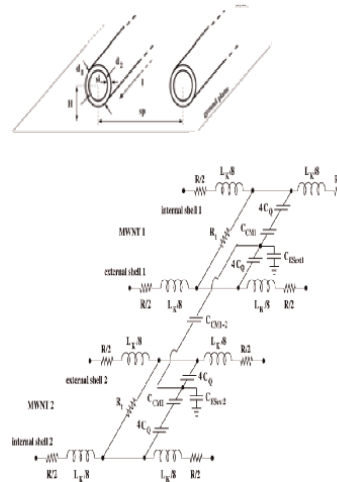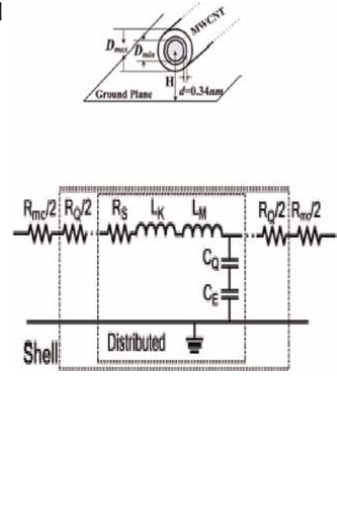
The first model based on the Luttinger liquid theory has been developed by Burke. Indeed, he has modeled the nanotube as a nano-transmission line with distributed kinetic and magnetic inductance as well as distributed quantum and electrostatic capacitance but it has neglected the resistance effect, which may lead to several incoherent results when stimulated. The model proposed by Salahuddin et al. [41] is more accurate since it takes into consideration the resistance effect of the nanotube, it modeled the CNTs as an (R, L, and C) transmission line. Their research distinguishes two modes of resistance behavior, one in the low field, where only acoustic phonons are effective, and the other one in the high field, where the optical phonons have consistent effects. Other models [51] have considered the same transmission line model for SWCNTs; thus, they demonstrate that the quantum resistance of SWCNTs is equal to 6.45 KΩ [52], which stays quite high for a copper interconnection substitute. It can be only used for some specific applications such as short local interconnects where the capacitance plays a key role [53], subthreshold circuits, and sub-10 nm circuits [54–56]. The third model is a modeling of two SWNTs in parallel over ground, the idea behind this model is to reduce the total quantum resistance. Indeed, in this case, the resistance is considered to vary according to the comparison between length and the mean free path, which may vary between $\lambda_{low} \sim 1.6\mu m$ and $\lambda_{high} \sim 26nm$ [57]. In fact, the resistance is length independent at a small size to indicate the ballistic electronic transport phenomenon, and at a large scale, the resistance is length dependent due to the scattering mechanisms. The absence of magnetic inductance in this model due to its neglect in front of the kinetic inductance may lead to incoherence results, particularly in the case of the presence of external magnetic field.

Ref	Compact model	Model-related formulas
[58]		$L_M = \frac{\mu}{2\pi}\cosh^{-1}\left(\frac{2h}{d}\right) \approx \frac{\mu}{2\pi}\ln\left(\frac{h}{d}\right) \approx 1pH/\mu m$ $L_K = \frac{h}{2e^2 v_F} \simeq 16nH/\mu m$ $C_Q = \frac{2e^2}{hv_F} \simeq 100aF/\mu m$ $C_{ES} = \frac{2\pi\varepsilon}{\cosh^{-1}\left(\frac{2h}{d}\right)} \approx \frac{2\pi\varepsilon}{\ln\left(\frac{h}{d}\right)} \approx 50aF/\mu m$ $-\mu,\varepsilon,d,h,$ and v_F are the permeability, the permittivity of the medium between the nanotube and the ground plane, the nanotube diameter, the height of the nanotube from the ground plane, and the Fermi velocity, respectively.

Ref	Compact model	Model-related formulas
[41]		$$R = \begin{cases} \dfrac{h}{4e^2}\left[1+\dfrac{L}{\lambda_{acc}}\right](if\_low\_frequency) \\ \dfrac{h}{4e^2}\left[1+L\left(\dfrac{1}{\lambda_{acc}}+\dfrac{1}{0.16L/V+L_{hp}}\right)\right] \\ (if\_High\_frequency) \end{cases}$$ $G_0 = \frac{2e^2}{h}$ (conductance quantum) $C_Q = \frac{G_0}{v_F}; C_E = \frac{2\pi\varepsilon}{\ln\left(\frac{b}{a}\right)}$ $L_K = \frac{1}{G_0 v_F}; L_M = \frac{\mu}{2\pi}\ln\left(\frac{b}{a}\right)$ -where $a, b, h, \mu, \varepsilon, L, \lambda_{acc}, L_{hp}$, and V are the radius of the wire, the height from the ground plane and the Plank constant, the permeability, the permittivity, the wire length, the mean free path, the optical phonon scattering mean-free path, and the applied voltage, respectively.
[59, 60]		$$R = \begin{cases} \dfrac{h}{4e^2}, \left(l < \lambda_{high}\right) \\ \dfrac{h}{4e^2}\left[\dfrac{l}{0.64\left(l-\lambda_{high}\right)+\lambda_{high}}\right], \left(\lambda_{high} < l < \lambda_{low}\right) \\ \dfrac{h}{4e^2}\left[\dfrac{l}{0.64\left(\lambda_{low}-\lambda_{high}\right)+\lambda_{high}}\right], \left(\lambda_{low} < l\right) \end{cases}$$ $L_K = \frac{h}{2e^2 v_F} \simeq 16nH/\mu m$ $C_{ES} = \frac{2\pi\varepsilon}{\cosh^{-1}\left(\frac{2H}{d}\right)} \approx 50aF/\mu m C_{CS} = \frac{\pi\varepsilon}{\cosh^{-1}\left(\frac{sp}{d}\right)}$(can be neglected if nonadjacent) $C_Q = \frac{2e^2}{h v_F} \simeq 100aF/\mu m$ -where l, H, and h are the nanotube length, the distance to the ground plane, and Plank constant, respectively.

4.2 Multi-walled carbon nanotube models

The DWCNTs have been modeled by Rossi et al. [59] similarly to two SWCNTs in parallel by the addition of an inter-shell resistance R_t, which has a value of 10 KΩ/μm, and neglecting the magnetic inductance, although the value of the quantum resistance is still high. The model given by Rossi et al. [59] representing DWCNTs in parallel is more interesting and the one for MWCNTs [61] is more interesting since the resistance will be reduced according to the number of dual or multi-carbon nanotubes either in parallel or nested. In addition, it will provide a better delay performance than that of an alternative such as copper.

Ref	Compact model	Model-related formulas
[59]		$R = \begin{cases} \dfrac{h}{4e^2}, & (l < \lambda_{high}) \\[2mm] \dfrac{h}{4e^2}\left[\dfrac{l}{0.64(l - \lambda_{high}) + \lambda_{high}}\right], & (\lambda_{high} < l < \lambda_{low}) \\[2mm] \dfrac{h}{4e^2}\left[\dfrac{l}{0.64(\lambda_{low} - \lambda_{high}) + \lambda_{high}}\right], & (\lambda_{low} < l) \end{cases}$ $R_t = 10 k\Omega/\mu m$ $L_K = \frac{h}{2e^2 v_F}$ $C_{ES} = \frac{2\pi\varepsilon}{\cosh^{-1}\left(\frac{2H}{d_{OUT}}\right)}; C_{CM} = \frac{2\pi\varepsilon}{\ln\left(\frac{d_{OUT}}{d_{IN}}\right)}$ $C_Q = \frac{2e^2}{h v_F}$ -where R_t, d_{OUT}, d_{IN}, h, and H represent the inter-shell resistance, the diameters of the outer and inner nanotubes, Plank constant, and the height from the ground plane, respectively.
[59]		$R = \begin{cases} \dfrac{h}{4e^2}, & (l < \lambda_{high}) \\[2mm] \dfrac{h}{4e^2}\left[\dfrac{l}{0.64(l - \lambda_{high}) + \lambda_{high}}\right], & (\lambda_{high} < l < \lambda_{low}) \\[2mm] \dfrac{h}{4e^2}\left[\dfrac{l}{0.64(\lambda_{low} - \lambda_{high}) + \lambda_{high}}\right], & (\lambda_{low} < l) \end{cases}$ $R_t = 10 k\Omega/\mu m$ $L_K = \frac{h}{2e^2 v_F}$ $C_{ES} = \frac{2\pi\varepsilon}{\cosh^{-1}\left(\frac{2H}{d_{OUT}}\right)}; C_Q = \frac{2e^2}{h v_F}$ $C_{CM} = \frac{2\pi\varepsilon}{\ln\left(\frac{d_{OUT}}{d_{IN}}\right)}$ -where R_t, h, and H represent the inter-shell resistance, Plank constant, and the height from the ground plane, respectively.
[61, 62]		$R = R_Q + R_S = \frac{h}{2e^2 N} + \frac{h}{2e^2 N} \cdot \frac{L}{\lambda}$ -where L, λ, and N are the length, MFP, and the number of conducting channels of the shell, respectively. With D, shell diameter: $N \approx \begin{cases} [0.0306(D_{MAX} + D_{MIN}) \\ \quad + 0.425].\left[1 + \left(\dfrac{D_{MAX} - D_{MIN}}{2\delta}\right)\right], & (D_{MAX} > 6nm) \\[2mm] \dfrac{2}{3}.\left[1 + \left(\dfrac{D_{MAX} - D_{MIN}}{2\delta}\right)\right], & (D_{MAX} < 6nm) \end{cases}$ - δ is the van der Waals distance approximated as 0.34 nm. $L_{magnetic} = \frac{\mu}{2\pi} \cosh^{-1}\left(\frac{2H}{D}\right)$ $L_{K/shell} = L_{K/channel}/(0.0612 \cdot D + 0.425)$ $L_{K/channel} = \frac{h}{2e^2 v_F} \times \frac{1}{2} \approx 8 \, nH/\mu m$ $C_{Q/shell} = C_{Q/channel} \times (0.0612 \cdot D + 0.425)$ $CQ/channel = 2 \times \frac{2e^2}{h v_F} \approx 193 \, aF/\mu m$ $C_E = \frac{2\pi\varepsilon}{ln(D_{out}/D_{in})}$

4.3 Graphene nanoribbon models

Even if the SLGNR can be easily controlled horizontally, the model presented in ref. [63] demonstrates that SLGNR is too resistive. This resistance effect may be reduced by introducing MLGNR, which has been presented in ref. [64]. Other studies [65] have compared MLGNR with both copper interconnects and SWCNT bundle interconnects. The result of that comparison has shown the performance superiority of multi-layer GNR interconnects over conventional copper interconnects for small widths (<15 nm).
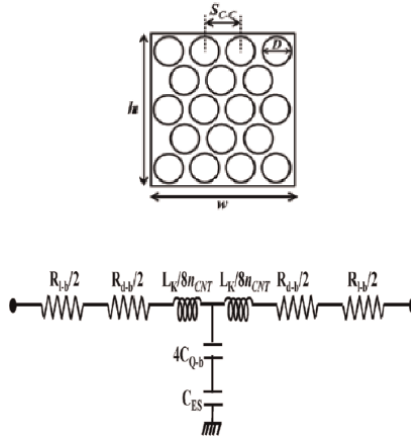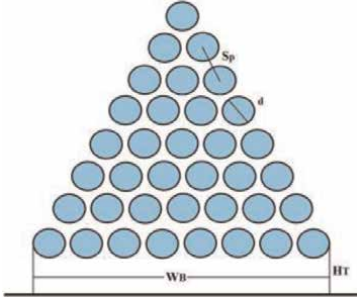
Ref	Compact model	Model-related formulas
[63]		$R_Q = (h/2q^2)/N_{ch}N_{layer}$ $C_Q = N_{layer}N_{ch}4q^2/hv_f$ $L_K = (h/4q^2v_f)/N_{layer}N_{ch}$ $N_{ch} = \sum_n \left[1 + exp\left(\frac{E_{n,electron}-E_F}{k_BT}\right)\right]^{-1}$ $+ \sum_n \left[1 + exp\left(\frac{E_F-E_{n,hole}}{k_BT}\right)\right]^{-1}$ $E_n = \frac{|n|+1/2)\cdot hv_f}{2w}$ -where h, E_F, $E_{n,electron}$, $E_{n,hole}$, w, n, and v_f are the Plank constant, the Fermi level, the total energy of an electron, the total energy of a hole, the width of the GNR, the corresponding index, and the fermi velocity, respectively.
[64]		$N_{layer} = 1 + Integer\left[\frac{t}{\delta}\right]$ $R_{total} = \frac{h}{2e^2}\left[\sum_i\left(1+\frac{L}{\lambda_{eff,i}}\right)^{-1}\right]^{-1}$ $L = L_M + L_K$ $L_K = \frac{4e^2}{N_{layer}N_{ch}hv_f}$ $C = \frac{C_E C_Q}{C_E+C_Q}$ $C_Q = \frac{4e^2}{hv_f}N_{layer}N_{ch}$ -The magnetic inductance (L_M) and electrostatic capacitance (C_E) of GNR are assumed to be the same as copper with equal dimensions.
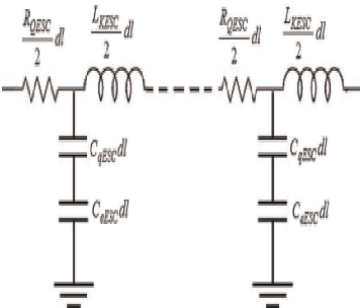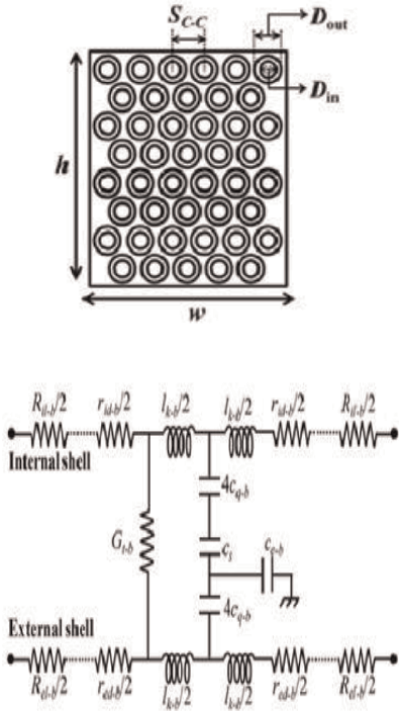
4.4 Nanotube bundles models

In the wake of reducing the quantum resistance, the literature shows the successful fabrication of bundled SWCNTs [66]. The biggest advantages of CNT bundles are contrary to Cu wires; CNTs can be arranged in different shapes such as circular, hexagonal, and triangular. In addition, some studies like the one in ref. [67], showed that T-CNT bundles outperform the other kind of bundles.

But since the study in Ref. [68] demonstrated that the MWCNT on average necessitates 97.8% lesser area as compared with the bundled-SWCNT interconnects for the same performance in a matter of crosstalk time delay. Mixed carbon nanotube bundles (MCBs) [7] are considered to be highly potential interconnect solutions in the current nanoscale regime. Encouragingly, a significant reduction in propagation delay and crosstalk delay is observed for a spatial arrangement of an MCB wherein MWCNTs are placed peripherally to the centrally located SWCNTs. Typically, the average delay with and without crosstalk is improved by 82.8% and 80%, respectively, compared to the MCB having randomly distributed SWCNTs and MWCNTs.

The proposed configuration in a study by Amin et al. [69] has demonstrated better performance for 32 nm and 16 nm technology.

Ref	Compact model	Model-related formulas
[68]		$n_{SWNT} = \begin{cases} n_W n_H - \left(\frac{n_H}{2}\right), (n_H even) \\ n_W n_H - \left(n_H - \frac{1}{2}\right), (n_H odd) \end{cases}$ $n_W = \left[\frac{w-D}{S_{C-C}}\right] + 1; n_H = \left[\frac{h-D}{S_{C-C}}\right] + 1$ $\begin{cases} R_{bundles} = \frac{R_{CNT}}{n_{SWNT}} = \frac{R_C + R_Q\left(1 + \frac{l_{CNT}}{\lambda_{mfp}}\right)}{n_{SWNT}} \\ R_{l-b} = \frac{R_C + R_Q}{n_{SWNT}} \\ r_{d-b} = \frac{R_Q}{n_{SWNT}.\lambda_{mfp}} \end{cases}$ $l_{k-b} = \frac{\frac{h}{2e^2 v_F}}{4.n_{SWNT}}$ $C_{q-b} = \frac{2e^2}{hv_F}.n_{SWNT}; C_{e-b} = \frac{2\pi\varepsilon_0\varepsilon_r}{\ln(h/d)}.n_x$ n_x: number of SWNT facing the ground plane.
[67]		$N_i = \begin{cases} 3.87.10^{-4} \times T \times Di + 0.2; Di > \frac{1300}{T} \\ 2; Di < \frac{1300}{T} \end{cases}$ N_i: the number of conducting channel; Di: is the diameter of the ith shell; $n_{TCNT} = \frac{n_b(n_b+1)}{2}$; n_b: the number of CNTs at base of the bundle; $R_b(T) = \frac{R_{SWCNT}}{n_{CNT}} = \begin{cases} \frac{R_c + R_Q}{n_{CNT}} ; l < \lambda_{eff} \\ \frac{R_c + R_S}{n_{CNT}} ; l > \lambda_{eff} \end{cases}$ $R_Q = \frac{h}{4e^2}; R_S = \frac{h}{2N_ie^2}\left[\frac{l}{\lambda_{eff}(T)}\right]$ $L^b_{ESC}(T) = \frac{L_m + (L_k/N)}{n_b}$

Ref	Compact model	Model-related formulas
		$L_m = \frac{\mu}{2\pi} \ln\left(\frac{H}{d}\right); L_K = \frac{h}{2e^2 v_F}$ $C_{ESC}^b(T) = \left(\frac{C_E^b \cdot C_Q^b}{C_E^b + C_Q^b}\right)$ $C_E^b = n_W \times \frac{2\pi\varepsilon}{\cosh^{-1}\left(\frac{H}{d}\right)}; C_E^b = n_B \times \frac{2Ne^2}{hv_F}$ n $_W$: number of CNTs along the width of the bundle.
[7]		$\begin{cases} R_{\text{int}-bundles} = \dfrac{R_{CNT}}{n_{DWNT}} = \dfrac{R_C + R_{Q_i}\left(1 + \dfrac{l_{CNT}}{\lambda_{mfp}}\right)}{n_{DWNT}} \\ R_{il-b} = \dfrac{R_C + R_{Q_i}}{n_{DWNT}} \\ r_{id-b} = \dfrac{R_{Q_i}}{n_{DWNT} \cdot \lambda_{mfp}} \end{cases}$ $\begin{cases} R_{ext-bundles} = \dfrac{R_{CNT}}{n_{DWNT}} = \dfrac{R_C + R_{Q_e}\left(1 + \dfrac{l_{CNT}}{\lambda_{mfp}}\right)}{n_{DWNT}} \\ R_{el-b} = \dfrac{R_C + R_{Q_e}}{n_{DWNT}} \\ r_{ed-b} = \dfrac{R_{Q_e}}{n_{DWNT} \cdot \lambda_{mfp}} \end{cases}$ $l_{k-b} = \dfrac{\frac{h}{2e^2 v_F}}{4 \cdot n_{DWNT}}$ $C_{q-b} = \dfrac{2e^2}{hv_F} \cdot n_{DWNT}$ $C_s = \dfrac{2\pi\varepsilon_0}{\ln(d_{OUT}/d_{IN})}$

Ref	Compact model	Model-related formulas
[70]		$N_i = \begin{cases} 3.87.10^{-4} \times T \times Di + 0.2; Di > \dfrac{1300}{T} \\ 2; Di < \dfrac{1300}{T} \end{cases}$ N_i: the number of conducting channel; Di: is the diameter of the ith shell; $N_{total} = \sum\limits_{i=1}^{n_{CNT}} N_i$; $\lambda_{mfp,i} = \dfrac{10^3 D_i}{(T(K)/100)-2}$ $R_{tESC} = \dfrac{R_0}{N_{total}} + R_m$ $R'_{tESC} = \left(\dfrac{h}{4e^2}\right) \cdot \dfrac{1}{\lambda_{mfp} N_{total}}$ $L'_{ESC} = L'_{kESC} + L'_{eESC}$; $C'_{ESC} = \left(C'^{-1}_{qESC} + C'^{-1}_{eESC}\right)^{-1}$ $L'_{kESC} = \dfrac{h}{4e^2 v_F N_{total}}$; $L'_{eESC} = \dfrac{1}{N_{total}}\left[\dfrac{\mu_0 \varepsilon_0}{C'_{e-CM0}}\right]$ $C'_{qESC} = \dfrac{4e^2 N_{total}}{h v_F}$; $C'_{eESC} = \left[\dfrac{2\pi e}{cosh^{-1}(H/d_g)}\right]$ $C'_{e-CM} = \sum\limits_{i=1}^{N_{ground}} C'_{eESC}(i)$ $H = \left(h_t + d_g/2\right)$
[69]		$N_i = \begin{cases} 2.04.10^{-4} \times T \times Di + 0.425; Di > \dfrac{1300}{T} \\ \dfrac{2}{3}; Di \le \dfrac{1300}{T} \end{cases}$ N_i: the number of conducting channel; Di: is the diameter of the ith shell; $R_{bundle} = \left[\left(\dfrac{R_q}{N_{MW}} + l\dfrac{R_s}{N_{MW}}\right)^{-1} + \dfrac{R_{SW}}{N_{SW_{\sum}}}\right]^{-1}$ $L_{bundle} = \begin{cases} \left(\dfrac{N_{MW}}{L_{m_{MW}}+L_{k_{MW}}} + \dfrac{N_{SW_{\sum}}}{L_{m_{SW}}+L_{k_{SW}}}\right)^{-1}; if\ l \le \lambda_{CNT} \\ \left(\dfrac{N_{MW}}{L_{m_{MW}}+L_{k_{MW}}} + \dfrac{N_{SW_{\sum}}}{L_{m_{SW}}}\right)^{-1}; if\ l > \lambda_{CNT} \end{cases}$ $C_{bundle} = \dfrac{N_{MW_H} C_E \left(N_{MW} C_{ESC_{MW}} + N_{SW_{\sum}} C_{SW}\right)}{N_{MW} C_{ESC_{MW}} + N_{SW_{\sum}} C_{SW} + N_{MW_H} C_E}$
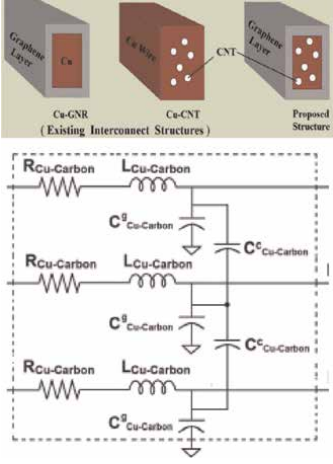
4.5 Composite graphene-based models

Even if the hilarious progress of the synthesis and the modeling of graphene or CNTs shows theoretically promising solutions to replace copper interconnects, the reality demonstrates the opposite. Indeed, the assumption of the closely packed CNTs

is invalid even with state-of-the-art fabrication technology [71]. In addition, the study in ref. [72] demonstrates that the conductivity of CNTs is much lower than copper. To overcome these deficiencies, an experimental study was realized in ref. [73] over (Cu-CNT) composite and showed that the previous composite has a comparable conductivity yet 100 times higher ampacity than its Cu counterpart. The study in ref. [74] also demonstrated a high electromigration resistance of the Cu-CNT composite, which may conclude the balance between the performance and reliability of Cu-CNT composite. Thus, it makes sense of the investigation led in ref. [13], where the results from this modeling study suggest that TSV interconnects composed of a Cu/CNT matrix exhibit enhanced performance compared to pure Cu, and the study in ref. [38] shows that the resistivity of Cu-CNT composite is not far from Cu resistivity, and therefore much smaller than that of the pure CNTs.

A study by Mehta et al. [75], which is a comparison among Cu, Cu-GNR hybrid, and Cu-CNT composite interconnects, has observed that the Cu-GNR hybrid has better performance than the Cu-CNT composite interconnects in terms of signal integrity and power consumption.

Ref	Compact model	Model-related formulas
[76]		$Z(\omega) = \frac{1}{\frac{1}{R_{Cu}} + \frac{n}{Z_{CNT}(\omega)}}$ $n = \frac{\pi D_{TSV}^2}{4(D_{CNT}+d)^2}$ $Z_{CNT}(\omega) = R_{CNT} + \frac{i\omega L L_k}{N}$ $L_k = \frac{R_Q}{2v_F}; R_{CNT} = \frac{R_Q + R_S L}{N}$ $N = \begin{cases} 2, (DCNT < 5600/T) \\ 3.26 \times 10^{-4} \times DCNT \times T - 0.2, (DCNT \geq 5600/T) \end{cases}$ -L, n, N, D_{TSV}, D_{CNT}, and d refer to the length of the CNT, the total number of CNTs, the number of conducting channels, the diameters of the combination cylinder of CNTs, the CNT diameter, and the distance between two CNTs, respectively.
[38]		$R_c = \frac{f_{CNT}}{N} \times \left(R_{mc} + \frac{R_Q}{N_{ch}}\right) R = \frac{\rho_{eff}}{wt} = \text{Re}\left(\frac{1}{\sigma_{eff}}\right)\frac{1}{wt}$ $\sigma_{eff} = (1 - f_{CNT})\sigma_{Cu} + f_{CNT}\sigma_{CNT}$ $f_{CNT} = \frac{N\pi(D+0.31)^2}{4wt}$ $L = Lin + Lex = \text{Im}\left(\frac{1}{\sigma_{eff}}\frac{1}{wt}\right) + \frac{\mu_0 \varepsilon_0 \varepsilon_r}{C_E}$ $\frac{C_E}{\varepsilon_0 \varepsilon_r} = \frac{w}{d} + \frac{4}{\pi}\ln\left(1 + \frac{t}{d}\right) + \frac{6}{\pi} + \frac{2}{\pi}\ln\left[1 + \frac{\pi w}{2(1+\pi)(t+d)}\right]$ $C_Q = N N_{ch}\frac{2e^2}{hv_F}$

Ref	Compact model	Model-related formulas
[75]		$R_{Cu-Carbon} = \left(\frac{1}{R_{Cu-CNT}} + \frac{1}{R_{GNR^{T,B}}} + \frac{1}{R_{GNR^{L,R}}} \right)^{-1}$ $R_{GNR} = \frac{h}{2e^2 N_L N_{ch}} \left[\sum_i \left(1 + \frac{L}{\lambda_{eff}^r} \right)^{-1} \right]^{-1}$ $R_{Cu-CNT} = \frac{\rho_{eff}}{wt}$ $L_{Cu-Carbon} = \left(\sum_{j=T,B,L,R} \frac{1}{L_j} \right)_{GNR}^{-1} + L_{CNT} + L_{Cu}$ $C_{Cu-Carbon_g} = \left[\left(\sum_{j=T,B} C_{GNR}^j \right)^{-1} + \frac{1}{C_{CNT}^g} + \frac{1}{C_e^g} \right]^{-1}$ $C_{Cu-Carbon_c} = \left[\left(\sum_{j=L,R} C_{GNR}^j \right)^{-1} + \frac{1}{C_{CNT}^c} + \frac{1}{C_e^c} \right]^{-1}$

5. Conclusion and perspective

In this chapter, we provide an overview of the general properties of graphene-based interconnects, the semiclassical and quantum theory explaining the electrical transport inside nanowire, and finally the advancements in electrical circuit modeling of graphene nanoribbon, carbon nanotube, and copper composite-based interconnects. In sum, electrical modeling of conductors CNT or GNR based has been performed for over 25 years, but their simulation shows little performance compared with the cost to invest for their production. Thus, more worthy alternatives should be studied in the following areas to pursue in the future. (1) Cu-GNR has shown interesting properties for further studies in terms of electromigration, crosstalk, and power consumption. (2) More models based on Cu-CNT should be studied, for instance, Cu-CNT bundles with mixed configuration, Cu-TCNTs, and so on. (3) Since aluminum is relatively cheaper and has a higher specific conductivity, approximately twice the one for copper, more research should be oriented toward Al-CNT or Al-GNR to have a deeper knowledge about the performance of this composite.

Author details

Youssef Nadir[1,2]*, Hassan Belahrach[2,3], Abdelilah Ghammaz[3], Aze-Eddine Naamane[1,2] and Mohammed Radouani[1]

1 L2MC Laboratory, National School of Arts and Crafts, Meknes, Morocco

2 Electrical Laboratory, Royal School of Aeronautics, Marrakech, Morocco

3 Laboratory LSEEET, University Cadi Ayyad, Marrakech, Morocco

*Address all correspondence to: josse.nadir@gmail.com

IntechOpen

References

[1] Moore GE. Cramming more components onto integrated circuits. Electronics. 1965;**38**:114-117

[2] Mittal J, Lin K. Carbon nanotube-based interconnections. Journal of Materials Science. 2017; **52**:1-5. DOI: 10.1007/s10853-016-0416-4

[3] International Technology Roadmap for Devices and Systems—Systems and Architectures. 2021 [online]. Available from: https://irds.ieee.org/editions/2021

[4] Nylander A. Fundamental Characterization of Low Dimensional Carbon Nanomaterials for 3D Electronics Packaging. 2021. p. 21. DOI: 10.13140/RG.2.2.13693.49128

[5] Kaushik BK. Carbon Nanotube Based VLSI Interconnects. 2015. p. 5. DOI: 10.1007/978-81-322-2047-3

[6] Khursheed A, Khare K, Haque F. Designing of ultra-low-power high-speed repeaters for performance optimization of VLSI interconnects at 32 nm. International Journal of Numerical Modelling: Electronic Networks, Devices and Fields. 2019; **32**:1-2. DOI: 10.1002/jnm.2516

[7] Sathyakam U, Mallick P. Design and Crosstalk Analysis in Carbonotube Interconnects. 2020. p. 2. DOI: 10.1007/ 978-981-15-8888-4

[8] Steinhogl W et al. Comprehensive study of the resistivity of copper wires and lateral dimension of 100nm and smaller. Journal of Applied Physics. 2005;**97**:023706

[9] Khursheed A, Khare K. Nano Interconnects Device Physics, Modeling and Simulation. 2021. pp. 63-66. DOI: 10.1201/9781003104193

[10] Todri-Sanial A, Ramos R, Okuno H, Dijon J, Dhavamani A, Widlicenus M, et al. A survey of carbon nanotube interconnects for energy efficient integrated circuits. IEEE Circuits and Systems Magazine. 2017;**17**:47-62. DOI: 10.1109/MCAS.2017.2689538

[11] Zhang S, Nguyen N, Leonhardt B, Jolowsky C, Hao A, Park JG, et al. Carbon-nanotube-based electrical conductors: Fabrication, optimization, and applications. Advanced Electronic Materials. 2019;**5**:9-10. DOI: 10.1002/ aelm.201800811

[12] ALVORN CNT YARN/WIRE/ROPE. Available from: https://dexmat.com/ cntproducts/cnt-yarn-wire-rope/ [Accessed: November 2020]

[13] Zhao WS, Yin WY. Carbon-based interconnects for RF nanoelectronics. In: Webster JG, editor. Electronic Engineering. 2012. pp. 1-20. DOI: 10.1002/047134608X.W8147

[14] Behnam A, Lyons AS, Bae MH, Chow EK, Islam S, Neumann CM, et al. Transport in nanoribbon interconnects obtained from graphene grown by chemical vapor deposition. Nano Letters. 2012;**12**:4424-4443

[15] Kosynkin DV, Higginbotham AL, Sinitskii A, Lomeda JR, Dimiev A, Price BK, et al. Longitudinal unzipping of carbon nanotubes to form graphene nanoribbon. Nature. 2009;**458**:872-876

[16] Novoselov NS, Geim AK, Morozov SV, Jiang D, Zhang Y, Dubonos SV, et al. Electric field effect in atomically thin carbon films. Science. 2004;**306**:666-669

[17] Zhao W-S, Fu K, Wang D, Li M, Wang G, Yin W-Y. Mini-review: Modeling and performance analysis of nanocarbon interconnects. Applied Sciences. 2019;**9**. DOI: 10.3390/app9112174

[18] Yao Z, Kane CL, Dekker C. High-field electrical transport in single-wall carbon nanotubes. Physical Review Letters. 2000;**84**:2941

[19] Wei BQ, Vajtai R, Ajayan PM. Reliability and current carrying capacity of carbon nanotubes. Applied Physics Letters. 2001;**79**:1172

[20] Marconnet AM, Panzer MA, Goodson KE. Thermal conduction phenomena in carbon nanotubes and related nanostructured materials. Reviews of Modern Physics. 2013;**85**: 1295

[21] Berger C, Yi Y, Wang ZL, de Heer WA. Multiwalled carbon nanotubes are ballistic conductors at room temperature. Applied Physics A: Materials Science & Processing. 2002; **74**:363

[22] Li S, Yu Z, Yen S-F, Tang WC, Burke PJ. Carbon nanotube transistor operation at 2.6 GHz. Nano Letters. 2004;**4**:753

[23] Kim S, Kulkarni DD, Rykaczewski K, Henry M, Tsukruk VV, Fedorov AG. Fabrication of an ultralow-resistance ohmic contact to MWCNT–Metal interconnect using graphitic carbon by electron beaminduced deposition (EBID). IEEE Transactions on Nanotechnology. 2012; **11**:1223

[24] Subramaniam C, Sekiguchi A, Yamada T, Futaba DN, Hata K. Nano-scale, planar and multi-tiered current pathways from a carbon nanotube–copper composite with high

conductivity, ampacity and stability. Nanoscale. 2016;**8**:3888

[25] Subramaniam C, Yamada T, Kobashi K, Sekiguchi A, Futaba DN, Yumura M, et al. One hundred fold increase in current carrying capacity in a carbon nanotube–copper composite. Nature Communications. 2013;**4**(1)

[26] Subhajit D, Sandip B, Debaprasad D, Hafizur R. A Short Review on Graphene Nanoribbon Interconnect. IEEE; 2020. pp. 1-7. DOI: 10.1109/ISDCS49393. 2020.9263018

[27] Benedict LX, Crespi VH, Louie SG, Cohen ML. Static conductivity and superconductivity of carbon nanotubes —Relations between tubes and sheets. Physical Review B, Condensed Materials. 1995;**52**(20):14935-14940

[28] Xie S, Li W, Pan Z, Chang B, Lianfeng S. Mechanical and physical properties on carbon nanotube. Journal of Physics and Chemistry of Solids. 2000;**61**:1153-1158. DOI: 10.1016/ S0022-3697(99)00376-5

[29] Kumar PSSR, Smart DSR, Alexis SJ. Corrosion behaviour of aluminium metal matrix reinforced with multi-wall carbon nanotube. Materials Today Communications. 2020;**5**:71-75

[30] Arora N, Sharma NN. Arc discharge synthesis of carbon nanotubes: Comprehensive review. Diamond and Related Materials. 2014;**50**:135-150

[31] Su Y, Zhang Y. Carbon nanomaterials synthesized by arc discharge hot plasma. Carbon N. Y. 2015;**83**:90-99. DOI: 10.1016/j.carbon.2014.11.023

[32] Harris PJF. Solid state growth mechanisms for carbon nanotubes. Carbon N. Y. 2007;**45**:229-239. DOI: 10.1016/j.carbon.2006.09.023

[33] Arepalli S. Laser ablation process for single-walled carbon nanotube production. Journal of Nanoscience and Nanotechnology. 2004;**4**:317-325. DOI: https://doi.org/10.1166/jnn.2004. 072

[34] Khueshed BAT. Synthesis of carbon nanotubes by catalytic chemical vapour deposition: A review on carbon sources, catalysts and substrates. Material Science and Semiconductor Process. 2016;**41**: 67-82

[35] Jourdain V, Bichara C. Current understanding of the growth of carbon nanotubes in catalytic chemical vapour deposition. Carbon N. Y. 2013;**58**:2-39

[36] Mubarak NM, Abdullah EC, Jayakumar NS, Sahu JN. An overview on methods for the production of carbon nanotubes. Journal of Industrial and Engineering Chemistry. 2014;**20**: 1186-1197. DOI: 10.1016/j. jiec.2013. 09.001

[37] Koziol K, Boskovic BO, Yahya N. Synthesis of carbon nanostructures by CVD method. Carbon and Oxide Nanostructures. 2010;**2010**:23-49

[38] Cheng Z-H, Zhao W-S, Dong L, Wang J, Zhao P, Gao H, et al. Investigation of copper-carbon nanotube composites as global VLSI interconnects. IEEE Transactions on Nanotechnology. 2017;**16**:891-900. DOI: 10.1109/ TNANO.2017.2756928

[39] Jiang J, Kang J, Cao W, Xie X, Zhang H, Chu J, et al. Intercalation doped multilayer-graphene-nanoribbons for next-generation interconnects. Nano Letters. 2017;**17**:2-4. DOI: 10.1021/acs. nanolett.6b04516

[40] Hu Y, Shen Y, Bao H. Optimized phonon band discretization scheme for efficiently solving the nongray Boltzmann transport equation. ASME.

Journal of Heat Transfer. July 2022; **144**(7):072501. DOI: 10.1115/1.4054300

[41] Salahuddin S, Datta S. Transport effects on signal propagation in quantum wires. Electron Devices, IEEE Transactions on. 2005;**52**:1734-1742. DOI: 10.1109/TED.2005.852170

[42] Martin PC, Schwinger J. Theory of many-particle systems. I. Physical Review. 1959;**115**(6):1342-1373. DOI: 10.1103/physrev.115.1342

[43] Kadanoff L, Baym G. Quantum Statistical Mechanics. New York: Benjamin; 1962

[44] Keldysh LV. Diagram technique for nonequilibrium processes. Soviet Physics–JETP. 1965;**20**(4):1018-1026

[45] Danielewicz P. Quantum theory of nonequilibrium processes, I. Annals of Physics. 1984;**152**(2):239-304. DOI: 10.1016/0003-4916(84)90092-7

[46] Mahan GD. Quantum transport equation for electric and magnetic fields. Physics Reports. 1987;**145**(5):251-318. DOI: 10.1016/0370-1573(87)90004-4

[47] Datta S. Steady-state quantum kinetic equation. Physical Review B. American Physical Society. 1989;**40**(8):5830-5833. DOI: 10.1103/PhysRevB.40.5830

[48] McLennan MJ, Lee Y, Datta S. Voltage drop in mesoscopic systems: A numerical study using a quantum kinetic equation. Physical Review B. American Physical Society. 1991;**43**(17):13846-13884. DOI: 10.1103/PhysRevB.43.13846

[49] Meir Y, Wingreen NS. Landauer formula for the current through an interacting electron region. Physical Review Letters. American Physical Society. 1992;**68**(16):2512-2515. DOI: 10.1103/PhysRevLett.68.2512

[50] Datta S. Lessons from Nanoelectronics: A new perspective on transport. Part B, Quantum Transport. Singapore, Hackensack, NJ: World Scientific Publishing Co. Pte. Ltd.; 2018. pp. 41-45. DOI: 10.1142/10440-vol2

[51] Xu Y, Srivastava A. A model for carbon nanotube interconnects. International Journal of Circuit Theory and Applications. 2009;**38**:559-575. DOI: 10.1002/cta.587

[52] Li H et al. Modelling of carbon nanotube interconnects and comparative analysis with Cu interconnects. In: Proceedings of Asia-Pacific Microwave Conference. 2006

[53] Naeemi A, Meindl JD. Monolayer metallic nanotube interconnects: Promising candidates for short local interconnects. IEEE Electron Device Letters. 2005;**26**:544-546

[54] Jamal O, Naeemi A. Ultralow-power single-wall carbon nanotube interconnects for subthreshold circuits. IEEE Transactions on Nanotechnology. 2011;**10**:99-101

[55] Pable SD, Hasan M. Interconnect design for subthreshold circuits. IEEE Transactions on Nanotechnology. 2012;**11**:633-639

[56] Ceyhan A, Naeemi A. Cu interconnect limitations and opportunities for SWNT interconnects at the end of the roadmap. IEEE Transactions on Electron Devices. 2013;**60**:374-382

[57] Park J, Rosenblatt S, Yaish Y, Sazonova V, Ustunel H, Braig S, et al. Electron-phonon scattering in metallic single-walled carbon nanotubes. Nano Letters. 2004:517-520

[58] Burke PJ. Corrections to "Luttinger liquid theory as a model of the gigahertz electrical properties of carbon nanotubes". Nanotechnology, IEEE Transactions on. 2004;**3**:331-331. DOI: 10.1109/TNANO.2004.828580

[59] Rossi D, Cazeaux J, Metra C, Lombardi F. Modeling crosstalk effects in CNT bus architectures. Nanotechnology, IEEE Transactions on. 2007;**6**:133-145. DOI: 10.1109/TNANO.2007.891814

[60] Raychowdhury A, Roy K. Modeling of metallic carbon-nanotube interconnects for circuit simulations and a comparison with Cu interconnects for scaled technologies. IEEE Transactions on Computer-Aided Design of Integrated Circuits and Systems. 2006;**25**:58-65. DOI: 10.1109/TCAD.2005.853702

[61] Li H, Yin W-Y, Banerjee K, Mao J-F. Circuit modeling and performance analysis of multi-walled carbon nanotube interconnects. Electron Devices, IEEE Transactions on. 2008;**55**:1328-1337. DOI: 10.1109/TED.2008.922855

[62] Naeemi A, Meindl JD. Compact physical models for multiwall carbon-nanotube interconnects. IEEE Electron Device Letters. 2006;**27**(5):338-340

[63] Xu C, Li H, Banerjee K. Modeling, analysis, and design of graphene nano-ribbon interconnects. Electron Devices, IEEE Transactions on. 2009;**56**:1567-1578. DOI: 10.1109/TED.2009.2024254

[64] Das S, Bhattacharya S, Das D, Rahaman H. RF performance analysis of graphene nanoribbon interconnect. In: IEEE TechSym 2014 - 2014 IEEE Students' Technology Symposium. 2014

[65] Ragheb T, Massoud Y. On the modeling of resistance in Graphene Nanoribbon (GNR) for future interconnect applications. 2008:593-597

[66] Harutyunyan AR, Chen G, Paronyan TM, Pigos EM, Kuznetsov OA, Hewaparakrama K, et al. Preferential growth of single-walled carbon nanotubes with metallic conductivity. Science. 2009;**326**:116-120

[67] Sathyakam U, Mallick P. Triangular carbon nanotube bundle interconnects for subthreshold VLSI circuits. Journal of Electronic Materials. 2019;**48**. DOI: 10.1007/s11664-019-07431-z

[68] Pandya N, Kaushik BK, Manhas S. Analysis of MWCNT and bundled SWCNT interconnects: Impact on crosstalk and area. Electron Device Letters, IEEE. 2012;**33**:1180-1182. DOI: 10.1109/LED.2012.2200872

[69] Amin B, Ullah S, Sana M. A Theoretical Modeling Analysis of Adapted Composite CNT Bundle for High-Speed VLSI Interconnect. 2021

[70] Kaushik BK, Manhas S. Analysis of delay and dynamic crosstalk in bundled carbon nanotube interconnects. IEEE Transactions on Electromagnetic Compatibility. 2014;**56**:1-8. DOI: 10.1109/TEMC.2014.2318017

[71] Zhang G, Warner JH, Fouquet W, et al. Growth of ultrahigh density single-walled carbon nanotube forests by improved catalyst design. ACS Nano. 2012;**6**(4):2893-2903

[72] Zhao WS, Zheng J, Hu Y, et al. High-frequency analysis of cu-carbon nanotube composite through-silicon vias. IEEE Transactions on Nanotechnology. 2016;**15**(3):506-511

[73] Subramaniam C, Yamada T, Kobashi K, et al. One hundred fold increase in current carrying capacity in a carbon nanotube-copper composite. Nature Communication. 2013;**4**:2202

[74] Chai Y, Chan PCH, Fu Y, et al. Electromigration studies of Cu/carbon nanotube composite interconnects using Blech structure. IEEE Electron Device Letters. 2008;**29**(9):1001-1003

[75] Ruchit M, Sunny C, Zhihong C. Enhanced electrical and thermal conduction in graphene. Nano Letters. 2015

[76] Feng Y, Burkett S. Modeling a copper/carbon nanotube composite for applications in electronic packaging. Computational Materials Science. 2015;**97**:1-5. DOI: 10.1016/j.commatsci.2014.10.014

Estimation and Modification of Electrical Parameters of Organic Device in the Presence of Single Walled Carbon Nanotubes

Sudipta Sen and Nabin Baran Manik

Abstract

Present work will mainly focus on one of the most important applications of single-walled carbon nanotubes (SWCNTs). In this work, the different electrical parameters that are associated with the charge injection process at the metal−organic contact of the organic device will be estimated and subsequently, the effect of SWCNTs on those parameters will be measured. As we all know that high charge carrier trapping and high Schottky barrier at the metal−organic contact significantly affect the charge flow at the junction of organic dye-based device. It is of paramount importance to reduce these parameters which hinder the charge flow in the organic device. SWCNTs are one of the most prominent materials which can improve this charge flow at the metal−organic contact. Our main aim will be to study the physics behind the improvement of these electrical parameters in the presence of SWCNTs which will allow the device to perform more efficiently.

Keywords: metal−organic contact, Schottky barrier, space - charge layer width, SWCNT, threshold voltage, trap concentration

1. Introduction

Nanotechnology and nanomaterials play a significant role in the present scenario of research works. In the emerging fields of research works, nanotechnology will form the base for other technologies to emerge at nanoscopic level [1]. One of the most significant innovations in the field of nanotechnology is the discovery of Carbon nanotubes (CNTs), which is an allotrope of carbon. CNTs are arranged in hexagon and pentagon with a diameter of 3–30 nm [2]. CNTs consist of single or multiple layers of graphene sheets. Depending on number of layers, CNTs can be of two types, single-walled carbon nanotubes (SWCNTs) and multi-walled carbon nanotubes (MWCNTs). MWCNTs were discovered by Sumio Iijima in 1991 by a simple arc evaporation method and consist of multiple graphene layer sheets [3]. SWCNTs comprise single-layer graphene sheets, and their outer diameter is basically in the range of 1−2 nm [4]. Inbuilt structural defects and undefined diameter make

MWCNTs less stable than SWCNTs [5]. Researchers have shown great interest in SWCNTs due to their excellent thermal, electrical, and mechanical properties. These excellent properties can be attributed to large aspect ratio as the length and diameter of SWCNTs are in the range of micrometer and nanometers respectively [6]. The structure of SWCNTs is akin to cylindrical shape with hexagonal carbon atoms which are sp^2 hybridized [7]. It has a hollow inner structure. SWCNTs take the form of one – dimensional (1D) material and they are used in membranes, capacitors, polymers, metallic surfaces, ceramics, nanomedicine etc. [8].

In this work, we will study one of the major applications of SWCNTs in the organic device regarding charge injection process at metal–organic contact, when the organic dye is sandwiched between two metallic electrodes to form the organic device. These organic devices possess several advantages compared to inorganic devices, such as low cost, mechanical flexibility, copious availability, light weight, low-temperature processing, and easy tunability of their properties via molecular tailoring [9–11]. In spite of these advantages, there are indisputable impediments to these devices. One of the impediments of these organic devices is low charge injection from metallic electrodes to organic layer. The poor injection of charges can be ascribed to the high trap concentration at the metal–organic contact. Traps basically act as recombination centers or as defects in the amorphous organic materials, in which active charge carriers get adrift. High Schottky barriers at the metal–organic contact also allow less charge carriers to flow through the interfacial area and it causes the formation of space charge layer at the junction area. Researchers are striving for reducing the parameters which affect the charge injection process at metal–organic contact, such as high trap concentration, Schottky barrier, and space-charge layer width to improve the device performance. In this work, we will incorporate SWCNT in the organic device and subsequently study the effect of SWCNTs on these above-mentioned parameters in order to improve the charge injection at metal–organic contact. Phenosafranin dye has been chosen as organic dye and it has been sandwiched in between Indium Tin Oxide (ITO) and Aluminum (Al). The current flow in the prepared organic devices will be analyzed by using Richardson – Schottky thermionic emission model. Dark current–voltage (I-V) and capacitance-voltage (C-V) analysis of the prepared organic device will be performed in this present work.

2. Experimental details

2.1 Materials and sample preparation

Phenosafranin (PSF) dye (3, 7-Diamino-5-phenylphenazinium chloride) belongs to cationic phenazine group of dyes [12–13]. It can be used as photosensitizer in energy and electron transfer reactions [14]. It has amine functionalities which make it a useful material for future polymer composite work [15]. The product we have used in this experiment has 80% dye content and its molecular weight is 322.79 g/mol. This dye has been procured from Sigma Aldrich, Germany. **Figure 1a** shows the structure of this dye. **Figure 1b** shows the schematic diagram of SWCNT, which is obtained from Sisco Research Laboratories (SRL), India. We have used SWCNT of 2 nm outer diameter and 30 μm length.

A 75 mm × 25 mm x 1.1 mm ITO coated glass slide (surface resistivity ~20 Ω/sq) is used as front electrode and Al is used as back electrode for preparing the organic
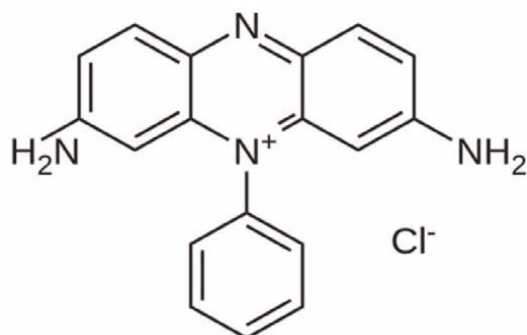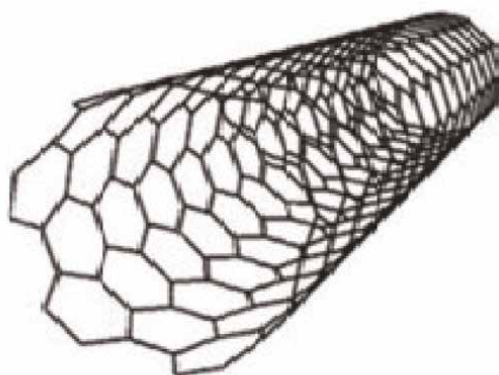
Figure 1.
(a) Structure of Phenosafranin (PSF) dye and (b) schematic diagram of SWCNT.

device. ITO-coated glass and Al have also been purchased from Sigma Aldrich. Poly vinyl alcohol (PVA) has been used in this work, as it is an excellent transparent inert binder. PVA was obtained from S. D. Fine Chem. Ltd., Boisar, India.

At first, the PVA solution is prepared. In a cleaned beaker, 5 mg of PVA is added to 15 ml of distilled water and is stirred with a magnetic stirrer for 30 minutes at 60°C. PVA is of laboratory grade. PVA is utilized to enhance the mechanical properties of organic dye films because it has compatible structure and hydrophilic properties. Molecular weight of PVA is approximately 1,25,000. PVA is used to stick the dye solution on the electrodes [13].

1 mg of PSF dye is added in the PVA solution and stirred for 30 minutes. One part of this solution is kept aside in a pre-cleaned test tube and in other part of PSF dye solution, 1 mg SWCNT is added and well stirred. After that, PSF dye solution without SWCNT is spin coated at 2500 rpm speed and dried at 4000 rpm speed on a pre cleaned ITO coated glass substrate. Similarly, the same solution is deposited on the Al and then ITO coated glass and Al are intercalated together to form the PSF cell without SWCNT. Similarly, the PSF solution with SWCNT is also spin coated to prepare the PSF cell consisting of SWCNT. The prepared devices are kept in vacuum desiccators for 12 hours to dry before characterization. **Figure 2** expresses schematic diagram of PSF dye based organic device.
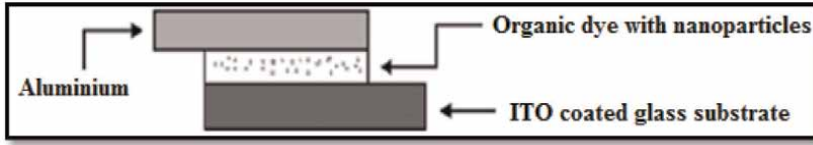
Figure 2.
Schematic diagram of prepared PSF dye based organic device.

2.2 Measurements

Dark I—V characteristics and C-V characteristics of the cells have been measured with a Keithley 2400 source measure unit and by using LCR meter respectively. For dark I–V measurement, the front electrode ITO is connected to the positive terminal of the battery and the back electrode Al is connected to the negative terminal of the battery [16]. The applied voltage is varied from 0 to 5 V in steps of 0.25 V with a delay of 1000 ms. Room temperature was kept at 25°C during the experiment.

3. Results and discussion

As stated by Richardson-Schottky model, interfacial current at metal–organic layer is shown in the eq. (1)

$$I = AA^*T^2 \, \exp . \left(-\frac{q\phi_b}{kT} \right) \left(\exp \left(\frac{qV}{nkT} \right) \left[1 - \exp \left(\frac{-qV}{kT} \right) \right] \right) \qquad (1)$$

I_0 is the saturation current, which is expressed in eq. (2).

$$I_0 = AA^*T^2 \, \exp . \left(-\frac{q\phi_b}{kT} \right) \qquad (2)$$

The interfacial Schottky barrier at metal- organic junction can be determined from the eq. (2) which has been expressed in eq. (3)

$$\phi_b = \frac{kT}{q} \ln \left(\frac{AA^*T^2}{I_0} \right) \qquad (3)$$

Here, q is the charge of electron, V is the voltage that is applied to the device, A is the device area, k is the Boltzmann's constant, T is absolute temperature, A^* is the effective Richardson constant, n is the ideality factor and ϕ_b is Schottky barrier [17–22]. The saturation current is determined by the interpolation of exponential slope of I at V = 0 and ϕ_b is obtained from the extrapolation of I_0 in the semi log forward bias I - V characteristics. The term $\frac{q}{kT}$ can be replaced by the term β.

The Schottky barrier can also be expressed as shown in the eq. (4)

$$\phi_b = \frac{1}{\beta} \ln \left(\frac{AA^*T^2}{I_0} \right) \qquad (4)$$

Figure 3 shows the dark I-V plots of device without and with SWCNTs have been shown in. **Figure 3** depicts that with SWCNT, the current flow in the PSF dye based
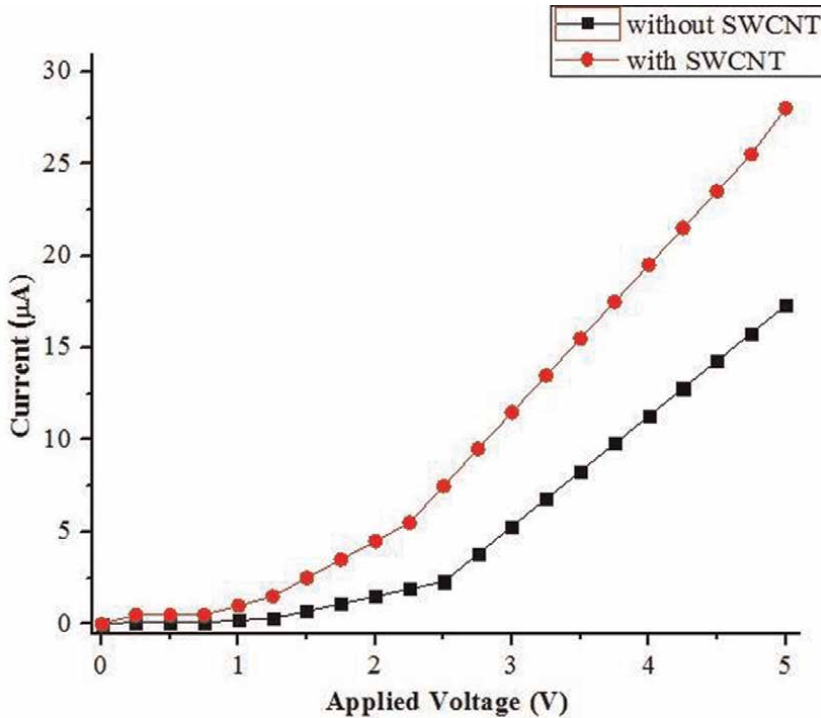
Figure 3.
Current–voltage (I-V) plot of organic device without and with SWCNT.

organic device increases about two times. The threshold voltage has also been estimated from **Figure 3**. The threshold or turn-on voltage of the device is 2.5 V without SWCNT and the value of the threshold voltage lowers to 1 V with SWCNT.

   Figure 4 shows the semilogarithmic current – voltage (lnI –V) plots of **Figure 3** to calculate the Schottky barrier at the metal – organic junction of the PSF dye based organic device in absence and in presence of SWCNT. Schottky barrier is obtained from the extrapolation of I_0 in the semi log forward bias I - V characteristics, which are shown in **Figure 4**. The estimated value of I_0 is found to be 0.74 µA and 1.45 µA in absence and in presence of SWCNT. Putting the values of I_0 in eq. (4), the Schottky barrier of PSF dye based organic device has been calculated without and with SWCNT.

   The space - charge layer width can be estimated from following eq. (5)

$$W_d = \sqrt{\frac{2\varepsilon_0 \varepsilon_s V_d}{qN_D}} \tag{5}$$

W_d = space - charge layer width, ε_0 = vacuum permittivity, ε_s = semiconductor permittivity, V_d = diffusion potential, q = charge of an electron, N_D = donor atom concentration.

   In this work, we have considered the value of ε_s = 11.9 ε_0 and N_D is in the order of 10^{17} cm^{-3} respectively.

   C–V measurement is one of the most important methods to obtain the particulars of rectifying contact interfaces [23]. Diffusion capacitance dominates in the forward bias region and for reverse biased region, the junction capacitances [24].
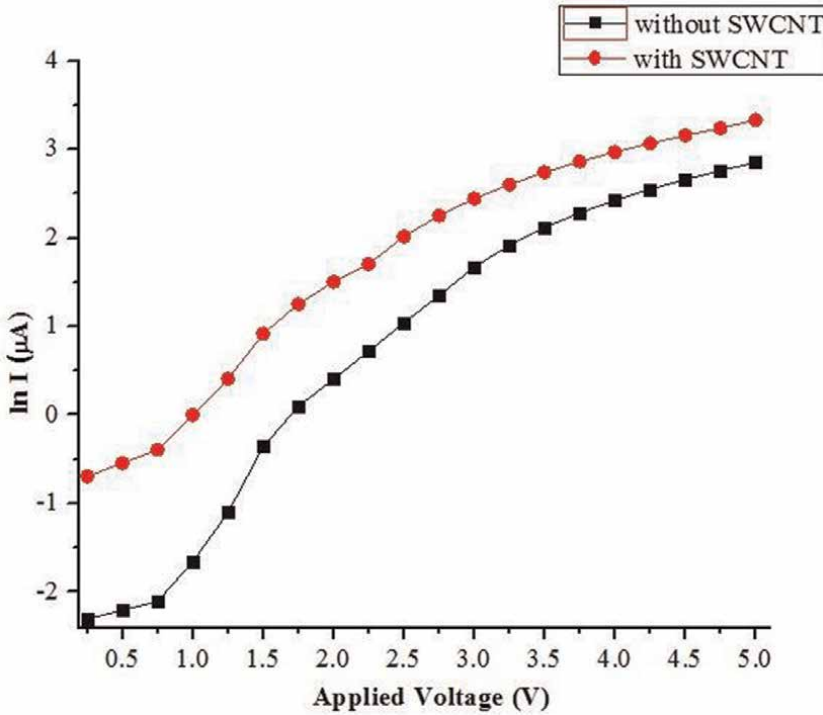
Figure 4.
Semi-logarithmic (ln I-V) plot of organic device without and with SWCNT.

Figure 5 shows C-V curves of PSF dye based organic device without and with SWCNT respectively at a fixed frequency of 10 kHz. It has been observed from the **Figure 5**, that with SWCNT, under forward bias region, the diffusion capacitance increases considerably.

Figure 6 shows C^{-2}-V curves of PSF dye based organic device without and with SWCNT respectively. The linear pattern of C^{-2}-V curves is an indication of forming the Schottky contact at metal – organic junction. The values of diffusion potential and the Schottky barrier have been estimated by using C^{-2}-V characteristics. Voltage axis intercept of C^{-2}-V curves gives the estimated value of diffusion potential which is about to be 3.3 V without SWCNT and about 2.7 V with SWCNT. Putting the values of diffusion potential in eq. (5), the values of space – charge layer width have been calculated without SWCNT and with SWCNT.

Trap energy has been measured by using double logarithmic current – voltage (ln I- ln V) plot which is shown in **Figure 7** without and with SWCNT respectively.

The trap energy can be written as expressed in the following eq. (6)

$$E_t = mkT \tag{6}$$

Where, E_t = trap energy, m = T_c/T, where, T_c denotes the effective temperature of trap distribution and T denotes the room temperature in Kelvin scale, k is the Boltzmann's constant [25] and m is calculated from ln I- ln V plot of **Figure 7**.

Comparing eq. (3) and eq. (6), it can be inferred that Schottky barrier and trap energy are proportional to each other, which means that $\phi_b \propto E_t$, considering other
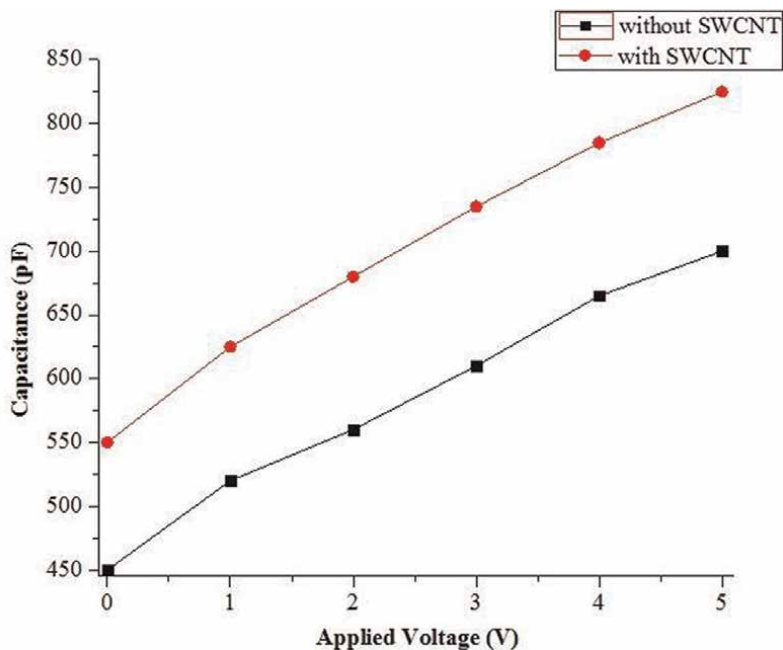
Figure 5.
Capacitance – Voltage (C-V) plot of organic device without and with SWCNT.
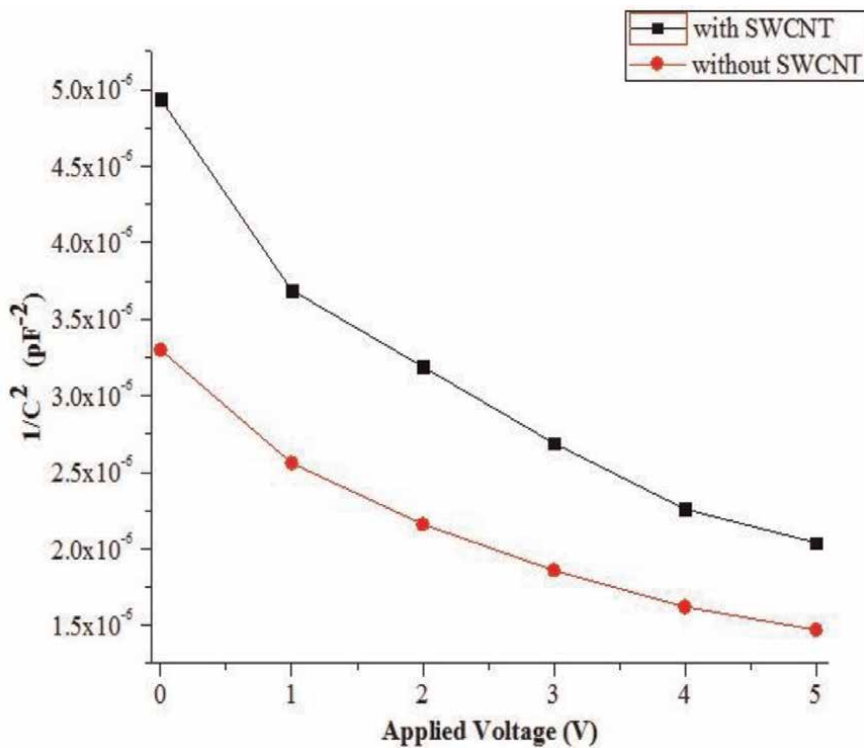
Figure 6.
C^{-2}-V plot of organic device without and with SWCNT.
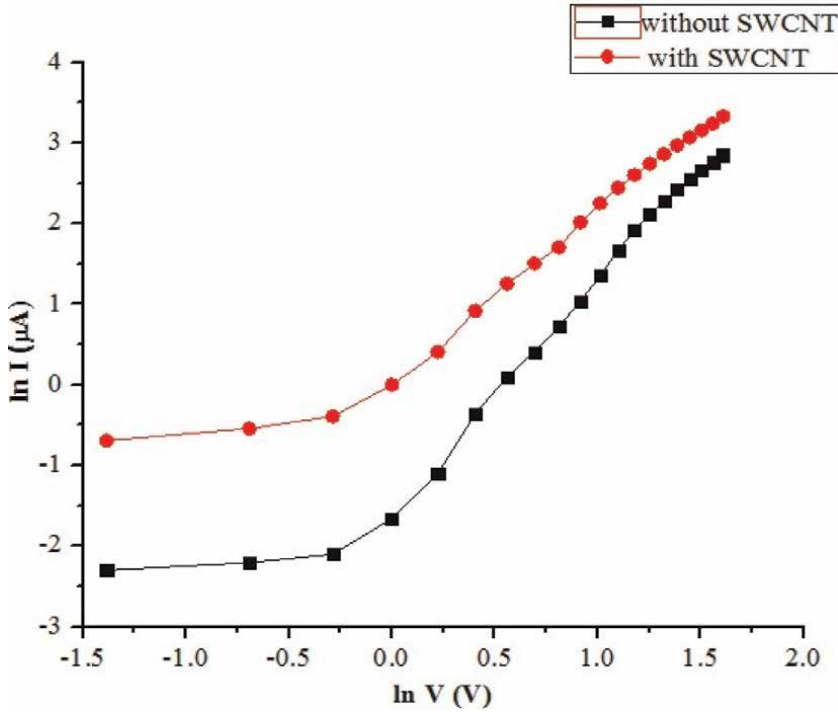
Figure 7.
Double -logarithmic current – Voltage (ln I-ln V) plot of organic device without and with SWCNT.

parameters remain unchanged. So, when the concentration of traps reduces, the Schottky barrier also decreases. Hence, the interconnection between Schottky barrier and trap energy can be established analytically.

The space – charge layer width can also be related to the Schottky barrier by using the following eq. (7)

$$W_d = \frac{\phi_b}{F}$$
(7)

Where, F = applied electric field.

From eq. (7), it can be said that when the applied electric field remains constant, the space – charge layer width is directly proportional to the Schottky barrier.

Hence, the interrelationship among these three parameters, namely, trap energy, Schottky barrier and space – charge layer width can be analytically established. When the SWCNT is incorporated within the organic device, reduction of one of these three parameters will lead to lowering of other two parameters as they are directly proportional to each other.

The values of threshold voltage, trap energy, Schottky barrier and space – charge layer width of organic devices without and with SWCNT are shown in **Table 1**.

Table 1 shows that, in presence of SWCNT, the trap energy has been reduced from 0.053 eV to 0.042 eV, resulting in 20.75% decrease in the concentration of traps. Estimation of Schottky barrier from both I – V characteristics and C – V characteristics has also shown a reduction of 13.58% and 14.47% respectively in the presence of SWCNT. There is a small discrepancy in measuring the Schottky barrier using both the C-V and I-V techniques. C-V method averages over the whole area and estimates the

PSF Dye Based Organic Device	Threshold Voltage (V)	Value of "m"	Trap Energy (eV)	Schottky Barrier (eV) using I-V characteristics	Schottky Barrier (eV) using C-V characteristics	Space - Charge Layer Width (W_d) (cm) $\times 10^{-6}$
Without SWCNT	2.50	2.05	0.053	0.81	0.76	8.15
with SWCNT	1.00	1.63	0.042	0.70	0.65	7.45

Table 1.
Calculation of threshold voltage, trap energy, Schottky barrier, space – charge layer width of organic devices in absence and in presence of SWCNT.

Schottky barrier [26]. As organic devices are prone to traps, the difference between the barrier height values can also be ascribed to interfacial trap states in organic device. With SWCNT, space – charge layer width has also been lowered by 8.59%. All these parameters, which are associated with the charge injection process at the metal – organic contact, such as trap energy, Schottky barrier and space – charge layer width have been decreased considerably in the presence of SWCNT. Lowering of these parameters will result in improvement of charge injection at the interfacial contact and will also enhance the device performance by enhancing the conductivity in the device.

4. Conclusions

In this work, we have studied the effect of SWCNT on the different electrical parameters, affecting significantly the charge flow at metal – organic interface of PSF dye based organic device. We all know that, SWCNT has wide range of applications. Present work shows one of the applications of SWCNT in which lowering of the trap energy, Schottky barrier and space – charge layer width happen at metal – organic contact due to the incorporation of SWCNT in the organic device. With SWCNT, the device will be turned on at lower voltages, as the threshold voltages gets reduced and this can also be attributed to the increasing flow of mobile charge carriers in the organic device. Schottky barrier has been measured by both I-V and C-V methods in presence and in absence of SWCNT. Both the methods are congruous to each other, indicating notable lowering of Schottky barrier in presence of SWCNT. In terms of device physics, it can be inferred that SWCNT acts as conductive fillers to the traps which permit more active charge carriers to flow, resulting in reduction of Schottky barrier and space – charge layer width. SWCNT basically provides more conductive pathways in the organic device by filling out the traps. Due to reduction of trap energy, space – charge layer width and barrier lowering, the current flow in the devices also increases considerably. The notable findings of the work is to study one of the major applications of SWCNT in the organic device in terms of lowering of parameters that affect the charge flow at metal – organic contact which will improve the device performance.

Acknowledgements

Conflict of interest

On behalf of all authors, the corresponding author states that there are no competing financial interests or personal relationships that could have appeared to influence the present work.

Author details

Sudipta Sen* and Nabin Baran Manik
Department of Physics, Condensed Matter Physics Research Centre, Jadavpur University, Kolkata, India

*Address all correspondence to: sagnike000@gmail.com

IntechOpen

References

[1] Rathinavel S, Priyadharshini K, Panda D. A review on carbon nanotube: An overview of synthesis, properties, functionalization, characterization, and the application. Materials Science & Engineering B. 2021;**268**:1-28. DOI: 10.1016/j.mseb.2021.115095

[2] Georgakilas V, Perman JA, Tucek J, Zboril R. Broad family of carbon Nanoallotropes: Classification, chemistry, and applications of fullerenes, carbon dots, nanotubes, graphene, Nanodiamonds, and combined superstructures. Chemical Reviews. 2015;**115**:4744-4822. DOI: 10.1021/cr500304f

[3] Iijima S. Helical microtubules of graphitic carbon. Nature. 1991;**354**:56-58. DOI: 10.1038/354 056a0

[4] Iijima S, Ichihashi T. Single-shell carbon nanotubes of 1-nm diameter. Nature. 1993;**363**:603-605. DOI: 10.1038/363603a0

[5] Dresselhaus MS, Dresselhaus G, Charlier JC, Hernández E. Electronic, thermal and mechanical properties of carbon nanotubes. Philosophical Transactions of the Royal Society A: Mathematical, Physical and Engineering Sciences. 2004;**362**:2065-2098. DOI: 10.1098/rsta.2004.1430

[6] Aqel A, Abou E-NKMM, Ammar RAA, Al-Warthan A. Carbon nanotubes, science and technology part (I) structure, synthesis and characterization. Arabian Journal of Chemistry. 2012;**5**:1-23. DOI: 10.1016/ j.arabjc.2010.08.022

[7] Saifuddin N, Raziah AZ, Junizah AR. Carbon nanotubes: A review on structure and their interaction with proteins.

Journal of Chemistry. 2012;**2013**:1-18. DOI: 10.1155/2013/676815

[8] Kaur R, Vatta P, Kaur M. Carbon nanotubes: A review article. International Journal for Research in Applied Science & Engineering Technology. 2018;**6**:5075-5079. DOI: 10.22214/ijraset.2018.4827

[9] Ahmad S. Organic semiconductors for device applications: Current trends and future prospects. Journal of Polymer Engineering. 2014;**34**:279-338. DOI: 10.1515/polyeng-2013-0267

[10] Zhang Q, Hu W, Sirringhaus H, Müllen K. Recent Progress in emerging organic semiconductors. Advanced Materials. 2022;**34**:1-4. DOI: 10.1002/ adma.202108701

[11] Forrest SR. The path to ubiquitous and low-cost organic electronic appliances on plastic. Nature. 2004;**428**: 911-918. DOI: 10.1038/nature02498

[12] Curran SA, Ellis AV, Vijayaraghavan A, Ajayan PM. Functionalization of carbon nanotubes using phenosafranin. Journal of Chemical Physics. 2004;**120**:4886-4889. DOI: 10.1063/1.1644109

[13] Sen S, Manik NB. Effect of zinc oxide (ZnO) nanoparticles on interfacial barrier height and band bending of Phenosafranin (PSF) dye-based organic device. Journal of Electronic Materials. 2020;**49**:4647-4652. DOI: 10.1007/ s11664-020-08202-x

[14] Gopidas KR, Kamat PV. Photophysics and photochemistry of phenosafranin dye in aqueous and acetonitrile solutions. Journal of Photochemistry and Photobiology A:

Chemistry. 1989;**48**:291-301.
DOI: 10.1016/1010-6030(89)87010-8

[15] Jana AK, Roy S, Bhowmik BB.
Photoelectrochemical and spectral
studies of phenosafranin in different
reducing agents. Chemical Physics
Letters. 1990;**168**:365-370. DOI: 10.1016/
0009-2614(90)85626-N

[16] Sen S, Manik NB. Effect of back
electrode on trap energy and interfacial
barrier height of crystal violet dye-based
organic device. Bulletin of Materials
Science. 2020;**43**:1-4. DOI: 10.1007/
s12034-020-2047-2

[17] Svensson J, Campbell EEB. Schottky
barriers in carbon nanotube-metal
contacts. Journal of Applied Physics.
2011;**110**:111101-1-111101-16.
DOI: 10.1063/1.3664139

[18] Harrabi Z, Jomni S, Beji L,
Bouazizi A. Distribution of barrier
heights in Au/porous GaAs Schottky
diodes from current–voltage–
temperature measurements. Physica B:
Condensed Matter. 2010;**405**:3745-3750.
DOI: 10.1016/j.physb.2010.05.079

[19] Al-Taii HMJ, Amin YM,
Periasamy V. Calculation of the
electronic parameters of an Al/DNA/p-Si
Schottky barrier diode influenced by
alpha radiation. Sensors. 2015;**15**:
4810-4822. DOI: 10.3390/s150304810

[20] Al-Taii HMJ, Periasamy V,
Amin YM. Electronic properties of
DNA–based Schottky barrier diodes in
response to alpha particles. Sensors.
2015;**15**:11836-11853. DOI: 10.3390/
s150511836

[21] Yildirim M. Determination of
contact parameters of Au/n-Ge Schottky
barrier diode with Rubrene interlayer.
Journal of Polytechnic. 2017;**20**:165-173.
DOI: 10.2339/2017.20.1

[22] Sen S, Das PK, Manik NB. Study on
the effect of single walled carbon
nanotubes on junction properties of
safranin –T dye-based organic device.
Journal of Physics Communications.
2021;**5**:1-9. DOI: 10.1088/2399-6528/
abf2cf

[23] Güllü Ö, Aydoğan Ş, Türüt A.
Fabrication and electrical characteristics
of Schottky diode based on organic
material. Microelectronic Engineering.
2008;**85**:1647-1651. DOI: 10.1016/
j.mee.2008.04.0039

[24] Güllü Ö. Barrier modification by
methyl violet organic dye molecules of
Ag/P-Inp structures. European Journal of
Interdisciplinary Studies. 2016;**2**:7-17.
DOI: 10.26417/ejis.v5i1

[25] Haldar A, Maity S, Manik NB. Effect
of back electrode on photovoltaic
properties of crystal-violet-dye-doped
solid-state thin film. Ionics. 2008;**14**:
427-432. DOI: 10.1007/s11581-007-
0194-8

[26] Sen S, Manik NB. Modification of
barrier height and depletion layer width
of methyl red (MR) dye-based organic
device in the presence of single-walled
carbon nanotubes (SWCNT). Indian
Journal of Physics. 2022;**96**:385-390.
DOI: 10.1007/s12648-020-01972-4

Section 3

State-of-the-Art Applications

Chapter 7

Modification and Application of Carbon Nanotubes for the Removal of Emerging Contaminants from Wastewater: A Review

Abu Taleb, Mohammed Naif Al-sharif,

Mohammed Ali Al-mutair, Saleh Almasoudi,

Osama Madkhali and Mohammed Muzibur Rahman

Abstract

The emerging contaminants (ECs) refer to chemical compounds either naturally originated or synthetically modified having potential toxic effects to the environment. The ECs include different pollutants such as biocides, pesticides, pharmaceuticals (antibiotic, analgesics, and hormones) and personal care products (cosmetics, fragrances, and hygiene products). The ECs are considering the top priority pollutants by the European Union (EU) and the United States Environmental Protection Agency (US EPA). Among other materials, the carbon nanotubes (CNTs) are one of widely used materials for the removal of ECs applying diverse techniques of wastewater decontamination. The momentous advancement of these functional nanostructured materials has found to be cost-effective, reusable, smart materials for the application of ECs removal. The aim of this chapter was to explore the modification routes and advancement of functionalization of CNTs with other functional groups by the reported works. The possible mechanistic insight of ECs removal reactions was also evaluated applying different methods for decontamination reported in the past studies. This review will be significant sources of information of CNTs-based materials for the application of wastewater treatment especially ECs removal from wastewater and ultimate environmental remediation.

Keywords: wastewater treatment, carbon nanotubes, emerging contaminants, removal

1. Introduction

The concurrent increasing trend of human needs and subsequent technological advancements, expansion of urban and transportation facilities, rapid growth of agricultural and manufacturing activities as well as over exploitation of environmental components are few instances among others human induced activities which are responsible for distressing water quality [1–4]. Lack of sufficient sanitation also

is lead to water contamination across the world at large [5]. Almost 2.5 billion of world's citizen are lives without appropriate sanitation. According to the recent estimation of United Nations (UN) that the world wide 1500 km^3 of wastewater annually has been produced due to industrial effluents [5]. More than 33% of untreated industrial effluents and about 70% household sewage are directly discharging into the aquatic system [5]. In this connection, millions of previous studies have been reported that, wastewater has been carrying a series of pollutants including emerging contaminants (ECs) [6–10]. The ECs including pharmaceuticals and personal care products (PPCPs) are presents in aquatic system of different locations of the world with higher concentration beyond permissible limit [11–16]. One of the pharmaceutical products, the antibiotics are using for killing of human and animal host pathogenic fungi and bacteria [5]. The water bodies are serving as main pans of misused antibiotics are prominently coming from the hospitals output, effluents from the pharmaceutical industries, sewage from animal farms, municipal runoff and effluents from wastewater treatment plants. Life cycle of ECs is depicted in **Figure 1**
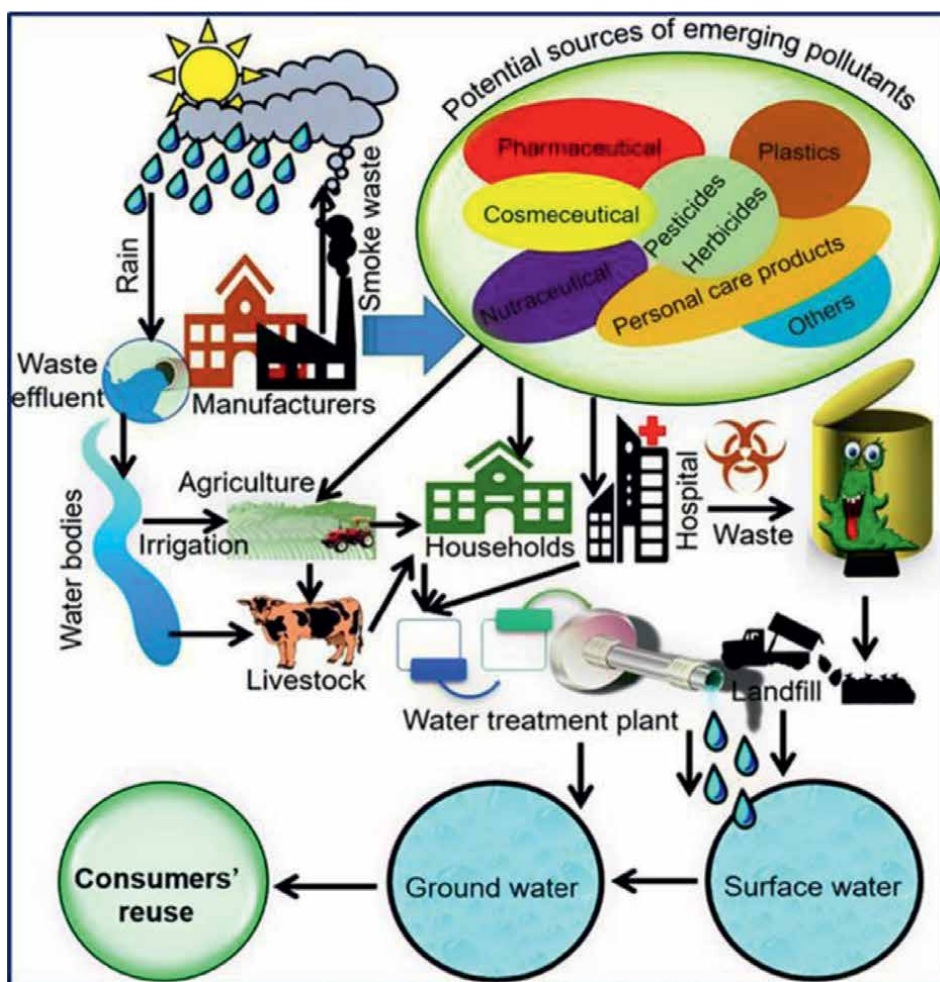
Figure 1.
Life cycle of ECs from sources to environment [17].

from sources to the environment [17]. Consequently, the aquatic system is carrying such kind of toxicants and subsequent severe impacts on human health and on other biotic components in the ecosystem as seen in **Figure 2** illustrated by Rasheed et al., [17]. Hence, researchers are looking for special concerned to removal of ECs from wastewater. The traditional wastewater treatment plants are facilitating the sequestration of some known pollutants and suspended solids apart from emerging contaminates, which are not efficient for appropriately removal of some ECs including antibiotics due to their registrant and persistence nature [1, 17]. Different materials are utilizing for purification and decontamination of wastewater using various forms including tubes, films, powder, gels (hydrogel and aerogels) etc. [18–20]. Recent trends of wastewater treatment process are to modifying the composite materials with nanostructured materials due to their exclusive characteristics such as enlarged surface area, small size, available reactive sites and regeneration facilities [1–3]. Among other nanostructured materials, the carbon nanotubes (CNTs) are widely using for removal of ECs from wastewater [21–24]. The CNTs having hexagonal sheets of carbon atoms revolved up into hollow structure taking diverse helicities
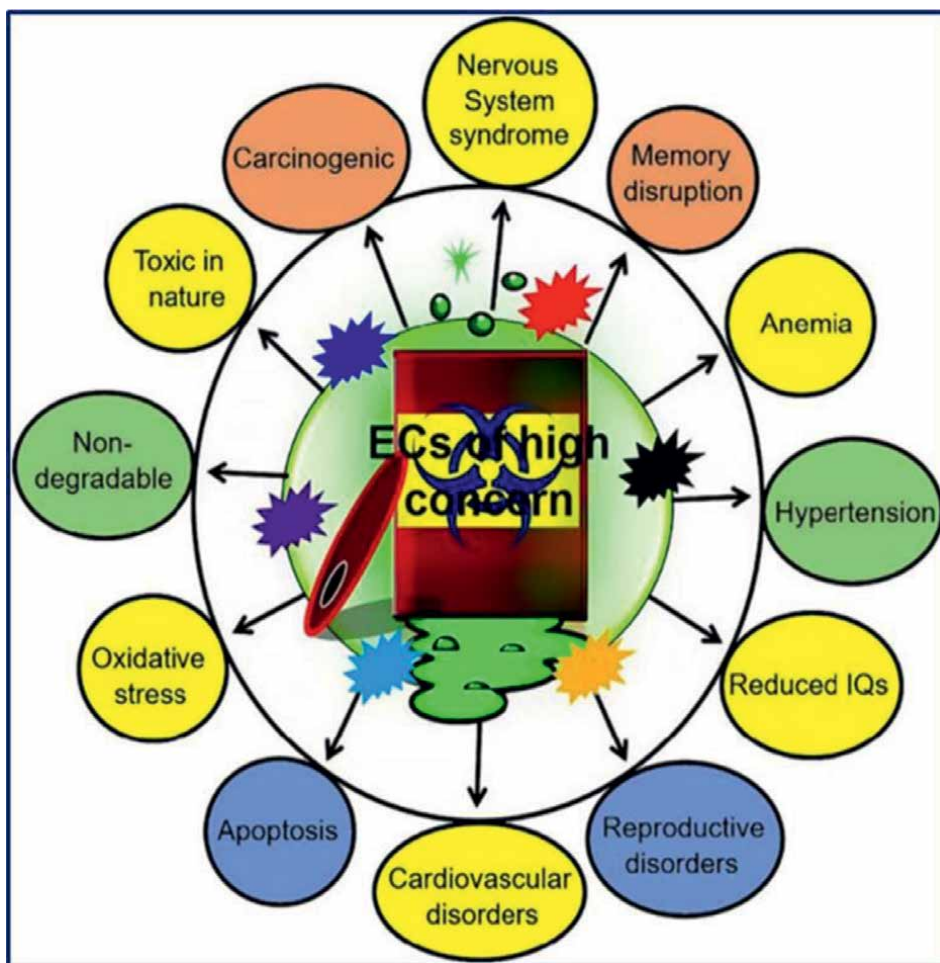
Figure 2.
Effect of ECs on environment and human health [17].

seamless of graphitic sheets. CNTs are mainly two types, containing at least 2 layers of graphite sheets arranging between 4 and 30 nm in diameter and tabular shape of allotropes of carbon is denoted as multiwall carbon nanotubes (MWCNTs) while a single unified cylindrical closed by each of end graphene is defined as single-walled carbon nanotubes (SWCNTs) [25–29].

The CNTs are plying one of the promising nanostructured filler types materials for wastewater decontamination due to their exciting physical and chemical properties including good aspect ratio, excellent mechanical strength, high thermal conductivity, high electrical conductivity and electron emission, very good optical absorption and few loss of energy etc. [17, 20–22]. Generally, CNTs can be modify using facile method from graphene and subsequently owing high flexible strength, very low density and high thermal and electrical conductivities [22, 24]. Therefore, CNTs materials are promising and guarantee with exciting surface properties and subsequently utilizable in several engineering applications including wastewater treatment applications. Since last few decades, the CNTs are widely applying for removal of ECs including pharmaceuticals as because of their enlarged surface area and porous structured [27]. To get highest performance of CNTs, different methods of wastewater treatment have been used including adsorption, ozonation and catalytic ozonation etc. [28].

Besides adsorption process, the advanced oxidation processes (AOPs) is mostly used methods for removal of pharmaceutical pollutants. Different AOPs method are applying including photocatalysis, ozonation and photocatalytic ozonation etc. [30, 31].

The aimed of this chapter was to explore the modification routes, advancement of functionalization of CNTs with other functional groups by reported works. The possible mechanistic insight of ECs removal reactions was also evaluated applying different methods of decontamination reported in the past studies. Herein, the future prospects and promising research potentials of CNTs based materials were also proposed for removal of ECs and ultimate environmental remediation. Therefore, considering adsorption efficiency as well as process cost, the CNTs are promising for the decontamination of water pollution including ECs from wastewater.

2. Surface properties of carbon nanotubes (CNTs)

Carbon having atomic number six (6) is an abundant chemical element sprawling on the earth surface as native or with others compounds [32]. Carbon occupy its four electrons as the tetravalent position can make covalent chemical bond and its atomic orbital pattern is 1s22s22p2 [33]. CNT one of carbon based material was invented by Sumio Iijima in 1991 applying arc-discharge method [34]. CNTs having hexagonal sheets of carbon atoms revolved up into hollow structure taking diverse helicities seamless of graphitic sheets. CNTs have exclusive strength because they are composing sp2 structure with stronger bonds rather than diamond having sp3 bonds. Some salient physical properties of CNTs are; BET surface area ranging among 90–350 m^2/g, density 1.7 g/cm^3, 15–30 μm length with tensile strength 150 GPa and purity 99% [27]. CNTs are promising nanostructured filler types materials for wastewater decontamination due to their exciting physical and chemical properties including high mechanical strength, high aspect ratio, high thermal conductivity, high electrical conductivity and electron emission, very good optical absorption and few loss of energy etc. [26–28].

3. Types of carbon nanotubes (CNTs)

CNTs are mainly two types, containing at least 2 layers of graphite sheets arranging between 4 and 30 nm in diameter and tabular shape of allotropes of carbon is denoted as multiwall carbon nanotubes (MWCNTs) while a single unified cylindrical closed by each of end graphene is defined as single-walled carbon nanotubes (SWCNTs) as seen in **Figure 3** [33]. Usually almost same thermal and electrical conductivities seem in both types of CNTs. The purity of SWCNTs is more than 70% and they can soluble in organic solvent but insoluble in aqueous while MWCNTs is more than 95% having aqueous solubility [28]. Generally, the length of MWCNTs are in between 30 and 50 nm of diameter and SWCNTs are in between 0.7 and 1.2 nm of diameter [28].

4. Synthesis routes of carbon nanotubes (CNTs)

Different sources of carbon are using to prepare the carbon nanotubes such as xylene, methane, acetylene, carbon monoxide ethylene and benzene etc. [35]. Widely applying synthesis routes of CNTs modification are including arc discharge, chemical vapor deposition and laser deposition methods [26]. All methods of CNTs modification has their own merits and demerits are presented in **Table 1**. At the very beginning of CNTs modification, the arc discharge method was used by Sumio Iijima in 1991. Basic principle of the arc discharge process CNTs preparation is applying 600 mbar of pressure using helium and argon as well as maximum 6000°C of temperature is generated by electric discharge for subsequent ejection of carbon atoms into plasma and consequently produced atoms deposited on the cathode [34]. On the other hand, laser tempted redirection of metallic elements and graphite mixture is being utilized in quartz tube based reactor at 2700–3200°C temperature for CNTs fabrication which
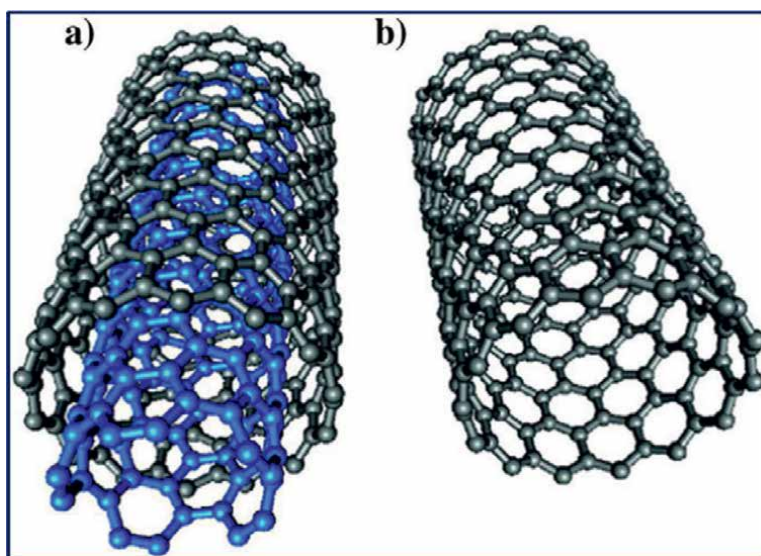
Figure 3.
(a) Multiwall carbon nanotubes (MWCNTs) and (b) single-walled carbon nanotubes (SWCNTs) [33].

CNTs synthesis route	Merits	Demerits	Refs.
Chemical vapor deposition	Low temperature, mass production, economically viable for large scale industrial production	Best method for MWCNTs but not suitable for SWCNTs	[36]
Arc discharge	Limited structural defect, simple method	High temperature, required, short nanotube, low production	[37]
Laser ablation	High purity, very few structural defects	Intensive cost and labor required	[38]

Table 1.
Some salient merits and demerits of different CNTs synthesis routs.

is denoted as laser ablation method [26–28]. The high temperature required in the process is the low rate of CNTs production is one of the constrains of synthesis route for the industrial production of CNTs. Nowadays, the chemical vapor deposition (CVD) is applying for mass production of CNTs at low temperature (600–1200°C) [34]. In this CVD method can produce large scale industrial CNTs at remarkable lower heat. Among other methods of CNTs preparation, the CVD is now widely use method due to the low temperature require, economically viable and mass production of CNTs [39–41].

5. Functionalization of carbon nanotubes (CNTs)

To enhance the surface properties and subsequent removal efficiency of pollutants CNTs can modified by coupling/wrapping with versatile functional groups [26]. Functionalization can improve the compatibility, solubility of CNTs and also overawed the complexity of dispersion. The CNTs materials can functionalized by non-covalent physical coupling or wrapping with other molecules by rounded over the tabular structure of CNT. On the other hand, CNTs can modified by chemical functionalities with new functional groups by covalent or chemical bonding with carbon atoms in the tubes of CNTs.

5.1 Covalent/chemical functionalization

Chemical functionalization of CNTs are usually using several techniques including acidic treatment, oxidation reactions and modification by using chemical in gaseous media. Wet functionalization applying acidic treatment on CNTs surface is mostly used method due to its dual benefit, firstly coupling with new functional groups and secondly possible sequestration of amorphous carbon and metal residuals. Generally, nitric acid (HNO_3), sulfuric acid (H_2SO_4), and piranha solution/hydrogen peroxide etc. are commonly using acids for acidic oxidation in presence of aqueous media of CNTs functionalization. Functionalization of CNTs surface by nitric acid is widely applied method due to better performance of functionalization. The functionalization CNTs using piranha solution can be dispersing in both polar no-polar media also can be attaching in both hydroxyl and carboxylic groups without deformation of sole structure of CNTs. Previous studies have been proved that, the acidic functionalization

can decrease contact angle among CNTs vertical angle and water from 176°C (hydro-phobic) to 25°C (hydrophilic). More wettability is occurring due to more oxygen containing functional groups on the surface of CNTs. The functionalization of CNTs surface without acidic treatment also reported in the literatures which called oxidation reactions without acids. Several previous studies reported that the oxidation reactions of CNTs surface functionalization is possible at lower oxygen content occurrence with slighter deformation of the honeycomb lattice. In this connection, Wepasnick et al. [27] was evaluated and compered the rate of CNTs oxidation using oxidizing chemical agents including ammonium per sulfate, potassium permanganate and hydrogen peroxide with nitric acid or sulfuric acid/nitric acid. The experiment was successfully illustrated that oxidation reactions can sufficiently decorate the surface of CNTs with abundant polar functional groups without acid treatment. Beside acidic and oxidation functionalization, another method was explored to oxidize CNTs using gaseous phase. This process assurances a significant reduction of waste release of the process and better homogenous functionalization than the acid based functionaliza-tion. For instance, Xia et al. [28] investigated the CNTs functionalization applying nitric acid vapor treatment in a gas-phase route and subsequently explored as 21% of oxygen containing functional groups on the surface of CNTs which is three-time higher efficiency than the use of conventional liquid nitric acid (7.9%).

5.2 Non-covalent/physical functionalization

It is proven that the chemical/covalent methods are more efficient to introduce functional groups on the surface of CNTs [26]. Conversely, the chemical function-alization has some disadvantages: (i) reduction of mechanical properties and dis-turbance of p-electron system of CNTs surface due to huge amount of lattice defects formed on the CNTs, and (ii) more chemical reactants requirement is not environ-mental friendly at all [26–28]. So that, to find alternative and cost effective method of CNTs functionalization is prime concerned and non-covalent process is the option concerning about prevention of structural damage of CNTs and make lesser process cost as well as invention of more environmental friendly approach. Polymer wrap-ping and physysortion interaction between chemical and CNTs are the main types of no-covalent functionalization of CNTs [26, 27]. Several chemical and non-covalent CNTs functionalization are reported in the previous research but all processes have their own advantages and disadvantages as listed in the **Table 2**.

Types of CNTs functionalization	Advantages	Disadvantages	Refs.
Chemical/ covalent	i. Highly efficient; ii. Decorate CNTs surface with functional groups; iii. No structural damage; iv. Both functionalization and removal of residuals are occurred;	Costly, huge reactants are required not environmental friendly, some cases high temperature required;	[27, 28]
Physical/ non-covalent	i. Dispersion allows on nanotubes; ii. No lattice damages; iii. Environmental friendly; iv. Low cost;	Low rate of efficiency, Low interaction rate between filler and matrix;	[27, 28]

Table 2.
Some advantages and disadvantages of different methods of CNTs functionalization.

6. CNTs for removal of ECs

6.1 Adsorptive removal of ECs

The adsorptive removal of ECs using CNTs are widely studied and subsequently finds high removal efficiencies due to large surface area and highly porous materials [27]. But some of constrains exists that including low rate of dispersion, small size and difficulties of separation of CNTs residuals from aquatic phase [26]. Therefore, researchers were modified the surface of CNTs with numerous functional groups for removal of ECs from contaminated environment [26–28].

Yu et al. [42] was developed a multi-walled carbon nanotubes (MWCNTs) and modified with different ratios of oxygen contents and subsequently applied for sequestration of tetracycline (TC) from wastewater. The study found that the maximum monolayer adsorption capacities were 269.25, 217.56, 217.8, and 210.43 mg/g for MWCNTs with 3.2, 4.7, 2.0, and 5.9% of oxygen, respectively. Another study by same author Yu et al. [43] was further evaluated the adsorption of ciprofloxacin antibiotic onto oxidize MWCNTs by introducing oxygen ratios from 2.0% to 5.9% and adsorption results were150.6, 178.9, 206.0, and 181.2 mg/g for MWCNTs with 2.0–5.9% of oxygen.

Zhang et al. [44] utilized the modified CNTs for removal of sulfamethoxazole. MWCNT was functionalized and adsorption sites was increased with improved surface properties due to more functional groups on the surface of CNTSs. The adsorption mechanism was proposed that the sulfamethoxazole absorption onto MWCNTs primly due to hydrogen bonding, electrostatic, π-π interactions and hydrophobic reactions. It was also proved that oxidization is the more facile method for introducing −OH and C=O groups on the surface of CNTs [44]. Peng et al. [45] was functionalized the MWCNT and SWCNTs for removal of ofloxacin and norfloxacin from wastewater. It was showed that the solubility of antibiotics and influence of functional groups were effected the adsorption rate, for instance, π-donor was increased due to OH group while, π-acceptor was increased due to C=O group [45].

Xu et al. [46] synthesized a core-shell CNTs based nanocomposite for the adsorption of 2-naphthol from aqueous solution applying fixed-bed column technique [46]. The excellent adsorption capacity was exposed for 2-naphthol adsorption onto CNTs nanocomposite [46]. Other study was utilized the modified CNTs with biochar namely CNT-SBC for removal sulfamethoxazole (SMX) from wastewater [47]. Modified materials were significantly improved their surface properties due to existence of CNTs subsequently gained better adsorption capacity. Generally, adsorption mechanism of ECs including antibiotics onto CNTs surface is mainly proposed by chemisorption and physisorption. The physical adsorptions were occurred by hydrogen bond, pore filling and valence force. On the other hand, chemical adsorption was proposed through electrostatic interaction and hydrophobic reactions as depicted the scheme in **Figure 4** [47].

Wang et al. [48] synthesized the functional SWCNTs and MWCNTs for the removal of triclosan as one of the personal care products and paracetamol as one of the drugs from water. The results were showed excellent adsorption capacity due to more functional groups present in the surface of CNTs and significantly allowed the wide range of solution pH from 4 to 10 [48]. So that, the CNTs materials are plying one of the promising nanostructured filler types materials for wastewater decontamination including ECs removal from the contaminated environment due to their exciting physical and chemical properties.
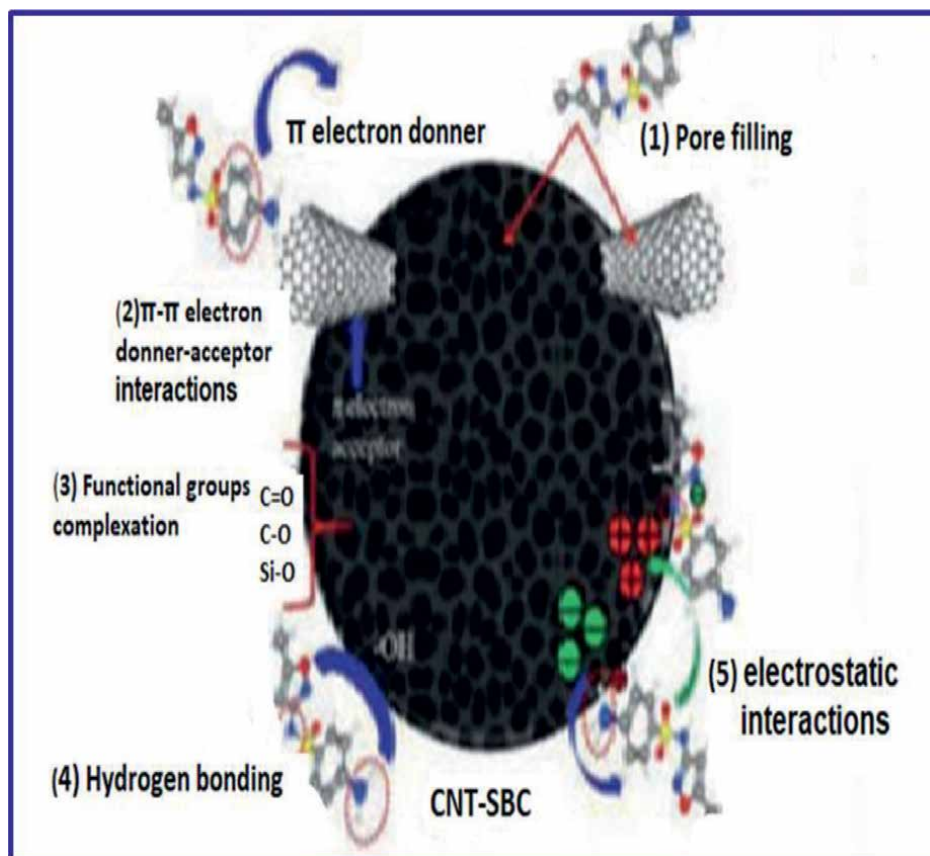
Figure 4.
Proposed adsorption mechanisms of ECs adsorption onto CNTs materials [47].

6.2 Catalytic degradation of ECs using CNTs

The previous studies reported that, the photocatalytic ozonation have gained great attention of scientists due to their degradation and mineralization efficiency of ECs and possibility of carbon dioxide production as the end product [30, 49]. Therefore, researchers are using this method for water treatment as well as for hydrogen production. Among other catalysts, the CNTs based materials are considering as good alternatives candidates for the degradation of ECs from the wastewater due to the large surface area, possibility of more functional groups attaching in edges of CNTs, and cost effective modification facility [27]. The photocatalytic ozonation process is producing high rate OH* radicals than the oxidation process due to more electrophilic nature of ozone than the oxygen to photogenerated electrons; hence, the faster and high rate of mineralization might be occurred in the photocatalytic ozonation process. The mechanism of photocatalytic ozonation is presenting in the following **Figure 5** [30].

Substantial number of studies reported that CNTs modified nanomaterials are promising catalyst for catalytic degradation of ECs. Some of studies were evaluated the degradation of sulfamethoxazole, oxalic acid [50, 51] and oxytetracycline (OTC) [52] applying photocatalytic ozonation. The studies explored that the rate
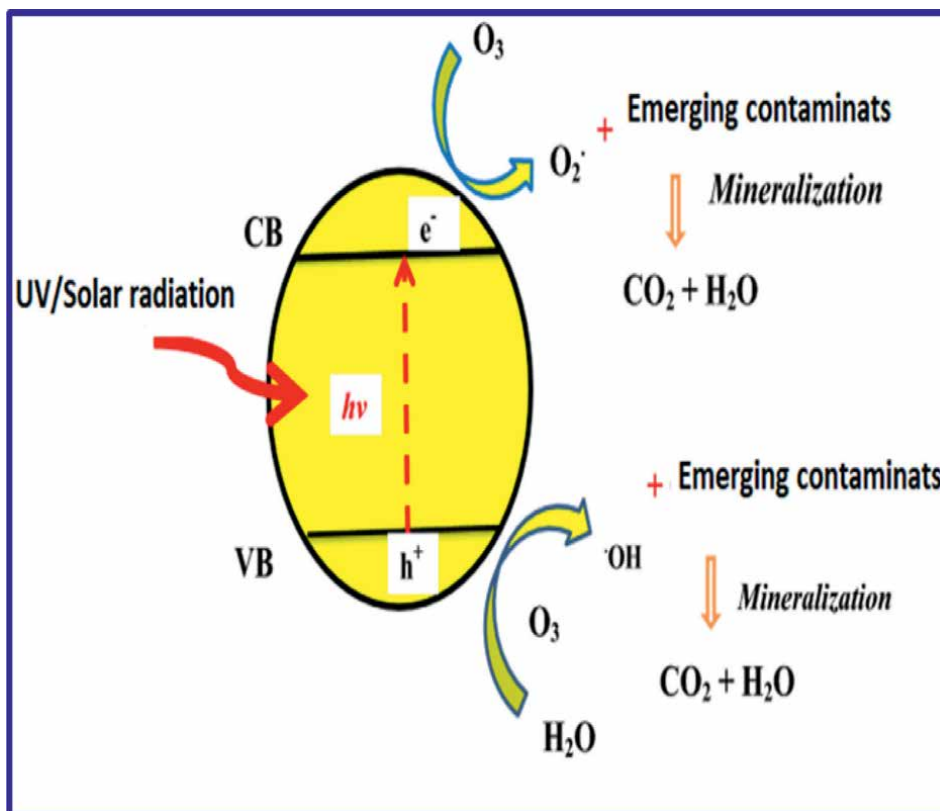
Figure 5.
Mechanism of photocatalytic ozonation process for degradation of ECs [30].

of degradations were higher than the conventional oxidation process even the literature agreed that the mineralization were higher while toxicity of MWCNTs/O_3 were scarcer than conventional catalytic reduction of ECs from water. The abundant functional groups available on the surface functionalized CNTs influence the effective degradation of ECs in the of photocatalytic ozonation process. Zhang et al. [53] investigated catalytic ozonation using CNTs to form ROS. The proposed mechanisms were mainly directed by the following paths (i) interphase "HO* zone" might be produced in the surface of CNTs by straight confronting of reactive sites on Material surface with ozone and (ii) ozone reduced into oxygen O_2 by influences of CNTs as seen in **Figure 6** [53].

Besides catalytic ozonation, CNTs modified materials can also be couple in a combined system with other technology and subsequently oxidation capacity may perhaps much higher due to synchronizing and synergistic effect on the degradation of ECs. Orge et al. [54] evaluated the oxamic acid (OMA) degradation applying a combined system using TiO_2-CNTs by ozonation and ultraviolet illumination consequent results showed OMA removal was much higher than other control system [54]. Other study explored that the carbon nanotubes can be utilize in the electrochemical filtration (ECF) as an anode with ozonation. The system was found effective synergistic reaction as well as more cost effective than the other oxidation process of ECs removal.
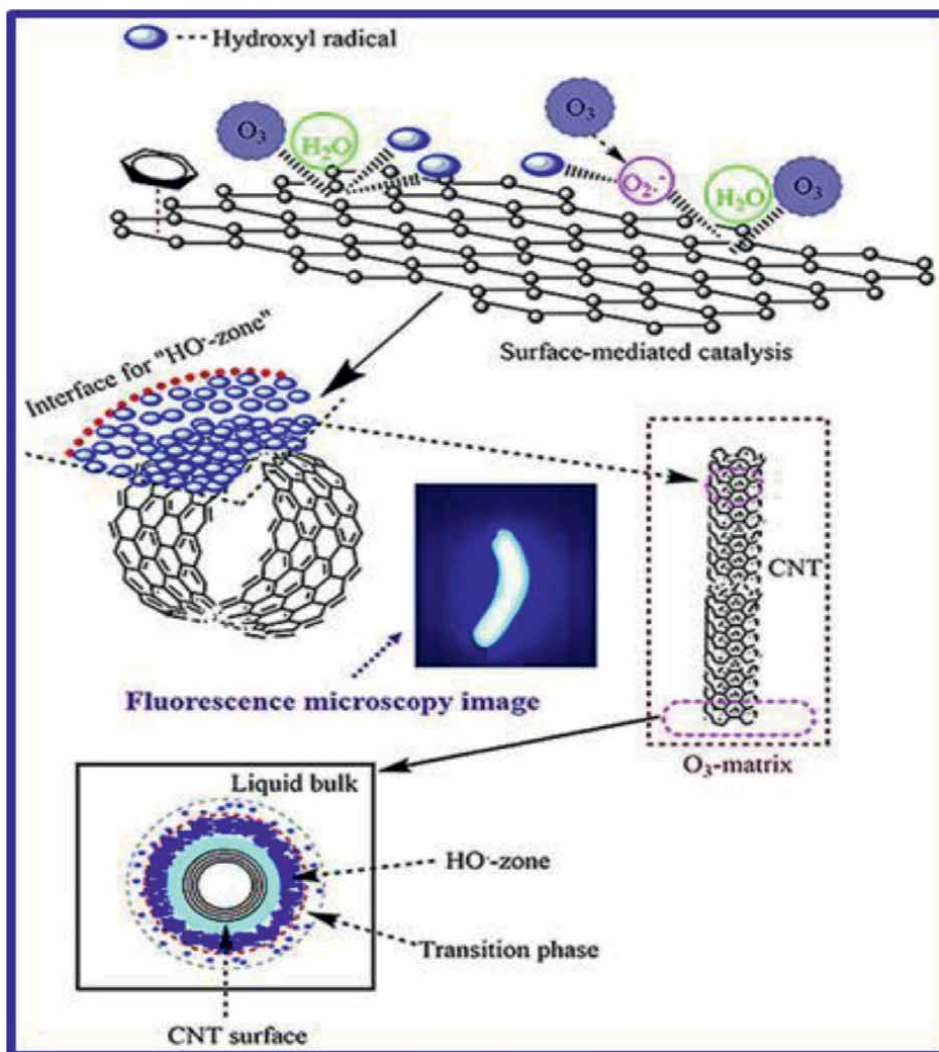
Figure 6.
Illustration of catalytic ozonation mechanism using CNTs based catalyst [53].

7. Conclusions

The ECs including pharmaceuticals and personal care products (PPCPs) are carrying in aquatic system with higher concentration beyond permissible limit, such kind of toxicants have severe impacts on human health and on other biotic components in the ecosystem. The traditional wastewater treatment plants are facilitating the sequestration of some known pollutants and suspended solids apart from emerging contaminants, which are not efficient for appropriately removal of some ECs including antibiotics due to their registrant and persistence nature in the environment. CNTs are widely applying for removal of ECs due to their enlarged surface area and porous structure. To enhance the surface properties and subsequent removal efficiency of pollutants CNTs can modified by coupling/wrapping with versatile

functional groups. Functionalization can improve the compatibility, solubility of CNTs and also overawed the complexity of dispersion. The adsorption mechanism of ECs including antibiotics onto CNTs surface is mainly reported by chemisorption and physisorption. The physical adsorptions were occurred by hydrogen bond, pore filling and valence force. On the other hand, chemical adsorption was proposed through electrostatic interaction and hydrophobic reactions.

Author details

Abu Taleb[1], Mohammed Naif Al-sharif[1], Mohammed Ali Al-mutair[1], Saleh Almasoudi[1], Osama Madkhali[2] and Mohammed Muzibur Rahman[3]*

1 Faculty of Meteorology, Department of Environmental Science, Environment and Arid Land Agriculture, King Abdulaziz University, Jeddah, Saudi Arabia

2 Department of Physics, College of Science, Jazan University, Jazan, Kingdom of Saudi Arabia

3 Faculty of Science, Department of Chemistry, King Abdulaziz University, Jeddah, Saudi Arabia

*Address all correspondence to: mmrahman@kau.edu.sa

IntechOpen

References

[1] Kumar R, Barakat MA, Taleb MA, Seliem MK. A recyclable multifunctional graphene oxide/SiO2@ polyaniline microspheres composite for Cu(II) and Cr(VI) decontamination from wastewater. Journal of Cleaner Production. 2020;**20**(268):122290

[2] Taleb MA, Kumar R, Al-Rashdi AA, Seliem MK, Barakat MA. Fabrication of $SiO_2/CuFe_2O_4$/polyaniline composite: A highly efficient adsorbent for heavy metals removal from aquatic environment. Arabian Journal of Chemistry. 2020;**13**(10):7533-7543

[3] Barakat MA, Kumar R, Balkhyour M, Taleb MA. Novel Al_2O_3/GO/halloysite nanotube composite for sequestration of anionic and cationic dyes. RSC Advances. 2019;**9**(24):13916-13926

[4] Kumar R, Barakat MA, Alseroury FA, Al-Mur BA, Taleb MA. Experimental design and data on the adsorption and photocatalytic properties of boron nitride/cadmium aluminate composite for Cr(VI) and cefoxitin sodium antibiotic. Data in Brief. 2020;**1**(28):105051

[5] Geissen V, Mol H, Klumpp E, Umlauf G, Nadal M, Van der Ploeg M, et al. Emerging pollutants in the environment: A challenge for water resource management. International Soil and Water Conservation Research. 2015;**3**(1):57-65

[6] Dey S, Bano F, Malik A. Pharmaceuticals and personal care product (PPCP) contamination—A global discharge inventory. In: Pharmaceuticals and Personal Care Products: Waste Management and Treatment Technology. Butterworth-Heinemann; 2019. pp. 1-26. Available from: https://www.sciencedirect.com/science/article/pii/B9780128161890000019

[7] Morin-Crini N, Lichtfouse E, Fourmentin M, Ribeiro AR, Noutsopoulos C, Mapelli F, et al. Removal of emerging contaminants from wastewater using advanced treatments. A review. Environmental Chemistry Letters. 2022;**12**:1-43

[8] Sivaranjanee R, Kumar PS, Saravanan R, Govarthanan M. Electrochemical sensing system for the analysis of emerging contaminants in aquatic environment: A review. Chemosphere. 2022;**31**:133779

[9] Varsha M, Kumar PS, Rathi BS. A review on recent trends in the removal of emerging contaminants from aquatic environment using low-cost adsorbents. Chemosphere. 2022;**1**(287):132270

[10] Khan S, Naushad M, Govarthanan M, Iqbal J, Alfadul SM. Emerging contaminants of high concern for the environment: Current trends and future research. Environmental Research. 2022;**207**:112609

[11] Mukhopadhyay A, Duttagupta S, Mukherjee A. Emerging organic contaminants in global community drinking water sources and supply: A review of occurrences, processes and removal. Journal of Environmental Chemical Engineering. 2022;**16**:107560

[12] Ahmad HA, Ahmad S, Cui Q, Wang Z, Wei H, Chen X, et al. The environmental distribution and removal of emerging pollutants, highlighting the importance of using microbes as a potential degrader: A review. Science of the Total Environment. 2022;**25**(809):151926

[13] Huff Chester A, Gordon C, Hartmann HA, Bartell SE, Ansah E, Yan T, et al. Contaminants of emerging concern in the Lower Volta River,

Ghana, West Africa: The agriculture, aquaculture, and urban development nexus. Environmental Toxicology and Chemistry. 2015;**41**(2):369-381

[14] Sahani S, Sharma YC, Kim TY. Emerging contaminants in wastewater and surface water. In: New Trends in Emerging Environmental Contaminants. Singapore: Springer; 2022. pp. 9-30

[15] Lee TH, Chuah J, Snyder SA. Occurrence of Emerging Contaminants in Southeast Asian Environments: Present Status, Challenges, and Future Prospects. ACS ES &T Watermark; 2022. p. 27. Available from: https://pubs.acs.org/doi/10.1021/acsestwater.1c00453

[16] Shaheen JF, Sizirici B, Yildiz I. Fate, transport, and risk assessment of widely prescribed pharmaceuticals in terrestrial and aquatic systems: A review. Emerging Contaminants. 2022;**2022**:22

[17] Rasheed T, Bilal M, Nabeel F, Adeel M, Iqbal HM. Environmentally-related contaminants of high concern: Potential sources and analytical modalities for detection, quantification, and treatment. Environment International. 2019;**1**(122):52-66

[18] Minamisawa H, Kojima Y, Aizawa M. Adsorption of inositol phosphate on hydroxyapatite powder with high specific surface area. Materials. 2022;**15**(6):2176

[19] Wang Y, Lin Z, Zhu J, Liu J, Yu J, Chen R, et al. Ultra-high flexibility amidoximated ethylene acrylic acid copolymer film synthesized by the mixed melting method for uranium adsorption from simulated seawater. Journal of Hazardous Materials. 2022;**15**(426):127808

[20] Fang Y, Ren G, Ma Y, Wang C, Li M, Pang X, et al. Adsorption and reutilization of Pb (II) based on

acid-resistant metal-organic gel. Separation and Purification Technology. 2022;**11**:121253

[21] Duarte ED, Oliveira MG, Spaolonzi MP, Costa HP, da Silva TL, da Silva MG, et al. Adsorption of pharmaceutical products from aqueous solutions on functionalized carbon nanotubes by conventional and green methods: A critical review. Journal of Cleaner Production. 2022;**24**:133743

[22] Nyairo WN, Shikuku VO, Sanou Y. Carbon nanotubes in water treatment: Progress and challenges. Innovative Nanocomposites for the Remediation and Decontamination of Wastewater. 2022;**2022**:171-184

[23] Adeyanju CA, Ogunniyi S, Selvasembian R, Oniye MM, Ajala OJ, Adeniyi AG, et al. Recent advances on the aqueous phase adsorption of carbamazepine. ChemBioEng Reviews. 2022;**2022**:19

[24] Ozkan A. Novel research on the use of Multi-Wall carbon nanotubes functionalized with copper oxide nanocomposite in the adsorptive desulphurization of crude oil: Laboratory research. ECS Journal of Solid State Science and Technology. 2022;**2022**:20

[25] Peng J, He Y, Zhou C, Su S, Lai B. The carbon nanotubes-based materials and their applications for organic pollutant removal: A critical review. Chinese Chemical Letters. 2021;**32**(5):1626-1636

[26] Ndlwana L, Raleie N, Dimpe KM, Ogutu HF, Oseghe EO, Motsa MM, et al. Sustainable hydrothermal and solvothermal synthesis of advanced carbon materials in multidimensional applications: A review. Materials. 2021;**14**(17):5094

[27] Lavagna L, Nisticò R, Musso S, Pavese M. Functionalization as a way to

enhance dispersion of carbon nanotubes in matrices: A review. Materials Today Chemistry. 2021;**1**(20):100477

[28] Rathinavel S, Priyadharshini K, Panda D. A review on carbon nanotube: An overview of synthesis, properties, functionalization, characterization, and the application. Materials Science and Engineering B. 2021;**1**(268):115095

[29] Kruusenberg I, Alexeyeva N, Kozlova J, Sammelselg V, Tammeveski K. Effect of purification of carbon nanotubes on their Electrocatalytic properties for ORR in acid solution. ECS Meeting Abstracts 2011, 1;31:1673

[30] Mecha AC, Chollom MN. Photocatalytic ozonation of wastewater: A review. Environmental Chemistry Letters. 2020;**18**(5):1491-1507

[31] Omar Ouda KM. Treated wastewater use in Saudi Arabia: Challenges and initiatives. International Journal of Water Resources Development. 2016;**32**(5):799-809

[32] Dai H. Carbon nanotubes: Opportunities and challenges. Surface Science. 2002;**500**(1-3):218-241

[33] Ebbesen TW. Carbon nanotubes. Annual Review of Materials Science. 1994;**24**(1):235-264

[34] Iijima S. Helical microtubules of graphitic carbon. nature. Nature. 1991;**354**(6348):56-58

[35] Akter M, Halawani RF, Aloufi FA, Taleb MA, Akter S, Mahmood S. Utilization of agro-industrial wastes for the production of quality oyster mushrooms. Sustainability. 2022;**14**(2):994

[36] Hou PX, Zhang F, Zhang L, Liu C, Cheng HM. Synthesis of carbon nanotubes by floating catalyst chemical vapor deposition and their applications. Advanced Functional Materials. 2022;**32**(11):2108541

[37] Aabir A, Naz MY, Shukrullah S. Synthesis of carbon nanotubes via plasma arc discharge method. In: Emerging Developments and Applications of Low Temperature Plasma. 2022. pp. 85-102. Available from: https://www.igi-global. com/chapter/synthesis-of-carbon-nanotubes-via-plasma-arc-discharge-method/294712

[38] Eskandari MJ, Araghchi M, Daneshmand H. Aluminum oxide nanotubes fabricated via laser ablation process: Application as superhydrophobic surfaces. Optics and Laser Technology. 2022;**1**(155):108420

[39] Anzar N, Hasan R, Tyagi M, Yadav N, Narang J. Carbon nanotube-a review on synthesis, properties and plethora of applications in the field of biomedical science. Sensors International. 2020;**1**(1):100003

[40] Prasek J, Drbohlavova J, Chomoucka J, Hubalek J, Jasek O, Adam V, et al. Methods for carbon nanotubes synthesis. Journal of Materials Chemistry. 2011;**21**(40):15872-15884

[41] Ikegami T, Nakanishi F, Uchiyama M, Ebihara K. Optical measurement in carbon nanotubes formation by pulsed laser ablation. Thin Solid Films. 2004;**457**(1):7-11

[42] Yu F, Ma J, Han S. Adsorption of tetracycline from aqueous solutions onto multi-walled carbon nanotubes with different oxygen contents. Scientific Reports. 2014;**4**(1):1-8

[43] Yu F, Sun S, Han S, Zheng J, Ma J. Adsorption removal of ciprofloxacin by multi-walled carbon nanotubes with

different oxygen contents from aqueous solutions. Chemical Engineering Journal. 2016;**1**(285):588-595

[44] Zhang D, Pan B, Wu M, Wang B, Zhang H, Peng H, et al. Adsorption of sulfamethoxazole on functionalized carbon nanotubes as affected by cations and anions. Environmental Pollution. 2011;**159**(10):2616-2621

[45] Peng H, Pan B, Wu M, Liu Y, Zhang D, Xing B. Adsorption of ofloxacin and norfloxacin on carbon nanotubes: Hydrophobicity-and structure-controlled process. Journal of Hazardous Materials. 2012;**30**(233):89-96

[46] Xu L, Wang S, Zhou J, Deng H, Frost RL. Column adsorption of 2-naphthol from aqueous solution using carbon nanotube-based composite adsorbent. Chemical Engineering Journal. 2018;**1**(335):450-457

[47] Ma Y, Yang L, Wu L, Li P, Qi X, He L, et al. Carbon nanotube supported sludge biochar as an efficient adsorbent for low concentrations of sulfamethoxazole removal. Science of The Total Environment. 2020;**718**:137299

[48] Wang Y, Zhu J, Huang H, Cho HH. Carbon nanotube composite membranes for microfiltration of pharmaceuticals and personal care products: Capabilities and potential mechanisms. Journal of Membrane Science. 2015;**479**:165-174

[49] Harafan A, Gafoor SA, Kusuma TD, Maliyekkal SM. Graphene modified Photocatalysts for the abatement of emerging contaminants in water. New Trends in Emerging Environmental Contaminants. 2022;**2022**:371-406

[50] Liu ZQ, Ma J, Cui YH, Zhao L, Zhang BP. Factors affecting the catalytic activity of multi-walled carbon nanotube for ozonation of oxalic acid.

Separation and Purification Technology. 2011;**78**(2):147-153

[51] Gonçalves AG, Órfão JJ, Pereira MF. Catalytic ozonation of sulphamethoxazole in the presence of carbon materials: Catalytic performance and reaction pathways. Journal of Hazardous Materials. 2012;**15**(239):167-174

[52] Agasti N, Gautam V, Pandey N, Genwa M, Meena PL, Tandon S, et al. Carbon nanotube based magnetic composites for decontamination of organic chemical pollutants in water: A review. Applied Surface Science Advances. 2022;**1**(10):100270

[53] Zhang S, Quan X, Zheng JF, Wang D. Probing the interphase "HO zone" originated by carbon nanotube during catalytic ozonation. Water Research. 2017;**122**:86-95

[54] Orge CA, Faria JL, Pereira MF. Removal of oxalic acid, oxamic acid and aniline by a combined photolysis and ozonation process. Environmental Technology. 2015;**36**(9):1075-1083

Chapter 8

Synthesis of Pt-Mo/WMCNTs Nanostructures Reduced by the Green Chemical Route and Its Electrocatalytic Activity in the ORR

Esther Torres-Santillan, Selene Capula-Colindres,
Gerardo Teran, Carmen M. Reza-San German,
Miriam Estrada Flores and Oscar Guadalupe Rojas Valencia

Abstract

Platinum (Pt) and molybdenum (Mo) nanoparticles were supported on multiwall carbon nanotubes (MWCNTs) by a green chemical route. Different relations of Pt:Mo (10:0, 8:2, 5:5, 2:8, and 0:10, respectively) in weight percent were compared to their electrocatalytic activity in the oxygen reduction reaction (ORR) in an acid medium. The morphologies and the structure were analyzed by X-ray diffraction (XRD), scanning electron microscopy (SEM), and transmission electron microscopy (TEM). The rotary disc electrode (RDE) and linear voltammetry (LV) techniques were employed to observe the electron transfer and mass transport phenomena. The surface activation of the samples was conducted by cyclic voltammetry (CV) technique According to the TEM analysis. The TEM analysis, shows that Mo and Pt nanoparticles have a good dispersion on the tubular carbon support, with sizes between 3.94 and 10.97 nm. All Pt-containing ratios had exhibited a first-order transfer in the ORR without inhibition of the reaction. Molybdenum is a reducing agent (oxyphilic metal) that benefits the adsorption of oxygenated species. The Pt:Mo 8:2 wt.% ratio presents the maximum benefits in the kinetic parameters. The Mo_{10}/MWCNTs nanostructure inhibits the ORR due to the strong bonds it presents with oxygen. Molybdenum at low concentrations with platinum is conducive to oxygen molecule adsorption-desorption by increasing the ORR's electroactivity.

Keywords: molybdenum, platinum, oxygen reduction, MWCNTs, oxyphilic metal

1. Introduction

It is widely recognized in the field of electrochemistry that there are many important electrochemical reactions. Some cases are the oxygen reduction reaction

(ORR) and the hydrogen oxidation reaction (HOR). These reactions can be set in the proton exchange membrane fuel cells (PEMFCs) for the generation and storage of clean energy [1–3]. ORR takes place at the cathode of the PEMFCs where it is highly sensitive to the surface of the electrode and the presence of adsorbed oxygenated species. As pointed out above, this is due to the stability of the oxygen molecule and the double bond, requiring a greater potential (1.23 V) to take place a reduction [4–7]. To obtain a high conversion at ORR, the catalyst Pt/C has been used for its high catalytic activity and chemical stability [8–10]. The previous properties of Pt induce a direct transfer of four electrons to form water, therefore presenting a first-order transfer. However, several investigations have reported a kinetic inhibition in the ORR by the adsorption of different pollutants (CO, SOx, and NOx) on the electrode surface, causing poisoning of the Pt catalysts [11, 12]. The commercial carbon support is a crucial factor in the deactivation of PEMFCs by its corrosion at high potentials (>0.5 V) [12–14]. Due to the high cost of Pt, various catalysts have been proposed, such as oxides [15, 16], carbides [17, 18], Pd [19, 20], binary, tri-metallic alloys (Pt, Ru, Pd, or Ir) [21–25], non-precious metals, and supercycles (porphyrins or phthalocyanines) [26, 27]. Despite the efforts made, it is difficult to replace the Pt as a catalyst in the cathode for the PEMFCs. It is because the catalyst should have good electrocatalytic activity and resistance for both CO and acid [28–30]. Furthermore, it must present efficient adsorption and desorption of oxygenated species in the interface electrode/ electrolyte. If the adsorption–desorption of oxygenated species is deficient in the OER, then there will not be a good electronic transfer, or desorption of species when the ORR is carried out.

Nepel et al. [31] and Mukerjee et al. [32] have found that molybdenum is a metal that allows greater tolerance to CO. Besides, Mo is used by biological systems mainly for its oxidative and reducing properties [33]. Additionally, it is used as a catalyst for desulfurization and denitrogenating processes in the petrochemical industry [34]. Molybdenum is an element with a "d" band characteristic in its electronic configuration. It can have different crystalline phases and superficial and electronic properties according to its geometric arrangements. It can be polymerized to form anionic poly-molybdates (Mo^{VI}), which present reactions of transfer of oxygen atoms to potential chemicals, less than 0.1 V. According to Pérez et al. [35] and Nikolaychuk et al. [36], these polymolybdates undergo redox reactions to potentials higher than 0.2 V. The molybdenum is one of the few affordable elements that act as a "source" of electrons and can transfer oxygen atoms to low potential values. These properties, electronics, and transference (adsorption–desorption) of oxygen atoms have not been widely investigated for the ORR in the acid medium [33, 37]. Another alternative of research to improving the electrocatalytic activity of the ORR is the study of various supports. Recent works performed by Hussain et al. [38] and Huang et al. [39] indicated that carbon in its allotropic tubular form has a greater specific area and chemical stability in the ORR than conventional commercial carbon. The CNTs (carbon nanotubes) have considerable advantages, including greater resistance to potentials greater than 0.5 V without generating CO. Efficient dispersion of the nanoparticles on the support, which generate a high activity, in comparison to the conventional carbon support [40–42].

This study aims to synthesize Pt-Mo/MWCNTs nanostructures by the wet impregnation method, produce different Pt-Mo loads in the nanostructures, achieve an elevated dispersion of the nanoparticles on the support (MWCNTs), conduct

an electrochemical work to determine the effect of the molybdenum content in the electroactivity for the ORR, examine the importance of the content of an oxyphilic metal such as molybdenum in a bimetallic catalyst for the ORR in an acidic medium, determine the best ratio of Pt-Mo to achieve the first-order mechanism without inhibition of the reaction, and finally, obtain the kinetics parameters and the type of electronic transference mechanism that takes place.

2. Experimental section

2.1 Synthesis of nanostructures

Commercially available MWCNTs synthesized by the method CVD (chemical vapor deposition, ≥97% purity) were used as support and acquired from Sigma-Aldrich. Commercial MWCNTs were pretreated by warming to reflux in a mixture of HNO_3 and H_2SO_4 (8 M) at 80°C for 3 h [43]. MWCNTs were thoroughly filtered and washed with deionized water, with subsequent drying on the stove for 24 h at 60°C. For the nanoparticles impregnation on the support, bis(acetylacetonate)dioxo-molybdenum [$MoO_2(CH_3COCH_2COCH_2)_2$, Sigma-Aldrich, 98% purity] and platinum acetylacetonate [$Pt(CH_3\text{-}COCHCO\text{-}CH_3)_2$, Sigma-Aldrich, 97% purity] were used as precursors. Different Pt-Mo relations were implemented to obtain 10 wt.% (10:0, 8:2, 5:5, 2:8, and 0:10, respectively). Pretreated MWCNTs support was set in a balloon flask with isopropanol and agitation of 900 rpm at 70°C for 1 h. Subsequently, the mixture of the precursors previously dissolved in isopropanol was added dropwise and stirred for 2 h until complete. A solution of eucalyptus extract (5 g/100 ml water) was added as a green reduction agent, and the mixture was stabilized with ethylene-glycol (EG). The solids were filtered, and the mixture was washed with deionized water. Eventually, the solids were dried at a temperature of 60°C. Consequently, the solids were placed in a quartz tube with a glass membrane and kept in an oven at 300°C for 30 minutes. At this step, a minimum flow of H2 for complete reduction.

2.2 Structural and morphological characterization

The crystalline structure and particle size were analyzed by X-ray diffraction (XRD) using an X-ray diffraction equipment, Siemens D5000 with a Cu-K α1 monochromatic radiation (λ = 1.548 A), operating at 40 kV and 40 mA at 10–90° 2θ range and a scan rate of 2°/s. The morphologies and chemical composition of the samples were determined by scanning electron microscopy (SEM) coupled with energy-dispersive spectroscopy (EDS) using a detector SEM-JEOL 6300. Transmission electron microscopy measurements were used to investigate the morphology, size, and dispersion of metal nanoparticles on MWCNTs. In this research, a Titan (FEI) microscope, operating at an accelerating voltage of 200 kV, was employed. The samples were prepared and deposited on the standard TEM sample grid covered with holey carbon film.

2.3 Electrochemical system

Oxygen reduction reaction activity was measured in a standard three-electrode system comprising a working electrode (RDE0008 commercial electrode), a

hydrogen reference electrode (ET070 Hydroflex), and a counter electrode (Pt coil). An electrolyte of 0.5 M H_2SO_4 was used. To prepare the catalyst ink, 1 mg of Pt-Mo/MWCNTs powder was weighed to which 75 µL of ethanol was added to disperse it. Afterward, 8 µL of a mixture of Nafion® liquid and ethanol (5 wt.%) were added as an adherent to the electrode and 15 µL of water. An ultrasonic bath was employed for 20 minutes to homogenize the catalyst ink. A 16 µL aliquot of the catalyst ink was then pipetted onto the glassy carbon disk of 0.19 cm^2 of the area. By applying the cyclic voltammetry technique with a scanning speed of 50 mV s^{-1}, the activation of the electrode is recorded between 0 and 1.2 V during 100 cycles in a solution of 0.5 M H_2SO_4 saturated with argon.

To obtain kinetic parameters, the technique of linear voltammetry in a range of potential from open circuit to 0 V in a cathode ray with a speed of 5 mVs^{-1} was collected at 100, 200, 400, 900, 1600 rpm on the disk in the oxygen-saturated electrolyte. The experimentation was performed at 25°C and an atmospheric pressure of 585 mmHg. A potentiostat-galvanostat Autolab PGSTAT302 was employed, and all reported voltages were referred to as the normal hydrogen potential (NHE).

3. Results and discussion

3.1 Morphological characterization of Pt-Mo/MWCNTs nanostructures

Figure 1(**a**)-(**f**) shows the XRD patterns of the MWCNTs support and Pt-Mo/MWCNTs nanostructures with different nominal ratios of Pt-Mo (0:0, 0:10, 2:8, 5:5, 8:2, and 10:0) wt.%. The large reflections at 2θ = 39.7°, 46.2°, 67.6°, and 81.4° are associated with the face-centered-cubic (*fcc*) Pt crystal structure corresponding to the (111), (200), (220), and (311) planes, respectively, according to (PDF 04-0802). The reflection at 2θ = 26.2° corresponds to a crystal plane (002) of the hexagonal graphite structure (PDF 056-0159). Reflections of Pt in Pt-Mo/MWCNTs nanostructures shift slightly to higher angles compared with those of Pt in Pt/MWCNTs, which is evidence of lattice contraction caused by alloying Pt-Mo. The extent of lattice contraction increases to increase Mo content, in Pt-Mo/MWCNTs nanostructures, as shown by the lattice listed in **Table 1**. Previous research shows that lattice contraction is an indication of partial substitution of Mo for Pt in the Pt lattice [44–46]. The particle sizes of Pt were calculated with Scherrer equation, on (200) for reflection are not affected by MWCNTs support. Pt particle size was between 3.78 and 6.18 nm. The intensity of the Pt reflection gradually increases with a higher Pt content and broadens further in the XRD patterns indicating a smaller particle size. This behavior can be attributed to the high mobility of metal nanoparticles on carbon nanotube surfaces due to weak interaction between metal and support [47].

Figure 2(**a**-**f**) shows TEM micrographs of Mo_{10}/MWCNTs, Pt_2Mo_8/MWCNTs, Pt_5Mo_5/MWCNTs, Pt_8Mo_2/MWCNTs, and Pt_{10}/MWCNTs nanostructures. The images reveal nanoparticles evenly distributed on the MWCNTs surface. The shape of Mo nanoparticles is elongated with an average particle size of 10.97 nm (**Figure 2a**). All the nanostructures with Pt exhibited a circular shape with an average size for the nanoparticles between 3.94 and 6.96 nm (**Figure 2b**-**d**, **f**). The particle dimensions measured by TEM are consistent with the average size determined from the corresponding XRD patterns. In the Pt_8Mo_2/MWCNTs nanostructure, the size in TEM images is slightly larger. High-resolution transmission electron microscopy (HR-TEM) images of the Pt_8Mo_2/MWCNTs revealed their crystalline nature (Inset **Figure 2e**).
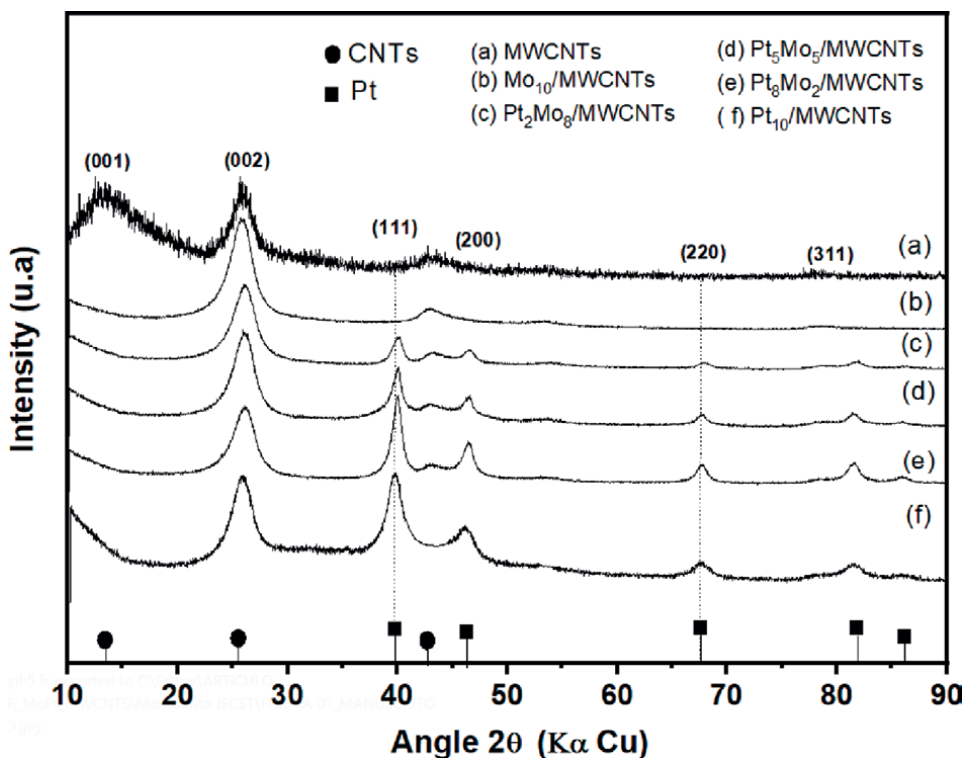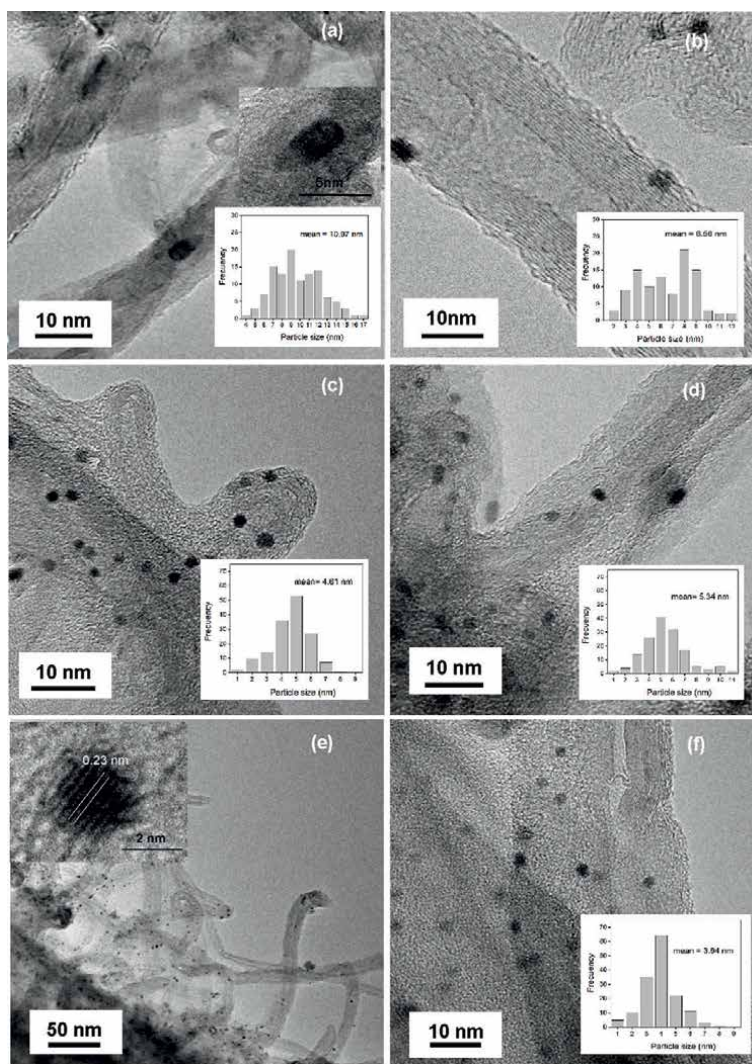
Figure 1.
XRD patterns of MWCNTs and Pt-Mo/MWCNTs nanostructures.

Nanostructures	Pt:Mo atomic Ratio		Lattice Parameter	Particle size by XRD
	Nominal	EDS	Å	(nm)
Mo10/MWCNT	100	83	—	—
Pt2-Mo8/MWCNTs	20:80	24:76	3.805	6.18
Pt5-Mo5/MWCNTs	50:50	53:46	3.908	4.61
Pt8-Mo2/MWCNTs	80:20	83:17	3.913	5.54
Pt10/MWCNTs	100	92	3.985	3.78

Table 1.
Data obtained from XRD-EDS analysis.

The spacing between adjacent lattice planes is around 0.23 nm, corresponding to (111) plane of *fcc* structure Pt [44]. For the inset (HR-TEM) image of the Mo_{10}/MWCNTs nanostructure, there is no d-spacing lattice of metallic Mo, Mo oxide, or Mo carbide structure.

Images of Pt_{10}/MWCNTs and Pt_5Mo_5/MWCNTs obtained by SEM are displayed in **Figure 3(a-b)**. The tubular structure of MWCNTs support can be observed in these images. The average diameter of an MWCNT is within 20–30 nm. EDS spectrum shows the presence of Mo and Pt in the structure (**Figure 3c-d**). The elemental chemical composition of Mo and Pt is also provided in **Table 1**. The atomic ratios of Pt

Figure 2.
TEM micrographs (a) Mo10/MWCNTs, (b) Pt2Mo8/MWCNTs, (c) Pt5Mo5/MWCNTs, (d-e) Pt8Mo2/ MWCNTs, and (f) Pt10/MWCNTs.

and Mo are close to nominal composition, suggesting the effective reduction of Pt and Mo by the impregnation method used.

3.2 Electrochemistry characterization

Cyclic voltammograms of Mo_{10}/MWCNTs, Pt_2Mo_8/MWCNTs, Pt_5Mo_5/MWCNTs, Pt_8Mo_2/MWCNTs, and Pt_{10}/MWCNTs nanostructures are graphically presented in **Figure 4**. The samples with 5, 8, and 10 wt.% of Pt manifested a typical behavior of an electrode with this material in an acid medium [9, 40]. The area associated with the adsorption–desorption of protons is presented in the region from 0 to 0.30 V/ NHE for all nanostructures. The samples containing Pt_{10} and Pt_2Mo_8 present a peak more intense in the previous zone, it is indicating greater performance in the
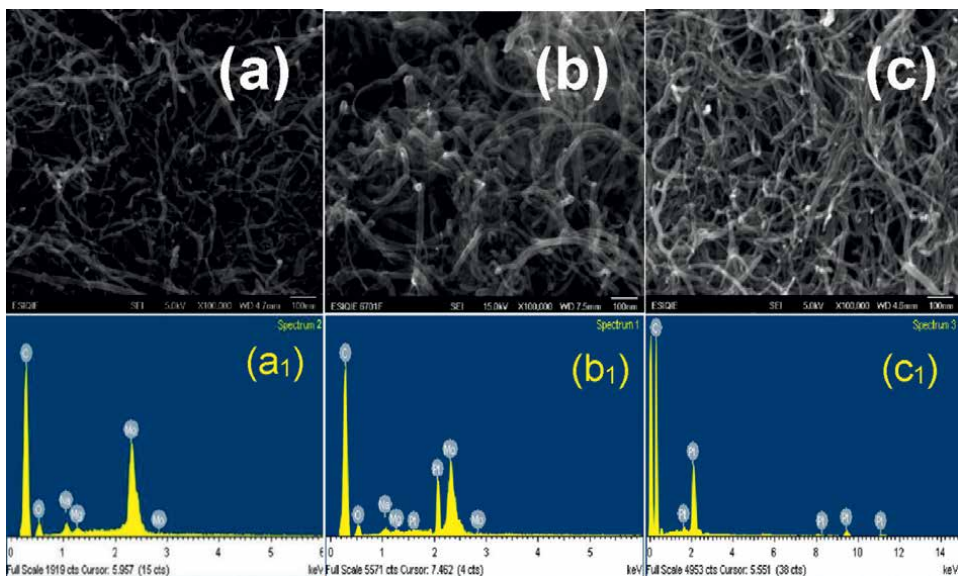
Figure 3.
SEM-EDS imaging of (a-a1) Mo10/MWCNTs and (b-b1) Pt5Mo5/MWCNTs and (c-c1) Pt10/MWCNTs samples.
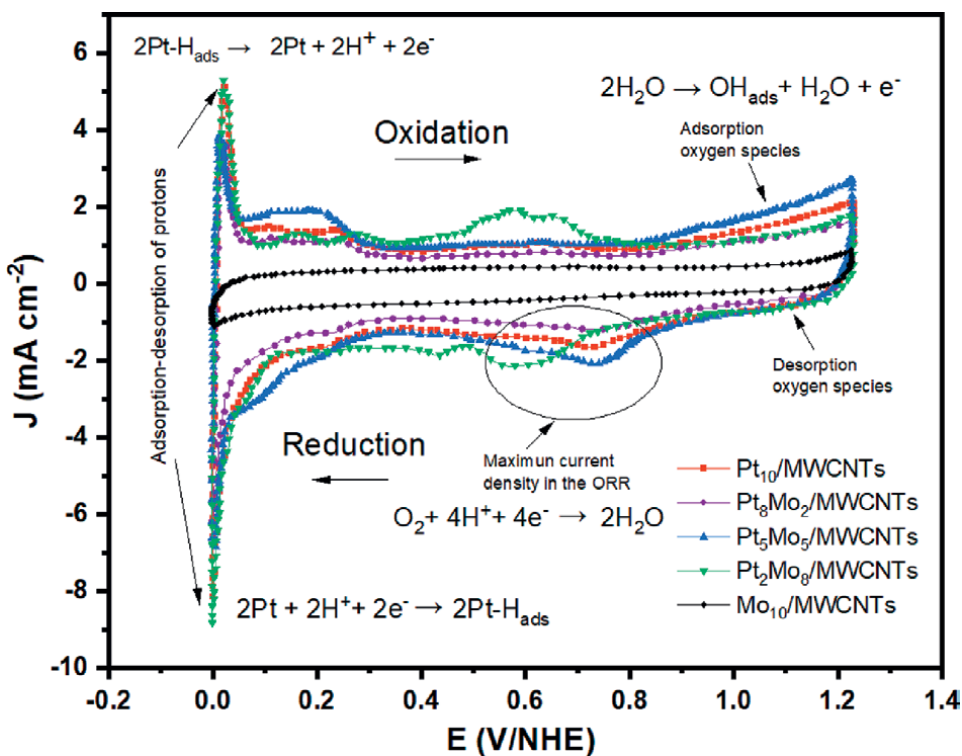
Figure 4.
Cyclic voltammetry Pt-Mo/MWCNTs nanostructures (sweep speed 50 mVs^{-1}, 25°C, last cycle).

hydrogen evolution reaction and the hydrogen oxidation reaction (HOR). According to Grgur et al. [48], the mechanism for interaction of oxygenated species with bimetallic surfaces must contain a metal capable of dissociating hydrogen and a metal that forms strong $M - O$ bonds. The high activity of Pt for the hydrogen oxidation reaction is attributed to its ability to dissociate hydrogen as presented in Eq. (1).

$$2Pt + 2H_{ads} \rightarrow 2Pt + 2H^+ + 2e^- \tag{1}$$
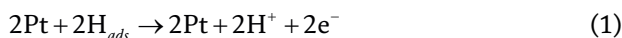
In the case of the Pt_2Mo_8/MWCNTs nanostructure, the high selectivity for HOR is attributed to the interaction between the OH^- group with the oxyphilic metal (Mo) and the Pt nanoparticles that provide active sites for hydrogenation as indicated by the following Eq. (2) [47]:

$$2Pt + Mo - OH \rightarrow Pt + M + H^+ + e^- \tag{2}$$
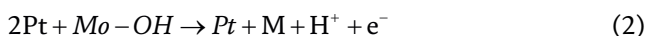
Nakajama and Kita [49] found that the redox couple of Mo^{+2}/Mo^{+3} plays a key role in the enhancement of the catalytic activity of the Pt electrode at low overpotentials. Mo shifts the oxidation of weakly adsorbed OH^- to lower potentials, and therefore, the co-catalytic effect of Pt can set in. The anodic sweep to a greater potential of 0.51 V starts with the adsorption of oxygenated species. The Pt_2Mo_8/MWCNTs nanostructure presents more adsorption of oxygenated species between a potential of 0.51 and 0.66 V. According to the Pourbaix diagram of Mo, at that condition, it forms intermediates mainly oxide species as MoO^{+2}; $MoO2$; $Mo4O11$; $Mo8O23$; $Mo9O26$; $MoO3$ and produces a protective oxide film on the metal surface [36]. The adsorption of OH^- and of different oxide species formed on the working electrode surface of the Pt-Mo/MWCNTs nanostructures arises after 0.8 V/NHE. The Pt_5Mo_5/MWCNTs present more adsorption of oxygenated species, from 0.8 to 1.2 V/NHE.

In the cathodic sweep, oxides and their desorption reduction begin approximately at 1.0 V/NHE. All samples reach a maximum current density between 0.71 and 0.63 V/NHE for the ORR. Pt_5Mo_5/MWCNT and Pt_2Mo_8/MWCNTs exhibited a greater oxygen reduction reaction. **Figure 4** confirms this behavior due to the highest intensity in the peak. The oxygen reduction takes place to low potential (0.63 V) by the Pt_2Mo_8/MWCNTs nanostructure. Finally, the capacitive zone is observed in a potential range of 0.35 at 0.45 V, an area without adsorbed or desorbed chemical species. In the case of cyclic voltammogram for the sample Mo_{10}/MWCNTs, it was no observed electrocatalytic activity in the ORR. This is confirmed by the low current density presented and by the absence of peaks in the redox processes at different voltage values. The absence of electroactivity of the Mo/MWCNTs nanostructure is attributed to the high affinity of Mo to oxygenated species (Mo-O bond of 607 bond strength kJ mol^{-1}) [50]. The strong adsorption causes the electrode surface to be saturated with too many layers of oxygenated chemical species inhibiting the reaction [51]. Therefore, it is important to include al Mo in bimetallic or trimetallic alloys in an adequate amount for the ORR.

Figure 5(**a-e**) presents polarization curves obtained by the linear voltammetry technique with different rotation speeds of the different Pt-Mo/MWCNTs nanostructures. Lineal voltammetry of relationships Pt_{10}, Pt_8Mo_2, Pt_5Mo_5, and Pt_2Mo_8 (**Figure 5a-d**) presents a stable behavior in the region I (0.98–0.864 V). In this region, I, the reaction's

speed is controlled by the electronic transfer [52]. Region III is a diffusion zone controlled by mass transport, which is observed at a less positive potential. In this region, there is an influence on the speed of rotation of the electrode. The well-defined horizontal plateaus whose density of current increases as the electrode rotation speed increases indicates a good distribution of active sites and a correct diffusion of oxygen on the surface of the electrode [5, 53]. Region II is a mixed zone, presenting an electronic and mass transference. Linear voltammetry of **Figure 5(e)** confirms that the nanostructure
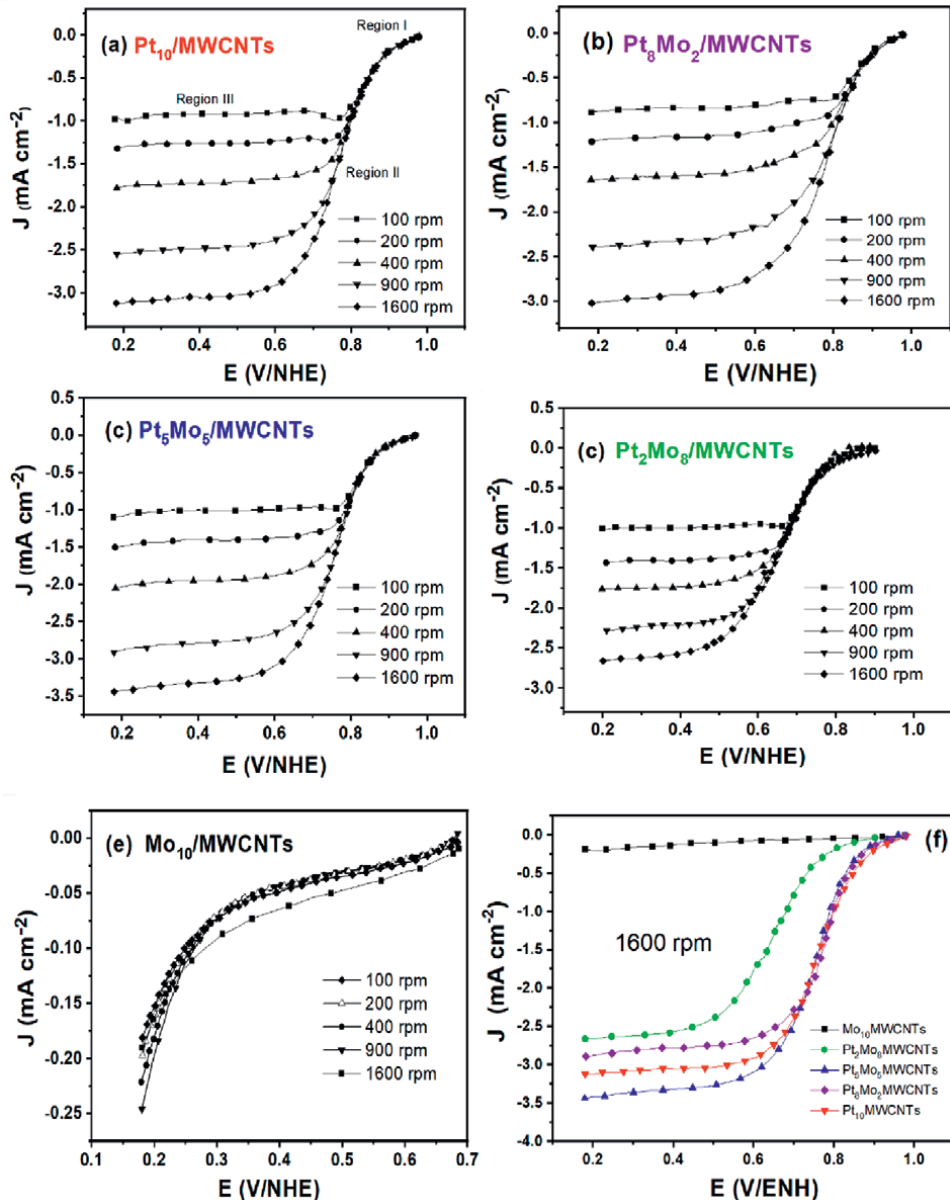

Figure 5.
(a-e). Lineal voltammetry of Pt10/MWCNTs, Pt8Mo2/MWCNTs, Pt5Mo5/MWCNTs, Pt2Mo8/MWCNTs, and Pt10/MWCNTs. (f) Lineal voltammetry comparative at 1600 rpm.

Mo_{10}/MWCNTs does not present electrocatalytic activity in the ORR, because it presents a minimum current density for the different curves. Furthermore, there is an absence of the three control zone characteristics of the ORR. There is no influence by the rotation speed of not presenting the horizontal plateaus that define this type of diffusion. So, in this sample, there is no transfer control of mass.

The electrochemical activity of the five nanostructures is compared through the RDE to 1600 rpm, analysis, see **Figure 5(f)**. The best performance of nanostructures at 1600 rpm, in descending form, is found as follows: $Pt_5Mo_5 > Pt_{10} > Pt_8Mo_2 > Pt_2Mo_8 > Mo_{10}$ with its highest current densities of −3.45, −3.3, −3.2, −2.4, and − 0.25 mA cm^2, respectively. The most negative value of the current density is attributed to the smaller particle size of Pt-Mo and a better dispersion on the MWCNT support [54].

Partial slopes of Tafel are depicted in **Figure 6**. The current response is reported in a low range of potential (0.75–0.95 V/NHE), where a linear relation of potential (V) versus log kinetic current density (J_k) is appreciated.

Table 1 summarizes the kinetic parameters for the ORR. Tafel slope values between 60 and 120 mVdec^{-1} showed that ORR catalyzed by Pt-Mo/MWCNTs nanostructures follows a four-electron reduction path to produce water molecules. Representing the well-known reaction of oxygen electro-reduction in an acid solution, it can be written as follows Eq. (3):

$$O_{2ads} + 4H^+ + 4e^- \rightarrow H_2O \qquad (3)$$

For a fuel cell (PEMFC), the reaction must take place by the previous path since sometimes it can present peroxides as reaction intermediaries that damage the components of the fuel cells device [55]. To quantitatively determine the percentage of peroxide formed should complement the study with other techniques such as the mass spectrophotometer and impedance, which are not within the scope of this work.
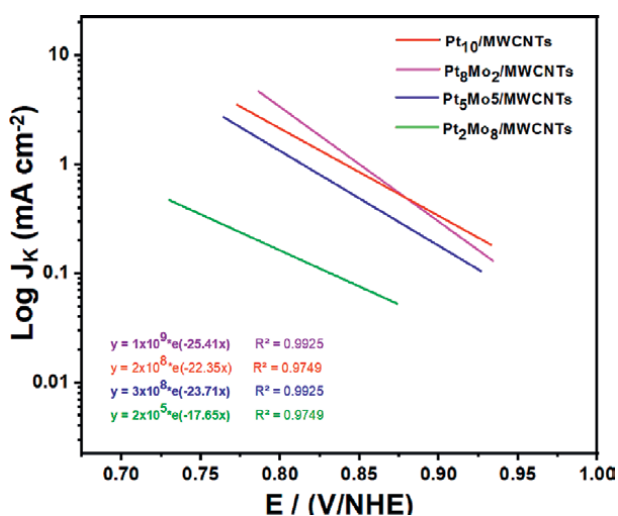
Figure 6.
Partial slopes of Tafel of Pt2Mo8/MWCNTs, Pt5Mo5/MWCNTs, Pt8Mo2/MWCNTs, and Pt10/MWCNTs nanostructures for ORR.

Catalysts	E_{oc} [V/NHE]	b [Vdec−1]	α	j_0 [mAcm−2]	E [V/NHE] to a current of 1 mAcm−2	η overpotential [V/NHE]
Pt10/MWCNTs	0.981	−0.102	0.577	1.23×10^{-4}	0.940	0.249
Pt8Mo2/MWCNTs	0.984	−0.092	0.648	5.58×10^{-5}	0.942	0.246
Pt5Mo5/MWCNTs	0.967	−0.097	0.609	5.70×10^{-5}	0.920	0.263
Pt2Mo8/MWCNTs	0.864	−0.129	0.456	6.87×10^{-5}	0.820	0.336
Mo10/MWCNTs	0.680	—	—	—	—	0.550

Table 2.
Kinetic parameters for the ORR.

When the kinetic parameters are measured for the ORR (**Table 2**), a comparison of the open circuit potential (E_{oc}) with concern to a specific current is obtained. The Pt_8Mo_2/MWCNTs nanostructure presented a potential (0.984 V) closer to the reference potential (1.23 V) with better performance.

In the column of E [V/NHE], the potential is reported to a current density of 1 mA cm^{-2}, confirming that the Pt_8Mo_2/MWCNTs nanostructure is the one that presents the greatest potential that is 0.942 V/NHE. Pt_{10}/MWCNTs nanostructure has similar behavior (0.940 V/NHE). Exchange currents and transfer coefficients are qualitative values and are in the range of platinum catalysts for the ORR [56]. The Pt_8Mo_2/MWCNTs showed a lower slope of Tafel, with a potential value of −0.092 V indicating a mechanism of first order [56, 57]. This means a formation of O_2 directly to the water with a lower potential value (E) of 0.920 V but very close to that obtained with the nanostructure from Pt_5Mo_5/MWCNTs, (−0.097 V) with the advantage of reducing the Pt amount of 50 wt.% in the nanostructure. Additionally, the Pt_8Mo_2/MWCNTs nanostructure has the lowest overpotential concerning 1.23 V required in the oxygen reduction reaction with a value of 0.246 V. The nanostructures of Pt_2Mo_8/MWCNTs and Mo_{10}/MWCNTs require a higher overpotential of 0.354–0.550 V, indicating a different mechanism of four electrons in the ORR.

Mo_{10}/MWCNTs nanostructure could not obtain the kinetic parameters since it does not present electrocatalytic activity toward the ORR. Exchange currents (j_o) and the transference coefficients (α) are qualitative values closing for Pt_5Mo_5/MWCNTs and Pt_{10}/MWCNTs samples. Their catalytic activity is in the range of platinum catalysts for the ORR.

4. Conclusions

Synthesis of Pt-Mo/MWCNTs nanostructures by a green chemical route was presented. The Pt-Mo/MWCNTs with different ratios Pt:Mo were structurally and morphologically characterized, obtaining particle sizes between 3.94 and 10.97 nm by the TEM technique. Particle size and good dispersion are important factors in the performance of an electrocatalytic activity in the ORR. Molybdenum is a reducing

agent (oxyphilic metal) that benefits the adsorption of oxygenated species. The Pt:Mo 8:2 wt.% ratio presents the maximum benefits in the kinetic parameters. The Mo_{10}/MWCNTs nanostructure inhibits the ORR due to the strong bonds it presents with oxygen. Molybdenum at low concentrations with platinum is conducive to the adsorption–desorption of oxygen molecules by increasing the electroactivity in the ORR. Concerning Pt_8Mo_2, it can improve the electrocatalytic activity closer to the response of the catalyst Pt_{10}/MWCNTs with a transference of first order and without inhibition of the reaction. According to the slopes of Tafel obtained in this work for all Pt-Mo/MWCNTs nanostructures, the main stage of the reaction is the transference of the first electron from the electrode to the oxygen molecule adsorbed on the surface of the electrode. The mechanism found is of four electrons for the nanostructures with Pt_{10}, Pt_5Mo_5, Pt_2Mo_8 content; however, for the Pt_8Mo_{10} and Mo_{10} samples, a deeper study will have to be done to determine it.

Acknowledgements

Author details

Esther Torres-Santillan[1]*, Selene Capula-Colindres[2,3], Gerardo Teran[1,3], Carmen M. Reza-San German[1], Miriam Estrada Flores[1] and Oscar Guadalupe Rojas Valencia[1]

1 Departamento de Ingeniería Química, CDMX, México

2 Centro de Investigación en Computación, CDMX, México

3 Departamento de Metalurgia, CDMX, México

*Address all correspondence to: estorress@ipn.mx

IntechOpen

References

[1] Dresselhaus MS, Thomas IL. Alternative energy technologies. Nature. 2001;**414**:332-337. DOI: 10.1038/35104599

[2] Su H, Felix C, Barron O, Bujilo P, Blandergroen B, Pollet B, et al. High-performance and durable membrane electrode assemblies for high-temperature polymer electrolyte membrane fuel cells. Electrocatalysis. 2014;**5**(4):361-371. DOI: 10.1007/s12678-014-0202-5

[3] Kuzume A, Herrero E, Feliu JM. Oxygen reduction on stepped platinum surfaces in acidic media. Journal of Electroanalytical Chemistry. 2007;**599**(2):333-343. DOI: 10.1016/j.jelechem.2006.05.006

[4] Hongchao Y, Yejun Z, Feng H, Qiangbin W. Urchin-like CoP nanocrystals as hydrogen evolution reaction and oxygen reduction reaction dual-electrocatalyst with superior stability. Nano Letters. 2015;**15**(11):7616-7620. DOI: 10.1021/acs.nanolett.5b03446

[5] Pozio A, Giorgi L, Antolini E, Passalacqua E. Electroxidation of H_2 on Pt/C Pt–Ru/C and Pt–Mo/C anodes for polymer electrolyte fuel cell. Electrochimica Acta. 2000;**46**:555-561

[6] Anderson AB, Cai Y, Sidik RA, Kang DB. Advancements in the local reaction center electron transfer theory and the transition state structure in the first step of oxygen reduction over platinum. Journal of Electroanalytical Chemistry. 2005;**580**(1):17-22. DOI: 10.1016/j.jelechem.2005.03.009

[7] Kundu PP, Dutta K. Hydrogen fuel cells for portable applications.

In: Compendium of Hydrogen Energy. Vol. 4. Woodhead Publishing (Elsevier); 2016. pp. 111-131

[8] Bing Y, Liu H, Zhang L. Nanostructured Pt-alloy electrocatalysts for PEM fuel cell oxygen reduction reaction. Chemical Society Reviews. 2010;**39**(6):2184-2202

[9] Wang H, Macomber C, Christ J, Benser G, Pivovar B, Dinh HN. Evaluating the influence of PEMFC system contaminants on the performance of Pt catalyst via cyclic voltammetry. Electrocatalysis. 2014;**5**(1):62-67. DOI: 10.1007/s12678-013-0159-9

[10] Mao L, Jackson L, Davies B. Investigation of PEMFC fault diagnosis with consideration of sensor reliability. International Journal of Hydrogen Energy. 2018;**43**(35):16941-16948. DOI: 10.1016/j.ijhydene.2017.11.144

[11] Park IS, Tong YYJ. Sulfide-Adsorption enhanced oxygen reduction reaction on carbon-supported Pt electrocatalyst. Electrocatalysis. 2013;**4**(3):117-122. DOI: 10.1007/s12678-013-0132-7

[12] Fernandes AC, Paganin VA, Ticianelli EA. Degradation study of Pt-based alloy catalysts for the oxygen reduction reaction in proton exchange membrane fuel cells. Journal of Electroanalytical Chemistry. 2010;**648**:156-162. DOI: 10.1016/j.jelechem.2010.07.013

[13] Shao M, Chang Q, Dodelet J-P, Chenitz R. Recent advances in electrocatalysts for oxygen reduction reaction. Chemical Reviews. 2016;**16**:3594-3657. DOI: 10.1021/acs.chemrev.5b00462

[14] Sharma S, Pollet BG. Support materials for PEMFC and DMFC electrocatalysts—A review. Journal of Power Sources. 2012;**208**:96-119

[15] Dong Y, Xue Y, Gu W, Yang Z, Xu G. MnO_2 nanowires/CNTs composites as efficient non-precious metal catalyst for oxygen reduction reaction. Journal of Electroanalytical Chemistry. 2019;**837**(15):55-59. DOI: 10.1016/j.jelechem.2019.02.012

[16] Delmondo L, Salvador GP, Muñoz JA, Sacco A, Garino N, Castellino M, et al. Nanostructured MnxOy for oxygen reduction reaction (ORR) catalysts. Applied Surface Science. 2016;**338**(B):631-639. DOI: 10.1016/j.apsusc.2016.03.224

[17] Yufei M, Guoqing G, Xiaogang H, Ji C, Abuliti A. Molybdenum carbide as alternative catalyst for hydrogen production – A review. Advanced Materials Research. 2017;**75**:1101-1129. DOI: 10.1016/j.rser.2016.11.092

[18] Zhang X, Shi C, Chen B, Kuhn AN, Ma D, Yang H. Progress in hydrogen production over transition metal carbide catalysts: Challenges and opportunities. Current Opinion in Chemical Engineering. 2018;**20**:68-77. DOI: 10.1016/j.coche.2018.02.010

[19] Liu J, Sun CQ, Zhu W. Origin of efficient oxygen reduction reaction on Pd monolayer supported on Pd-M (M= Ni, Fe) intermetallic alloy. Electrochimica Acta. 2018;**282**(20):680-886. DOI: 10.1016/j.electacta.2018.06.041

[20] Shao M, Yu T, Odell JH, Xia Y. Structural dependence of oxygen reduction reaction on palladium nanocrystals. Chemical Communications. 2011;**47**(23):6566-6568

[21] Nekooi P, Amini MK. Effect of support type and synthesis conditions on the oxygen reduction activity of Ru*x*Se*y* catalyst prepared by the microwave polyol method. Electrochimica Acta. 2010;**55**(9):3286-3294. DOI: 10.1016/j.electacta.2009.12.102

[22] Patel PR, Kuruba R, Damodaran K, Jampani P, Gattu B, Shanthi PM, et al. Noble metal-free bifunctional oxygen evolution and oxygen reduction acidic media electro-catalysts. Scientific Reports. 2016;**6**(28367):1-14. DOI: 10.1038/srep28367

[23] Luo J, Yin J, Loukrakpam R, Wanjala BN, Fang B, Shan S, et al. Design and electrochemical characterization of ternary alloy electrocatalysts for oxygen reduction reaction. Journal of Electroanalytical Chemistry. 2013;**688**:196-206. DOI: 10.1016/j.jelechem.2012.09.032

[24] Zagal JH. Handbook of Fuel Cells - Fundamentals Technology and Applications2003. pp. 545-554

[25] Nguyet NAT, Shim JH. Facile one-step synthesis of Ir-Pd bimetallic alloy networks as efficient bifunctional catalysts for oxygen reduction and oxygen evolution reactions. Journal of Electroanalytical Chemistry. 2018;**827**(15):120-127. DOI: 10.1016/j.jelechem.2018.09.012

[26] Jahan M, Bao Q, Yang JX, Loh KP. Electrocatalytically active graphene–porphyrin MOF composite for oxygen reduction reaction. Journal of the American Chemical Society. 2012;**134**(15):6707-6713. DOI: 10.1021/ja211433h

[27] Mpeta LS, Nyokong T. Electrocatalytic activity of ethynylbenzyl phthalocyanines when linked to quantum dots via click chemistry: Towards efficient oxygen reduction reaction and H_2O_2 oxidation. Journal

of Electroanalytical Chemistry. 2019;**840**:218-229. DOI: 10.1016/j. jelechem.2019.03.064

[28] Zhang K, Feng C, He B, Dong H, Zhang X. An advanced electrocatalyst of Pt decorated SnO_2/C nanofibers for oxygen reduction reaction. Journal of Electroanalytical Chemistry. 2016;**781**:198-203

[29] Lebedeva NP, Janssen GJM. On the preparation and stability of bimetallic PtMo/C anodes for proton-exchange membrane fuel cells. Electrochimica Acta. 2005;**51**(1):29-40. DOI: 10.1016/j. electacta.2005.04.034

[30] Lee CH, Jun B, Lee SU. Metal-free oxygen evolution and oxygen reduction reaction bifunctional electrocatalyst in alkaline media: From mechanisms to structure–catalytic activity relationship. ACS Sustainable Chemistry & Engineering. 2018;**6**(4):4973-4980

[31] Nepel TCM, Lopes PP, Paganin VA, Ticianelli EA. CO tolerance of proton exchange membrane fuel cells with Pt/C and PtMo/C anodes operating at high temperatures: A mass spectrometry investigation. Electrochimica Acta. 2013;**88**:217-224. DOI: 10.1016/j. electacta.2012.10.039

[32] Mukerjee S, Lee SJ, Ticianelli EA, McBreen J, Grgur BN, Markovic NM, et al. Investigation of enhanced CO tolerance in proton exchange membrane fuel cells by carbon supported PtMo alloy catalyst. Electrochemical and Solid-State Letters. 1999;**2**(1):12-15

[33] Puello PE, Ayala M, Brito JBL. Activated carbon supported cobalt-molybdenum carbides: effect of the synthesis method, heating rate, type of cobalt precursor and presulfiding agent on thiophene hydrodesulfurization. Revista Facultad de Ingeniería. 2014;**70**:75-85

[34] Dai Y, Sun K, Li Y. Mo-Pt core–shell nanoparticles as an efficient electrocatalyst for oxygen reduction reaction. Journal of Electroanalytical Chemistry. 2015;**757**:94-99. DOI: 10.1016/j.jelechem.2015.09.020

[35] Pérez- González A, Gómez-Peralta JI, Garza-Ortiz A, Barba-Behrens N. The relevance of molybdenum in biological systems and its role in the mononuclear enzymes with the *Moco* cofactor. Educación química. 2012;**23**(1):24-33

[36] Nikolaychuk PA, Tyurin AG. The revised Pourbaix diagram for molybdenum. Butlerov Communications. 2011;**24**(2):101-105. Available from: http://butlerov.com/files/reports/2011/vol24/2/101/101-105.pdf

[37] Iwamoto M, Yoda Y, Yamazoe N, Seiyama T. Study of metal oxide catalysts by temperature programmed desorption. 4. Oxygen adsorption on various metal oxides. The Journal of Physical Chemistry. 1978;**82**(24):2564-2570. DOI: 10.1021/j100513a006

[38] Hussain S, Erikson H, Kongi N, Merisalu M, Ritslaid P, Sammelselg V, et al. Heat-treatment effects on the ORR activity of Pt nanoparticles deposited on multi-walled carbon nanotubes using magnetron sputtering technique. International Journal of Hydrogen Energy. 2017;**42**(9):5958-5970

[39] Huang B, Peng L, Yang F, Liu Y, Xie Z. Improving ORR activity of carbon nanotubes by hydrothermal carbon deposition method. Journal of Energy Chemistry. 2017;**26**:712-718. DOI: 10.1016/j.jechem.2017.03.016

[40] Fang B, Pinaud BA, Wilkinson DP. Carbon-supported Pt hollow nanospheres as a highly efficient electrocatalyst for the oxygen reduction reaction. Electrocatalysis.

2016;**7**(4):336-344. DOI: 10.1007/
s12678-016-0311-4

[41] Luais E, Mery A, Abou-Rjeily J, Sakai J. A self-standing and binder-free electrodes fabricated from carbon nanotubes and an electrodeposited current collector applied in lithium-ion batteries. Journal of Electrochemical Science and Technology. 2019;**10**(4):373-380. DOI: 10.33961/jecst.2019.03132

[42] Alhamoud Y, Yang D, Kenston SSF, Liu G, Liu L, Zhou H, et al. Advances in biosensors for the detection of ochratoxin A: Bio-receptors, nanomaterials, and their applications. Biosensors and Bioelectronics. 2019;**141**:11418. DOI: 10.1016/j.bios.2019.111418

[43] Torres-Santillan E, Capula S, Reza CM, Cayetano NC, Villagarcia EC. Effect of functional groups in the structure of carbon nanotubes to adsorption grade of cadmium ions. Revista Mexicana de Ingenieria Quimica. 2018;**17**(3):955-961. DOI: 10.24275/uam/izt/dcbi/revmexingquim/2018v17n3/Torres

[44] Gao J, Zou J, Zeng X, Ding W. Carbon supported nano Pt–Mo alloy catalysts for oxygen reduction in magnesium–air batteries. RSC Advances. 2016;**6**:83025-83030. DOI: 10.1039/C6RA16142A

[45] Del Colle V, Perroni PB, Feliu JM, Tremiliosi-Filho G, Varela H. The role of surface sites on the oscillatory oxidation of methanol on stepped $Pt[n(111) \times (110)]$ electrodes. Journal of Physical Chemistry C. 2020;**124**(20):10993-10004. DOI: 10.1021/acs.jpcc.0c01897

[46] Zhao Y, Fan L, Ren J, Hong B. Electrodeposition of Pt–Ru and Pt–Ru–Ni nanoclusters on multi-walled carbon nanotubes for direct methanol fuel cell. International Journal of

Hydrogen Energy. 2014;**39**(9):4544-4557. DOI: 10.1016/j.ijhydene.2013.12.202

[47] Capula SC, Aguir K, Cervantes FS, Villa LV, Moncayo JS, Garibay VF. Ozone sensing based on palladium decorated carbon nanotubes. Sensor. 2014;**14**:6806-6818

[48] Grgur BN, Markovy NM, Ross PN. Electrooxidation of H2, CO and H_2/CO mixtures on well characterized PtMo alloy. Journal of the Serbian Chemical Society. 2003;**68**(3):191-205

[49] Nakajima H, Kita H. The role of surface molybdenum species in methanol oxidation on the platinum electrode. Electrochimica Acta. 1990;**35**(5):849-853

[50] Robinson M, Montemore MM, Tenney SA, Sutter P, Medlin JW. Interactions of hydrogen, CO, oxygen, and water with molybdenum-modified Pt(111). Journal of Physical Chemistry C. 2013;**117**(50):26716-26724. Available from: https://pubs.acs.org/doi/10.1021/jp410563s

[51] Robinson AM, Hensley JE, Medlin JW. Surface chemistry of aromatic reactants on Pt- and Mo-modified Pt Catalysts. Journal of Physical Chemistry C. 2016;**120**(47):26824-26833. DOI: 10.1021/acs.jpcc.6b08415

[52] Torres-Santillan E, Vargas-Garcia JR, Ramirez-Meneses E, Manzo-Robledo A, Hernandez-Perez MA. Induced electrochemical reduction of nitrates species on interface of Pt/MWCNTs prepared by vapor-phase impregnation-decomposition method. Revista Mexicana de Ingenieria Quimica. 2019;**18**(2):431-443. DOI: 10.24275/uam/izt/dcbi/revmexingquim/2019v18n2/Torres

[53] Antolini E. Formation of carbon-cupported PtM alloys for low temperature fuel cells. Materials

Chemistry and Physics. 2003;**28**:563-573.
DOI: 10.1016/S0254-0584(02)00389-9

[54] Rossmeisl J, Qu Z-W, Zhu H,
Kroes G-J, Nørskov JK. Electrolysis
of water on oxide surfaces. Journal
of Electroanalytical Chemistry.
2007;**607**(1-2):83-89. DOI: 10.1016/j.
jelechem.2006.11.008

[55] Morante-Catacora TY,
Ishikawa Y, Carlos R. Cabrera Sequential
electrodeposition of Mo at Pt and
PtRu methanol oxidation catalyst,
particles on HOPG surfaces. Journal
of Electroanalytical Chemistry.
2008;**621**:103-112. DOI: 10.1016/j.
jelechem.2008.04.029

[56] Zhang J, Cui R, Li X, Liu X,
Huang W. A nanohybrid consisting
of NiPS3 nanoparticles coupled with
defective graphene as a pH-universal
electrocatalyst for efficient hydrogen
evolution. Journal of Materials
Chemistry A. 2017;**5**(45):23536-23542.
DOI: 10.1039/c7ta07672j

[57] Cui Y, Zhou C, Li X, Gao Y, Zhang J.
High-performance electrocatalysis for
hydrogen evolution reaction using
nickel-doped CoS2 nanostructures:
Experimental and DFT insights.
Electrochimica Acta. 2017;**228**:428-435.
DOI: 10.1016/j.electacta.2017.01.103

Chapter 9

Role of Carbon Nanotube for Flexible Supercapacitor Application

Shalu Rani, Sanjay Kumar and Ritesh Bhardwaj

Abstract

In this current era, with the ever-increasing demand for portable and wearable energy storage devices, the supercapacitor (SC) plays a very positive role to fulfill this gap. Carbon nanotubes (CNTs) are extremely promising material candidate in flexible SC where it works as an electrode to enhance the energy and power densities of the SC because of their remarkable mechanical property, high electrical conductivity, large surface area, and ease to functionalize. Moreover, CNTs can assemble into various macroscopic structures with different dimensions such as single-wall CNTs (SWCNTs), double-wall CNTs (DWCNTs), and multi-wall CNTs (MWCNTs). In this book chapter, a comprehensive discussion on the synthesis, characterization and further utilization of CNTs in metal oxide-based SC has been outlined. Here, the metal oxide can be 1D nanofibers, 2D thin films, and 3D aerogels. Further, a detailed study has been framed on the design methodology and fabrication techniques for the supercapacitor. Recently, various developments and state-of-the-art applications have been proposed for such structures wherein CNTs have been used as electrodes in flexible SCs with varied device configurations such as sandwiched and interdigital in-plane. Furthermore, the flexible CNT-based electrodes have shown great bendability, and compressibility, as well as a long cycle lifetime.

Keywords: CNTs, flexible supercapacitor, nanofibers, energy, electrodes, conductivity

1. Introduction

Recent advancement in the wearable technologies and portable electronics, for example, intelligent clothes, human-like electronic skins, flexible cell phones, and smart ornaments, and increasing interests of diverse scientific communities have developed a flexible supercapacitor (SCs) able to deliver high energy and power output [1–4]. However, the current commercial SC technology is too rigid and very difficult to fulfill the demands of flexible electronics. Thus, it is urgent and right time to develop flexible SCs, which can offer several advantages such as pliable, light-weighted, and mechanically robust [5–7]. It is well known that typical flexible SCs consist of different flexible electrodes developed in various device configurations [8–10]. The important key to construct the flexible SCs lies with the selection of electrodes with light weight and intrinsic flexibility. Generally, based on the charge storage mechanism, SCs are categorized into two different ways namely as electrical double layer capacitors and pseudocapacitors and both offer a high-power density and

a long cycling life [11–13]. The charge storage mechanism in pseudocapacitor is where conductive polymers and transition metal compounds are utilized as an active material and the faradic reactions proceed on the surface of electroactive species [14–16]. On the other hand, in the case of carbon-based nanomaterials, energy storage is due to the accumulation of electrostatic charge at electrode/electrolyte interface, and the performance of the device is strongly dependent on the effective surface area [17–19].

Several carbon-based materials are used in the SC as an electrode but one-dimensional (1D) carbon nanotubes (CNTs) have gained much more attention as it offers high-specific surface area that has great potential to fulfill the requirement for flexible SCs [20–22]. The sp^2 hybridization in carbon-carbon (C-C) bonds supports the excellent mechanical strength of CNT, and better electronic and thermal conductivity along with chemical stability [23, 24]. The large aspect ratio (width-to-length ratio) and comparatively easy surface functionalization further make CNTs are more suitable candidate wherein different nanomaterials can be easily chemically attached [25, 26]. To date, several positive approaches have been implemented for the design and realization of CNT-based flexible SCs devices. CNTs exhibit excellent electrical conductivity, and ballistic ionic transport can be optimized by the mesostructured mesh-like frameworks when CNTs are stacked. These mess-like frameworks offer a large surface area that minimizes charge redistribution and allows full-charge storage capacity at higher frequencies, as compared with porous carbons (PCs) or graphene [27–30]. Previously, different carbon composite films have been widely used to combine the complementary strengths such as CNTs and graphene composite has been demonstrated wherein good ionic conductivity and high volumetric energy density have been reported by utilizing the CNTs to PCs to enhance the electrical conductivity [31–33]. However, the electrical conductivity of the CNT mesostructured frameworks can be affected by the dispersion methods used in their synthesis [34–37].

In this book chapter, we provide a detailed comprehensive view of the current status and state-of-the-art achievements made in flexible SCs with CNT electrodes. Moreover, in this book chapter, various flexible CNT assemblies with different dimensions including 1D fibers, 2D films, and 3D aerogels have been discussed. Furthermore, we present a detailed summary of the CNT-based nanostructures that are utilized in flexible SCs device configurations. Finally, the current challenges and future outlook for the research opportunities on flexible SCs based on CNT electrodes are discussed.

2. Carbon nanotubes (CNTs)

Herein, a detailed discussion about the classifications, useful properties such as electrical, mechanical, thermal, and electronics have been outlined in brief manner.

2.1 Classifications of CNTs

As it is well known that the CNTs are the most powerful candidate from the carbon family, they play a very critical role to enhance the performance of various devices in various applications. For the classification point of view, CNTs can be classified into two types: (1) single-walled carbon nanotubes (SWCNTs) and (2) multi-walled carbon nanotubes (MWCNTs). In 1991, SWCNTs were accidently synthesized by Iijima and Ichihashi [38] *via* arc-discharged method. The as-synthesized SWCNTs have a cylindrical structure made of one layer of graphene by folding it from

edge-to-edge. The effective diameter and length of the SWCNTs are nearly 1 nm and up to 1 mm, respectively. However, the production cost of the SWCNTs is more expensive, as compared to the MWCNTs [39]. On the other hand, a MWCNT has a concentric tube made of graphene sheets. The diameter of the MWCNT is varying in nature, as it is the multiple folds of the graphene sheets. As the MWCNT is made of the multiple folds to from concentric cylinders, the interplanar distance between each of the concentric cylinders is maintained by the internal Coulombic force and fixed in the range of 0.32 nm to 0.35 nm [40]. Here, it should be noted that the interplanar distance is nearly equal to the interplanar distance between two successive graphene layers in graphite [39]. However, for the electronic device applications, the utilization of MWCNTs is comparatively higher as compared to the SWCNTs as SWCNT has weaker adhesion profile with the used substrate surface [41]. On the other hand, in the case of MWCNTs, more active sites are available at the end of the tube [42] which further enhanced the adhesion properties of tube with the used substrate surface [41]. Sometimes, in the extreme case, MWCNT can also be considered as a double-walled carbon nanotube (DWCNT) wherein the formed structure is similar to the cylinders of the graphene layers with interlayer space of 0.335 nm. The physical and chemical properties of the DWCNT are very close to the SWCNT [39]. **Figure 1** depicts the illustration of SWCNTs, DWCNTs, and MWCNTs.

2.2 Properties of CNTs

In this section, the various remarkable properties of the CNTs such as electrical, mechanical, thermal, and electronics and its interrelation for utilizing areas of applications have been discussed.

2.2.1 Electrical properties of CNTs

The electrical properties of the CNTs are mainly utilized in electronics areas, as its show remarkable current density in order of 10^9 A/cm [44] and specific capacitance. The specific capacity of 25-µm-thick CNT sheet electrode is found to be in the range of 39–90 F/cm^3 [45]. Moreover, CNTs can be behaved like a semiconductors or metal depending upon its structure [46]. The various electrical parameters of CNTs such as conductivity, resistivity [47], and capacitance [45] can be manipulated by functionalizing them with the appropriate chemical functional groups, as it creates defects over the CNTs surface. For example, the doping of gold nanoparticles in
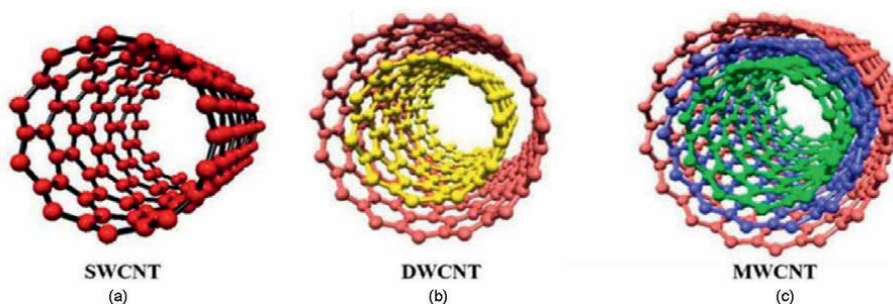
Figure 1.
Illustration of (a) single-wall CNT, (b) double-wall CNT, (c) multi-wall CNT [43] © Applied Sciences 2021.

CNTs makes covalent bonds on its surface which further leads to the increment in conductivity [47].

To increase the electrochemical performance of the CNTs by opening the caps at the CNTs ends, chemical treatment can be performed [48]. On the other hand, under the heat treatment in the gaseous environment, the electrical conductivity of the CNTs is reduced due to the formation of sp^3 bonds with the gaseous atoms [47]. It should be noted that the significant modulation in SWCNTs structure by enabling defects and functionalization shows 23% increment in the energy density, as compared to the graphite [42]. Moreover, variations in the electrical properties make change in the chirality factor, temperature, originating defects, and atmosphere change [47]. However, the electrical conduction in SWCNTs is comparatively lower than the MWCNTs [47]. The pure SWCNTs show electrical resistivity in the order of 10^{-6} Ω.cm, while commercially available SWCNTs which are grown by chemical vapor deposition (CVD) showing an electrical resistivity in the range of $1–7 \times 10^{-4}$ Ω cm may be due to the presence of defects during manufacturing process.

Besides that, it is widely reported that the electrical properties of the CNTs are also varied due to their interfacial contact resistance [47], as it is created when two CNTs are connected in series. It is observed that if contact area between two CNTs increases, the contact resistance decreases. Due to its Schottky barrier connection with the matrix, it is a promising candidate for field emission transistors [49], as it enhances the recovery time and reduces the turn-on voltage.

2.2.2 Mechanical properties of CNTs

The mechanical properties of CNTs are dependent on various production and structural factors such as the methods of production, the number of created defects, and structure, diameter, and symmetry of nanotubes [50, 51]. As reported [51], the arc discharge grown MWCNTs have higher mechanical strength, as compared to catalyst grown MWCNTs, which may be due to the fewer structural defects in arc-grown MWCNTs [51]. The covalent sp^2 hybridization in CNT plays a major role in their strength [51] and due to this strong hybridization, MWCNTs can be bent at higher angles without destroying the structure [52]. Initially, it was very difficult to evaluate the mechanical strength of the CNTs due to its nanoscopic dimension but latterly, the transmission electron microscopy (TEM) is utilized to calculate the Young's modulus of SWCNTs and MWCNTs. Experimentally, for the MWCNTs, the observed highest Young's modulus is 4.15 TPa, and for the SWCNTs, it is around 1.3 TPa [51, 52]. However, the TEM method has many errors in measurement [30] and not provided accurate Young's modulus. Alternatively, atomic force microscopy (AFM) is used to obtain the Young's modulus in which pressure is applied on the CNTs *via* AFM tip made of Si_3N_4 and corresponding load displacement curves have been plotted. As observed, MWCNTs with varying diameter in the range of 26–76 nm have shown a Young's modulus of 1.28±0.5 TPa and SWCNTs have nearly 1 TPa [51]. However, many researchers have used SWCNTs for the Young's modulus calculation because SWCNTs have fewer defects as compared to MWCNTs and, hence, exhibit more strength [52].

2.2.3 Thermal properties of CNTs

The thermal properties of CNTs are dependent on the acoustic phonons of the nanotubes [53]. The mean free path of phonons helps to determine the range of

thermal conductivity of the CNTs [53]. As it is well known that the CNTs have a one-dimensional (1D) cylindrical tube structure by folding a two-dimensional (2D) graphene sheet, the phonon band structure becomes tough in the CNT [54]. The phonon density of states (P-DOS) is isolated in the isolated SWCNTs until the surrounding temperature must be low because the P-DOS is linearly depended on the specific heat above 1 K [53]. However, the temperature increases beyond 1 K, and the longitudinal and acoustic phonons increase, which further leads to the linear increment in specific heat. The value of specific heat in the SWCNT rope, 3D SWCNT, and graphene has found to be coincided and reflected phonon structure in 3D graphite at high temperature [54]. Moreover, certain experiments have been demonstrated in which thermal conductivity of CNTs were investigated at the room temperature and the obtained value is around 6600 W/mK [54]. On the other hand, the SWCNTs and MWCNTs have shown values of the thermal conductivities are 200 W/mK [54] and 3000 W/mK [53], respectively.

3. CNT-based metal oxide/sulfide thin film for flexible supercapacitor (SCs)

Generally, flexible SCs architecture has two electrodes and polymer gel electrolyte is filled inside the electrode gaps. This gel electrolyte is playing the role of separator in the SCs configuration. Broadly, the SCs configuration can be categorized into three ways namely as (a) sandwiched architecture, (b) interdigital in-plane architecture, and (c) cable-type architecture. The different SCs configurations can be shown and utilized in different characteristics and applications. In the following sections, we have outlined the different device configurations facilitated with the CNT-based electrolytes.

3.1 Sandwiched configuration

The sandwiched configuration is the well-known and widely popular design in flexible SCs. However, previously flexible SCs faced problem with appropriate choice of electrolyte and electrodes, which can be avoid the usage of heavy current collectors. Kaempgen et al. [55] have reported the sprayed SWCNT thin films that act as both active electrodes and current collectors in bendable and ultralight SC device. The developed SC devices exhibited high values of specific capacitance, that is, 36 F/g due to the high electrical conductivity and porous channels under a discharge current density of 1 mA/cm^2. Based on the internal resistance measurement analysis, there are no significant differences observed between the liquid H_3PO_4 and solid PVA/H_3PO_4 electrolyte. The obtained research outcomes confirm the feasibility of gel electrolyte as reported by previous studies [56, 57].

Further, Kanninen et al. [58] have developed a dry deposition technology to fabricate SWCNT thin films. Here, it should be noted that the fabricated bendable SCs exhibited a remarkable and favorable electrochemical property with high optical transparency up to 92%. The fabricated SCs devices may be used as a power source in smart transparent electronics such as display screen, sensor, and photovoltaic devices [59]. Therefore, the combination of CNTs with pseudocapacitive materials has proven efficient to improve the capacitance and energy density of flexible SCs and also maintain the robust mechanical behavior [20, 60, 61]. Here, **Figure 2** shows the sandwich structure-based SCs devices.
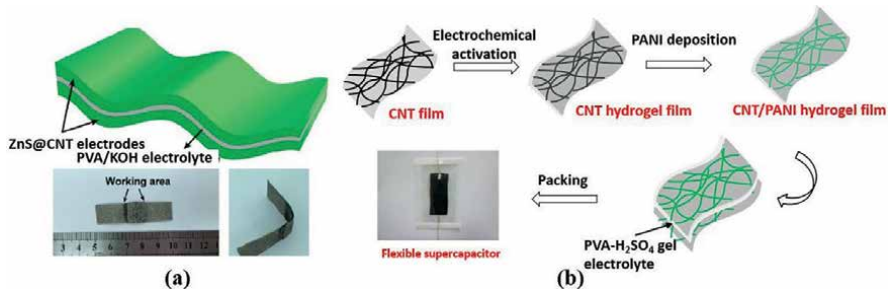
Figure 2.
(a) Schematic and photographs of the all-solid-state device with ZnS/CNT electrode [62], © Tsinghua University Press and Springer-Verlag Berlin Heidelberg 2017. (b) Fabrication process for flexible all-solid-state SC based on CNT/PANI hydrogel [63], © The Royal Society of Chemistry 2015.

3.2 Interdigital in-plane configuration

In the case of conventional sandwiched configuration, the electrodes usually suffer from large ion transport resistance, which may be induced from the thick and dense electrode design to store comparatively more energy. While in the case of interdigitated in-plane structural configuration, the electrode materials, current collectors, and gel electrolyte are on the same plane and the design methodology well addressing the issue related to the SCs for flexible electronics [64–67]. Moreover, interdigitated in-plane configuration offers fast ion transport *via* effectively controlling the interdigitated gap between the successive electrodes, which further helps to enhance the power density. Moreover, the ionic transport does not affect this configuration as it is in-plane structure and also supports the folding, rolling, and twisting [68, 69] without affecting the electrochemical performance of device. Therefore, in this section, we are focusing on the advanced SCs technologies that have been widely used for fabricating flexible SCs devices with interdigitated in-plane configuration by insertion of CNT to enhance the electrochemical performance.

Recently, Rani et al [70] have fabricated in-plane, interdigitated architecture-based microsupercapacitor (MSC) devices developed by utilizing electrophoretic deposition (EPD) wherein TiO_2 nanofibers (NFs) are used as an active electrode material and Mo is used as a current collector in interdigitated configuration for flexible electronic applications. In this reported work, TiO_2 NF is used as an active material, which offers one-dimensional (1D) nanostructured morphology and continuous nanofibric network, which can further provide the high electroactive surface area, reduced diffusion path length, and increased power density of the MSC device [71]. Further, to perform an EPD of active material, a disperse solution of TiO_2 NFs with 2 wt.% MWCNTs is prepared using ethanol [72] and deposited over Mo-coated PET substrate by applying a constant direct current (DC) voltage of 50 V. Moreover, TiO_2 is prominent candidates for the supercapacitor devices as it is economically viable and abundancy in nature, and has structure-wise stability and environmentally friendly properties in various electronic applications [72]. Besides that, the utilized fabrication approach, that is, EPD is the offers several benefits for electrode fabrication such as cost-effectiveness, room temperature operation, better control over the process parameters, and no involvement of electrochemically inactive binder [72, 73]. The fabricated MSC device exhibited an excellent areal capacitance of ~9.4 mF/cm^2 [70].

Here, **Figure 3** shows the fabrication process flow, which is utilized during the fabricating of MSC device as reported by Rani et al [70].

Here, **Figure 4a** depicts the micrograph of surface of the active material-coated over the interdigitated electrode configuration of MSC device using the field emission scanning electron microscope (FESEM; Carl Zeiss). As seen in **Figure 4a**, it is clear that the TiO_2 NFs and MWCNT are coated over the flexible Mo-coated PET substrate wherein MWCNTs form a highly dense conductive network between TiO_2 NFs [72]. Further, due to entangled structure of MWCNTs, it helps to improve the electrical conductivity of the coated thin film of active material by creating electronic wiring between TiO_2 NFs [72]. Furthermore, the cross-sectional analysis of fabricated structure is revealed that the device has compact electrode/electrolyte structure that further enhances the possibility of electrochemical stability of the fabricated device, as depicted in **Figure 4b**.

Further, Rani et al [70] have performed the electrochemical analysis for the fabricated MSCs device by utilizing cyclic voltammetry (CV) and galvanostatic charge/discharge (GCD) method by considering various scan rates and current densities, respectively, with potential window of 0–0.7 V. **Figure 5a** shows the CV curves for all the MSCs recorded at 10 mV/s scan rate which exhibit quasi-rectangular behavior. Herein, it should be noted that an enhanced area or also known as memory window of the CV curve for MSC3 device shows the improved capacitive performance as compared to MSC1 and MSC2 because in the case of MSC3 the reduction in ionic diffusion path by decreasing the interspace between adjacent interdigitated fingers further enables the faster diffusion of electrolytic ions inside the interspace [71, 75]. Besides that, the MSC4 device structure exhibited the highest electrochemical performance because it facilitated with minimum finger interspace (500 μm), which might reduce the ionic diffusion path and corresponding increment in the active sites as these significantly contributed to improve the electrochemical performance. Herein, **Figure 5b** depicts the galvanostatic charge/discharge curves for all the fabricated MSCs device
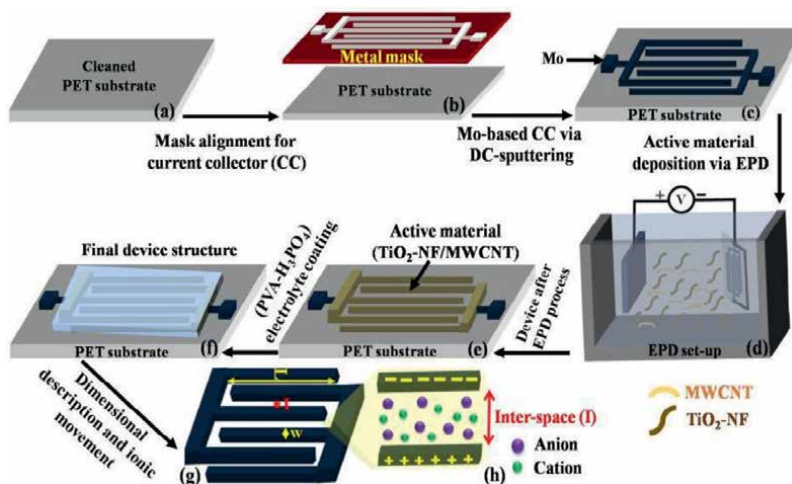
Figure 3.
(a) Ultrasonically cleaned polyethylene terephthalate (PET) substrate. (b) Alignment of metal mask on cleaned PET substrate to pattern the current collector (CC). (c) Deposition of Mo metal contact on PET substrate. (d) Deposition of active materials on Mo-coated PET via EPD. (e) Active materials deposited MSC structure. (f) MSC device structure with gel electrolyte. (g) MSC structure with length and with description. (h) Illustration for ionic movement [70], © IEEE 2021.
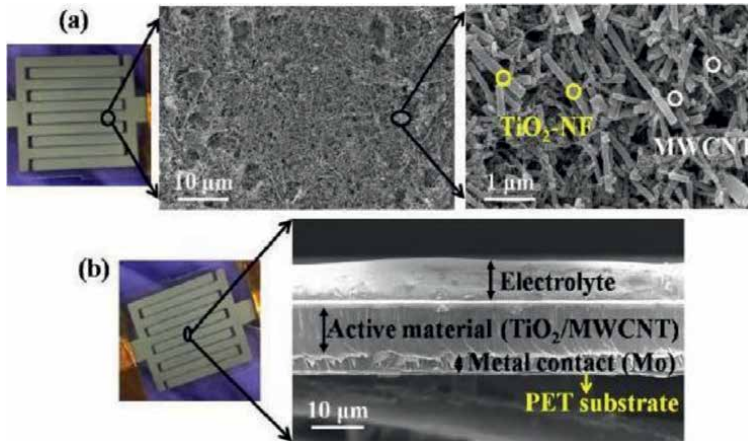
Figure 4.
(a) Surface FESEM micrograph of MSC device. (b) Cross-sectional FESEM of MSC device [70], © IEEE 2021.
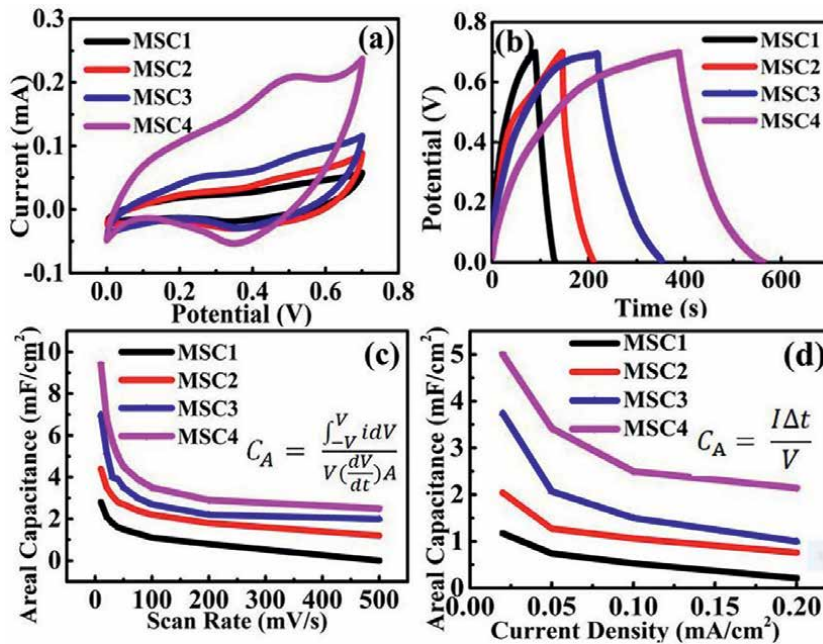
Figure 5.
Electrochemical analysis of MSC devices. (a) Current-voltage curves at 10 mV/s scan rate. (b) GCD plots at 0.02 mA/cm² current density (I). (c) C_A vs. scan rates, and inset depicts the mathematical formulation used to calculate C_A (at mV/s), whereas dV/dt is the scan rate (V/s), i: current (mA), A: gel electrolyte coated active area (cm²) of MSC with fingers and their interspace, and V: voltage window (V) [74]. (d) C_A vs. current densities, and inset depicts the mathematical equation used to evaluate C_A (at mA/cm²), where I: current density (mA/cm²) and Δt: discharge time (s) [70, 72], © IEEE 2021.

structures that are not perfect in triangular shape as verified by the CV analysis [76]. It should be noted that the MSC4 device shows the maximum discharge time (Δt) other than three MSC devices (MSC1, MSC2, and MSC3), which contributes in higher areal capacitance.

Here, **Figure 5c** shows the effect of scan rates on the areal capacitance of all MSCs structures. The areal capacitances vs. discharge current densities (I) for all the MSCs are examined by their respective GCD curves as shown in **Figure 5d**. Here, it can be investigated that the MSC4 device structure shows better areal capacitances ~9.4 mF/cm^2 at 10 mV/s scan rate and ~5 mF/cm^2 at 0.02 mA/cm^2 current density as depicted in **Figure 5c** and **d**. The enhanced values of the areal capacitance of the MSC device can also be correlated with the enhanced surface morphology of active material (TiO$_2$/MWCNT) and optimized number of gaps considered at a particular EPD voltage [72]. Furthermore, the enhanced surface morphology helps to improve ionic transport in the active material, which further leads to the higher utilization of available active sites near to the interspace region and there is no requirement of the addition of inactive binder to enhance the electrochemical performance and, hence, further improves its charge storage properties [72]. The areal capacitance of MSC4 device is higher than many previously reported MSC devices [74, 77–81].

To examine the application of fabricated MSCs device in flexible electronics as an energy storage, various bending angles such as 120°, 135°, and 145° have been investigated. As seen in **Figure 6a**, the CV curves for the MSC4 device at 120° and 135° bending angles show the minor changes in the CV area suggesting better flexibility of the device [71, 77]. Furthermore, under the bending conditions the long cyclability in MSC4 at 0.2 mA/cm^2 for 2000 GCD cycles at 145° as shown in **Figure 6b** proves that the device is able to maintain nearly 73% capacitance retention, which further can be associated with the excellent flexibility of the device. However, the decrement in the capacitance retention under bending condition is associated with the increment in the resistance as shown in **Figure 6c** and corresponding decrement in the electrical conductivity of the active material film wherein the generation of cracks on the surface is caused by bending force [82].

Therefore, under the bending conditions it is more difficult for the electrolytic ions to move freely and come in contact with the available electroactive sites in active material. As a result, the areal capacitance of the MSC device is decreased as compared with the unbending state [83–85]. The fabricated interdigitated in-plane MSC device exhibited maximum areal energy density and areal power density are 0.64 μWh/cm^2 and 307.2 μW/cm^2, respectively, which are comparatively better than the previously published reports [74, 86–89] and the fabricated devices have potential applications in flexible microelectronic devices area with high performance and stability.

3.3 Cable-type configuration

Recently, cable-type configuration for SCs devices has gained very much attention from the scientific communities as these offer the excellent opportunity to enhance the mechanical property for portable/wearable electronics devices [90–92]. The straight cable's structure can be categorized into large-scale textiles for specific area applications [93, 94]. However, one of the major concerns for this SCs structure is to realize into linear-shaped electrode that can offer excellent flexibility along with desired capacitive properties. Therefore, by considering the striking physical and chemical properties, CNTs have been considered as a promising candidate in flexible SCs to enhance the electrochemical performance of the device.

Most recent, Rani et al [95] have developed all-solid-state flexible yarn SC (YSC) device by utilizing EPD technique wherein TiO$_2$ NFs and MWCNTs are used as
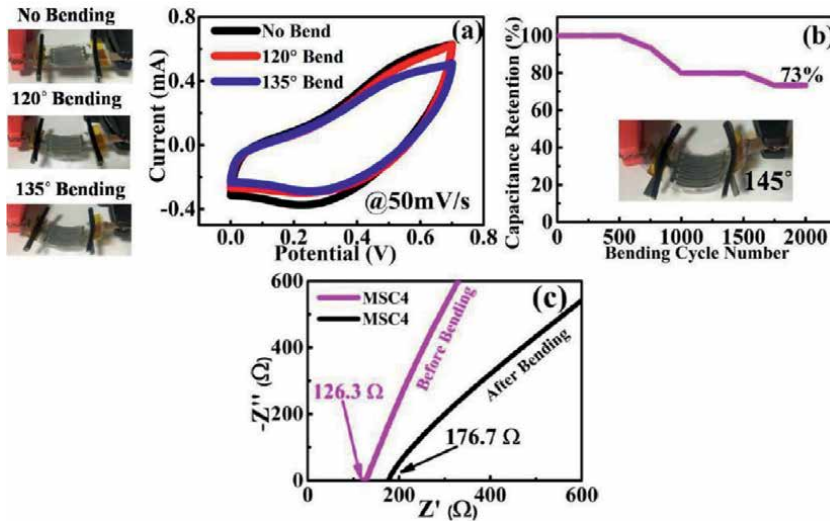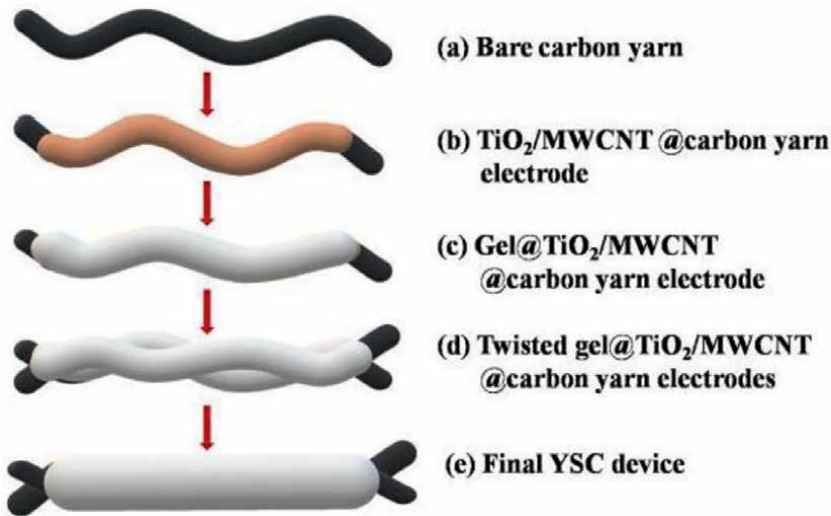
Figure 6.
(a) Current-voltage plots for MSC4 device at various bending angles. (b) Capacitance retention curve of MSC4 at 0.2 mA/cm² for 2000 GCD cycles at 145°. (c) Impedance spectroscopy analysis of MSC4 with and without bending cycles [70], © IEEE 2021.

an active material, while flexible and low-density carbon yarn is used as a current collector. Herein, to fabricate the YSC devices, the gel electrolyte is used. Further, to enhance the capacitance and the energy density of the YSC device, a small amount of redox additive is mixed into the gel electrolyte at room temperature. The as-fabricated YSC device exhibits the excellent electrochemical and mechanical flexibility. After the successful investigation of the electrochemical characteristics and mechanical flexibility of the fabricated device, three-similar YSCs are connected in series into a wearable fabric wherein a red LED is glowing for more than 5 min even under bending condition at different bending angles. Hence, the excellent electrochemical performance with and without bending further proves the potential applications in practical flexible and smart textile.

For the fabrication of the cable-type configuration SC, firstly, TiO_2 NFs are synthesized by utilizing the facile electrospinning technique. The detailed synthesis process for the TiO_2 NFs is outlined elsewhere [72]. After the synthesis of TiO_2 NFs, a dispersed solution of TiO_2 NFs is prepared into the ethanol through ultrasonication process and 2 wt.% MWCNTs are also mixed to improve the adhesion between TiO_2 NFs to enhance the conductivity of the coated yarn electrode. Here, it should be noted that the surface of the active material must be electrically charged when it is dipped into dispersed solution as it moves toward the working electrode, which has opposite charge under the excitation of an external electric field in EPD process. Hence, a small quantity of charging additive; that is, hydrochloric acid ~100 µL, 36.4 wt.% is incorporated into the active material solution before ultrasonication to generate positive charges on the surface of the active material during cathodic EPD method.

The induced surface electric potential is measured *via* Malvern Zeta sizer Nano ZS90 system and known as a zeta potential which is 36 mV. Further, a commercial bare carbon is taken and cleaned *via* acetone and deionized (DI) water followed by heat treatment at 450°C temperature for 2 h to activate its surface for the deposition. The activated bare carbon yarn, as shown in **Figure 7a** is served as a cathode and
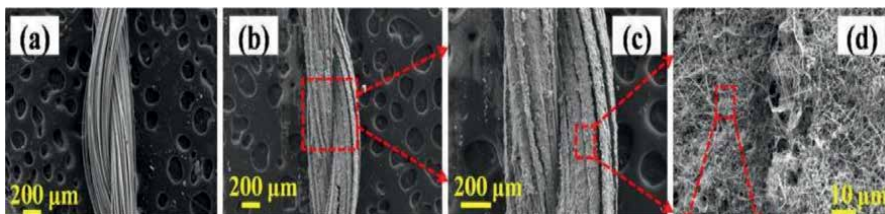
Figure 7.
Step-by-step fabrication process for flexible YSC device [95], © IEEE 2022.

stainless steel is served as an anode. For the deposition, both electrodes are placed into the prepared disperse solution by keeping distance 1 cm between them and applied DC voltage of 50 V for 10-min supply. Furthermore, active material-coated yarn electrode is dried at 60°C temperature in vacuum for 12 h, as shown in **Figure 7b**.

The gel electrolyte has been prepared with polyvinyl alcohol (PVA: 6 g) powder and DI water (60 mL) and constantly stirred at 90°C to get a homogeneous and transparent solution and added 1 M H_3PO_4 to the prepared solution with 40 mM sodium molybdate (Na_2MoO_4) mixed into the solution and stirred for 30 min. Next, for the fabrication of all-solid-state flexible YSC devices, two yarn electrodes with active material are dipped into the gel electrolyte for 1 h and dried at 30 °C for 12 h, as shown in **Figure 7c** and these two yarns are further twisted with each other to fabricate the YSC device, as depicted in **Figure 7d** and further coated with the gel electrolyte and dried at 30°C for 12 h, as shown in **Figure 7e**. Here, it should be noted that the gel acts as an electrolyte as well as the separator between two carbon yarn electrodes.

Here, **Figure 8** shows the surface morphology of the bare and coated carbon yarn electrodes that are investigated by FESEM analysis. **Figure 8a** and **b** clearly shows the difference between bare and coated carbon yarn wherein active material is densely
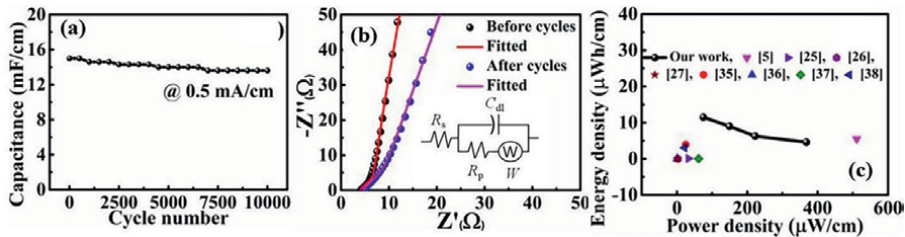

Figure 8.
(a) FESEM image of bare carbon yarn electrode. (b-d) FESEM images of active material coated carbon yarn electrode, [95], © IEEE 2022.
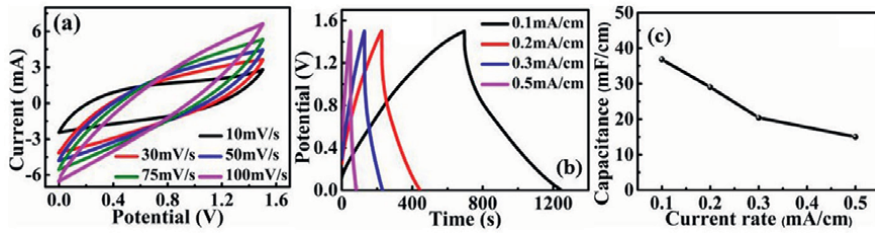
Figure 9.
Electrochemical properties of YSC device: (a) CV plots at 10–100 mV/s sweep rates. (b) GCD data plots at 0.1–0.5 mA/cm current rates. (c) Rate capability graph, [95], © IEEE 2022.

Figure 10.
(a) Long cyclability graph, (b) EIS data plots (before and after cycling); inset displays the electrical equivalent circuit. (c) Energy density vs. power density of the YSC device in a Ragone plot [95], © IEEE 2022.

coated over the yarn surface, which acts as a current collector. **Figure 8c** and **d** depicts the enlarge FESEM image of the coated yean.

After the morphological and structural analysis of the fabricated YSC device, the electrochemical analysis has been performed in two electrode configurations. The CV graphs for the fabricated YSC devices are exhibited in **Figure 9a** with varied sweep rate from 10 to 100 mV/s. The nature of obtained CV is similar to pseudocapacitive behavior and follows the same change storage mechanism within the potential window of 0–1.5 V due to the involvement of the redox reactions and transfer of electrons on the surface as well as in the bulk of the active materials [72]. Further, the increment in the CV area is associated with the faster redox reaction at the higher sweep rate [96]. **Figure 9b** shows the GCD plots with different current rates ranging from 0.1 to 1.5 mA/cm, which are nearly triangular shapes and further confirm the pseudocapacitive charge storage mechanism, as outlined in **Figure 9a**.

The linear variations in YSC capacitances at different current rates are plotted in **Figure 9c** and as seen in **Figure 9c** and the maximum linear capacitance of the fabricated device is 36.8 mF/cm at 0.1 mA/cm current rate *via* GCD and 43.3 mF/cm at 10 mV/s via CV. At the higher current rates, the lower capacitance values are observed in **Figure 9c**, which may be due to the slower ionic diffusion of the electrolytic into the inner active site regions of the active material at higher applied current rates [72].

Next, to evaluate the cyclic stability of the fabricated YSC devices, a GCD analysis has been carried out at 0.5 mA/cm up to 10,000 cycles as shown in **Figure 10a**. Here, after the 10,000 cycles, the fabricated YSC devices exhibited 90% capacitance retention of its initial value which further confirmed the better stability for the device. Therefore, the higher linearity, areal, and volumetric capacitances and better cyclability of the YSC device have confirmed that the coated materials are highly dense and has hierarchical architecture of the active materials (TiO_2 NFs and MWCNT) over

carbon yarns during the EPD process. Here, it should be noted that the hierarchical structure of the active materials is more favorable to improve the charge transport and ionic diffusion without binder materials as MWCNTs improve the electronic conduction by enabling the charge transportation in NFs network [70]. Therefore, the modified EPD-deposited architecture of the active materials (TiO$_2$ NFs/MWCNT) can be added following features:

1. Modified EPD avoids the inactive binders;

2. Improves the movement of the electrolytic ions inside the active materials;

3. Improves the interface between electrode and electrolyte;

4. Improves the electrolytic ions transport by reducing diffusion path;

5. Minimizes the contact resistance between the substrate and the active materials;

6. Enables the active sites inside the active materials that improve the electrochemical performance.

Furthermore, to significantly increase the redox reaction, a little amount (5 mL) of Na$_2$MoO$_4$ has been added into the PVA-H$_3$PO$_4$ gel electrolyte, which increases the capacitance and energy density of the fabricated YSC devices [97]. **Figure 10b** shows the cyclic stability of the fabricated YSC device before and after cycling wherein the impedance spectroscopy data are evaluated by utilizing ZView software and the examined data are displayed with their equivalent electrical circuit [98] in the inset of **Figure 10b**. In the equivalent electrical circuit, R_s signifies the ohmic resistance, R_p and C_{dl} denotes the faradic charge transfer resistance at the electrode/electrolyte interface and the double-layer capacitance, respectively, while W is associated with the Warburg impedance [99]. The two important terms such as energy and power densities are the very critical terms, which determine the performance of the SC devices. **Figure 10c** shows the energy and power densities of the fabricated devices as compared to the other reported literature [100–104].

Herein, **Figure 11** clearly depicts the role of active materials and MWCNTs in the performance of the YSC devices. As seen in **Figure 11a–c**, the electrochemical performance of the YSC devices is based on bare carbon yarns, MWCNT@carbon yarns, and TiO$_2$ NFs@carbon yarns, wherein bare carbon yarns, MWCNT@carbon
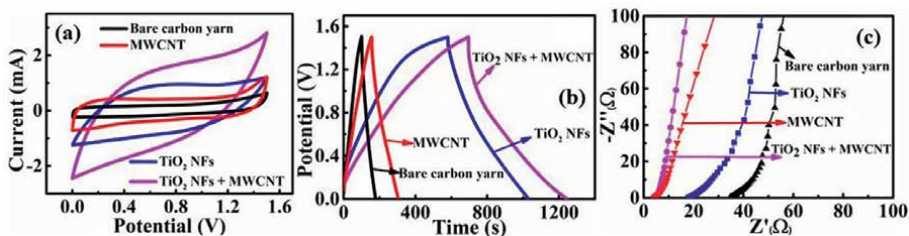
Figure 11.
Performance of bare and active materials coated yarn device: (a) CV curves at 10 mV/s. (b) GCD curves at 0.1 mA/cm. (c) EIS data plots, [95], © IEEE 2022.

yarns, and TiO$_2$ NFs@carbon yarns depict the capacitance values of 5, 10, and 31 mF/cm, respectively, at 0.1 mA/cm.

To realize the particle applications, the fabricated YSC device structure must exhibit the better flexibility and mechanical bending stability against the varied bending angle to use as a power source in textile-based wearable/portable electronics applications. Therefore, to analysis the capability of the flexible YSC device structure to store and release the energy in the flexible electronics system, the electrochemical characterizations have been carried out under different bending states. **Figure 12a** shows the YSC device under different angles of bending, such as 0°, 45°, 90°, and 145°. It can be observed that the under the different bending angles the CV response of the fabricate devices has not been affected effectively, as shown in **Figure 12b**, and, hence, retains its supercapacitive behavior [71]. Further, the capacitive retention has also been analyzed under bending condition of 145° for 2000 cycles at 0.5 mA/cm *via* GCD as shown in **Figure 12c** and after 2,000 cycles, YSC device attends 95% of its initial capacitance, showing remarkable mechanical stability. Moreover, the robustness and durability of the YSC device is also associated with the superior flexibility and mechanical strength of the carbon yarn as a current collector, and the gel electrolyte which tightly bound all the components of the device to improve its electrochemical performance under extreme bending conditions. Herein, **Figure 12d–e** shows the CV and GCD plots for three similar YSC devices are fixed in a wearable fabric under series connection. As observed, the CV and GCD curves of series-connected YSCs at 10 mV/s and 0.1 mA/cm, respectively. The series-connected YSCs has successfully
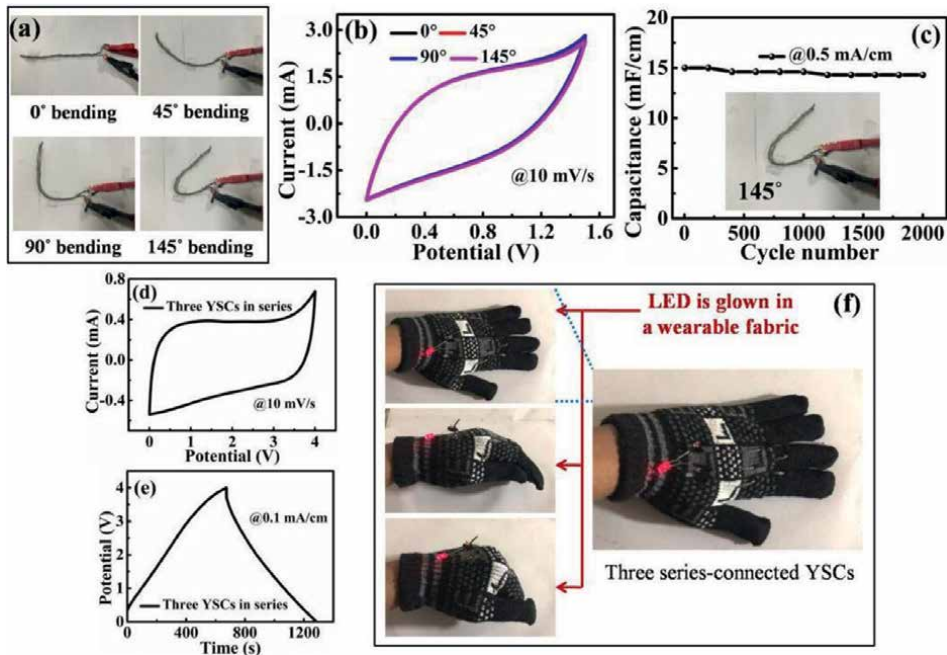
Figure 12.
(a) Various bending angles of the flexible YSC device, (b) current-voltage plots (@10 mV/s) for YSC device at different bending stages, (c) cyclability plot of YSC up to 2000 GCD cycles at 0.5 mA/cm at 145° bending angle. (d) CV curve (@10 mV/s) of three series-connected YSCs devices. (e) GCD curve (@0.1 mA/cm) of three series-connected YSCs devices. (f) Three series-connected YSCs devices fixed into a wearable fabric and glow a red LED at different bending states, [95], © IEEE 2022.

lighted a red LED under bending conditions at different bending angles for more than 5 min, as depicted in **Figure 12f**. Therefore, after the analyzing of characterized data, it can be concluded that the fabricated devices are much compatible with the wearable, flexible, and portable electronic devices.

4. Conclusions and future perspectives

In summary, the rapid development of portable and wearable electronics has opened the new opportunities for miniatured flexible SCs. The unique cylindrical shape and remarkable and excellent mechanical properties are toward stability and bendability of the CNTs to form flexible interconnected network within the active materials. Several synthesis and fabrication processes such as electrospinning, EPD, and hydrothermal and solution process have been utilized to synthesize the active materials and CNTs to develop the flexible SCs device to fulfill the demand of the current flexible electronic market. In the pseudocapacitive materials, CNTs can also be incorporated to improve the electrochemical performance of the fabricated flexible devices. Moreover, different device configurations such as sandwiched, interdigital in-plane, and cable-type have been widely investigated as per the desired applications. The involvement of flexible CNTs into electrode and active materials helps to enhance the high flexibility in SCs that are bendable or foldable, stretchable or compressible, wearable, and twistable and under all the extreme conditions, the fabricated devices are to maintain the electrochemical performance of the energy storage devices. Based the configurations, the sandwiched SCs are extensively studied as it has simple device structure but poor electrochemical performance due to the lower rate of ionic transport. While in the case of interdigital in-plane device structure, wherein fast ionic transport can be facilitated *via* optimized and well-controlled gap distances between interdigitated electrode fingers without hindering the ion transport. The cable-type configuration also facilitated to maximize the mechanical property, which further enables the flexibility and bendability of the fabricated devices.

Specifically, the incorporation of CNTs nanostructured into metal oxide nanofibers/nanobelts/nanotubes attended the higher arial and specific capacitance that are the backbone of the any energy storage devices especially in the case of flexible SCs. However, accelerated progresses have been achieved in flexible SCs devices, which are equipped with CNT materials but some critical challenges are still exist, which are extensively need to be addressed to realize these for their practical applications. The solid-state electrolyte is the key component of flexible SCs, and currently available solid state gel electrolytes have issues with high viscosity and low ionic conductivity that further limited the power output of flexible SCs. Therefore, a novel solid-state electrolyte who can support high ionic conductivity and excellent mechanical behavior is required to accelerate the flexible SC research. However, the electrochemical mechanism in CNTs-oriented solid-state electrolyte for flexible devices is still unclear and it is essentially required to understand the correct energy storage mechanism to design and fabricate of more effective flexible SCs. It should be noted that the large-scale preparation of CNTs nanotube and fibers by utilizing wet/dry spinning techniques are readily available, which can hold the great potential to facilitate the application of flexible SCs. We strongly believe that research and development in these areas will be beneficial and significantly contribute to the development and commercialization of flexible SCs in the near future.

Conflict of interest

The authors declare no conflict of interest.

Author details

Shalu Rani[1]*, Sanjay Kumar[2] and Ritesh Bhardwaj[3]

1 Centre of Nanotechnology, Indian Institute of Technology Roorkee, Roorkee, India

2 Department of Electrical Engineering, Indian Institute of Technology Indore, Indore, Madhya Pradesh, India

3 Department of Electronics and Communication Engineering, Dr. B. R. Ambedkar National Institute of Technology, Jalandhar, Punjab, India

*Address all correspondence to: shalu29singh@gmail.com

IntechOpen

References

[1] Shao YL, El-Kady MF, Wang LJ, Zhang QH, Li YG, Wang HZ, et al. Graphene-based materials for flexible supercapacitors. Chemical Society Reviews. 2015;**44**:3639-3665

[2] Ko Y, Kwon M, Bae WK, Lee B, Lee SW, Cho J. Flexible supercapacitor electrodes based on real metal-like cellulose papers. Nature Communications. 2017;**8**:536

[3] Wang YQ, Ding Y, Guo XL, Yu GH. Conductive polymers for stretchable supercapacitors. Nano Research. 2019;**12**:1978-1987

[4] Li WW, Gao FX, Wang XQ, Zhang N, Ma MM. Strong and robust polyaniline-based supramolecular hydrogels for flexible supercapacitors. Angewandte Chemie International Edition. 2016;**55**:9196-9201

[5] Liu LL, Niu ZQ, Chen J. Design and integration of flexible planar micro-supercapacitors. Nano Research. 2017;**10**:1524-1544

[6] Liu LL, Niu ZQ, Chen J. Flexible supercapacitors based on carbon nanotubes. Chinese Chemical Letters. 2018;**29**:571-581

[7] Huang P, Lethien C, Pinaud S, Brousse K, Laloo R, Turq V, et al. On-chip and freestanding elastic carbon films for micro-supercapacitors. Science. 2016;**351**:691-695

[8] El-Kady MF, Strong V, Dubin S, Kaner RB. Laser scribing of high-performance and flexible graphene-based electrochemical capacitors. Science. 2012;**335**:1326-1330

[9] Zhu S, Li YT, Zhu HY, Ni JF, Li Y. Pencil-drawing skinmountable micro-supercapacitors. Small. 2019;**15**: 1804037

[10] Fu YP, Cai X, Wu HW, Lv ZB, Hou SC, Peng M, et al. Fiber supercapacitors utilizing pen ink for flexible/wearable energy storage. Advanced Materials. 2012;**24**:5713-5718

[11] Salanne M, Rotenberg B, Naoi K, Kaneko K, Taberna PL, Grey CP, et al. Efficient storage mechanisms for building better supercapacitors. Nature Energy. 2016;**1**:16070

[12] Zhu S, Wang ZD, Huang FZ, Zhang H, Li SK. Hierarchical Cu(OH)2@ Ni2(OH)2CO3 core/shell nanowire arrays in situ grown on three-dimensional copper foam for high-performance solid-state supercapacitors. Journal of Materials Chemistry A. 2017;**5**:9960-9969

[13] El-Kady MF, Shao YL, Kaner RB. Graphene for batteries, supercapacitors and beyond. Nature Reviews Materials. 2016;**1**:16033

[14] Dubal DP, Ayyad O, Ruiz V, Gomez-Romero P. Hybrid energy storage: The merging of battery and supercapacitor chemistries. Chemical Society Reviews. 2015;**44**:1777-1790

[15] Wu CZ, Lu XL, Peng LL, Xu K, Peng X, Huang JL, et al. Two-dimensional vanadyl phosphate ultrathin nanosheets for high energy density and flexible pseudocapacitors. Nature Communications. 2013;**4**:2431

[16] Zuo WH, Li RZ, Zhou C, Li YY, Xia JL, Liu JP. Battery-supercapacitor hybrid devices: Recent progress and future prospects. Advancement of Science. 2017;**4**:1600539

[17] Borenstein A, Hanna O, Attias R, Luski S, Brousse T, Aurbach D. Carbon-based composite materials for supercapacitor electrodes: A review. Journal of Materials Chemistry A. 2017;**5**:12653-12672

[18] Ni JF, Li Y. Carbon nanomaterials in different dimensions for electrochemical energy storage. Advanced Energy Materials. 2016;**6**:1600278

[19] Zhu S, Wu M, Ge MH, Zhang H, Li SK, Li CH. Design and construction of three-dimensional CuO/polyaniline/rGO ternary hierarchical architectures for high performance supercapacitors. Journal of Power Sources. 2016;**306**:593-601

[20] Sun GZ, Zhang X, Lin RZ, Yang J, Zhang H, Chen P. Hybrid fibers made of molybdenum disulfide, reduced graphene oxide, and multi-walled carbon nanotubes for solid-state, flexible, asymmetric supercapacitors. Angewandte Chemie, International Edition. 2015;**54**:4651-4656

[21] Zhou QY, Fan TW, Li YY, Chen DC, Liu SL, Li X. Hollow-structure NiCo hydroxide/carbon nanotube composite for high-performance supercapacitors. Journal of Power Sources. 2019;**426**:111-115

[22] Zhou YS, Zhu YC, Xu BS, Zhang XJ. High electroactive material loading on a carbon nanotube/carbon nanofiber as an advanced free-standing electrode for asymmetric supercapacitors. Chemical Communications. 2019;**55**:4083-4086

[23] Dalton AB, Collins S, Munoz E, Razal JM, Ebron VH, Ferraris JP, et al. Supertough carbon-nanotube fibres. Nature. 2003;**423**:703

[24] Zeng YX, Zhang XY, Qin RF, Liu XQ, Fang PP, Zheng DZ, et al.

Dendrite-free zinc deposition induced by multifunctional CNT frameworks for stable flexible Zn-ion batteries. Advanced Materials. 2019;**31**:1903675

[25] Ni JF, Wang GB, Yang J, Gao DL, Chen JT, Gao LJ, et al. Carbon nanotube-wired and oxygen-deficient MoO3 nanobelts with enhanced lithium-storage capability. Journal of Power Sources. 2014;**247**:90-94

[26] Jin Q, Jiang S, Zhao Y, Wang D, Qiu JH, Tang DM, et al. Flexible layer-structured Bi2Te3 thermoelectric on a carbon nanotube scaffold. Nature Materials. 2019;**18**:62-68

[27] Black J, Andreas HA. Effects of charge redistribution on self-discharge of electrochemical capacitors. Electrochemica Acta. 2009;**54**:3568-3574

[28] Taberna PL, Portet C, Simon P. Electrode surface treatment and electrochemical impedance spectroscopy study on carbon/carbon supercapacitors. Applied Physics A: Materials Science & Processing. 2006;**82**:639-646

[29] Frackowiak E. Carbon materials for supercapacitor application. Physical Chemistry Chemical Physics. 2007;**9**:1774-1785

[30] Dinh TM, Armstrong K, Guay D, Pech D. High-resolution on-chip supercapacitors with ultra-high scan rate ability. Journal of Materials Chemistry A. 2014;**2**:7170-7174

[31] Zhu Y, Murali S, Stoller MD, Ganesh KJ, Cai W, Ferreira PJ, et al. Carbon-based supercapacitors produced by activation of graphene. Science. 2011;**332**:1537-1541

[32] Kim TY, Jung G, Yoo S, Suh KS, Ruoff RS. Activated graphene-based carbons as supercapacitor electrodes

with macro- and mesopores. ACS Nano. 2013;**7**:6899-6905

[33] Zhang LL, Zhao X, Stoller MD, Zhu Y, Ji H, Murali S, et al. Highly conductive and porous activated reduced graphene oxide films for high-power supercapacitors. Nano Letters. 2012;**12**:1806-1812

[34] Niu C, Sichel EK, Hoch R, Moy D, Tennent H. High power electrochemical capacitors based on carbon nanotube electrodes. Applied Physics Letters. 1997;**70**:1480-1482

[35] Simon P, Gogotsi Y. Charge storage mechanism in nanoporous carbons and its consequence for electrical double layer capacitors. Philosophical Transaction on Royal Society A. 2010B;**368**:3457-3467

[36] Tung VC, Chen LM, Allen MJ, Wassei JK, Nelson K, Kaner RB, et al. Low-temperature solution processing of graphene-carbon nanotube hybrid materials for high-performance transparent conductors. Nano Letters. 2009;**9**:1949-1955

[37] Xu Z, Li Z, Holt CMB, Tan X, Wang H, Amirkhiz BS, et al. Electrochemical supercapacitor electrodes from sponge-like graphene nanoarchitectures with ultrahigh power density. Journal of Physical Chemistry Letters. 2012;**3**:2928-2933

[38] Iijima S, Ichihashi T. Single-shell carbon nanotubes of 1-Nm diameter. Nature. 1993;**363**:603

[39] Saifuddin N, Raziah AZ, Junizah AR. Carbon nanotubes: A review on structure and their interaction with proteins. Journal of Chemistry. 2013;**676815**

[40] Kharissova OV, Kharisov BI. Variations of interlayer spacing in carbon nanotubes. RSC Advances. 2014;**4**:30807

[41] Bichoutskaia E, Popov AM, Lozovik YE. Nanotube-based data. Insight. 2008;**11**:38

[42] Kohler AR, Som C, Helland A, Gottschalk F. Studying the potential release of carbon nanotubes throughout the application life cycle. Journal of Cleaner Production. 2008;**16**:927

[43] Rathinavel S, Priyadharshini K, Panda D. A review on carbon nanotube: An overview of synthesis, properties, functionalization, characterization, and the application. Materials Science and Engineering B. 2021;**268**:115095

[44] Tanabi H, Erdal M. Effect of CNTs dispersion on electrical, mechanical and strain sensing properties of CNT/Epoxy nanocomposites. Results Physics. 2019;**12**:486

[45] Ma R, Wei B, Xu C, Liang J, Wu D. Development of supercapacitors based on carbon nanotubes. Science in China, Series E Technological Sciences. 2020;**43**:178

[46] Zeng Q, Li Z, Zhou Y. Synthesis and application of carbon nanotubes. Journal of Natural Gas Chemistry. 2006;**15**:235

[47] Li Q, Li Y, Zhang X, Chikkannanavar SB, Zhao Y, Dangelewicz AM, et al. Structure-dependent electrical properties of carbon nanotube fibers. Advanced Materials. 2007;**19**:3358

[48] Fu YB, Ma RB, Chen YM, Jiang DD, Zhang QY, Ma XH. The effect of acidic treatment on the lithium storage capacity of multi-walled carbon nanotubes. Journal of Materials Science: Materials in Electronics. 2007;**20**:709

[49] Robertson J. Growth of nanotubes the roadmap for semiconductor devices

envisages that carbon. Review: Literature and Arts of the Americas. 2007;**10**:36

[50] Grobert N. Carbon nanotubes – importance of clean CNT material for the success of future applications. Materials Today. 2007;**10**:28

[51] Salvetat JP, Bonard JM, Thomson NH, Kulik AJ, Forro L, Benoit W, et al. Mechanical properties of carbon nanotubes. Applied Physics A: Materials Science & Processing. 1999;**69**:255

[52] Someya T, Small J, Kim P, Nuckolls C, Yardley JT. Alcohol vapor sensors based on single-walled carbon nanotube field effect transistors. Nano Letters. 2003;**3**:877

[53] Popov VN. Carbon nanotubes: Properties and application. Materials Science Engineering Report. 2004;**43**:61

[54] Hone J, Llaguno MC, Biercuk MJ, Johnson AT, Batlogg B, Benes Z, et al. Thermal properties of carbon nanotubes and nanotube-based materials. Applied Physics A: Materials Science & Processing. 2002;**74**:339

[55] Kaempgen M, Chan CK, Ma J, Cui Y, Gruner G. Printable thin film supercapacitors using single-walled carbon nanotubes. Nano Letters. 2009;**9**:1872-1876

[56] Vincent C. Polymer electrolytes. Progress in Solid State Chemistry. 1987;**17**:145-261

[57] Nohara S, Wada H, Furukawa N, Inoue H, Morita M, Iwakura C. Electrochemical characterization of new electric double layer capacitor with polymer hydrogel electrolyte. Electrochimica Acta. 2003;**48**:749-753

[58] Kanninen P, Luong ND, Sinh LH, Anoshkin IV, Tsapenko A, Seppala J,

et al. Transparent and flexible high-performance supercapacitors based on single-walled carbon nanotube films. Nanotechnology. 2016;**27**:235403

[59] Zhu S, Ni J, Li Y. Carbon nanotube-based electrodes for flexible supercapacitors. Nano Research. 2020;**13**:7

[60] Jiang YC, Wu ZY, Jiang L, Pan ZC, Yang PY, Tian WC, et al. Freestanding $CoSeO_3 \cdot H_2O$ nanoribbon/carbon nanotube composite paper for 2.4 V high-voltage, flexible, solid-state supercapacitors. Nanoscale. 2018;**10**:12003-12010

[61] Wang Q, Wang HX, Du PC, Liu JL, Liu D, Liu P. Porous polylactic acid/carbon nanotubes/polyaniline composite film as flexible free-standing electrode for supercapacitors. Electrochimica Acta. 2019;**294**:312-324

[62] Hou XY, Peng T, Cheng JB, Yu QH, Luo RJ, Lu Y, et al. Ultrathin ZnS nanosheet/carbon nanotube hybrid electrode for high-performance flexible all-solid-state supercapacitor. Nano Research. 2017;**10**:2570-2583

[63] Zeng S, Chen HY, Cai F, Kang YR, Chen MH, Li QW. Electrochemical fabrication of carbon nanotube/polyaniline hydrogel film for all-solid-state flexible supercapacitor with high areal capacitance. Journal of Materials Chemistry A. 2015;**3**:23864-23870

[64] Guo RS, Chen JT, Yang BJ, Liu LY, Su LJ, Shen BS, et al. In-plane micro-supercapacitors for an integrated device on one piece of paper. Advanced Functional Materials. 2017;**27**:1702394

[65] Liu ZY, Wu ZS, Yang S, Dong RH, Feng XL, Mullen K. Ultraflexible in-plane micro-supercapacitors by direct printing of solution-processable

electrochemically exfoliated graphene. Advanced Materials. 2016;**28**:2217-2222

[66] Du JW, Mu XM, Zhao YR, Zhang YX, Zhang SM, Huang BY, et al. Layered coating of ultraflexible graphene-based electrodes for high-performance in-plane quasi-solid-state micro-supercapacitors. Nanoscale. 2019;**11**:14392-14399

[67] Liu NS, Gao YH. Recent progress in micro-supercapacitors with in-plane interdigital electrode architecture. Small. 2017;**13**:1701989

[68] Pu X, Liu MM, Li LX, Han SC, Li XL, Jiang CY, et al. Wearable textile-based in-plane microsupercapacitors. Advanced Energy Materials. 2016;**6**:1601254

[69] Li JH, Shi QW, Shao YL, Hou CY, Li YG, Zhang QH, et al. Cladding nanostructured AgNWs-MoS$_2$ electrode material for high-rate and long-life transparent in-plane micro-supercapacitor. Energy Storage Mater. 2019;**16**:212-219

[70] Rani S, Kumar N, Tandon A, Sharma Y. Electrophoretic grown TiO$_2$-based interdigitated microsupercapacitor: Device fabrication and characterization for flexible electronics. IEEE Transactions on Electron Devices. 2021;**68**:10

[71] Song Y, Chen XX, Zhang JX, Cheng XL, Zhang HX. Freestanding micro-supercapacitor with interdigital electrodes for low power electronic systems. Journal of Microelectromechanical System. 2017;**26**:1055

[72] Rani S, Kumar N, Tandon A, Sharma Y. Fabrication of binder free TiO$_2$ nanofiber electrodes via electrophoretic deposition for low power electronic applications. IEEE Transactions on Electron Devices. 2021;**68**:251

[73] Chen CC et al. Performance enhancement on an InGaP/InGaAs PHEMT with an electrophoretic deposition gate structure. IEEE Electronic Device Letters. 2014;**35**:18

[74] Singh BK, Shaikh A, Dusane RO, Parida S. Nanoporous Gold-Nitrogen-doped carbon nano-onions all-solid-state microsupercapacitor. Nano-Struct. Nano-Objects. 2019;**17**:239-247

[75] Rani S, Kumar N, Sharma Y. Recent progress and future perspectives for the development of micro-supercapacitors for portable/wearable electronics applications. Journal of Physics Energy. 2021;**3**:230

[76] Kumar N, Singh M, Kumar A, Tseng TY, Sharma Y. Facile and one-step in situ synthesis of pure phase mesoporous Li2MnSiO4/CNTs nanocomposite for hybrid supercapacitors. ACS Applied Energy Materials. 2020;**3**:2450-2464

[77] Boruah BD, Maji A, Misra A. Flexible array of microsupercapacitor for additive energy storage performance over a large area. ACS Applied Materials & Interfaces. 2018;**10**:15864-15872

[78] Zhang L et al. Photolithographic fabrication of graphene-based all-solid-state planar on-chip microsupercapacitors with ultrahigh power characteristics. Journal of Applied Physiscs. 2019;**126**:16

[79] Lee KH, Lee SS, Ahn DB, Lee J, Byun D, Lee SY. Ultrahigh areal number density solid-state on-chip microsupercapacitors via electrohydrodynamic jet printing. Science Advances. 2020;**6**:eaaz16

[80] Wang J, Wang X, Lee SW, Zhang Q. Enhanced performance of an electric double layer microsupercapacitor

based on novel carbon encapsulated cu nanowire network structure as the electrode. ACS Applied Materials Interface. 2019;**11**:43

[81] Chen T, Dai L. Flexible and wearable wire-shaped microsupercapacitors based on highly aligned Titania and carbon nanotubes. Energy Storage Mater. 2016;**2**:21-26

[82] Jeong HT, Du JF, Kim YR. Development of flexible energy storage device by using polymer electrolyte based on ionic liquid. ChemistrySelect. 2017;**2**:6057-6061

[83] Zhang J, Dong L, Xu C, Hao J, Kang F, Li J. Comprehensive approaches to three-dimensional flexible supercapacitor electrodes based on MnO_2/carbon nanotube/activated carbon fiber felt. Journal of Material Science. 2017;**52**:5788-5798

[84] Iqbal N, Wang X, Babar AA, Zainab G, Yu J, Ding B. Flexible Fe_3O_4 carbon nanofibers hierarchically assembled with MnO_2 particles for high-performance supercapacitor electrodes. Scientific Reports. 2017;**7**:15153

[85] Li X et al. High energy flexible supercapacitors formed via bottom-up infilling of gel electrolytes into thick porous electrodes. Nature Communications. 2018;**9**:1

[86] Lee K, Lee H, Shin Y, Yoon Y, Kim D, Lee H. Highly transparent and flexible supercapacitors using graphene-graphene quantum dots chelate. Nano Energy. 2016;**26**:746-754

[87] Lee G et al. Fully biodegradable microsupercapacitor for power storage in transient electronics. Advanced Energy Materials. 2017;**7**:1700157

[88] Liu W et al. Paper-based all-solid-state flexible micro-supercapacitors

with ultra-high rate and rapid frequency response capabilities. Journal of Material Chemistry A. 2016;**10**:3754

[89] Zhang CJ et al. Stamping of flexible, coplanar micro-supercapacitors using MXene inks. Advanced Functional Materials. 2018;**28**:1705506

[90] Lee SY, Choi KH, Choi WS, Kwon YH, Jung HR, Shin HC, et al. Progress in flexible energy storage and conversion systems, with a focus on cable-type lithium-ion batteries. Energy & Environmental Science. 2013;**6**:2414-2423

[91] Vellacheri R, Zhao HP, Muhlstadt M, Al-Haddad A, Jandt KD, Lei Y. Rationally engineered electrodes for a high-performance solid-state cable-type supercapacitor. Advanced Functional Materials. 2017;**27**:1606696

[92] Chen YJ, Xu BG, Wen JF, Gong JL, Hua T, Kan CW, et al. Design of novel wearable, stretchable, and waterproof cable-type supercapacitors based on high-performance nickel cobalt sulfide-coated etching-annealed yarn electrodes. Small. 2018;**14**:1704373

[93] Pu X, Li LX, Liu MM, Jiang CY, Du CH, Zhao ZF, et al. Wearable self-charging power textile based on flexible yarn supercapacitors and fabric nanogenerators. Advanced Materials. 2016;**28**:98-105

[94] Liu LB, Yu Y, Yan C, Li K, Zheng ZJ. Wearable energy dense and power-dense supercapacitor yarns enabled by scalable graphene–metallic textile composite electrodes. Nature Communications. 2015;**6**:7260

[95] Rani S, Sharma Y. Fabrication of binder-free and high energy density yarn supercapacitor for wearable electronics. IEEE Transactions on Power Electronics. 2022;**37**:11

[96] Pandit B et al. Two-dimensional hexagonal SNSE nanosheets as binder free electrode material for high-performance supercapacitors. IEEE Transactions on Power Electronics. 2020;**35**:11344

[97] Sandhiya M, Balaji SS, Sathish M. Na_2MoO_4- incorporated polymer gel electrolyte for high energy density flexible supercapacitor. ACS Applied Energy Materials. 2020;**2**:11368

[98] Elkholy AE, Dhmees AS, Heakal FET, Deyab MA. Mesoporous znmoS4 as a supercapacitor electrode material with battery-like behavior. New Journal of Chemistry. 2019;**43**:1987-1992

[99] Jain D, Kanungo J, Tripathi SK. Synergistic approach with redox additive for the development of environment benign hybrid supercapacitor. Journal of the Electrochemical Society. 2019;**166**:A3168-A3181

[100] He N, Liao J, Zhao F, Gao W. Dual-core supercapacitor yarns: An enhanced performance consistency and linear power density. ACS Applied Materials & Interfaces. 2020;**12**:15211-15219

[101] Shewale PS, Yun KS. $NiCo_2O_4$/ RGO hybrid nanostructures on surface-modified ni core for flexible wire-shaped supercapacitor. Nanomaterials. 2021;**11**:852

[102] Li T, Wu Y, Wang Q, Zhang D, Zhang A, Miao M. TiO_2 crystalline structure and electrochemical performance in two-ply yarn CNT/TiO_2 asymmetric supercapacitors. Journal of Materials Science. 2017;**52**:7733

[103] Zhao P et al. Iodine-steam functionalized reduced graphene oxide/ oxidized carbon yarn electrodes for knittable fibriform supercapacitor. Journal of Power Sources. 2019;**442**

[104] Zhao P et al. Three-dimensional ordered macroporous $NiFe_2O_4$ coated carbon yarn for knittable fibriform supercapacitor. Electrochimica Acta. 2018;**281**:717-724

Edited by Mohammed Muzibur Rahman,
Abdullah Mohammed Asiri
and Mohammad Asaduzzaman Chowdhury

Carbon Nanotubes - Recent Advances, New Perspectives and Potential Applications
covers all the important nanotechnological aspects of carbon materials, including
their growth and characterization, processing and fabrication, development and
potential applications. Recent developments, innovative preparation methods and
promising new frontiers around this advanced nanotechnology are reviewed under
the editorship of an internationally renowned scientist. This book will be useful to a
diverse range of readers and will be important for research organizations, government
research centers, academic libraries, and those involved in the research and
development of carbon materials.

IntechOpen